Chemodynamical Modeling of Young Disk Galaxies

Inauguraldissertation

zur
Erlangung der Würde eines Doktors der Philosophie
vorgelegt der
Philosophisch – Naturwissenschaftlichen Fakultät
der Universität Basel

von

Andreas Immeli

aus Gempen (SO)

Basel, 2003

Genehmigt von der Philosophisch-Naturwissenschaftlichen Fakult¨at
auf Antrag von Prof. Dr. O. E. Gerhard und Prof. Dr. D. Pfenniger

Basel, den 21. Oktober

Prof. Dr. M. Tanner
Dekan

Contents

1 Introduction **7**

1.1 Motivation . . . 8
1.2 Cosmological Model and Structure Formation . . . 8
1.3 Galactic Evolution from Observations . . . 9
1.3.1 Observations at High Redshift . . . 9
1.3.2 Observations of Local Galaxies . . . 11
1.4 Galaxy Evolution Models . . . 12
1.5 Bulge Formation . . . 13
1.6 Units and Constants . . . 14
1.7 Outline of the Thesis . . . 14

2 The Chemodynamical Model **15**

2.1 Overview . . . 16
2.2 The Interstellar Medium . . . 16
2.2.1 Dynamics of the ISM . . . 17
2.2.2 Cooling of the ISM . . . 18
2.2.3 Evaporation and Condensation . . . 19
2.3 The Stars . . . 21
2.3.1 Dynamics of the Stars . . . 21
2.3.2 Star Formation . . . 22
2.3.3 Stellar Lifetimes . . . 24
2.3.4 Mass Return Rate . . . 24
2.3.5 High Mass Stars ($M > 10\ \mathrm{M}_\odot$) . . . 25
2.3.6 Intermediate Mass Stars ($0.8\ \mathrm{M}_\odot < \mathrm{M} < 10\ \mathrm{M}_\odot$) . . . 26
2.3.7 Low Mass Stars ($M < 0.8\ \mathrm{M}_\odot$) and Stellar Remnants . . . 27
2.3.8 Supernova of Type Ia . . . 27
2.4 Dark Matter Halo . . . 29
2.5 Gravitation . . . 30
2.6 Self-Regulation and Equilibria . . . 30
2.7 Extensions to the Model . . . 31
2.7.1 Calculation of Intrinsic Colors . . . 31
2.7.2 Calculation of Absorption . . . 31
2.7.3 Calculations of Colors at Non-Zero Redshift . . . 31
2.7.4 An Efficient Way to Derive Restframe Colors . . . 32

3 Numerical Methods **33**

3.1 The Grid . . . 34

3.2 Hydrodynamics . . . 34
3.2.1 Operator Splitting . . . 34
3.2.2 Transport Steps . . . 35
3.2.3 Discretization of the Source Steps . . . 37
3.2.4 Artificial Viscosity . . . 37
3.3 Gravitational Potential . . . 38
3.3.1 Successive Overrelaxation . . . 38
3.3.2 Fast Fourier Transformation . . . 40
3.3.3 SOR versus FFT . . . 40
3.3.4 Boundary Condition for the Gravitational Potential . . . 41
3.4 Test Calculations . . . 41
3.4.1 Shock-Tube . . . 41
3.4.2 Blast Waves . . . 42
3.4.3 Free Collapse . . . 43
3.5 Particle Mesh Method for the Stars . . . 43
3.6 Interactions . . . 44
3.7 Time Step Control . . . 45
3.8 Boundary Conditions . . . 46
3.8.1 Boundary Condition Used in the Disk Evolution Models . . . 47
3.9 Initial Conditions . . . 47
3.10 Flowchart of the Numerical Model . . . 48
3.11 Code Optimization . . . 49
3.12 The New Parallel Chemodynamical Evolution Code . . . 49

4 Gas Physics, Disk Fragmentation,and Bulge Formation in Young Galaxies 51
4.1 Introduction . . . 52
4.2 The Model . . . 53
4.3 Morphological Evolution . . . 54
4.3.1 Settling of the Disk . . . 54
4.3.2 Face-On Evolution . . . 55
4.4 Global Properties . . . 58
4.4.1 Stability of the Disk . . . 58
4.4.2 Star Formation Rate . . . 59
4.4.3 Metallicity Distribution . . . 61
4.5 Bulge Formation . . . 62
4.5.1 Clump Merging . . . 63
4.6 Bar Evolution . . . 64
4.7 Conclusion . . . 65

5 Sub-Galactic Clumps at High Redshift: A Fragmentation Origin? 67

5.1 Introduction . . . 68
5.2 The Model . . . 68
5.3 Results and Comparison to Observations . . . 68
5.3.1 Global Evolution . . . 68
5.3.2 Comparison with Observations . . . 69
5.4 Merger or Fragmentation? . . . 71
5.5 Conclusions . . . 72

6 Supernova Induced Gas Flows 73

6.1 Introduction . . . 74
6.2 The Model . . . 74
6.3 Wind Structure . . . 75
6.3.1 Peak Star Formation in a Clumpy Disk (B0) . . . 75
6.3.2 Gas Flows in the Thin Disk (B1) . . . 75
6.3.3 Gas Flows in the Extended Disk Model D1 . . . 76
6.4 Galactic Superwinds . . . 77
6.5 Discussion of Wind Properties . . . 78
6.6 X-ray Fluxes of Winds . . . 79

7 Summary and Outlook 81

7.1 Summary . . . 82
7.2 Outlook . . . 83
7.2.1 Physical and Technical Improvements . . . 83
7.2.2 Future Scientific Projects . . . 84

A Appendix: Dynamical Equations 85

A.1. Introduction . . . 86
A.2. Vlasov and Boltzmann Equation . . . 86
A.3. Dynamical Equations of a Collision Free System . . . 87
A.3.1. Mass Conservation . . . 88
A.3.2. Momentum Conservation . . . 88
A.3.3. Energy Conservation . . . 88
A.4. Dynamical Equations of a Collision Dominated System . . . 90
A.4.1. Mass Conservation . . . 91
A.4.2. Momentum Conservation . . . 91
A.4.3. Energy Conservation . . . 91
A.5. Formal Analogy and Description of the CM and the ICM . . . 93

B Appendix: High Performance Computing **95**

B.1. Code Optimization 96

B.1.1. Data Output 97

B.1.2. Profiling 98

B.2. Vectorization 98

B.3. Parallelization 99

B.3.1. Parallelization with HPF 99

B.4. Analysis Library 101

C Appendix: Abbreviations and Symbols **103**

C.1. Abbreviations 104

C.2. Symbols 105

Bibliography **107**

List of Figures **115**

List of Tables **117**

Acknowledgements **119**

Declaration **121**

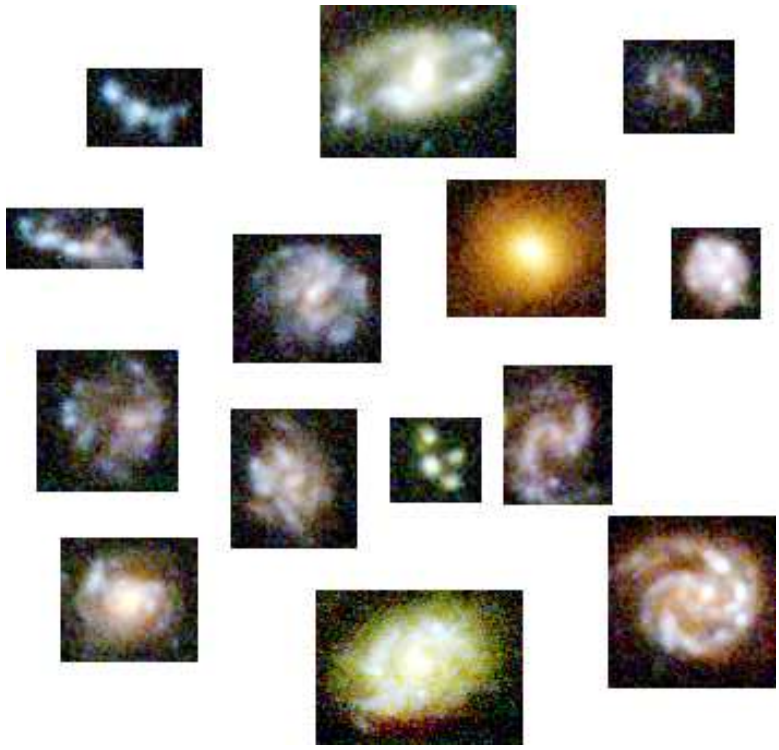

1

Introduction

The theory of the formation of galaxies is one of the great outstanding problems of astrophysics, a problem that today seems far from solution.
Weinberg (1977)

Even though in the last quarter of a century the astronomical community gained an overwhelming amount of new observational and theoretical knowledge about galaxy formation, the statement of Weinberg remains true.
In the introduction I present first a short overview over the current standard cosmological model and the structure formation within this cosmology. In a second part I discuss the observational signatures of galaxy evolution, which can be gained from high redshift observations as well as from local galaxies. In a third part, an overview of galaxy evolution and bulge formation models is given.

1.1. Motivation

Most of the large galaxies known in the local universe can be assigned to a type on the Hubble sequence. This scheme divides the galaxies, according to their shape and appearance into elliptical, spiral and irregular galaxies. There are subgroups in all these categories. The question of galaxy formation is closely linked to the question of how and when did the Hubble sequence appear. Due to the various physical processes involved in galaxy formation it was soon realized that observational data of young galaxies are needed. In the past decade much progress has been made on the search for young, i.e. high redshift galaxies. Data obtained with powerful observation facilities, like e.g. the Very Large Telescope (VLT), or the Hubble Space Telescope (HST) gave new insight on the process of galaxy formation and a fair amount of observational data out to redshift $z = 4$ is available now, with the most distant galaxy lying at $z = 6.56$. This data will be largely enhanced by the planned observation facilities like the James Webb Space Telescope (JWST), the Atacama Large Milimeter Array (ALMA), the Planck Surveyor satellite, or the Global Astrometric Interferometer for Astrophysics (GAIA).

This puts forward the need for realistic galaxy formation models, which can be compared to observations. With the rising computational power it has become possible to simulate the formation and evolution of galaxies in three dimensional numerical models, including the important physical processes. Hence galactic evolution is an active field and due to the large observational and computational power available in the next decades, it will remain an active field of astronomical research.

1.2. Cosmological Model and Structure Formation

Following Hu & Dodelson (2002) the current working cosmological model is: *A critical density universe consisting of mainly dark matter and dark energy, which formed its structure through gravitational instability from quantum fluctuations during an inflationary epoch.*

This cosmological model is mainly motivated through observations of the cosmic microwave background (CMB). The CMB predicted by Gamov (1948) and discovered by Penzias & Wilson (1965) resembles a black body radiation to a very high precision (Mather et al., 1990; Cheng et al., 1996), with a temperature $T_{\rm CMB} = 2.728 \pm 0.004$ K. Although the CMB is remarkably isotropic it shows temperature fluctuations of the order of 10^{-5} K (see Fig. 1.1). These fluctuations correspond to density fluctuations in the early universe (see Hu & Dodelson (2002) for a detailed description). These density fluctuations arisen from quantum mechanical fluctuations during the exponential expansion of the universe build the starting point for structure formation.

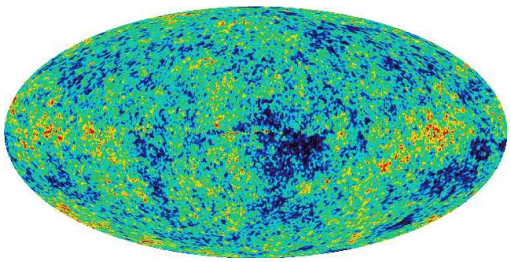

Figure 1.1. Detailed full sky may of the CMB from the Wilkinson Microwave Anisotropy Probe (WMAP). Warmer and cooler spots are indicated by red and blue colors respectively.

From the fluctuation spectrum, a variety of physical informations can be extracted. The location of the first peak, measured precisely in experiments like Toco (Miller et al., 1999), Boomerang (de Bernardis et al., 2000), and Maxima-1 (Hanany et al., 2000) leads to the conclusion that the universe is flat. The CMB measurements determined the baryon mass fraction Ω_b to 0.045 ± 0.005 of the critical density of the universe $\rho_{\rm crit}$ and the total mass fraction Ω_M to 0.27 ± 0.03 (Spergel et al., 2003). This is in a remarkable consistency with big bang nucleosynthesis models (e.g. Boesgaard & Steigman, 1985; Schramm & Turner, 1988). To get a flat universe (Ω_M + Ω_Λ = 1) the existence of dark matter, having a non-baryonic nature, and dark energy is implied. This is consistent with completely independent measurements of distant supernovae (Riess et al., 1998; Perlmutter et al., 1999; Eke et al., 2000), indicating an accelerated universe.

The amount and type of the dark matter in the universe determines the way in which structure grows. The structure formation models follow the evolution from the first density fluctuations to the formation of the dark matter halos. Currently, the Λ cold dark matter (ΛCDM) paradigm is favored. In these models, the regions of enhanced density start to contract due to self gravity, decouple from the expanding universe and build the first dark halos. In the ΛCDM paradigm, the formation of low mass objects takes place first. Objects with higher masses form through hierarchical merging of the low mass objects.

In the last decade, several high resolution simulations of structure formation have been carried out (e.g., Navarro et al., 1996; Moore et al., 1998; Jenkins et al., 2001; Klypin et al., 2001). In Fig. 1.2 a slice through a 100 Mpc region in a ΛCDM simulation is shown. Gravity leads to dense structures (yellow) in which the galaxies evolve. The profiles of these dark halos are well reproduced through a universal profile (Navarro et al., 1997). Properties like mass growth and angular momentum distribution are available in approximate form (Bullock et al., 2001; Wechsler et al., 2002).

The currently favored model, the ΛCDM cosmology, seems to be the most promising model to explain structure for-

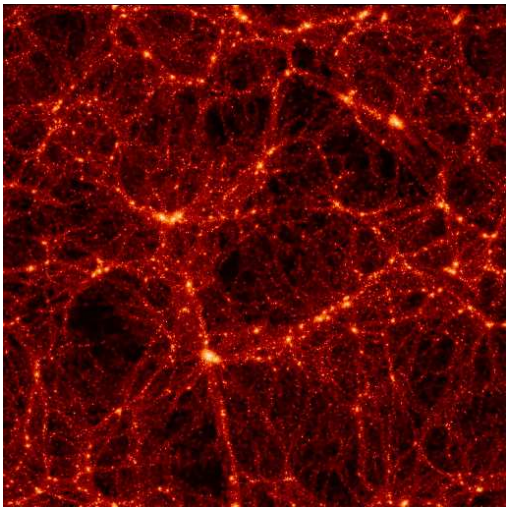

Figure 1.2. A slice through a 100 Mpc region of a ΛCDM Universe. The bright regions show the high density halos in which the galaxies form.

mation. It explains for example the spatial distribution of dark matter halos (Sheth & Tormen, 1999; Jenkins et al., 2001) as well as the measurements of distant supernovae (Riess et al., 1998; Perlmutter et al., 1999; Eke et al., 2000). However, severe problems remain like the satellite problem (Moore et al., 1999), the angular momentum problem (Sommer-Larsen et al., 2002), the disk heating through substructure (Font et al., 2001), and the predicted cuspy profiles of the dark halos in the center, which are not observed (e.g. Salucci & Burkert, 2000; de Blok et al., 2001).

As already proposed by White & Rees (1978), galaxies are thought to form in the dark halos when the baryonic matter condenses, cools and forms stars at the bottom of the potential wells of these halos. Hence the assembly of the dark halos as well as internal properties like mass, total angular momentum and angular momentum distribution have strong impact on the evolution of galaxies.

1.3. Galactic Evolution from Observations

Constraints on the evolution of galaxies can be obtained mainly through two different approaches. First, the observation of old stellar populations, having ages comparable to the lookback time to high redshift galaxies, in our own or in local galaxies can reveal information about their formation process. Second, the identification of young galaxies at high redshift reveals a possibility to directly observe the accumulation of the galaxies, at much lower resolution, of course.

1.3.1. Observations at High Redshift

Due to the complicated processes which are important during galaxy formation, like e.g. star formation, baryon dissipation, mass and energy feedback from the stars, no theory exists at the moment, which can explain the formation of galaxies from first principles. It was recognized already in the 70's that the search for young galaxies is an important cornerstone in the understanding of the galaxy formation process. Those, so-called primeval galaxies, were looked for using different methods (e.g. Partridge, 1974; Davis & Wilkinson, 1974), mostly concentrated on redshifted Lyman-α emission (e.g. Koo & Kron, 1980), but reporting no detections.

In the last decade it has become possible to observe galaxy scaled objects in the far universe through the use of the Lyman break technique. The frontier for the redshift surveys was shifted from $z \sim 1$ to $z \sim 4$, which corresponds to about 90% of the lookback time. In Fig. 1.3 some examples of observations at different redshifts are given. The dotted lines indicate, where the galaxies are located in the diagram. The amount of observational data for high and intermediate range redshifts grew rapidly in the last years and, in principle, galaxy evolution is now directly accessible through observations from about one Gyr after the big bang. However, a consistent picture for the formation of galaxies is still lacking.

Through the technique of band dropouts many galaxies at redshifts $z > 2$ could be detected. In this technique one uses the fact that the Lyman continuum discontinuity at 912 Å – a feature formed in atmospheres of massive stars as a result of the hydrogen ionization edge, often referred as Lyman break – is shifted out of a given band at a certain redshift. E.g. galaxies at $z \sim 3$ can be found by searching for U-band dropouts. These high redshift candidates are afterwards spectroscopically confirmed, with around $\sim 90\%$ of U-band dropouts being galaxies around $z \sim 3$. The yield gets worse for B and V band dropouts, sensitive to redshifts $z \sim 4$ and $z \sim 5$, where 50% and 20% could be confirmed respectively (Steidel et al., 1999). With this technique the number of high redshift galaxies rose to ~ 1000 and several thousand candidates (Steidel et al., 1999). The galaxies found through this technique are often referred to as Lyman Break Galaxies (see Giavalisco, 2002, for a review).

Observing galaxies at high redshifts introduces several observational challenges. Following Abraham & van den Bergh (2002) three effects have the most impact on high-redshift galaxy observations. First, the resolution/pixellation effects introduce an error. Mostly this is a minor source of error, because of the high resolution of HST and the evolution of the angular diameter distance at high redshift. However, compared to local galaxies the typical pixel number is a factor of 100

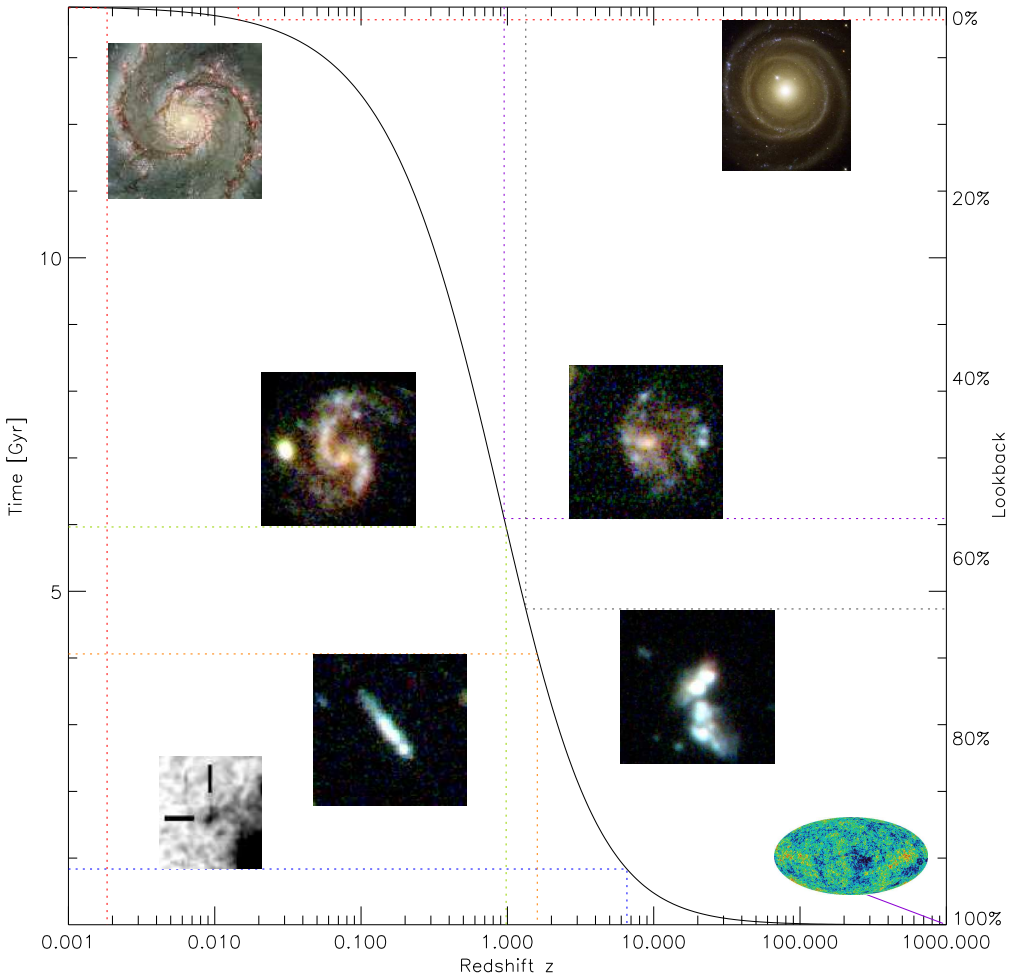

Figure 1.3. Galaxy evolution as seen in observations. The focus has been set on possible disk galaxies. The location of the galaxies on the black line is indicated through the dotted lines.

smaller. The situation will improve when the JWST is in duty.

Secondly, the band shifting of the rest frame wavelength of the observations introduces an incertitude to morphological investigations. Since the observed galaxies lie at different redshifts, the same filter bass-band traces different rest-frame wavelengths. The for morphological investigations mostly used F814W filter (approx. I-band) corresponds to the B-band at the redshift $z \simeq 0.7$. Hence the effects of the so-called morphological k-correction may not be severe until a redshift of $z \simeq 1$, but the uncertainty steadily increases when approaching higher redshifts. Galaxies farther away are observed in the ultraviolet restframe wavelength. This poses a problem for the morphological classification, since studies of nearby galaxies show large morphological differences of ultraviolet and optical wavelength (e.g. Marcum et al., 2001). However, the morphological structures remain even in HST images done with the Near-Infrared Camera Multi-Object Spectrometer (NICMOS) (Dickinson, 2000; Ferguson et al., 2000), which probes the visual restframe wavelength to much higher redshift. This implies that the morphological structures seen in the HDF cannot only be attributed to band-shifting effects at least to a redshift of $z = 3$.

Thirdly, the effects of cosmological surface brightness dimming and the evolution of the stellar populations enter the problem.

It is noteworthy that the determination of the redshifts of distant galaxies is far from trivial. Resolved spectra are necessary to conclusively determine the redshift of an object. Galaxies can be detected on CCDs to a much fainter level than can be investigated spectroscopically. The largest sample of spectroscopically determined redshifts was obtained by Brinchmann et al. (1998) taking HST images from galaxies, for which the redshifts were known spectroscopically from the Canada-France Redshift Survey.

Another technique is to determine photometric redshifts of the objects. In this procedure the colors of the galaxy are used to estimate its redshift. Assumptions of the intrinsic spectra have to be made which makes this procedure a fairly crude estimator ($\Delta z \sim 0.1$) of the real redshifts (Hogg et al., 1998). An extensive catalogue of photometric redshifts of the Hubble Deep Field (HDF) is given in Fernandez-Soto et al. (1999).

Despite the problems concerning the morphology and redshift determinations of high redshift objects, some results are well established. At $z \simeq 1$, the bright early and intermediate type galaxies ($L > 0.3\ L^*$) were largely formed (e.g Brinchmann & Ellis, 2000; Cimatti et al., 2002). It seems that the bulge-to-disk Hubble sequence is already in place and only evolved moderately from then to present (Abraham & Merrifield, 2000; Kajisawa & Yamada, 2001).

The fraction of irregular galaxies rises when observing at higher z (e.g. Abraham et al., 1996; van den Bergh et al., 2000), beyond the range that is expected from systematic miss-classifications. NICMOS observations (Dickinson, 2000; Ferguson et al., 2000) showed that the peculiar morphologies cannot only be attributed to band-shifting effects. The fraction of late type galaxies in the HDF drops by a factor of 2 out to $z \sim 1$, presumably because many late type galaxies were classified as peculiar at higher redshifts. This indicates that especially gas rich systems underwent an evolution from those redshifts until today. The fraction of the peculiar or merger classified objects shows a steady increase with growing redshift. While at $z \sim 0$ around 5% of the galaxies show peculiar or merger morphology, this fraction increases to 10% at $z \sim 0.4$ to 19% at $z \sim 0.7$ and to 30% at $z \sim 1$ (Abraham & van den Bergh, 2002).

Additionally it is well established that the fraction of barred spirals drops beyond $z = 0.5$ (e.g. Abraham et al., 1999). van den Bergh et al. (2002) showed that this is not a selection effect. They shifted a local galaxy sample to higher redshifts and concluded that most of the barred galaxies would still be visible. Thus, the absence of bars at higher redshifts seems to be real. Another possibility would be that the disks of barred galaxies at high redshifts are too faint to be detected. Hence, barred galaxies may be misclassified as edge on systems (Merrifield, 2002).

Unfortunately, a relatively large gap of observations exists in the redshift range $1 < z < 2$, where still only a small sample of observations is available (Giavalisco, 2002). A larger sample in this redshift range would by particularly interesting, because it is thought that the Hubble sequence is assembled in this epoch (Abraham & Merrifield, 2000; Kajisawa & Yamada, 2001).

Possibly the peculiar morphologies at the redshift range $1 < z < 3$ can be attributed to mergers. Due to the higher density of the early universe mergers should be more common than today. However, most objects classified as mergers in deep HST images are only merger candidates and a large-sample statistical analysis of the merger rate as a function of redshift has not been undertaken so far (Abraham & van den Bergh, 2001). Although it is very probable that some objects indeed are mergers, some peculiar systems exhibit properties, like synchronized internal colors, which are not observed in nearby mergers.

As can be already seen in the collection of objects from the HDF on the title page of this chapter, there are many knotty structures and peculiar morphologies visible at high redshifts. van den Bergh et al. (1996) give several examples of galaxies consisting of multiple clumps, or exhibiting very prominent spiral arms. Cowie et al. (1995) report the observations of chain galaxies. These are high redshift galaxies observed with HST in the Hawaii Survey Fields, with large major-to-minor axis ratios, knotty structures and very blue colors. CHS95 suggest that chain galaxies in the redshift range $0.5 - 3$ have a mass comparable to that of a present-day galaxy and that they represent a new population of galaxies. I discuss the chain galaxies and knotty structures in the context of the model presented here in Chap. 5. I suggest that these structures represent a fragmented disk, seen from different viewing angles.

1.3.2. Observations of Local Galaxies

While at high redshifts one can observe single galaxies in their early evolutionary state, the coarse resolution in these observations does not allow for detailed determination of e.g. stellar kinematics, metallicity distribution, etc. of these objects. But exactly these signatures can be used to constrain the formation of galaxies, when observed in local galaxies, and especially in the Milky Way. Because the oldest stars have ages comparable to high redshift objects, some signatures at least of the formation process of the Milky Way are stored in these populations.

The abundance of metals in the stellar atmospheres of low mass stars reflects the metallicity of the gas, from which these stars were formed (Tinsley, 1974; Argast et al., 2000). Through measuring this metallicity either with spectral or photometric methods, it is possible to obtain informations about the interstellar medium at the time when this star was formed. Deriving the ages of the stars allows to trace the gas metallicity of the respective region over an interval in time, provided the stars observed were born near this region of the galaxy. This assumption is mostly justified, since the stars form a collision-less system.

The metallicity distribution leads to insight about the star formation history of a galaxy. The different element pattern in the yields of supernovae of type II (SNII) (Woosley & Weaver, 1995; Thielemann et al., 1996) and supernovae of type Ia (SNIa) (Nomoto et al., 1984, 1996) combined with the longer evolutionary timescale of the

SNIa allows for the determination of the timescale of the star formation process. If most of the gas mass is converted into stars faster than the timescale for SNIa metal feedback, they will show the typical α-enhancement emerging from the SNII. Only when the ISM gets enriched by the metal feedback from the SNIa, the enhancement gets weaker and can disappear, because SNIa produce large amounts of iron. Through observing the evolution of [α/Fe] it is possible to roughly determine the timescale of the enrichment process of a system or subsystem, and hence to constrain the star formation history (see Chap. 4).

Another tracer of the formation process of a galaxy is the kinematics of the stars. Eggen et al. (1962) already used the kinematical and metallicity signatures of high velocity stars to infer that the more metal poor stars are located in the halo which was created in a rapid collapse. Minor merger events may thicken the galactic disk, whereas a satellite with enough mass can cause severe damage to the disk (Huang & Carlberg, 1997) and hence constraints on the past merger events can be drawn from the kinematics of galactic discs.

There are several signs that mergers play a role in galaxy evolution even today. Recent evidence that cannibalism happens between galaxies was the discovery of the Sagittarius dwarf galaxy (Ibata et al., 1995), currently falling into the Galaxy. Multiple stellar populations have been detected in the globular cluster ω Cen (Lee et al., 1999). Additionally, the retrograde rotation and the very bound orbit of ω Cen suggests that it is the remainder of a captured dwarf galaxy (Freeman & Bland-Hawthorn, 2002). Also in the halo of M31 a giant stellar stream was identified (Ferguson et al., 2002). In the data of Edvardsson et al. (1993) the galactic disk shows an abrupt change in the vertical stellar velocity dispersion at an age of around 10 Gyr, possibly reflecting disk heating through a minor merger event, about 10 Gyr ago. However, other processes may lead to a thickening of the disk like the heating through transient spiral arms. The launch of GAIA will lead to large progress in this field (see Freeman & Bland-Hawthorn, 2002).

An example for an ongoing major merger is the famous Antennae galaxy. Most of the Ultra Luminous Infrared Galaxies (ULIRGs) are mergers (Scoville et al., 2000). In these major merger the galaxies change their morphology completely and a previously visible disk structure will presumably be destroyed.

The determination of the star formation history of local galaxies (Grebel, 2001) is very important for the understanding of the formation modes of the different galaxies. Although the general star formation histories of the different Hubble types seem to be understood (Sandage, 1986), influences of e.g. minor mergers have to be investigated in detail. Since the new telescopes now allow for the determination of spectra of single stars in nearby galaxies, metallicity of single stars and also their kinematics will be available for several nearby systems, which will lead to new insight into the galaxy formation process.

1.4. Galaxy Evolution Models

Eggen et al. (1962) proposed the first scenario for the evolution of the Galaxy, in which the halo and the bulge form through a rapid collapse within only 10^8 years approximately 10^{10} years ago. Their results were based on metallicity and kinematical observations of 221 dwarf stars. Sandage & Fouts (1987) expanded the sample to over 1100 stars and conclude that the halo formed through a slow collapse and that the angular momentum of the stars rises with increasing collapse factor. They also found a thick disk component which formed after the halo. They attribute the formation of a thick and thin disk (Gilmore & Wyse, 1986) to changing dissipation rates during the collapse.

As a cause of the rapid collapse in the simple scenario a metallicity gradient in the halo is expected. When investigating the metallicity gradient in globular clusters of the outer halo, Searle & Zinn (1978) did not find any significant metallicity gradient. Motivated through these observations, they propose a more chaotic origin of the galactic halo, in which the central regions form first. The stars and clusters in the outer halo are formed in transient regions of high density, which originate because of late infall of gas. Hence they proposed that the halo formed through continuous infall of matter, in the context of CDM this could be e.g. accreted dwarf galaxies.

It is noteworthy that the predictions of the simple galaxy formation scenarios are not reliable. A collapse model for galaxy formation does not necessarily produce a metallicity gradient in the halo (Samland et al., 1997). Implementing a two phase model for the ISM shows that outflow from the central regions can significantly destroy a gradient emerged during the collapse. On the other hand galaxy formation through mergers are thought to produce no metallicity gradient. But if the more massive clumps move to the central regions due to mass segregation, these due to their mass further evolved clumps will show a higher metallicity, hence producing a metallicity gradient. Therefore one has to be cautious in interpreting the observations with simple models. This puts forward the need for realistic models to describe e.g. local stellar metallicity distribution, age-metallicity relations or abundance gradients.

With closed box models (Tinsley, 1974, 1980) the local metallicity distribution, i.e. the G-dwarf problem, or the age-metallicity relation has been analyzed. Closed box models assume a perfect mixing of the gas at all times and that the volume under consideration is not affected by its environment. These models provide insight on local metallicity distributions but cannot account for self-

consistent description of the galaxy, since they do not include dynamical effects like spiral arms, super-bubbles, jets or outflows. However, these models help to understand how the ISM and the stars affect each other locally. The G-dwarf problem arisen in closed box models, was further investigated in open box models, where infall of primordial or processed gas was allowed (e.g. Rana & Wilkinson, 1986; Francois & Matteucci, 1993; Immeli, 1999). A further development came with the invention of coupled open one zone models, the so-called multi-zone models (Li & Ikeuchi, 1989; Hensler & Burkert, 1990; G¨otz & K¨oppen, 1992). These models investigate the influence of an arbitrary mass transfer between the one zone models.

A further group of models considered the purely dynamical evolution of galaxies (Larson, 1975; Burkert & Hensler, 1988). The purely dynamical models neglect the interactions between the gas phases and the stars and especially the heating and cooling processes and the evolution is therefore always determined by the dynamical timescales.

The cosmological models try to account for the formation of galaxies in the context of the large scale cosmological simulations (e.g. Navarro & White, 1994; Steinmetz, 1994; Moore et al., 1998; Jenkins et al., 2001; Klypin et al., 2001). These simulations follow the evolution of the dark halos (see Sect. 1.2). On galactic scales these simulations still lack the necessary resolution to describe the processes relevant for baryon dissipation and star formation. With semi-analytical models (e.g. Kauffmann et al., 1993; Guiderdoni et al., 1998; Cole et al., 2000) the observable global properties of a large sample of galaxies formed in the dark halos emerging in cosmological simulations are determined and compared to observations.

To account for the interactions between the gas phases and the stars and to be able to describe galaxies self-consistently, the chemodynamical approach was introduced (Theis et al., 1992; Samland et al., 1997; Bekki & Shioya, 1998; Berczik, 1999; Samland & Gerhard, 2003) . Chemodynamical models include different stellar populations, a multi-phase ISM and an interaction network for describing the mass, momentum and energy transfer between these phases. These models cannot be done analytically, since it is impossible to describe a multi-phase ISM and time delayed mass and energy feedback in an analytical way. Hence numerical models have to be developed and advanced to understand the processes which are important in the formation of galaxies.

The chemodynamical models are a powerful tool to investigate galaxy formation. They allow for comparing the young galaxies to objects at high redshift through direct determination of the model colors and morphology. On the other side, detailed kinematical structure and metallicity distribution of the stars are provided and can be compared with stars in the Milky Way or nearby galaxies.

1.5. Bulge Formation

The properties of bulges are diverse and thus probably their formation mechanisms. There is an overall trend that small bulges of late type disk galaxies show similar properties to their disks, while the large early type bulges tend to be connected to elliptical galaxies (e.g. Carollo et al., 1998; Wyse, 1999). It is not clear when and how the bulges formed. It is important to note that even if the stars in the bulge are old, not necessarily the bulge as a morphological component has to be old. Another point to mention is that there exist ultra-thin disk galaxies, which exhibit large axial ratios and do not show a bulge component (Matthews et al., 1999). Hence bulge formation is not ubiquitous in disk galaxies.

There are several formation scenarios for a galactic bulge (see Wyse et al., 1997, and references therein). First, the bulge could have formed out of the halo. Assuming that the Galaxy is typical, investigations from halo and bulge rotation infer a very similar angular momentum distribution of these components (Wyse & Gilmore, 1992), contrary to the disk. This suggests that the bulge formed as the central part of the halo with significant higher dissipation, like in the scenario proposed by Eggen et al. (1962).

A second model was proposed by Kauffmann (1996). The bulges in this model form through the destruction of disks in mergers. The stars of the destroyed disk build the bulge. Subsequently the disk has to be rebuilt. This implies that late type spirals should have older bulges that early types, since the build up of a large disk needs time in which the galaxy has to be undisturbed. This is not confirmed by observations (Wyse, 1999, and references therein) and this model seems rather oversimplified. Additionally, in a merger origin of galactic bulges one would expect the angular momentum of the bulge and the disk being misaligned or even counter-rotating components should be observed. This is not consistent with observations, although single examples exist (e.g. Sarzi et al., 2001), this is not the rule (Kuijken et al., 1996). Also the high metallicity and the narrow age distribution observed in bulges of local galaxies is not compatible with a merger origin of these objects (Wyse, 1999).

Sofue & Habe (1992) proposed a scenario of bulge formation, in which a significant amount of bulge stars form in clouds, which are ejected from a central starburst. Depending on the intensity of the central burst bulges with different sizes are formed. This scenario can explain the morphology-density relation found by Dressler (1980), in the sense that the early type galaxies are located in denser regions, where tidal encounters and mergers are more numerous and can trigger substantial gas inflow to the bulge. This results in a strong starburst and large-scale outflow leading to a larger bulge.

A further way of bulge formation would be through the accretion of stellar satellites (Aguerri et al., 2001;

Scannapieco & Tissera, 2003). In these models the bulge is formed through a collision-less accretion of dense satellites onto disk galaxies. The mass and the profile of the bulge depends on the mass and the orbit of the accreted satellite. In the context of these models, bulges of late type spirals can evolve to bulges of early type galaxies through accretion of a satellite.

The secular evolution of a galactic disk could also lead to the formation of a galactic bulge. Pfenniger & Norman (1990) have shown, that a barred potential in a flat disk can lead to heating of the stellar component in the center and a bulge like component in the central part of the disk is formed. The models of Friedli & Benz (1993) include a dissipative component which can lead to the destruction of the stellar bar producing a bulge component. In this scenario the gravitational torque induced by the bar causes an angular momentum redistribution in the gas phase leading to inflbw of gas to the center. This central mass accumulation then weakens or destroys the bar (Norman et al., 1996), possibly leading to a bulge. Especially for the late type galaxies often containing small exponential bulges this formation scenario seems probable. Courteau et al. (1996) find correlations between the disk and the bulge scale length which they interpret as a sign of secular evolution of disks. Additionally, measurements of the colors of the inner disk and the bulge reveal approximate equality, which also points to a disk bulge connection.

Noguchi (1999) propose a model of a unstable disk, which forms clumps. These clumps then merge and fall to the center, building a massive bulge.

It is one motivation for this work to investigate possible bulge formation scenarios out of a galactic disk. In the context of the evolution of young disk galaxies I discuss bulge formation, involving the scenario of a fragmenting galactic disk and the formation of the bulge through the influence of a bar (Chap. 4). I focus on the observable properties these two formation paths exhibit and also on the time in galactic evolution, when these path may happen.

1.6. Units and Constants

In the present model, I use galactic units. Masses are measured in solar masses $\mathrm{M}_\odot$, the length scale is pc and time is given in Myr. Conversions to SI units are

$$\begin{aligned} 1\ \mathrm{M}_\odot &= 1.989 \cdot 10^{30}\mathrm{kg} \\ 1\ \mathrm{pc} &= 3.086 \cdot 10^{16}\mathrm{m} \\ 1\ \mathrm{Myr} &= 3.156 \cdot 10^{13}\mathrm{s} \end{aligned}$$

The cosmological relations needed to calculate e.g. length scales at given redshifts are taken from Hogg (1999), where a nice compilation of the important relations is available. The cosmological parameters used in the model are collected in Tab. 1.1.

Matter density	$\Omega_M = 0.3$
Baryon fraction	$\Omega_b = 0.05$
Dark energy	$\Omega_\Lambda = 0.7$
Hubble constant	$\mathrm{H} = 70\ \mathrm{kms}^{-1}\mathrm{Mpc}^{-1}$

Table 1.1. Cosmological parameters used in the model.

1.7. Outline of the Thesis

After the introduction given in this chapter, the chemodynamical model is described in Chap. 2. Chap. 3 deals with numerical methods. The scientific results are presented in Chap. 4, Chap. 5, and Chap. 6:

- In Chap. 4 I investigate the influence of the cloud dissipation process on the evolution of a galactic disk. I discuss disk stability in the context of the Toomre Q parameter and follow the two bulge formation paths I obtained in the model sequence used for this investigation.
  Reference: *Immeli, A., Samland, M., Gerhard, O., Westera, P. 2003, A&A accepted*
- In Chap. 5 the model of a fragmented disk, calculated at high resolution, is compared to observations of high redshift objects. I show that several observations at high redshift, like prominent spiral arms, systems consisting of multiple clumps and chain galaxies can be understood in the context of a fragmented disk.
  Reference: *Immeli, A., Samland, M., Gerhard, O., Westera, P. 2003, ApJL submitted*
- Chap. 6 discusses the structure of supernova driven gas flows. I focus on the influence of a thin and extended ISM disk on the wind structure. This chapter is part of a publication, which is in preparation.

Since those chapters will be published independently, they also contain a short description of the model.

A summary and an outlook of possible future scientific projects is given in Chap. 7. The derivation of the dynamical equations is given in Appendix A. Appendix B deals with some issues concerning high performance computing and an overview over the symbols used throughout the thesis can be found in the Appendix C.

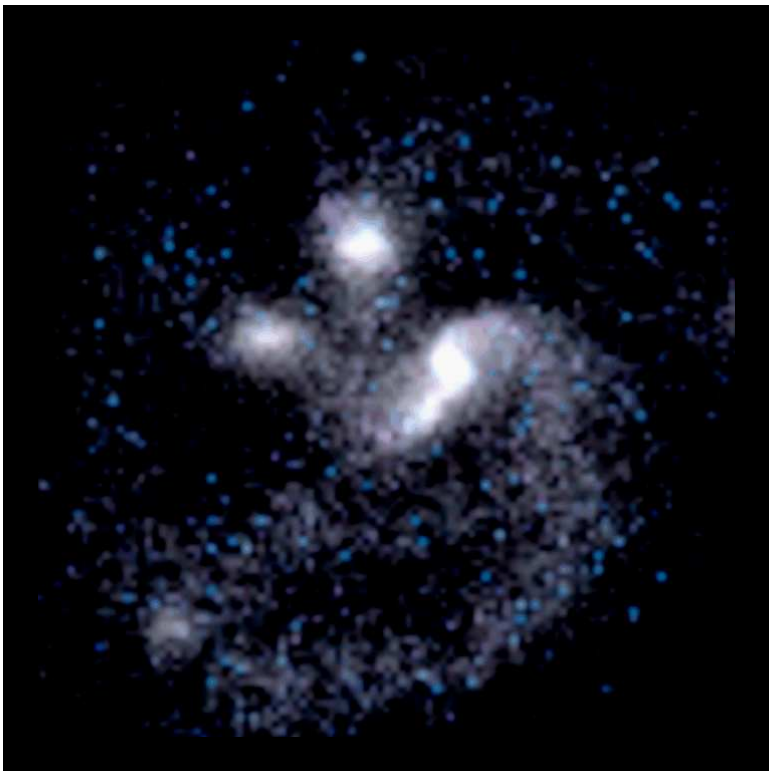

2

The Chemodynamical Model

Different aspects of the evolution of galaxies include ***dynamical****, involving diffuse material ("gas", which will be understood to include dust), stars and dark matter;* ***thermal*** *(mainly affecting the gas);* ***photometric + spectrophotometric*** *(involving stars and gas); and so-called* ***galactic chemical evolution*** *which is not really about chemistry (an important topic in its own right) but concerns the origin and distribution of nuclear species (loosely referred to as elements) in stars and gas.*
Pagel (1997)

This chapter addresses the chemodynamical model, which I applied to simulate the formation and evolution of young disk galaxies. The model consists of a fully three dimensional description of the dynamics of the stars and a two-phase ISM as well as interactions between the two gas phases and the stars. The stars and the two gas phases are embedded in a dark matter halo. The information naturally provided by the chemodynamical evolution code can be used to calculate colors (e.g. UBVK or HST) including absorption. This enables a direct comparison of the model with observations independent of further assumptions. The model presented here is based on the code CoDEx (Samland et al., 1997; Samland & Gerhard, 2003).

2.1. Overview

A galaxy can be described as a coupled star-gas system. The stars and the phases of the interstellar medium are dynamically distinct components, however, coupled by various mass, momentum and energy exchange processes. Fig. 2.1 gives an overview of the different components and the interaction network implemented in the present model.

Although there exists a large diversity of stars in real galaxies, a division into three main groups is possible. This division is based on the influence the stars of different mass have on the evolution of the galaxy. The high mass stars explode at the end of their life as supernovae and inject large amounts of energy and chemically enriched material into the interstellar medium. The intermediate mass stars account for two thirds of the mass return, but with an energy feedback that is negligible compared to the supernovae, whereas the mass in the low mass stars is never given back to the gas phases, because they stay on the main sequence for more than a Hubble time.

The space between the stars is filled with gas. The model distinguishes a cold gas phase, called the cloudy medium, and a hot gas phase, the intercloud medium. The cloudy medium consists of clouds which are embedded in a warm medium. The transition between the cloudy and the gaseous phase is smooth.

In addition, the stars and the gas phases are embedded in a dark halo, which in this model is assumed to be static.

Galactic evolution is closely linked to several interaction processes (Fig. 2.1). Due to computational limits, it is not possible to account for all processes acting from atomic to galactic scales. One therefore has to reduce to the fundamental processes, which determine the galactic evolution. Such processes are star formation, mass- and energy-feedback from stars, evaporation and condensation between the hot and cold gas phase, radiation cooling and dissipation.

2.2. The Interstellar Medium

The interstellar medium (ISM) plays an important role in the evolution of galaxies. The composition of the ISM is very complex. Depending on the density and radiation field, the ISM consists of ionized, atomic and molecular gas, and dust grains. Those are interacting through diverse physical as well as chemical processes. Observations reveal a highly inhomogeneous ISM, in which most of the mass is concentrated in dense cold clouds which are embedded in a hot intercloud gas. Field et al. (1969) showed that at the observed pressure range the cold neutral HI clouds can coexist with warm intercloud gas. McKee & Ostriker (1977) argued that these two phases are embedded in a hot intercloud medium, which covers a large volume and which is heated through supernovae explosions. Guided by the principle that all components must coexist in rough pressure equilibrium (Spitzer, 1956), they proposed a model for the ISM illustrated in Fig.2.2, in which the ISM consists of three phases:

- The cold neutral medium has a temperature of around 80 K and a high number density $n \simeq 100\ \mathrm{cm}^{-3}$. Most of the gaseous mass in a galaxy is in form of dense clouds, which are the sites of star formation.
- The warm medium, which is available in both, neutral and ionized form, has a temperature of around 8000 K. This medium forms the envelope of the dense cloud cores and is dynamically bound to them.
- The cold neutral medium and the warm medium are embedded in the hot low-density intercloud medium (ICM), which has temperatures of around 10^6 K and number densities of $n \simeq 10^{-3}\ \mathrm{cm}^{-3}$.

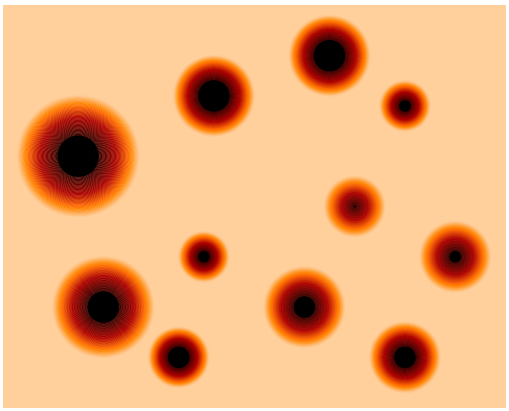

Figure 2.2. The gas phases as described in the three component model of McKee & Ostriker (1977). The clouds of the cold neutral medium (black) surrounded by a warm envelope (red), are embedded in the hot intercloud medium (orange). The smooth transition from the warm medium to the intercloud medium is indicated through the color gradient.

In this description the cold neutral medium and the warm medium are dynamically coupled, since the warm envelope follows its cold cloud core. Hence the dynamics of the ISM can be described by two dynamically distinct gas phases. Beside the ICM, the second phase is the cloudy medium (CM), which is the combination of the cold and the warm phase.

There have been several investigations to identify properties of the cloudy medium. Elmegreen (1989) derived a mass-radius relation for single clouds, which is given through

$$\frac{M_{\mathrm{cloud}}}{R^2_{\mathrm{cloud}}} = 190\sqrt{\tilde{P}} \qquad (2.1)$$

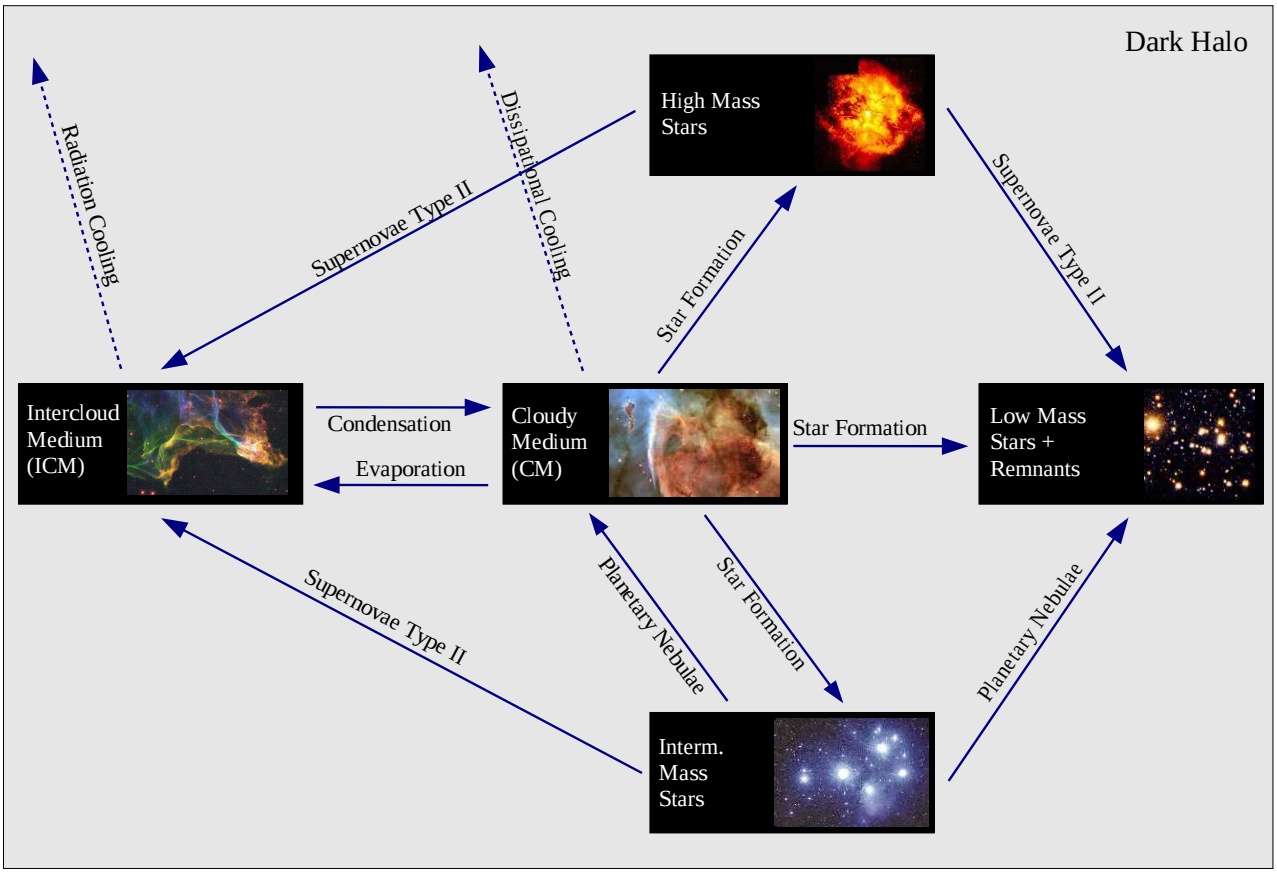

Figure 2.1. Components and interaction network of the model. Explanations are given in the text.

$M_{\rm cloud}$ is the mass of a single cloud and $R_{\rm cloud}$ its radius. $\tilde{P} := (P_{\rm icm}/k)/10^4$ is the pressure of the surrounding ICM given in units of $\mathrm{K/cm^3}$. Hence the clouds shrink if the ICM pressure is increased. Exploration of the cloud mass distribution revealed a cloud mass spectrum, which follows a potential law, although the spectral index varies between investigations from giant molecular clouds to cloud cores.

$$dN(m) \propto m^{-(1+\beta)} dm \tag{2.2}$$

where $\beta \in [0.5, 1.5]$ (Sanders et al., 1985; Motte et al., 1998; Testi & Sargent, 1998). It is worthwhile to note that the details of the mass function manifest themselves only in the efficiencies of certain processes, as is explained below.

Recent observations put forward the idea of a filamentary or sheet like structure of the cloudy medium. Several models of the cloudy medium use spherical clouds (McKee & Ostriker, 1977; Larson, 1969), hence implicitly assuming that the large scale filaments break up into approximately spherical clouds on small scales. This is also assumed in the present model. To date, the topology of the cloudy medium is under discussion.

The cloudy medium and the stars are embedded in the hot intercloud medium. In the three phase model of McKee & Ostriker (1977) the high temperatures of the ICM are maintained through recurring energy input of supernova explosions. This energy input is also responsible for the low density and large filling factor of the ICM. The high sound speed of the ICM effectuates that large fluctuations in the density structure are diminished comparably fast. The short timescale for collisions between electrons and ions assures that no anisotropic pressure can be built up in the ICM .

The three phase model is just a simplified description of the ISM in real galaxies. However, it is accurate enough to describe the ISM in the context of chemodynamical evolution of galaxies. For a discussion of the strong and weak points of this description the reader is referred to McKee (1990).

2.2.1. Dynamics of the ISM

The main difference in the dynamical description of the two gas phases lies in the fact that the particles of the cloudy medium are the clouds themselves, whereas the particles of the intercloud medium are the electrons and ions. Nevertheless, they can be characterized by the same equations. The dynamical evolution of both gas phases is described through the Euler equations, which are derivated in the appendix (App. A.1.).

The Euler equations are

- Continuity equation

$$\frac{D\rho}{Dt} + \rho\vec{\nabla}\vec{u} = 0 \tag{2.3}$$

  The continuity equation states that mass cannot be created or destroyed. The mass in a given volume can only change through the flow through the volume's surface.

- Equations of motion

$$\rho\frac{D\vec{u}}{Dt} = -\rho\vec{\nabla}\Phi - \vec{\nabla}P \tag{2.4}$$

  The local momentum density changes either through the flux through the surface of the volume or through gravitational or pressure gradients.

- Internal energy equation

$$\rho\frac{D}{Dt}(\frac{\epsilon}{\rho}) = -P\vec{\nabla}\vec{u} \tag{2.5}$$

  Internal energy can be increased or decreased in regions of compression or expansion, where the divergence of the velocity is non-vanishing. Additionally, it can be altered through the flux through the surface of the volume.

In the above equations ρ is the density, $\vec{u}$ the bulk velocity, P the pressure, and ϵ the inner energy density of the respective gas phase. Since the gravitational potential Φ is directly related to the total density field (see Sect. 2.5), there are 4 free variables in the 3 equations above. The last degree of freedom can be eliminated by connecting the pressure P to the inner energy density ϵ by means of the equation of state

$$P = (\gamma - 1)\epsilon \tag{2.6}$$

The set of the Euler equations is now complete and can be solved for the density ρ, momentum density $\rho\vec{u}$ and energy density ϵ at any location in the simulated volume for given initial conditions. The detailed procedure of solving these equations is given in Sect. 3.2.

2.2.2. Cooling of the ISM

a. Radiation Cooling of the Intercloud Medium

The rate at which a plasma cools is a fundamental parameter in many astrophysical problems, as well as in chemodynamical evolution of galaxies. A partly ionized gas cools through the conversion of kinetic energy into radiation by collisions between electrons, neutral and ionized constituents. At high temperatures electron impact excitations act on electronic levels whereas at low temperatures fine structure levels are excited. In a completely ionized gas bremsstrahlung is the main cooling process. The efficiency of cooling is a function of the composition of the gas, since the more transitions are available the more probable is the excitation with subsequent radiation emission. The gas must be optically thin to the emitted photons for cooling to be effective. Beside the metallicity dependence of the cooling mechanism obviously the temperature of the gas, representing the kinetic energy of the particles, and the density, influencing the number of collisions, play an important role.

In the present model a grid of metallicity dependent cooling functions for the collisional ionization equilibrium is used (Sutherland & Dopita, 1993). Beside electron collision ionization, processes like photoionization, charge transfer reactions, radiative and dielectronic recombination, line radiation processes and continuum radiation are included to calculate the energy loss of the hot gas. In Fig. 2.3 the principal cooling species are given for a gas with solar abundances.

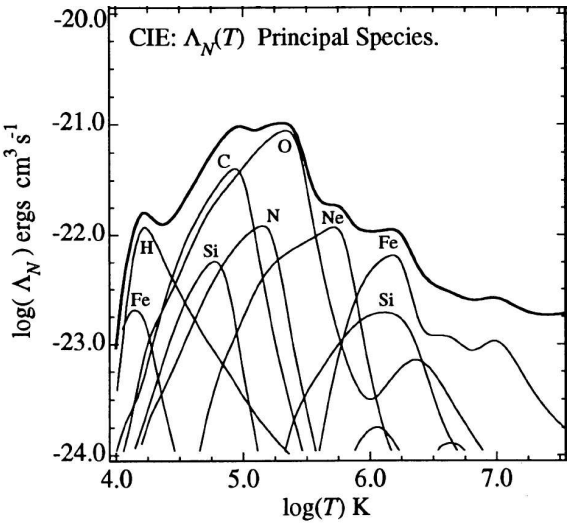

Figure 2.3. The contributions of the cooling processes (from Sutherland & Dopita, 1993): Hydrogen ionization dominates at temperatures around $\log(T) = 4.2$, resonance lines dominate cooling over a large range from $\log(T) = 4.5$ to $\log(T) = 7$ and above $\log(T) = 7$ bremsstrahlung is the main cooling source.

Sutherland & Dopita (1993) calculated the grid of cooling functions $\Lambda(Z, T)$ for several temperatures and metallicities (Fig. 2.4). The cooling is calculated for a homogeneous gas in thermal equilibrium. In the model I use these functions to interpolate the cooling rate for any given value of Z and T.

Because cooling is dominated by collisions between the particles, the cooling rate scales with the density squared.

Therefore the energy change is given by

$$\frac{\partial \epsilon_{\rm icm}}{\partial t} = c_{\rm rad}\rho_{\rm icm}^2 \Lambda(T_{\rm icm}, Z_{\rm icm}) \qquad (2.7)$$

$c_{\rm rad}$ is an efficiency parameter which is 1 for a homogeneous and constant density gas and it can be as high as 10 for strong density fluctuations (Borkowski et al., 1990). Following McKee & Ostriker (1977) the enhancement factor is in the range $c_{\rm rad} \in [2.3, 10]$. The cooling enhancement in the present model is chosen to be $c_{\rm rad} = 5$.

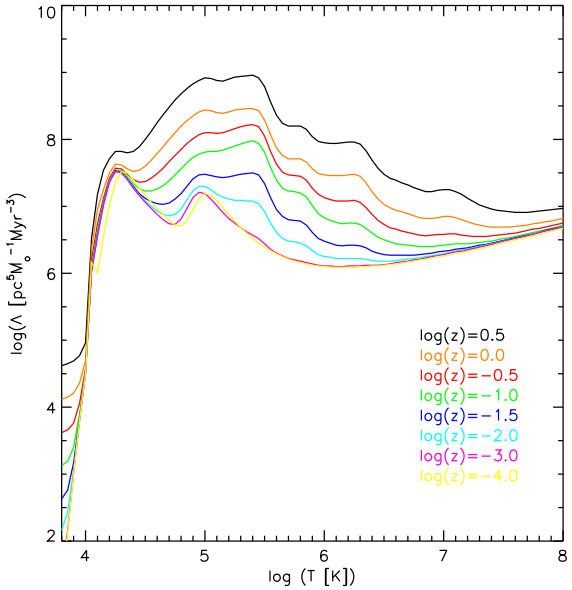

Figure 2.4. Cooling function of the hot gas for different metallicities. Higher metallicities enhance the cooling rate because of the higher number of available transitions at collisions.

b. Dissipation Cooling of the Cloudy Medium

In the present picture the cloudy medium is described as a hydrodynamical fluid in which the particles are the clouds themselves. Therefore cooling of the cloudy medium does not take place on atomic scales, but the cloudy medium loses energy through inelastic collisions between single clouds. The energy loss of identical spherical clouds with an isotropic velocity distribution and completely inelastic collisions, can be described through (Larson, 1969)

$$\frac{\partial \rho_{\rm cm}\sigma_{\rm cm}^2}{\partial t} = -c_{\rm coll} \cdot \frac{8\sqrt{\pi}}{3}\frac{R_{\rm cloud}^2}{M_{\rm cloud}} \cdot \rho_{\rm cm}^2 \sigma_{\rm cm}^3 \qquad (2.8)$$

$R_{\rm cloud}$ denotes the radius of a single cloud and $M_{\rm cloud}$ its mass. Using the mass-radius relation for clouds (Eq. 2.1) leads to

$$\frac{\partial \epsilon_{\rm cm}}{\partial t} = -c_{\rm coll} \cdot \frac{8\sqrt{\pi(\gamma-1)}}{3 \cdot 190}\tilde{P}^{-1/2} \cdot \rho_{\rm cm}^{1/2}\epsilon_{\rm cm}^{3/2} \qquad (2.9)$$

where $\rho_{\rm cm}\sigma_{\rm cm}^2$ was converted to a inner energy through the use of the equation of state $P_{\rm cm} = (\gamma - 1)\epsilon_{\rm cm}$ and the relation $P_{\rm cm} = \rho_{\rm cm}\sigma_{\rm cm}^2$ (Eq. A.24). $c_{\rm coll}$ is an efficiency parameter, the value of which is unfortunately very uncertain, because effects like magnetic fields and self-gravity can significantly change the cloud cross section and cloud structure. Samland & Gerhard (2003) found that $c_{\rm coll}$ is the most uncertain parameter in the chemodynamical description, which is also applied in the present model. In Chap. 4, I discuss simulations using different $c_{\rm coll}$.

c. Dynamical Cooling and Heating of the ISM

The compression and expansion of the ISM can also contribute significantly to its local heating or cooling (Eq. 2.5). Dependent on the dynamical state of the system, dynamical cooling and heating can become very important. However, mostly the energy budget of the ISM is determined by the interactions.

2.2.3. Evaporation and Condensation

In Fig. 2.5 an HST observation of the Eagle Nebula M16 is shown. Energy released from the young massive stars causes the evaporation of gas from globules into the ICM.

Figure 2.5. Evaporation gaseous globules in the Eagle Nebula M16.

In the ISM model applied here, the clouds are embedded in the hot gas of temperature $T_{\rm icm}$ (see Fig. 2.2) and through evaporation and condensation mass, momentum and inner energy can be exchanged between the CM and the ICM. Contrary to the stars, the clouds are not well defined objects with a clear boundary, but the density and temperature structure effectuates a transition zone between clouds

and ICM. The exchange takes place in this transition zone. The mixing of material between the two gas phases plays an important role in the evolution of the ISM since it tends to homogenize the two phases. In addition, heavy elements produced by supernovae initially returned to the ICM can enter the cloudy medium through condensation of the hot gas.

Evaporation and condensation are described according to the model of McKee & Begelman (1990) and Begelman & McKee (1990). There exist three length scales, which are important in the description of evaporation and condensation. The ratio of the three length scales determines, in which regime of evaporation or condensation the clouds are. The cloud radius $R_{\rm cloud}$ enters as a first length scale into the model.

Conduction suppresses thermal instabilities for wavelength shorter than a critical value, the Field length $\lambda_{\rm F}$. The Field length is the length scale at which the cooling or heating is comparable to the energy exchange by thermal conduction. Hence $\lambda_{\rm F}$ is the maximum range, where thermal conduction can by effective and the temperature structure in clouds with radii smaller than the Field length ($R_{\rm cloud} \ll \lambda_{\rm F}$) is dominated by conduction. The temperature structure of clouds with radii larger than the Field length $R_{\rm cloud} \gg \lambda_{\rm F}$ is therefore determined by external heating and radiative cooling. Without going into details of the derivation, the Field length is numerically given through (McKee & Begelman, 1990)

$$\lambda_{\rm F} = 53.35\sqrt{\phi_{\rm c}} \cdot \frac{T_6^{7/4}}{\sqrt{\rho_{\rm icm}^2 \Lambda(Z,T)}} \ [\rm pc]$$

where for the coefficient of thermal conduction the value of $\kappa \simeq 5.6 \cdot 10^{-7} T^{5/2}\,\mathrm{ergs^{-1}K^{-1}cm^{-1}}$ (Draine & Giuliani, 1984) was used. Additionally the electron-temperature is assumed to be equal to the ion temperature and the units of the cooling rate were converted to galactic units (Sect. 1.6). $\Lambda(Z,T)$ is the cooling function (Eq. 2.7). The Field length is calculated from the physical conditions of the hot component. The physical meaning is that the cold component evaporates on scales smaller than the Field length, where the thermal structure is dominated by conduction. On the other hand, if the cloud is larger than the field length its structure is dominated by cooling and it can gain matter through condensation of the hot component.

Assuming energy equipartition in the ICM, the effective mean free path for electron energy exchange $\lambda_{\rm k}$ is given through (McKee & Begelman, 1990)

$$\lambda_{\rm k} = 6.81 \cdot 10^{-5} \phi_c \frac{T_6^2}{\rho_{\rm icm}} \ [\rm pc]$$

where $T_6 := T_{\rm icm} \cdot 10^{-6}$ and $\phi_c \in [0,1]$ was introduced to account for the effect magnetic fields have on $\lambda_{\rm k}$. The ratio of $\lambda_{\rm k}$ and $R_{\rm cloud}$ determines whether there is classical or saturated evaporation (see below). For a cooling function of typical astrophysical fluids ($\log(\Lambda) \approx 7$, Fig. 2.4) one finds $\lambda_{\rm F} \gg \lambda_{\rm k}$.

a. Evaporation

Two cases of evaporation are distinguished depending on the ratio of the cloud radius and the effective free path for electron energy exchange. Without going into details the evaporation rates for the two cases are given below.

In the case where $R_{\rm cloud} > \lambda_{\rm k}$ one speaks of classical evaporation, since in this range the classical description for the heat flux equal to $-\kappa\Delta T$ can be applied. The numerical values for evaporation are given by Cowie et al. (1981). For classical evaporation

$$\begin{aligned} \dot{m} &= -2.75 \cdot 10^4 \phi_{\rm c} T^{5/2} R_{\rm cloud} \quad \left[\frac{\rm g}{\rm s\ cloud}\right] \\ &= -3.17 \cdot 10^{-2} \phi_{\rm c} \tilde{P}^{-1/4} T_6^{5/2} M_{\rm cloud}^{1/2} \quad \left[\frac{\rm M_\odot}{\rm Myr\ cloud}\right] \end{aligned}$$

where the mass-radius relation for clouds (Eq. 2.1) was used.

If $\lambda_{\rm k}$ is comparable to the cloud radius, the heat flux can no longer be described through $-\kappa\Delta T$. A detailed investigation of the saturated evaporation lead to the numerical expression (Cowie & McKee, 1977; Cowie et al., 1981)

$$\begin{aligned} \dot{m} &= -3.75 \cdot 10^4 \phi_{\rm c} T^{5/2} \left(\frac{\lambda_{\rm k}}{R_{\rm cloud}}\right)^{-5/8} R_{\rm cloud} \quad \left[\frac{\rm g}{\rm s\ cloud}\right] \\ &= -0.222 \phi_{\rm c} \tilde{P}^{-3/32} {\lambda_{\rm k}}^{-5/8} T_6^{5/2} M_{\rm cloud}^{3/16} \quad \left[\frac{\rm M_\odot}{\rm Myr\ cloud}\right] \end{aligned}$$

where again Eq. 2.1 was used. Samland (1994) showed that the influence of $\phi_{\rm c}$ is negligible. Since magnetic fields are not included elsewhere in the model, their effects are also neglected here and hence $\phi_{\rm c} = 1$.

The above evaporation rates are given per cloud. To get the total evaporation rate, one has to integrate $\dot{m}$ over the cloud mass spectrum (Eq. 2.2). Hence with M_λ and $M_{\rm F}$ being the corresponding mass to $\lambda_{\rm k}$ and $\lambda_{\rm F}$ (Eq. 2.1) one gets

$$\dot{m}_{\rm evap} = \int_{M_{\rm lower}}^{M_\lambda} \dot{m}_{\rm sat} N(m) dm + \int_{M_\lambda}^{M_{\rm F}} \dot{m}_{\rm cla} N(m) dm \tag{2.10}$$

Instead of evaluating this integral, a simpler parameterization is used in the model. The evaporation rate is set to be equal to

$$\dot{\rho}_{\rm evap} = c_{\rm evap} \rho_{\rm cm} T^{5/2} \tilde{P}^{-1/4} \tag{2.11}$$

All the uncertainties arising e.g. from the cloud mass spectrum or the geometry of the clouds are combined in the

constant $c_{\rm evap}$. Inserting typical quantities for a cloud mass spectrum $\beta = 0.7$, $M_{\rm lower} = 10^3$ $M_\odot$ and $M_{\rm upper} = 10^7$ $M_\odot$, one can calculate $c_{\rm evap}$ for different densities and temperatures using Eq. 2.10 as is shown in Fig. 2.6. Note that over the whole parameter range the value of $c_{\rm evap}$ changes only by one order of magnitude.

In the model I use $c_{\rm evap} = 2.2 \cdot 10^{-19}$. This value is consistent with the one used by Samland & Gerhard (2003), who showed that variations of about a factor of 10 have only minor impact on the galactic evolution. The insensitivity of

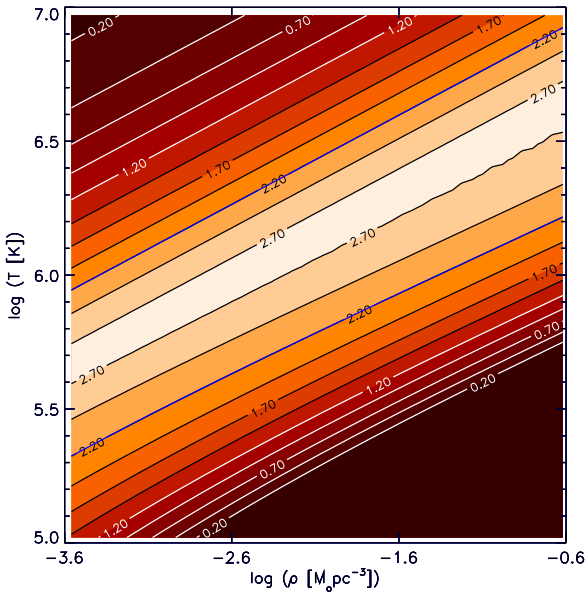

Figure 2.6. Values of $c_{\rm evap} \cdot 10^{19}$ for densities and temperatures typical for the ICM. The blue line indicates the value used in the model.

the model to the evaporation rate is one manifestation of the self-regulating character of the model (see Sect. 2.6).

b. Condensation and Cloud Formation

Condensation happens if the cloud radius exceeds the Field length. In this case cooling dominates the temperature structure of the clouds and hence the cloud can gain mass by condensation. According to McKee & Begelman (1990) the cooling time of the ICM and the timescale for condensation are of the same order.

Additionally, clouds can form through thermal instabilities from the hot gas phase. Following Elmegreen (1989b) the contraction and collapse of clumpy structures occur also on the cooling timescale. Therefore condensation and cloud formation can be described through

$$\dot{\rho}_{\rm cond} = c_{\rm cond} \frac{\rho_{\rm icm}}{\tau_{\rm cool}}$$

The upper limit of $c_{\rm cond}$ is 1, since the gas must cool before it can condensate or form clouds. Samland & Gerhard (2003) pointed out that when choosing $c_{\rm cond} < 0.3$ the hot gas phase can cool below 10^4 K before condensation and cloud formation are efficient. This is in contradiction to the two-phase ISM description assumed in the present model, in which the hot gas ($T \gg 10^4$ K) is in pressure equilibrium with the cloudy medium ($T < 10^4$ K). Samland & Gerhard (2003) use a value of $c_{\rm cond} = 0.5$, consistent with the approximation given by Elmegreen (1989b), which prevents the hot phase from reaching temperatures significantly below 10^5 K, and guarantees a stable hot gas phase.

2.3. The Stars

Stars are the fundamental building blocks of galaxies. In general, the stars in a galaxy differ in their intrinsic properties, like mass, chemical composition, age and evolutionary stage. They are very important for the evolution of a galaxy, since they contribute to a large part to the energy budget of a galaxy, and their mass return is responsible for the enrichment of the interstellar medium with heavy elements.

2.3.1. Dynamics of the Stars

A typical disk galaxy like the Milky Way hosts around 10^{11} stars. Since stars can be treated as point masses, the dynamical description of a star is in principle already known from classical mechanics. But due to the large number of the stars, it is far beyond the computational capabilities of even the fastest computation facilities to calculate the orbit of each star individually. To circumvent this problem, each stellar particle in the present model represents a single stellar population (SSP) with typical masses around a few 10^5 $M_\odot$. The detailed description follows later in this section. This procedure reduces the number of particles to a few 100'000. The orbits of the stellar particles are determined by their initial conditions, which are given by the dynamics of the cloudy medium at their formation time, and the evolution of the galactic gravitational potential. The detailed implementation of the dynamical description of the stellar particles is given in Sect. 3.5.

Another possibility to treat the dynamics of the stars is a statistical approach (Samland, 1994; Samland et al., 1997) analogously to the dynamics of the cloudy medium (see App. A.3.). However, such a description has the disadvantage that stellar systems cannot interpenetrate each other. Additionally, the metallicities of the stellar populations are averaged in such a way that a metal poor and a metal rich population result in a population with intermediate metallicity, which makes it difficult to directly compare the stellar metallicity distribution obtained in such a model to observations.

2.3.2. Star Formation

Figure 2.7. Over 200 newly formed stars were recently born in NGC 604, an expansive cloud of interstellar gas and dust in M33.

Image 2.7 shows a typical star forming region. NGC 604 is an expansive cloud lying in the disk of M33. Young stars form in the center. The complex interplay between the different processes in molecular clouds, like e.g self-gravity, turbulence, magnetic fields as well as atomic and molecular processes, is not understood in full detail. Hence there is no theory, which can exactly describe the process of star formation.

a. Star Formation Rate

Fortunately, for the purpose of galactic evolution, the exact mechanism of the formation of single stars is not so important. One needs a quantitative description of star formation on large scales. There is evidence that star formation on large scales is dependent on the gas surface density $\Sigma_{\rm gas}$ to an exponent α (Schmidt, 1959; Buat et al., 1989).

$$\Sigma_{\rm sfr} = c_{\rm sf} \cdot \Sigma_{\rm gas}^{\alpha} \tag{2.12}$$

where $\alpha \in [1,2]$. Although star forming galaxies show a large diversity in physical conditions and present star formation rate (SFR), the gas surface density $\Sigma_{\rm gas}$ and the star formation surface density $\Sigma_{\rm sfr}$ fit on a common power law over 5 to 6 orders of magnitude (Kennicutt, 1998):

$$\Sigma_{\rm sfr} = (2.5 \pm 0.7) \cdot 10^{-4} \left(\frac{\Sigma_{\rm gas}}{\rm M_\odot pc^2} \right)^{1.4\pm0.15} \frac{\rm M_\odot}{\rm yr\ kpc^2} \tag{2.13}$$

The error in the slope in Eq. 2.13 is dominated by the uncertainties of the SFR determination as well as the uncertainties in CO-derived gas surface densities. This tight relation

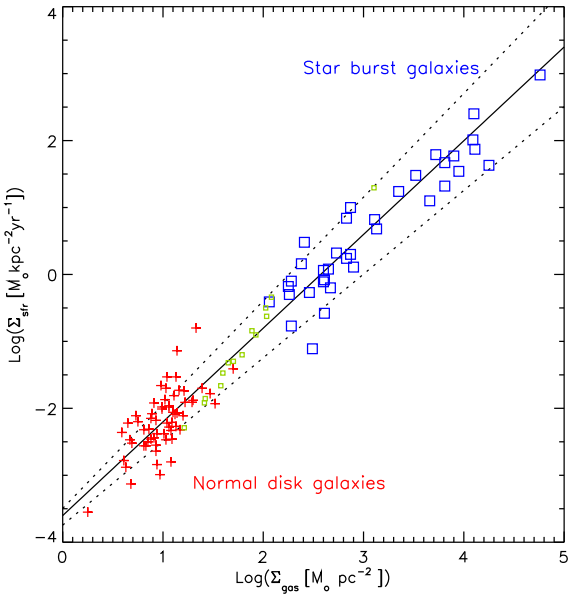

Figure 2.8. Star formation surface density against gas surface density for normal disks and starburst galaxies (Kennicutt, 1998). The green squares show the results from one of the disk galaxy models.

shows that a simple Schmidt law provides a good empirical parameterization of the SFR and suggests that the gas density is the primary determinant of the SFR on large scales. Furthermore Eq. 2.13 states that there seems to be a more or less constant star formation efficiency on large scales. This allows the determination of $c_{\rm sf}$ in Eq. 2.12. In Fig. 2.8 the observational data from Kennicutt (1998) together with the fitted power law and the model data is shown.

There exist various theoretical models, which produce a Schmidt law with $\alpha \in [1,2]$ (Kennicutt, 1998, and references therein). For a self-gravitating disk, a large-scale Schmidt law with index $\alpha \simeq 1.5$ would be expected, if the SFR scales as the ratio of gas density to the free fall timescale ($\propto \rho_{\rm cm}^{0.5}$) and the average gas scale height is roughly constant ($\Sigma \propto \rho_{\rm cm}$) (Elmegreen, 1994; Larson, 1992). It is noteworthy that the SFR per unit area correlates with the total gas surface density, but not with the surface density of molecular gas alone (Kennicutt, 1989; Buat et al., 1989).

In the present model, a star formation law

$$\dot{\rho_{\rm sf}} = c_{\rm sf} \rho^{3/2} \tag{2.14}$$

is applied. To fit the data in Fig. 2.8, the constant is set to $c_{\rm sf} = 0.01\ \rm pc^{3/2} M_\odot{}^{-1/2} Myr^{-1}$.

b. Initial Mass Function

The star formation law (Eq. 2.14) describes the amount of material converted into stars. To characterize the process of

star formation one additionally needs to know the mass distribution of a newly formed stellar population. This is specified by the initial mass function (IMF). Since a star's mass determines its lifetime, its luminosity and its contribution to the enrichment of the interstellar medium with heavy elements, the photometric and chemical evolution of a galaxy are sensitive to the IMF. Because of the complexity of the star formation process it is not possible at the moment to derive an IMF from first principles, but different theoretical approaches exist, as is nicely reviewed by Elmegreen (2001).

Salpeter (1955) observed in his pioneering work the luminosity distribution for the field stars in the solar neighborhood and converted this into a mass distribution, using an adopted mass-luminosity relation. The mass distribution was then corrected for the stars which have died during the disk evolution leading to an initial mass function with a simple parameterization

$$dn(m) = c_{\rm imf} \cdot m^{-(1+x)} dm \qquad (2.15)$$

The number distribution $n(m)$ of new born stars follows a potential law. x is often referred to as the slope of the IMF and takes the value of $x = 1.35$ over a large range of observed masses. The constant of the IMF $c_{\rm imf}$ is directly linked to the total mass $M_{\rm i}$ converted into stars in a star formation event through

$$c_{\rm imf} = \frac{M_{\rm i}}{\int_{M_{\rm l}}^{M_{\rm u}} n(m) m dm} = \frac{(-x+1)M_{\rm i}}{M_{\rm u}^{-x+1} - M_{\rm l}^{-x+1}} \qquad (2.16)$$

The slope inferred from local field stars is subject to significant uncertainty, because it depends on assumed stellar lifetimes and evolutionary history of the local galactic disk. Many attempts have been undertaken to measure the IMF in individual star clusters in our Galaxy as well as in the Magellanic clouds, because in a stellar cluster one deals with a single stellar population. However, the extraction of the faint cluster members is very difficult because of contamination with background galactic field stars. Additionally, clusters tend to loose single low-mass stars as a result of mass segregation and star-star encounters. A further bias enters from binary stars, since unresolved binaries are brighter than single stars (Kroupa, 2002). Hence, the determination of the IMF from stellar clusters is not more accurate than the one from the solar neighborhood stars. The results obtained are generally consistent with a Salpeter IMF (Larson, 1999, and references therein), at least in the mass range from 1 to 30 $\rm M_\odot$.

On a first view, one would expect the initial mass function to vary under different star-forming conditions. However, there is little evidence for large systematic variations in the IMF among star forming galaxies (Scalo, 1986) and Kroupa (2002) concludes that the IMF is surprisingly uniform in variable systems. Hence, the assumption of a universal and time independent IMF is justified.

The slope of the IMF over the mass range $1\ \rm M_\odot - 30\ M_\odot$ can be constrained using Hα equivalent widths and broadband colors of galaxies showing good consistency with a Salpeter IMF in disk galaxies (Kennicutt, 1994). The slope of the IMF for stars with masses below one solar mass is much more uncertain. In Fig. 2.9 different IMFs are shown. The largest differences exist in the range of the low mass stars, where some authors claim a flattening of the IMF. The exact value of x for low mass stars as well as lower mass cut of the IMF affects galactic evolution mainly through the fraction of the lock-up mass, which determines the gas consumption time. The low mass stars play a secondary role in galactic evolution. Because of their long lifetime there is no energy or mass feedback to the ISM and they influence the galaxy only through their contribution to the gravitational potential.

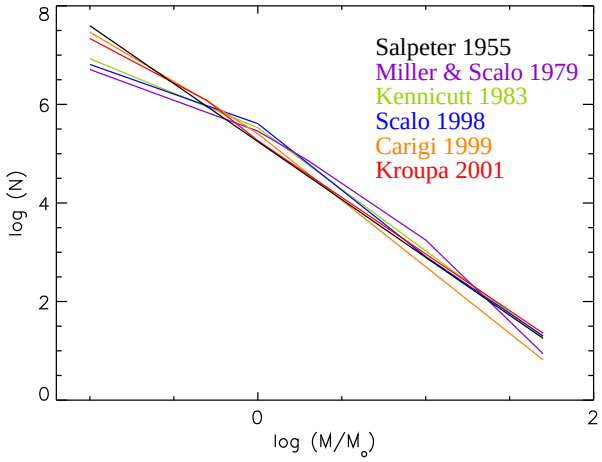

Figure 2.9. Compilation of different IMFs measured from the solar neighborhood (Salpeter, 1955; Miller & Scalo, 1979; Scalo, 1986, 1998), spiral galaxies (Kennicutt, 1983), and for irregular galaxies (Carigi et al., 1999). The number distribution for a single stellar population with $M = 10^6\ \rm M_\odot$ and $M_{\rm l} = 0.1$ and $M_{\rm u} = 50$ is given.

In the present model a time independent Salpeter-IMF is used, with an upper mass limit $M_{\rm u} = 50\ \rm M_\odot$ and a lower mass limit of $M_{\rm l} = 0.8\ \rm M_\odot$. The stars with masses lower than $0.8\ \rm M_\odot$ as well as the planets and brown dwarfs are described by the lock-up mass fraction, which in this model is 60%. With these assumptions, 10% of the mass converted into stars in a star formation event goes into stars with masses larger than $10\ \rm M_\odot$. But only two stars out of 1000 lie in the mass range of the high mass stars.

2.3.3. Stellar Lifetimes

It is well known that the evolution and the lifetime of a star depends on its mass. Whereas the massive stars burn their fuel very fast due to the high pressure and temperature in their core needed to counterbalance gravity, the low mass stars can live longer than a Hubble time. Secondly, the lifetime of a star depends on its metallicity, because heavy elements can create strong absorption in the atmosphere of low mass stars and therefore the energy loss and consequently the energy production of metal rich stars is lower resulting in a longer lifetime of metal rich low mass stars. Metallicity effects can cause differences in the lifetime of low mass stars of around a factor of 2. The stellar lifetime in the model is mass and metallicity dependent only and effects from stellar rotation (Meynet & Maeder, 1998) or star-star interactions are neglected.

In the context of the present model the lifetime of a star is defined by the time between the event of star formation and the time when the star becomes a stellar remnant. In the case of a high mass star the latter is defined by the supernova explosion and for intermediate mass stars by the ejection of the shell into the ISM. In other words, the stellar lifetime is the interval between gas conversion to stars and the inverse process of mass return.

To derive a mass-lifetime relation a metallicity and age dependent function of the form

$$\log(t) = a(Z)\log(M)^2 + b(Z)\log(M) + c(Z) \quad (2.17)$$

is fitted to the data of Maeder & Meynet (1989). After solving the quadratic equation for $\log(M)$, this is equivalent to

$$M = 10^{\frac{-b(Z)-\sqrt{b(Z)^2-4a(Z)(c(Z)-\log(t))}}{2a(Z)}} \quad (2.18)$$

Data are available for 5 different metallicities (Fig. 2.10). For each metallicity a function of the form 2.17 is fitted to the data. The coefficients $a(Z), b(Z)$ and $c(Z)$ are then linearly fitted

$$\begin{aligned} a(Z) &= a_0 + a_1 \cdot Z \\ b(Z) &= b_0 + b_1 \cdot Z \\ c(Z) &= c_0 + c_1 \cdot Z \end{aligned}$$

and therefore the mass-lifetime relation becomes

$$M(t,Z) = 10^{\frac{-(b_0+b_1 Z)-\sqrt{(b_0+b_1 Z)^2-4(a_0+a_1 Z)((c_0+c_1 Z)-\log(t))}}{2(a_0+a_1 Z)}} \quad (2.19)$$

with the numerical values

$$\begin{aligned} a_0 &= 3.79 & a_1 &= 0.24 \\ b_0 &= 3.10 & b_1 &= 0.35 \\ c_0 &= 0.74 & c_1 &= 0.11 \end{aligned}$$

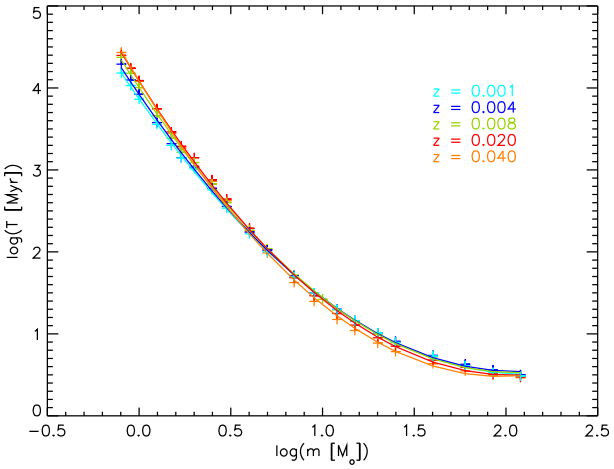

Figure 2.10. Mass lifetime relation for different metallicities. The data points (crosses) and fitted functions (solid lines) are shown.

2.3.4. Mass Return Rate

A stellar particle characterizes the evolution of a single stellar population of mass M_i. A SSP with mass M_i returns in the time interval dt the mass

$$M_{\rm ret}(t)dt = c_{\rm imf} \int_{M(t,Z)}^{M(t+dt,Z)} n(m)(m - m_{\rm rem}(m))dm \quad (2.20)$$

where $M(t,Z)$ and $M(t+dt,Z)$ are the masses of the stars that die at the time t and $t+dt$ after formation of the SSP respectively, given through the mass-lifetime relation (Eq. 2.19). Note that all stars of a population have the same metallicity Z, which is given here only for completeness. The constant $c_{\rm imf}$ is linked to the total mass of the population as described in Eq. 2.16. $m_{\rm rem}$ is the mass that remains in the stellar remnant. For stars with masses higher 10 $M_\odot$ a constant remnant mass of 2 $M_\odot$ is assumed (Woosley & Weaver, 1995) and for the intermediate mass stars a white dwarf mass of 0.6 $M_\odot$ is applied (Weidemann & Koester, 1983).

Fig. 2.11 shows the evolution of the mass return rate as well as the accumulated returned mass of an SSP as a function of time. A single stellar population can return about 30% of its initial mass to the ISM with a Hubble time. After 2 Gyr around 25% of the initial mass is given back to the ISM. This material can form new stars. This means that after three generations of stars, 97% of the mass is in stars and is not given back to the ISM any more. Due to the reprocessing of the material, the integrated star formation rate can reach higher values than the total baryonic mass. The maximum cumulated star formation rate is about a factor of 1.4 times the total baryonic mass of a galaxy.

Depending on its mass a star follows a completely different evolution. The detailed evolutionary processes can be

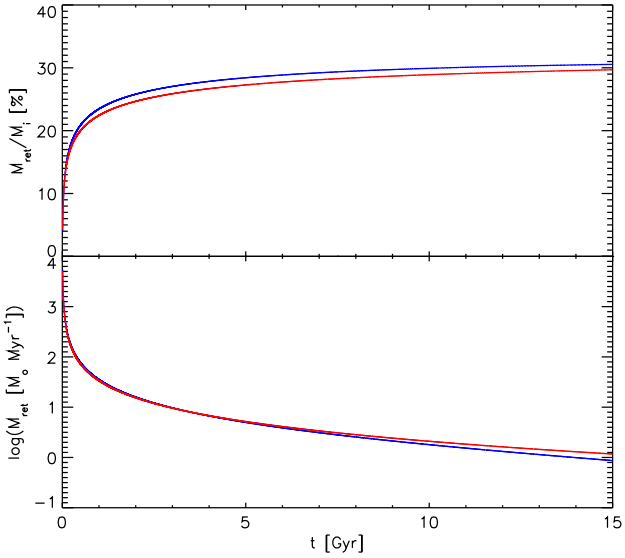

Figure 2.11. Returned mass of a single stellar population (top) and mass return rate (bottom) of a SSP with $M_{\rm i} = 10^6$ $\rm M_\odot$ with $Z = Z_\odot$ (red line) and $Z = 0.1 Z_\odot$ (blue line).

found in standard textbooks (e.g. Karttunen et al., 2000; Kippenhahn & Weigert, 1990). In the description of this model, the stars are divided in three groups corresponding to the different impact of the stars on galactic evolution. Nevertheless, their dynamical evolution is described identically, because the whole single stellar population is represented by the same stellar particle.

2.3.5. High Mass Stars ($M > 10$ $\rm M_\odot$)

After the main sequence, high mass stars can ignite different burning stages. The ignition of helium in the core leads to the build up of a carbon-oxygen core. Hydrogen burning now takes place in a shell around the core. Subsequently, different ashes are ignited with the consequence that the prior burning stage is ousted into a shell. The shells of earlier burning stages move outwards and in the end the star reaches a structure similar to an onion skin, where the heavier elements are burned in the inner parts. In the end silicon burning leads to a central iron core. When the growing iron core collapses under self-gravity, large amounts of energy are set free which lead to explosive shell burning and to an ejection of material with high kinetic energy. The star explodes in a core collapse supernovae or supernovae of type II (SNII) leaving a neutron star or black hole as a stellar remnant. In Fig. 2.12 the Crab Nebula, a core collapse supernovae remnant, is shown. The neutron star was found in the center of the nebula. Through the supernova explosion enriched material is injected into the hot gas phase and approximately 10^{51} erg of thermal energy is released. Both

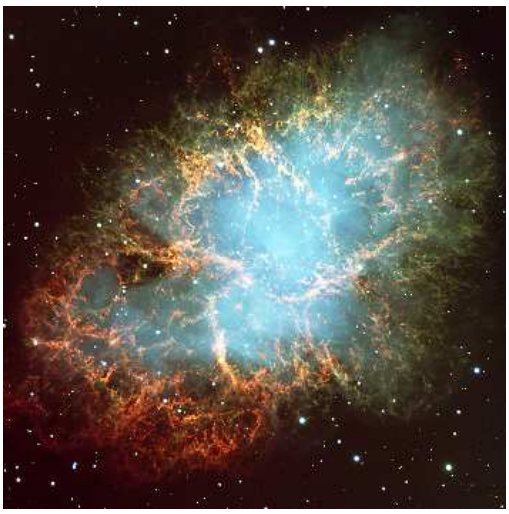

Figure 2.12. The Crab Nebula is a supernova remnant from a SN explosion happened around 1000 years ago, at a distance of around 1.7 kpc. At the center of the crab nebula a neutron star is located.

mass and energy feedback of the SNII are very important for the evolution of a galaxy.

a. Heating through SNII

The gas phases are heated through various processes, like stellar winds, stellar radiation, and the explosion of supernovae. Most important for galactic evolution is the energy input from massive stars, dominated by the energy release through supernovae, as in the model of McKee & Ostriker (1977), together with the winds in the Wolf-Rayet phase. Due to the short timescale of the stellar evolution of massive stars in the Wolf-Rayet phase, the heating through stellar winds can be included in the SNII energy release.

Typical values for the ejected energy of SNII are of the order of 10^{53} erg, where about 1% is injected into the baryonic gas phase. The rest of the energy is carried away by neutrinos (Woosley, 1988). Hence, the ISM gets an energy input of 10^{51} erg per supernova. The short timescale of the explosion justifies the assumption that the energy is converted instantaneously into inner energy density of the ejected material. This energy input causes the formation of bubbles and shells in the ISM. Since the mean ejected mass of a SNII $<M_{\rm SNII}>$ is given through

$$<M_{\rm SNII}> = \frac{\int_{M_{\rm m}}^{M_{\rm u}} (m - m_{\rm rem}) n(m) dm}{\int_{M_{\rm m}}^{M_{\rm u}} n(m) dm} = 16.74\,{\rm M_\odot}$$

with a remnant mass of $m_{\rm rem} = 2$ $\rm M_\odot$, a lower SNII mass of $M_{\rm m} = 10$ $\rm M_\odot$ and an upper IMF mass cut of $M_{\rm u} = 50$ $\rm M_\odot$, the energy input per returned solar mass is

$$e_{\rm SNII} = \frac{10^{51}\ {\rm erg}}{16.74\,{\rm M_\odot}} = 3.14 \cdot 10^6 {\rm pc^2 Myr^{-2}}$$

which corresponds to a temperature $T \sim 4 \cdot 10^8$ K, which is actually never reached, because the ejecta mix with cooler material and they can cool efficiently in the shock waves of SN-shells. According to McKee & Ostriker (1977), about 5% of the released energy is used to accelerate the clouds, and therefore heats the CM. The cooling time of the dense gas within the clouds is shorter than the dynamical timestep resolved in the model an therefore the assumption of thermal equilibrium of the cold gas within one cloud is valid.

b. Metallicity enrichment through SNII

Stellar metallicity distributions give important clues on the evolution history of galaxies (e.g. Chiba & Beers, 2000; Ferrara & Tolstoy, 2000; Edvardsson et al., 1993; Tinsley, 1980). The metallicity distribution depends on the star formation history as well as on the time delay between star formation and enrichment of the ISM. Additionally the spatial distribution of the star forming regions are important.

There have been numerous attempts to determine the yields of massive stars through calculation of supernovae explosions (e.g. Woosley & Weaver, 1995; Thielemann et al., 1996). Unfortunately, many assumptions go into these calculations, since to date it is not possible to calculate SNII explosions as a consequence of the iron core collapse. In the model calculations the energy needed for an explosion is set artificially in the inner region of the star. The location of this energy input and henceforth the location of the mass cut, which is the limit between ejected material and material remaining in the stellar remnant, is very uncertain. Additionally, the way of the artificial onset of the explosion can lead to differences of up to 30% in composition of the ejected material (Aufderheide et al., 1991). Since the energy is set artificially into a stellar evolution model, uncertainties in the stellar models, arising from rotation (Maeder, 2001) or uncertain reaction rates as $^{12}\mathrm{C}(\alpha,\gamma)^{16}\mathrm{O}$ (e.g. Buchmann et al., 1993; Imbrani et al., 2001), also affect the outcome of the supernovae calculation models.

One way to determine the yields of SNII, is to calibrate the theoretical yields from Woosley & Weaver (1995) with a chemodynamical model for the Galaxy. Samland (1998) determined IMF averaged yields of massive stars by using his self-consistent galactic evolution model. He found that the observed [α/Fe] ratios are best fit through a mean iron return of $0.046\ \mathrm{M}_\odot$ per SNII. This is about a factor of 2 lower than the Fe yield of the theoretical calculations of Woosley & Weaver (1995), and is in agreement with Timmes et al. (1995), who used a much simpler galactic evolution model. By applying the solar iron mass fraction of $1.267 \cdot 10^{-3}$ (Anders & Grevesse, 1989), this corresponds to a Fe yield of 2.17 times solar iron metallicity. The oxygen yield derived by Samland (1998) is consistent with the theoretical yields of Woosley & Weaver (1995). In the present model the weak metallicity dependent production of O found by Samland (1998) is neglected. Every HMS returns $1.02\ \mathrm{M}_\odot$ of oxygen to the ISM. Thus, taking into account the solar mass fraction of oxygen as $9.55 \cdot 10^{-3}$ (Anders & Grevesse, 1989), the oxygen yield of a massive star is 6.38 solar. Using the two yields one gets for the ratio of the two species

$$[\mathrm{O/Fe}]_{\mathrm{SNII}} = 0.47$$

The chemically enriched material is given back to the ISM at the end of the stellar lifetime. Due to the short evolutionary time of massive stars this assumption is justified.

In the model two fiducial chemical elements are included. One traces the α-elements mainly produced in SNII and the other the iron peak elements, which are produced mainly in SNIa. Using these fiducial elements, elements produced independent of metallicity can be readily calculated with every yield table without the need of recalculating the full dynamical model. This is possible because the dynamical evolution is not strongly affected by metallicity effects.

2.3.6. Intermediate Mass Stars ($0.8\ \mathrm{M}_\odot < \mathrm{M} < 10\ \mathrm{M}_\odot$)

In intermediate mass stars the temperature in the core after helium burning is not high enough to ignite the carbon/oxygen core. The stars enter the red giant phase. The hydrogen envelope is ejected in a stellar wind leaving the naked core which subsequently cools and forms a white dwarf. The ejected shell may be illuminated by the core producing a planetary nebula (PN). In Fig. 2.13 an example of a PN is shown. This HST exposure of the Little Ghost nebula shows the central star illuminating its repelled envelope.

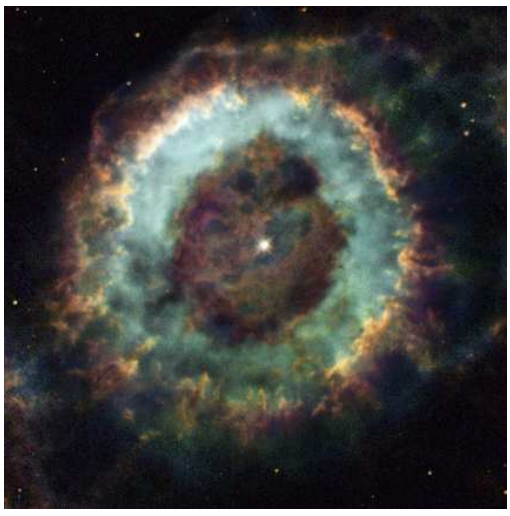

Figure 2.13. The Little Ghost Nebula (NGC 6369), an example of a planetary nebula.

a. Mass Return through PN

The material ejected in a PN has a fragmented structure and its properties are very similar to the cloudy medium. In the chemodynamical model it is assumed that the gas ejected by the intermediate mass stars goes into the cloudy phase of the ISM. The mass is given back according to the mass-lifetime relation, where the mass return of a star is given through its initial mass minus the mass of the white dwarf remnant ($0.6\ \mathrm{M}_\odot$). The intermediate mass stars account for two thirds of the mass returned to the ISM from a single stellar population.

b. Heating through PN

According to Osterbrock (1989) the typical temperature of the material ejected in a planetary nebula is around 10'000 K. Therefore the energy per mass is given by

$$e_{\mathrm{PN}} = \frac{\epsilon}{\rho} = \frac{T k_b}{m_{\mathrm{h}} \mu (\gamma_{\mathrm{int}} - 1)} = 1.53 \cdot 10^2\ \mathrm{pc}^2 \mathrm{Myr}^{-2}$$

m_h is the proton mass, μ the mean molecular weight, k_b the Boltzmann constant and γ_{int} is the adiabatic index of the cold gas within a single cloud.

c. Enrichment through PN

The gas expelled by intermediate mass stars is enriched with C and N and small amount of O (Van den Hoek & Groenewegen, 1997). In the red giant phase the production of Al and Na is possible. From these elements only oxygen is traced in my model. However, the production of O is negligible compared to the production in SNII, so that the metal feedback from intermediate mass stars can be neglected in the context of the present model.

2.3.7. Low Mass Stars ($M < 0.8\ \mathrm{M}_\odot$) and Stellar Remnants

The low mass star component consists of stars with masses below $0.8\ \mathrm{M}_\odot$. These stars stay on the main sequence longer than a Hubble time and therefore they do not return a significant mass back to the interstellar medium. 60% of the mass transformed to stars in a star formation event belongs to the low mass stars. The contribution of brown dwarfs and planets is also included in this component.

The stellar remnants are black holes, neutron stars and white dwarfs emerging from stellar evolution of the high and intermediate mass stars. Mass transformed to low mass stars or to the stellar remnants is locked up and has no impact on galactic evolution other than gravitational.

2.3.8. Supernova of Type Ia

In Fig. 2.14 a SNIa in the outer parts of an external galaxy is shown. The supernova exploded far from the disk of NGC 4526 with no star formation in its neighborhood. It has long been recognized that contrary to SNII, SNIa occur in galaxies of all types and there is no correlation with recent star forming regions. Since SNIa contain no hydrogen lines in their spectra, already Hoyle & Fowler (1960) suggested that the SNIa result from explosive carbon burning in a carbon-oxygen white dwarf.

Figure 2.14. Supernova 1994D exploded in the outskirts of the disk of the galaxy NGC 4526.

In a binary system the white dwarf can evolve further through mass accretion from its companion, which passes the red giant phase filling its Roche lobe. If the mass of the white dwarf crosses the Chandrasekhar mass limit the degenerate electron pressure can no longer counteract gravity and consequently the white dwarf contracts. This results in an ignition of nuclear reactions which lead to a thermonuclear runaway. The star is disrupted completely. This explosion is called a supernovae of type Ia (SNIa). Depending on the accretion rate it would also be possible for a sub-chandrasekhar white dwarf to explode (Nomoto et al., 1996). The description of the SNIa in this simulation is based on the W7 model of Nomoto et al. (1984, 1996).

a. Number of SNIa

Every massive star is expected to explode in a SNII. In the present description a white dwarf explodes as a SNIa in a binary system. Obviously not every WD has a companion from which it can accrete matter. The process of binary formation is not well understood and therefore no theory exists, from which the number of suitable binary systems could be estimated. However, observationally the ratio of SNII to SNIa is well established. Tammann et al. (1994)

found for the ratio between numbers of SNIa and SNII in Sbc galaxies a value of $c_{\rm SN} \simeq 1/10$. This is consistent with the ratio needed to fit the galactic metallicity distribution (Samland, 1998).

The number of white dwarfs in a SSP is given through the integral over the IMF from the mass of the stars ending there lives $M(t,Z)$ to the limiting mass for intermediate mass stars $M_{\rm m}$. These stars all have ended their evolution as a white dwarf and are now possible candidates for accretion from a red giant in a binary system. Due to the short timescale of the red giant phase of an IMS, the number of stars which are in the red giant phase and hence can lose matter to a companion white dwarf, is assumed to be equal to the number of dying stars in the time interval Δt. Therefore the number of SNIa occurring in a SSP in the time interval $[t, t+\Delta t]$ is given through

$$N_{\rm SNIa}(t,Z) = \int_{M(t+\Delta t,Z)}^{M(t,Z)} n(m)P(m)dm \qquad (2.21)$$

where $n(m)$ is the IMF and $M(t,Z)$ the mass of the stars dying at time t, according to mass-lifetime relation for the the stars (Eq. 2.19). $P(m)$ is the probability that a red giant has a white dwarf companion. This probability is given through

$$P(m) = N_0 \frac{\int_m^{M_{\rm m}} n(m')dm'}{\int_{M_{\rm l,SNIa}}^{M_{\rm m}} n(m')dm'} \qquad M_{\rm l,SNIa} < m < M_{\rm m}$$
$$P(m) = 0 \qquad \text{otherwise}$$

$M_{\rm m}$ is the limiting mass between intermediate and high mass stars and $M_{\rm l,SNIa}$ the lower cut for the stars that can explode as SNIa. The probability $P(m)$ grows for lower m, because more white dwarfs are available. N_0 is chosen in such a way that the for the integrated numbers of SNII and SNIa the relation

$$N_{\rm SNIa}^{\rm total} = c_{\rm SN} N_{\rm SNII}^{\rm total}$$

or equivalently

$$\int_{M_{\rm l,SNIa}}^{M_{\rm m}} n(m)P(m)dm = c_{\rm SN} \int_{M_{\rm m}}^{M_{\rm u}} n(m)dm$$

is valid. Inserting the values $c_{\rm SN} = 0.1$, $x = 1.35$, $M_{\rm l,SNIa} = 1.5\ {\rm M}_\odot$, $M_{\rm m} = 10\ {\rm M}_\odot$ and $M_{\rm u} = 50\ {\rm M}_\odot$ reveals $N_0 = 1.48 \cdot 10^{-2}$.

In Fig. 2.15 the supernova rates are given for SNII (red) and SNIa (blue and green). For the description for SNIa rates applied in the model it was assumed that the two stars in a binary system have random masses. The corresponding SNIa rate is given as a blue line. Additionally the SNIa rate for the assumption that the two stars in a binary system have equal masses, is given as a green line. In this case the supernova rate is calculated equally to the SNII rate by just using the mass-lifetime relation and applying the appropriate normalization. In the equal mass model the SNIa emerge earlier than in the description applied in the present model.

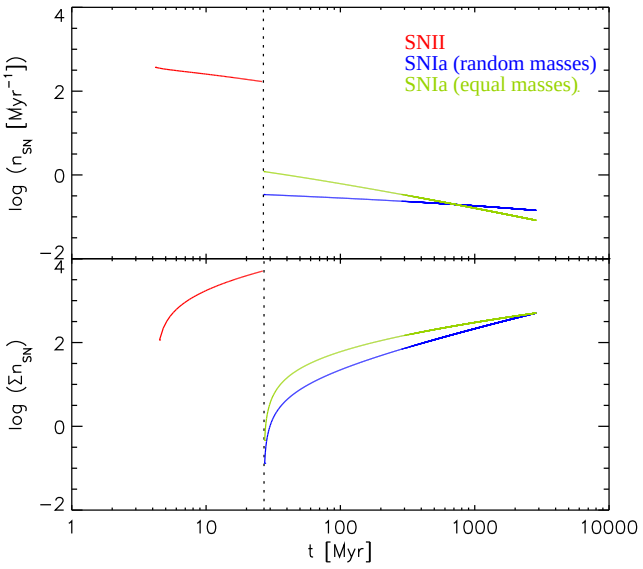

Figure 2.15. Supernova rate (top) and cumulated number of SNe (bottom). The description for the SNIa applied in the model (random masses) is compared to the case, where in binary systems the two stars have the same mass (equal masses) and consequently die at the same time.

b. Mass Return through SNIa

The low number of SNIa combined with their low ejected mass effectuates that the mass return from SNIa is insignificant for the galactic evolution. However, since SNIa produce large amounts of iron, which is important for the chemical enrichment of a galaxy, the mass return of SNIa is included in the model.

c. Heating through SNIa

The energy input of a SNIa is comparable to the one of a core collapse supernova but because of the smaller number of SNIa it is not that important for the galactic evolution. The ejected mass of a single SNIa is assumed to be $1.36\ {\rm M}_\odot$ (Nomoto et al., 1984) and hence the energy input per solar mass is

$$e_{\rm SNIa} = 3.86 \cdot 10^7 {\rm pc}^2 {\rm Myr}^{-2}$$

corresponding to a temperature of $T \sim 5 \cdot 10^9$ K of the ejected gas. Since the ejected material always mixes with

cooler material already present at the explosion location, this temperature is never reached in the ISM. The energy is transferred to 100% into the ICM, because of the long lifetime of the SNIa precursor the SNIa takes place far away from their birth place and are no longer connected to high density regions where the stars formed. SNIa are important for the chemical enrichment of the galaxy.

d. Enrichment through SNIa

As already mentioned, the W7 model of (Nomoto et al., 1984, 1996) is used to describe the SNIa. The W7 model ejects $0.717\ \mathrm{M}_\odot$ of iron and $0.143\ \mathrm{M}_\odot$ of oxygen. Since the total ejected mass is $1.36\ \mathrm{M}_\odot$ the iron yield of SNIa is 416 times the solar yield, whereas the oxygen yield is around 11 times the solar yield. This leads to

$$[\mathrm{O/Fe}]_{\mathrm{SNIa}} = -1.5$$

Whereas the ratio $[\mathrm{O/Fe}]_{\mathrm{SNII}}$ is reached in the beginning of galactic evolution, where only SNII contribute to the enrichment, the ratio $[\mathrm{O/Fe}]_{\mathrm{SNIa}}$ is never reached in galactic evolution, because there are always some SNII exploding before SNIa contribution gets important. In systems with high initial SFR the SNIa can dominate the feedback at late times and typically values of $[\mathrm{O/Fe}] = -0.5$ can be reached (Immeli, 1999).

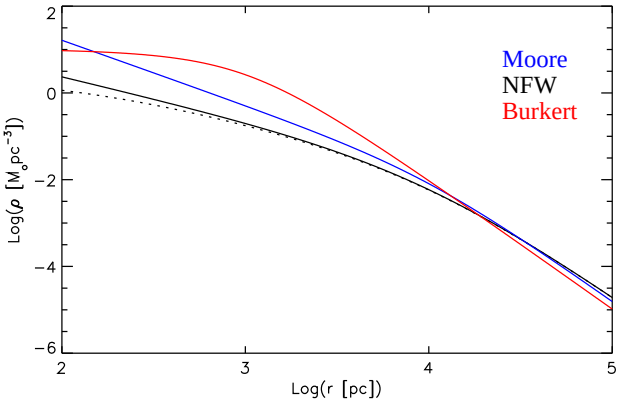

Figure 2.16. Density profile of the NFW halo (black) compared to the density profile applied in the simulation (dotted line), with a smoothing length $r_0 = 100$ pc. For comparison a Moore profile (blue) and a Burkert profile (red) are given.

2.4. Dark Matter Halo

As already mentioned in Sect. 1.2, structure formation models like cold dark matter (CDM), reveal the building of dark halos, in which the galaxies form. N-body CDM simulations show a universal density profile, the NFW profile (Navarro et al., 1997) for these dark halos. This radially symmetric density profile ρ_{dark} of the dark matter is given through

$$\rho_{\mathrm{dark}}(r) = \frac{\rho_0}{\frac{r}{r_{\mathrm{s}}}(1+\frac{r}{r_{\mathrm{s}}})^2} \qquad (2.22)$$

The scale radius r_{s} is the characteristic length scale of the halo and ρ_0 is a characteristic central density.

The NFW profile follows a r^{-3} profile for large r and evolves with r^{-1} for small r. Recent highest-resolution simulations appear to be consistent with a NFW-profile (Power et al., 2003; Klypin et al., 2002) until scales smaller than about 1 kpc. In the model I use a modified NFW halo profile, because the NFW profile diverges in the center and because observations reveal a flatter dark matter profile (e.g. Burkert, 1995; Salucci & Burkert, 2000; de Blok et al., 2001). I introduce a smoothing length r_0 in such a way that r is replaced by $r + r_0$ in Eq. 2.22. The resulting profile with a smoothing length of 100 pc is shown in Fig. 2.16. Note that the differences affect only the innermost region. There exist other profiles for the dark matter halo density distribution (Moore et al., 1999; Burkert, 1995). The Moore profile shows an even steeper core profile than the NFW-profile. The Burkert profile has a flat core, even flatter than the core of the artificially flattened NFW profile used in this simulation (Fig. 2.16). One can conclude that the artificially flattened profile lies within the uncertainties between the different profiles. The total mass of the halo is $7 \cdot 10^{11}\ \mathrm{M}_\odot$ and for the scale radius $r_{\mathrm{s}} = 12$ kpc was chosen. This leads to a total mass within the simulation volume of $10^{11}\ \mathrm{M}_\odot$.

More recent investigations of halo formation (Wechsler et al., 2002, W02) reveal a mass accretion history for the dark matter halos given through

$$M_h(z) = M_h(0) e^{-\frac{2z}{1+z_{\mathrm{f}}}} \qquad (2.23)$$

where z_{f} is the formation redshift and $M_h(0)$ the mass of the halo today. W02 give also a description of the evolution of the halo concentration. In Fig. 2.17 the inner dark matter profile ($R < 20$ kpc) in the context of the formation recipe of W02 is shown for a halo forming at $z_{\mathrm{f}} = 7$. The halo structure does not change significantly in the redshift range $1 < z < 5$ and the dark matter halo mainly grows in the outer regions. This is consistent with the findings of Bullock et al. (2001) that the scale radii for individual dark halos do not vary much as a function of redshift.

Hence, since the dark matter within a radius of 20 kpc does not change very much in the redshift range of $1 < z < 5$ and the scale length is constant, the assumption of a static non growing halo is justified for the central regions ($r <$ 20 kpc) in the context of the disk evolution models discussed in Chap. 4.

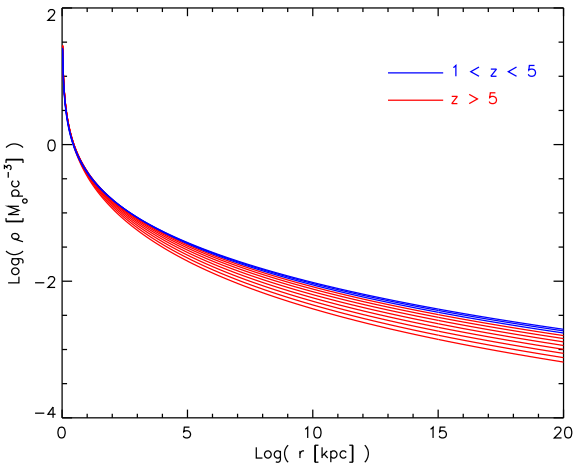

Figure 2.17. Growing dark halo for the halo formation model of W02. The density profile is given at different redshifts. The formation redshift is $z_f = 7$

2.5. Gravitation

All of the four components described so far, the cloudy medium, the hot gas, the stars, and the dark halo, interact with each other through gravity. The Poisson equation describes the relation between the gravitational potential and the density field.

$$\vec{\nabla}^2\Phi = 4\pi G\rho \tag{2.24}$$

The two different methods used in this model for solving the Poisson equation, including their advantages and drawbacks, are given in Sect. 3.3.

2.6. Self-Regulation and Equilibria

The evolution of galaxies is closely linked to self-regulation and feedback processes. Most of the important processes in galaxies are self-regulated (K¨oppen et al, 1995), which may be a reason that most galaxies can be classified along the few types of the Hubble sequence. It is one of the characteristics of the interaction network combined with hydrodynamics that it has a self-regulating character. Changing the efficiency of one process can lead to a back-reaction of the system in such away that the change is compensated. A necessary condition for such a self-regulation is the existence of reciprocal processes.

- *Star formation*

  Star formation is an example for a self-regulated process. On single cloud length scale, the stars forming in the dense part of the clouds ionize the clouds or can even disrupt them. Hence further star formation is prevented. This effect can be caused by stars of all masses (Cox, 1983; Bertoldi & McKee, 1995). On the large scale as described by the model, the energy input from SNII leads to a heating of the CM. The gradients in velocity dispersion lead to an expansion of the CM resulting in a lower density and hence a lower star formation at the location of the SNII.

- *Evaporation and condensation*

  The evaporation and condensation process together with the density dependent cooling leads to a self-regulation in the temperature of the gas phases which has a stabilizing influence on the multi-phase medium. The stabilizing effect of evaporation on the hot phase as a cause of the strong temperature dependence of the evaporation rate (Eq. 2.11) was already noted by McKee & Begelman (1990). If the ICM is strongly heated e.g. through energy input through SNII this leads to a higher evaporation rate, with the effect that the ICM density gets high and hence also the cooling is more effective. This process works also in the other direction. Note that for example changing the heating rate does not necessarily lead to a higher temperature, but it rather shifts the ICM to cloud mass ratio.

- *Dissipational cooling*

  An analog regulation happens if the dissipational cooling of the CM is enhanced. The clumping of the gas leads to a higher SF and subsequently higher heating and prevents the clouds from clumping together on a dynamical timescale. However, the change in the dissipation efficiency can not be compensated fully and the dissipation efficiency of the CM has a significant influence on galaxy evolution, as will be shown in Chap. 4 and Chap. 5.

In summary, the change in single processes is often counterbalanced by a reciproke process in the interaction network, although it is not always compensated. Note that there is no self-regulation in the enrichment process. For a more detailed discussion of the self-regulating character of the interaction network the reader is referred to Samland & Hensler (1996).

Under certain assumptions the density dependence of σ, $T_{\rm icm}$, and $\rho_{\rm icm}/\rho_{\rm cm}$ can be estimated in a one zone model. Samland & Gerhard (2003) did this in detail for their interaction network. They showed that even for density variations over several orders of magnitude, the temperature, velocity dispersion and relative gas masses do not change more than a factor of 10.

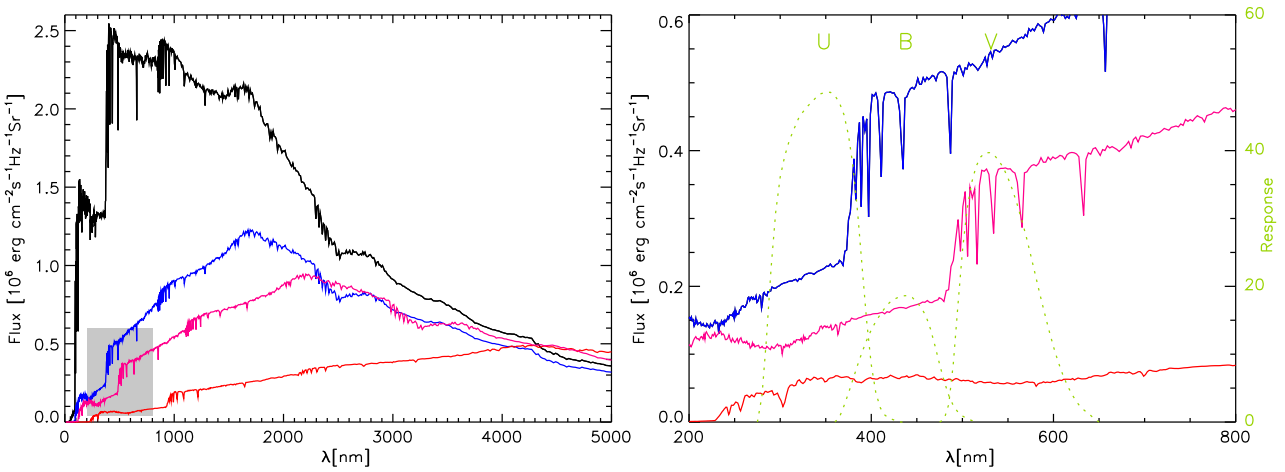

Figure 2.18. Left panel: Spectrum of the chain galaxy model (Chap. 5): intrinsic without absorption (black line), intrinsic with absorption (blue line), with absorption shifted to $z = 0.3$ (purple line) and shifted to $z = 1.5$ (red line). Right panel: Same as left panel together with typical response functions for U, B, and V-band (Landolt, 1983). The relevant spectral range is enlarged.

2.7. Extensions to the Model

2.7.1. Calculation of Intrinsic Colors

The chemodynamical evolution model naturally provides ages, metallicities and masses of the stars. From those it is possible to calculate the spectra of each stellar particle using spectro-photometric codes, like the Galaxy Isochrone Spectral Synthesis Evolution Library (GISSEL, Bruzual & Charlot, 1993). Those spectra are the added to a integrated spectrum of the area under consideration. An example of such a spectrum for a whole galaxy is given in Fig. 2.18. The black line represents the intrinsic spectrum of the galaxy. If one is interested in single colors, the integrated spectrum of the galaxy or of a region of the galaxy is passed through the the filter function of the respective filter (see Westera et al., 2002).

2.7.2. Calculation of Absorption

Absorption by dust is an important process which has to be dealt with when determining colors of galaxies. Due to the very complex and mostly unknown behavior of dust and its minor influence on the dynamical evolution, it is not directly included in the model. To calculate the absorption, a constant metallicity to dust ratio is assumed (Westera et al., 2002). The metallicity of the clouds is used. Hence the absorption is calculated as

$$A_\xi = \frac{\mathrm{pc}^2}{c_\xi \mathrm{M}_\odot} \int_{\mathrm{los}} \rho_Z(r) dr \qquad (2.25)$$

ρ_Z stand for the metal density and ξ is again an indicator of the band. For V-band Westera et al. (2002) use $c_\mathrm{v} = 15$. Transformations from A_V to other band are available in the literature (e.g Binney & Tremaine, 1987).

The effect of absorption can be seen in Fig. 2.18, where the blue line indicates the spectrum including absorption. The absorbed spectrum shows a maximum at $\lambda = 1800$ nm. Especially the blue parts of the spectrum are absorbed strongly, which of course is well known. The short UV-photons are absorbed by dust particles which then reradiate the energy in the sub-mm regime. This is far to the right of the scale in Fig. 2.18. Therefore the energy difference visible between absorbed and absorption-free spectra is reradiated in far infrared, and has no influence on the colors determined in this model.

2.7.3. Calculations of Colors at Non-Zero Redshift

To compare the model to observations of high redshift objects, it is necessary to calculate the colors one would observe if the model is situated at high redshift. In the left panel of Fig. 2.18 the zero redshift spectrum with absorption is shown together with the redshifted spectra of the model galaxy at $z = 0.3$ (purple line) and $z = 1.5$ (red line). Using the units given in the plot, the redshifting is done by multiplying the wavelength by $z+1$. The flux drops by a factor $z + 1$, for reasons of energy conservation.

Then the same procedure is used as for the intrinsic spectrum. The redshifted spectrum is passed through filter functions. In the right panel of Fig. 2.18 the range for the U-, B-, V-color determination is enlarged. Overplotted are the response functions for the U, B, and V-band filters from Landolt (1983).

UBVK colors (Buser, 1978) and the HST filter system colors (Williams et al., 1996) are used in this model. In princi-

ple the determination of the colors in arbitrary filter systems is possible as long as the filter function is available. No filter conversions (Fukugita et al., 1995) have to be applied.

2.7.4. An Efficient Way to Derive Restframe Colors

The calculation of spectra and the application of filter functions with GISSEL is time consuming. Since for example for movies the colors at many timesteps have to be calculated, a more efficient way of determining the colors is needed.

Since all of the stellar particles in the simulation represent single stellar populations, the faster way is to directly calculate the color of a single SSP dependent on its metallicity and age $\xi^*(Z,\tau)$ using again GISSEL, where ξ denotes the band index (e.g. UBVK, F606W, etc.). To get the total color, the fluxes of the particles in the volume of interest are simply added, where the mass of the particles has to be taken into account.

$$\xi = -2.5 \log \left(\sum_{\mathrm{stars}} M_{\mathrm{i}} 10^{-0.4 \xi^*(Z,\tau)} \right) \qquad (2.26)$$

M_{i} is the initial mass of the SSP. To get a surface brightness for comparison to observations, the area over which the flux is summed up, mostly given through the grid resolution, has to be set in relation to an arcsec.

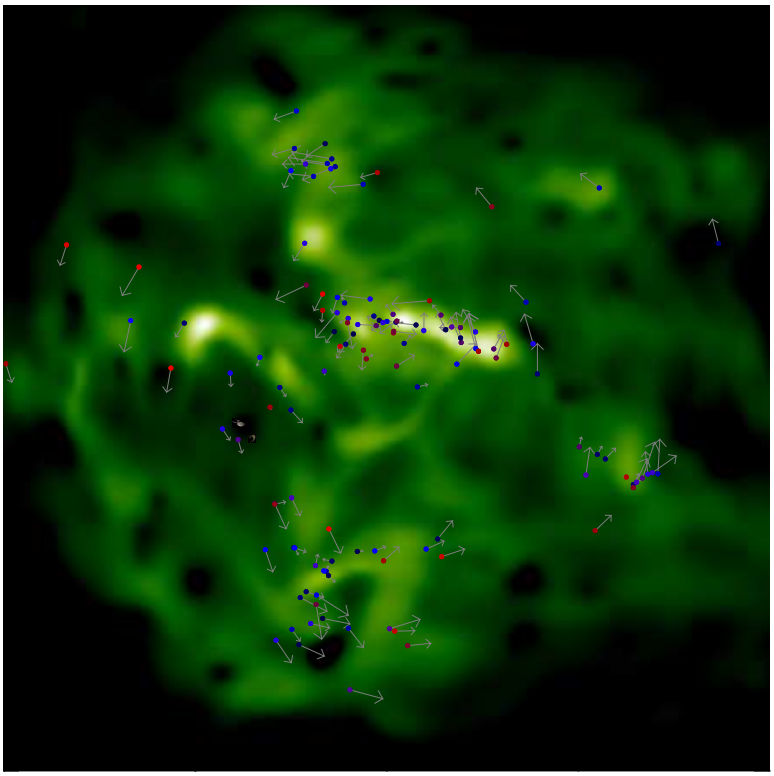

3

Numerical Methods

"We cannot have the whole universe in our computers"
heard at a conference in Santa Cruz de la Palma, Canary Island

This chapter addresses the numerical methods used to implement the equations derived in Chap. 2. In the first part I discuss the mathematical procedure applied. The numerical methods are similar to those described in Winkler & Norman (1986), Stone (1992), and Samland & Gerhard (2003). The code I developed during my thesis conforms FORTRAN 90 standards. This is the prerequisite for the Parallel Chemodynamical Evolution (PaCE) Code, which I am currently developing.

3.1. The Grid

The choice of the best suited grid is an important precondition for a successful simulation. On a first view the special geometry of a galactic disk leads to the thought that cylindrical or spherical coordinates would be best suited for the simulation. Unfortunately, the geometry of these grids introduces several problems. Since the grid cannot be pursued all the way to the very center, the central parts are generally represented by a hole with appropriate boundary conditions. This is not suitable for the present simulation, since the properties and evolution of the disk center, namely the bulge, are of special interest. Additionally, the representation of structures which do not exhibit spherical symmetry, like e.g. bars and spiral arms, is problematic since the grid cells get larger with distance from the center and hence the structures may be artificially broadened. Another problem arises with the conservation of angular momentum in hydrodynamical codes in spherical coordinates. M¨onchmeyer & M¨uller(1989) suggested a method to improve angular momentum conservation for these geometries, with the major disadvantage that it consumes a lot of computation time. A further point concerns the discretization of the equations, which cannot be done in an unambiguous way in spherical coordinates.

For all these reasons, the equations derived in the last chapter are solved on a Cartesian grid. The differentials emerging in the equations are replaced by the corresponding differences. This is formally equivalent to a Taylor expansion of the equations using only the leading terms. With the appropriate technique described below one gets a second order accuracy in space and time.

The relevant quantities needed to describe the numerical model are all known in the center of the grid cells. For purely hydrodynamical codes there exists a method called staggered grids or Marker-and-Cell method, where the velocities are known at the cell boundaries instead of the cell center. This reduces the amount of averaging compared to a description, where all quantities are known in the center of the cells. Unfortunately in the description of chemodynamical evolution, all the quantities are needed in the cell centers to calculate the interactions between the stars and the two gas phases, and therefore no net computation time saving is possible using staggered grids. Additionally, the averaging of the velocities during the interaction step leads to a diffusion (Samland, 1994), which does not appear if simple grids are used.

The equations are discretized on a three dimensional grid. The typical grid size is 100 grid points per dimension. In the following I use the three subscripts i, j, k to indicate the cell index of the x-, y- and z-direction respectively. Hence ρ_{ijk} denotes the density in the cell with the x-index i, the y-index j and the z-index k. Some geometrical quantities like the distance between two grid cells are numbered in such a way that the distance between the i^{th} cell center and the $i-1^{th}$ cell center has the i^{th} index (Fig. 3.1). In this

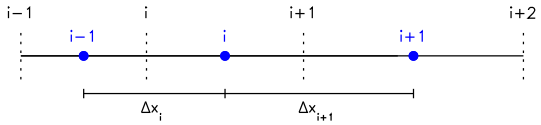

Figure 3.1. The grid numbering used in the code. Quantities known at the boundaries get the index of the adjacent cell at the right.

figure it is already indicated that the distance between two grid cells can vary over the simulation volume. For example, logarithmically scaled grids can be used to improve the spatial resolution in the center of the simulation volume. This is a possibility to enhance the central resolution without the need for more grid cells and henceforth without a significant rise in computation time and memory effort.

3.2. Hydrodynamics

3.2.1. Operator Splitting

To solve the Euler equations the method of the finite differences with an in time explicit operator splitting method is used. The operator splitting method divides the solution of the partial differential equations into several steps. Each part is solved noticing the change of the previous one. Writing the dynamical equations in the form

$$\frac{\partial y}{\partial t} = \mathbf{L}(y)$$

and making the assumption that $\mathbf{L}(y)$ can be divided in $\mathbf{L}(y) = \mathbf{L_1}(y) + \mathbf{L_2}(y) + ...$ one gets the solution through

$$\begin{aligned} y_1 &= y_0 + L_1(y_0) \\ y_2 &= y_1 + L_2(y_1) \\ y_3 &= y_2 + ... \end{aligned}$$

where L_i are representatives for the operators $\mathbf{L_i}(y)$ in the method of finite differences. Obviously this method is only an approximation to the real solution and there is a free choice for the order of the L_i. However, the order is chosen according to numerical experience, and numerical simulations have shown that this method can be trusted (Winkler & Norman, 1986).

To solve the Euler equations given in Sect. 2.2, they are splitted into two steps. The first step represented by the operator $\mathbf{L}_1$ is the so called source step. It describes the sources and sinks of the calculated quantities $a \in [\rho, \rho u_{\mathrm{i}}, \epsilon]$ in the volume V. The second operator $\mathbf{L}_2$ describes the

change of the quantity in the volume V by transport through the surface δV of the volume. It is called transport step. The transport step is obtained by splitting the Euler equations into terms containing an expression $\vec{\nabla}(a\vec{u})$ which through the use of the divergence theorem can be converted into a flux of the quantity a through the surface.

a. Mass equation

Writing out the Lagrange derivative (Eq. A.20) and using the product rule on the continuity equation (Eq. 2.3) one derives

$$\frac{\partial \rho}{\partial t} = -\vec{\nabla}(\rho\vec{u})$$

The source step is zero, which represents the physical law that mass cannot be created or destroyed. The transport step is obtained by integration over the volume V and exchanging the time derivative with the integration.

$$\frac{\partial}{\partial t}\int_V \rho dV = -\int_V \vec{\nabla}(\rho\vec{u})dV$$

This leads to the transport step of mass conservation by using the divergence theorem

$$\frac{\partial}{\partial t}\int_V \rho\, dV = -\int_{\delta V} \rho\, \vec{u} d\vec{S} \tag{3.1}$$

If the volume V stands for the volume of a single grid cell, the time change of the density in this cell is given through the flux through the cell surface.

b. Momentum equation

Rewriting the momentum equation (Eq. 2.4) makes for

$$\rho\frac{\partial \vec{u}}{\partial t} = -\rho\vec{\nabla}\Phi - \vec{\nabla}P - \rho\vec{u}\vec{\nabla}\vec{u}$$

The source step of momentum conservation is given by

$$\rho\frac{\partial \vec{u}}{\partial t} = -\rho\vec{\nabla}\Phi - \vec{\nabla}P \tag{3.2}$$

The transport step is obtained by transforming

$$\rho\frac{\partial \vec{u}}{\partial t} = -\rho\vec{u}\vec{\nabla}\vec{u}$$

to

$$\begin{aligned}\frac{\partial \rho\vec{u}}{\partial t} =& -\rho\vec{u}\vec{\nabla}\vec{u} + \vec{u}\frac{\partial \rho}{\partial t} \overset{2.3}{=} -\rho\vec{u}\vec{\nabla}\vec{u} - \vec{u}\vec{\nabla}(\rho\vec{u}) \\ =& -\rho\vec{u}\vec{\nabla}\vec{u} - \vec{\nabla}(\rho\vec{u}^2) + \rho\vec{u}\vec{\nabla}\vec{u} = -\vec{\nabla}(\rho\vec{u}^2)\end{aligned}$$

Again through integration over V, exchange of the time derivative with the integration and application of the divergence theorem leads to the transport step of the momentum equation

$$\frac{\partial}{\partial t}\int_V \rho\vec{u}\, dV = -\int_{\delta V} \rho\vec{u}\, \vec{u} d\vec{S} \tag{3.3}$$

c. Energy equation

The equation of energy conservation (Eq. 2.5) is rewritten to

$$\frac{\partial \epsilon}{\partial t} = \frac{\epsilon}{\rho}\frac{\partial \rho}{\partial t} - P\vec{\nabla}\vec{u} - \vec{u}\vec{\nabla}\epsilon + \frac{\epsilon}{\rho}\vec{u}\vec{\nabla}\rho$$

Again splitting up the equations analogously to above leads to the source step of energy conservation

$$\frac{\partial \epsilon}{\partial t} = -P\vec{\nabla}\vec{u} \tag{3.4}$$

and hence

$$\begin{aligned}\frac{\partial \epsilon}{\partial t} =& \frac{\epsilon}{\rho}\frac{\partial \rho}{\partial t} - \vec{u}\vec{\nabla}\epsilon + \frac{\epsilon}{\rho}\vec{u}\vec{\nabla}\rho \\ =& \frac{\epsilon}{\rho}\left[\frac{\partial \rho}{\partial t} + \vec{\nabla}(\vec{u}\rho)\right] - \frac{\epsilon}{\rho}\rho\vec{\nabla}\vec{u} - \vec{u}\vec{\nabla}\epsilon \overset{2.3}{=} -\vec{\nabla}(\vec{u}\epsilon)\end{aligned}$$

results with an analog procedure to the momentum equation in the transport step of energy conservation

$$\frac{\partial}{\partial t}\int_V \epsilon\, dV = -\int_{\delta V} \epsilon\, \vec{u} d\vec{S} \tag{3.5}$$

3.2.2. Transport Steps

In all three equations for the transport steps, the respective quantity is changed by integration of the quantity times the velocity over the surface of the volume under consideration. Since the volume is the Cartesian grid cell, the surface are the six areas of the cuboid, two in each dimension. The three dimensional description is reduced to one-dimensional procedure using dimensional splitting (Strang, 1968).

In principle, there exist many possibilities to describe one dimensional advection. Because numerical errors are inevitable, the independent advection of energy, momentum and density leads to artificial changes in temperature or velocity of the advected mass. To improve local energy and momentum conservation, the method of consistent advection, proposed by Norman et al. (1980), is used. In this description, specific energy (ϵ/ρ) and specific momenta ($\rho u_i/\rho$) are transported.

I discuss here two advection schemes, the upwind transport and the van Leer transport, which show differences in accuracy and computation time expense. To calculate the one dimensional flux one needs to know the velocity $\bar{u}$ at the boundary of the cell. This is simply the mean of the velocity of the two adjacent cells $\bar{u}_i = \frac{1}{2}(u_i + u_{i-1})$. Multiplying this by the timestep Δt yields the length over which the advected quantity is moved from one cell to the other. Therefore the one dimensional flux of a quantity a is

$$F = a^* \cdot \bar{u} \cdot \Delta t$$

where the way of calculating a^* differs in different advection schemes. The quantity a in cell i changes in the advection step according to

$$a_{\mathrm{i}}^{\mathrm{new}} = a_{\mathrm{i}}^{\mathrm{old}} + (a_{\mathrm{i}}^* \cdot \bar{u}_{\mathrm{i}} - a_{\mathrm{i+1}}^* \cdot \bar{u}_{\mathrm{i+1}})\Delta t$$

a. Upwind-Scheme

In the upwind advection all quantities are taken as constants over the grid cells (Fig. 3.2, top panel). This procedure smears out the gradients and is very diffusive. The calculation expense is very low but it is only first order accurate, which for many applications is not sufficient. For the advected quantity a one can write

$$\begin{aligned} a^* &= a_{\mathrm{i-1}} & \bar{u}_i > 0 \\ a^* &= a_{\mathrm{i}} & \bar{u}_i < 0 \end{aligned}$$

I implemented the upwind scheme in the numerical model, but due to its high diffusion it was only used in the test calculations (Sect. 3.4), and I mention it here only for illustrative reasons.

b. Van Leer-Scheme

In the van Leer advection scheme (Van Leer, 1977) the quantities are approximated with a stepwise linear function, where the step length equals the cell size (Fig. 3.2, bottom panel). At the cell boundaries the function is monotonic. Defining $\Delta a_{\mathrm{i+\frac{1}{2}}} = (a_{\mathrm{i+1}} - a_{\mathrm{i}})/\Delta x_{\mathrm{i}}$ one can calculate the van Leer gradients

$$\begin{aligned} \delta a_{\mathrm{i}} &= \frac{2(\Delta a_{\mathrm{i-\frac{1}{2}}} \Delta a_{\mathrm{i+\frac{1}{2}}})}{\Delta a_{\mathrm{i-\frac{1}{2}}} + \Delta a_{\mathrm{i+\frac{1}{2}}}} & \Delta a_{\mathrm{i-\frac{1}{2}}} \Delta a_{\mathrm{i+\frac{1}{2}}} > 0 \\ \delta a_{\mathrm{i}} &= 0 & \text{elsewhere} \end{aligned}$$

This means that if the slopes of two adjacent cells have the same algebraic sign, the van Leer gradient is given through and $\delta a_i \in [1b, 2b]$ where $b = \max(\Delta \mathrm{a}_{\mathrm{i-\frac{1}{2}}}, \Delta \mathrm{a}_{\mathrm{i+\frac{1}{2}}})$. If the slopes have different signs, the product of the slopes is negative and the van Leer gradient is zero. This corresponds to a local maximum or minimum in the approximated function. Hence for maximum and minimum values the van Leer advection scheme equals the upwind advection.

For the advected quantity a one then can write

$$\begin{aligned} a^* &= a_{\mathrm{i-1}} + \frac{1}{2}(\Delta x_{\mathrm{i-1}} - u_{\mathrm{i}}\Delta t)\delta a_{\mathrm{i-1}} & \bar{u}_{\mathrm{i}} > 0 \\ a^* &= a_{\mathrm{i}} + \frac{1}{2}(u_{\mathrm{i}}\Delta t - \Delta x_{\mathrm{i}})\delta a_{\mathrm{i}} & \bar{u}_{\mathrm{i}} < 0 \end{aligned}$$

which follows directly from basic geometrical considerations.

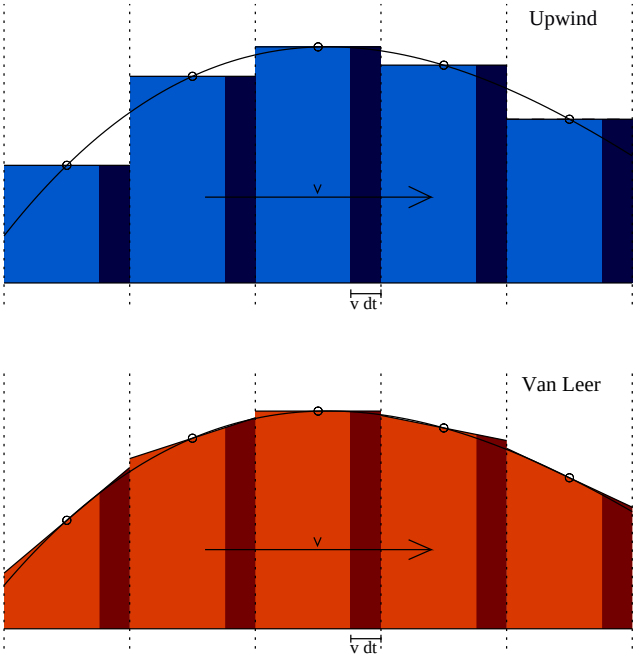

Figure 3.2. Approximations to the real function for the upwind advection (blue) and the van Leer advection scheme (red). Obviously, the van Leer advection scheme approximates the function much better.

As can be seen in Fig. 3.2, the van Leer advection scheme approximates the real function much better than an upwind advection scheme. Compared to the first order accuracy of the upwind advection, the van Leer advection is second order accurate. There exist more accurate advection schemes, like e.g. piecewise parabolic advection (PPA) (Colella & Woodward, 1984). In the PPA scheme, which is formally third order accurate, the advected interface values are calculated through parabolic approximation. Due to the much higher computational effort and the uncertain gain in precision in multi-dimensional simulations (Stone, 1992), I did not implement the PPA scheme in the numerical model.

c. Generalization to three dimensions

The generalization to three dimensions is straight forward. As already mentioned, each advection direction is calculated independently (Strang, 1968). For the three dimensional calculation of the flux the one dimensional flux has to be multiplied by the surface of the grid cell. Therefore the volume from which a^* is taken is $\bar{u}\Delta y\Delta z\Delta t$ and $F = a^* \cdot \bar{u}\Delta y\Delta z\Delta t$.

The three dimensional advection is obtained through aligning the one dimensional advection steps as follows, to prevent the introduction of a preferred direction and to get sec-

ond order accuracy (Samland & Gerhard, 2003).

$$\frac{1}{2}(\Delta A_x)\ \frac{1}{2}(\Delta A_y)\ (\Delta A_z)\ \frac{1}{2}(\Delta A_y)\ \frac{1}{2}(\Delta A_x)$$

ΔA_i denotes an advection step in direction $i = x, y, z$.

In this procedure five advection steps per iteration are needed. Since one advection step uses a large fraction of the total CPU time of the whole model iteration, it is desirable to reduce the advection steps. This is possible with a switching advection order. For even iteration indices the advection is done according to

$$(\Delta A_x)\ (\Delta A_y)\ (\Delta A_z)$$

and for odd indices the advection order is changed

$$(\Delta A_z)\ (\Delta A_y)\ (\Delta A_x)$$

Like this, 40% of calculation time can be saved, without loss of accuracy (Samland & Gerhard, 2003).

3.2.3. Discretization of the Source Steps

The discretization of the source steps is straight forward. Since the simulation is three dimensional, every quantity gets its three dimension indices i, j, k, which stand for the cell index in x, y, and z-direction respectively, as was already mentioned above.

Because gradients have to be calculated over two grid cells one gets as the discretization of the source step of the momentum equation

$$\rho_{\mathrm{ijk}}\frac{u^{\mathrm{x,new}}_{\mathrm{ijk}} - u^{\mathrm{x,old}}_{\mathrm{ijk}}}{\Delta t} = -\rho\frac{\Phi_{\mathrm{i+1,j,k}} - \Phi_{\mathrm{i-1,j,k}}}{\Delta x_{\mathrm{i}} + \Delta x_{\mathrm{i+1}}} - \frac{P_{\mathrm{i+1,j,k}} - P_{\mathrm{i-1,jk}}}{\Delta x_{\mathrm{i}} + \Delta x_{\mathrm{i+1}}}$$

where $u^{\mathrm{x,old}}_{\mathrm{ijk}} = u^{\mathrm{x}}_{\mathrm{ijk}}(t)$ and $u^{\mathrm{x,new}}_{\mathrm{ijk}} = u^{\mathrm{x}}_{\mathrm{ijk}}(t + \Delta t)$ are the x-component of the velocity at the time t and $t + \Delta t$. This leads to

$$\rho_{\mathrm{ijk}}u^{\mathrm{x,new}}_{\mathrm{ijk}} = \rho_{\mathrm{ijk}}u^{\mathrm{x,old}}_{\mathrm{ijk}} - \rho\frac{\Phi_{\mathrm{i+1,j,k}} - \Phi_{\mathrm{i-1,j,k}}}{\Delta x_{\mathrm{i}} + \Delta x_{\mathrm{i+1}}}\Delta t - \frac{P_{\mathrm{i+1,j,k}} - P_{\mathrm{i-1,jk}}}{\Delta x_{\mathrm{i}} + \Delta x_{\mathrm{i+1}}}\Delta t \tag{3.6}$$

The formulae for updating the momentum components in y- and z-direction are analog.

To get the discretization of the source step for the energy equation, the divergence of the velocity field has to be discretized first. Its discretization is again straight forward

$$\nabla u_{\mathrm{ijk}} = \frac{u_{\mathrm{i+1,j,k}} - u_{\mathrm{i-1,j,k}}}{\Delta x_{\mathrm{i}} + \Delta x_{\mathrm{i+1}}} + \frac{u_{\mathrm{i,j+1,k}} - u_{\mathrm{i,j-1,k}}}{\Delta y_{\mathrm{j}} + \Delta y_{\mathrm{j+1}}} + \frac{u_{\mathrm{i,j,k+1}} - u_{\mathrm{i,j,k-1}}}{\Delta z_{\mathrm{k}} + \Delta z_{\mathrm{k+1}}}$$

The the source step for energy conservation 3.4 is discretized to

$$\epsilon^{\mathrm{new}}_{\mathrm{ijk}} = \epsilon^{\mathrm{old}}_{\mathrm{ijk}} - (\gamma - 1)\epsilon^{*}_{\mathrm{ijk}}\nabla u_{\mathrm{ijk}}\Delta t$$

To improve energy conservation, one inserts in the right step of the above equation $\epsilon^* = (\epsilon_{\mathrm{old}} + \epsilon_{\mathrm{new}})/2$. This semi-implicit procedure reflects the idea that ϵ is best represented through the mean ϵ^* over the whole timestep (Winkler & Norman, 1986). This leads to

$$\epsilon^{\mathrm{new}}_{\mathrm{ijk}} = \epsilon^{\mathrm{old}}_{\mathrm{ijk}} \cdot \frac{1 - \frac{\gamma-1}{2}\nabla u_{\mathrm{ijk}}\Delta t}{1 + \frac{\gamma-1}{2}\nabla u_{\mathrm{ijk}}\Delta t} \tag{3.7}$$

3.2.4. Artificial Viscosity

To resolve shock fronts, special methods are required in the context of a hydrodynamical simulation, because at the shock front, unphysical oscillations can occur which influence the simulation result. To prevent this, one introduces an artificial viscosity, which spreads the shock wave over a few mesh points. Hence, the discontinuity is resolved. The artificial viscosity is not a real viscosity, it is introduced for numerical reasons. However, the artificial viscosity acts like a viscosity in the sense that is converts energy of motion into inner energy.

The artificial viscosity implemented in the numerical model uses the ansatz from Von Neumann & Richtmyer (1950)

$$\begin{array}{ll} q = l^2\rho(\frac{\partial u}{\partial x})^2 & \frac{\partial u}{\partial x} < 0 \\ q = 0 & \text{elsewhere} \end{array}$$

In a shock front is $\frac{\partial u}{\partial x} < 0$, which means that the matter behind runs into the matter in front which produces the shock. To avoid numerical inaccuracies at the sharp gradients the kinetic energy at the shock front is transferred into inner energy, which smears out the sharp gradients. The strength of this effect is given through the constant $C_q = l/(\Delta x)$, where l is the typical length, over which sharp gradients in shocks are smeared out.

Through the introduction of the artificial viscosity enter two additional source steps

$$\begin{aligned} \rho\frac{\partial u}{\partial t} &= -\frac{\partial q}{\partial x} \\ \frac{\partial \epsilon}{\partial t} &= -q\frac{\partial u}{\partial x} \end{aligned}$$

which represent the energy transfer from kinetic energy of the motion into inner energy. Discretizing this equation leads to

$$\rho u^{\mathrm{new}}_{\mathrm{i}} = \rho u^{\mathrm{old}}_{\mathrm{i}} - \frac{q_{\mathrm{i+1}} - q_{\mathrm{i-1}}}{\Delta x_{\mathrm{i}} + \Delta x_{\mathrm{i+1}}}\Delta t$$

and

$$\epsilon_{\rm i}^{\rm new} = \epsilon_{\rm i}^{\rm old} - q_{\rm i}\frac{u_{\rm i+1} - u_{\rm i-1}}{\Delta x_{\rm i} + \Delta x_{\rm i+1}}\Delta t$$

Unfortunately, the introduction of the artificial viscosity is not unproblematic. Applied to disk galaxy simulations, it leads to an unphysically high inflow of disk material into the central regions. This mass flow creates unrealistic massive bulges. Hence, artificial viscosity should only be used with caution in disk simulations. Already Gingold & Monaghan (1983) mentioned that the artificial viscosity is unsatisfactory in simulations of rotating clouds, since it does not conserve angular momentum, like any viscosity.

The effect of artificial viscosity, namely the redistribution of energy in high density regions is partly compensated by the interactions applied in this simulation. E.g. cooling prevents the build up of strong shocks, because energy is radiated away in high density regions. Hence artificial viscosity is not needed to describe the large scale galaxy evolution. Nevertheless it is included in the standard hydrodynamical tests (see Sect. 3.4).

It is noteworthy that there exist other possibilities of solving the equations derived in the last chapter. Many applications use the Godunov's approach (Godunov, 1959), in which the physical system is described through piecewise constant states within the cells. The discontinuities at the boundaries of the cells are treated as a set of Riemann problems. This method has been developed further by finding the appropriate Riemann solver for the problem (see LeVeque, 1992, 1998).

3.3. Gravitational Potential

I implemented two different methods to determine the gravitational potential of the mass distribution according to Eq. 2.24. One is the Successive Overrelaxation and the other the Fast Fourier Transformation. In the following I give a short outline of the methods and I mention some points to keep in mind while using these techniques.

3.3.1. Successive Overrelaxation

Successive Overrelaxation (SOR) belongs to the mesh relaxations methods, where initially guessed mesh values are relaxed to the solution by systematically adjusting the values on the mesh. I discuss here only the iteration method for solving the Poisson equation (Eq. 2.24), although several other applications exist. For an overview of different mesh relaxation methods and their convergence properties I refer the reader to the excellent book from Hockney & Eastwood (1988).

Mesh relaxations methods can be applied, if the difference equation for each mesh point can be written as a single matrix

$$A\Phi = q \tag{3.8}$$

where A is an N_g x N_g matrix and Φ is the vector of the N_g unknown values and q the given N_g sources. N_g is the number of grid point, i.e. $N_g = 10^6$ for a 100^3 grid. The matrix A is then splitted in an invertible matrix B and a remainder R, thus $A = B + R$. Eq. 3.8 can now be written as

$$B\Phi = -R\Phi + q = -(A - B)\Phi + q$$

Starting with an initial guess Φ_0 a series of iterates are generated through $B\Phi_{\rm t+1} = -(A - B)\Phi_{\rm t} + q$ and since B is invertible one gets

$$\Phi_{\rm t+1} = -B^{-1}(A - B)\Phi_{\rm t} + B^{-1}q = M\Phi_{\rm t} + B^{-1}q$$

where $M := -B^{-1}(A - B)$ is called the iteration matrix. Since for the error after t Iterations $\epsilon_{\rm t}$ the correlation

$$\frac{||\epsilon_{\rm t}||}{||\epsilon_0||} = ||M^t||$$

can be derived, it is important to choose the invertible matrix B in such a way that the norm of the iteration matrix is minimized and therefore the error decreases rapidly and the iteration converges fast. By choosing different forms of the matrix B the diverse iteration methods are obtained. An overview can be found in Hockney & Eastwood (1988).

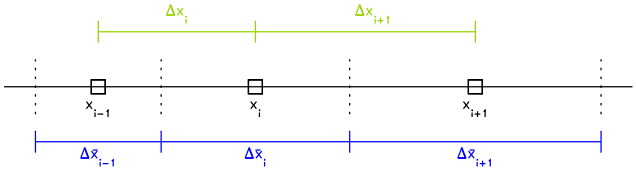

Figure 3.3. Visualization of the grid quantities used in SOR

While for convergence investigations the matrix representation of the relaxation procedure is appropriate, one needs for programming purposes the iteration on every grid point (i, j, k). The finite difference Poisson equation is

$$\begin{aligned}
&(\frac{\Phi_{\rm i+1,j,k} - \Phi_{\rm i,j,k}}{\Delta x_{\rm i+1}} - \frac{\Phi_{\rm i,j,k} - \Phi_{\rm i-1,j,k}}{\Delta x_{\rm i}})\frac{1}{\Delta \bar{x}_{\rm i}} \\
+&(\frac{\Phi_{\rm i,j+1,k} - \Phi_{\rm i,j,k}}{\Delta y_{\rm j+1}} - \frac{\Phi_{\rm i,j,k} - \Phi_{\rm i,j-1,k}}{\Delta y_{\rm j}})\frac{1}{\Delta \bar{y}_{\rm j}} \\
+&(\frac{\Phi_{\rm i,j,k+1} - \Phi_{\rm i,j,k}}{\Delta z_{\rm k+1}} - \frac{\Phi_{\rm i,j,k} - \Phi_{\rm i,j,k-1}}{\Delta z_{\rm k}})\frac{1}{\Delta \bar{z}_{\rm k}} = 4\pi G\rho_{\rm i,j,k}
\end{aligned}$$

where $\Delta\bar{\mu}_\mathrm{i} := \frac{\Delta\mu_{\mathrm{i}+1}+\Delta\mu_\mathrm{i}}{2}$ for $\mu = x, y, z$ and $\Delta\mu_\mathrm{i}$ is the cell size of cell i (see Fig. 3.3, j, k analogously). Expanding this equation and substituting $A_\mu = A^\mu_{\mathrm{ijk}} = (\Delta\bar{\mu}_{i+1}\Delta\mu_i)^{-1}$ and $B_\mu = B^\mu_{\mathrm{ijk}} = (\Delta\bar{\mu}_i\Delta\mu_i)^{-1}$ for $\mu = x, y, z$ one gets

$$\begin{aligned} &A_x\Phi_{\mathrm{i+1,j,k}} + B_x\Phi_{\mathrm{i-1,j,k}} \\ &+A_y\Phi_{\mathrm{i,j+1,k}} + B_y\Phi_{\mathrm{i,j-1,k}} \\ &+A_z\Phi_{\mathrm{i,j,k+1}} + B_z\Phi_{\mathrm{i,j,k-1}} \\ &-(A_x + B_x + A_y + B_y + A_z + B_z)\Phi_{\mathrm{i,j,k}} = 4\pi G\rho_{\mathrm{i,j,k}} \end{aligned} \tag{3.9}$$

which is an equation of the form

$$\begin{aligned} a_{\mathrm{ijk}}\Phi_{\mathrm{i+1,j,k}} + b_{\mathrm{ijk}}\Phi_{\mathrm{i-1,j,k}} + c_{\mathrm{ijk}}\Phi_{\mathrm{i,j+1,k}} + d_{\mathrm{ijk}}\Phi_{\mathrm{i,j-1,k}} \\ +e_{\mathrm{ijk}}\Phi_{\mathrm{i,j,k+1}} + f_{\mathrm{ijk}}\Phi_{\mathrm{i,j,k-1}} + g_{\mathrm{ijk}}\Phi_{\mathrm{i,j,k}} = h_{\mathrm{ijk}} \end{aligned} \tag{3.10}$$

where the values of the coefficients contain the geometrical quantities of the underlying grid, which can be inferred of direct comparison between Eq. 3.9 and Eq. 3.10. In the following I write $a := a_{\mathrm{ijk}}$ and equivalently for the other coefficients, keeping in mind that the coefficients can vary from grid point to grid point. Solving Eq. 3.10 for $\Phi_{\mathrm{i,j,k}}$ leads to

$$\begin{aligned} \Phi_{\mathrm{i,j,k}} = g^{-1}(h - a\Phi_{\mathrm{i+1,j,k}} - b\Phi_{\mathrm{i-1,j,k}} - c\Phi_{\mathrm{i,j+1,k}} \\ - d\Phi_{\mathrm{i,j-1,k}} - e\Phi_{\mathrm{i,j,k+1}} - f\Phi_{\mathrm{i,j,k-1}}) \end{aligned}$$

In the procedure of SOR the new $\Phi^{\mathrm{new}}_{\mathrm{i,j,k}}$ is calculated from the old $\Phi^{\mathrm{old}}_{\mathrm{i,j,k}}$ and the one derived through locally solving the Poisson equation in the above equation, denoted $\Phi^*_{\mathrm{i,j,k}}$. The relaxation factor ω determines the weight

$$\Phi^{\mathrm{new}}_{\mathrm{i,j,k}} = \omega\Phi^*_{\mathrm{i,j,k}} + (1-\omega)\Phi^{\mathrm{old}}_{\mathrm{i,j,k}}$$

Defining the residuum as

$$\begin{aligned} r_{\mathrm{ijk}} := a\Phi_{\mathrm{i+1,j,k}} + b\Phi_{\mathrm{i-1,j,k}} + c\Phi_{\mathrm{i,j+1,k}} + d\Phi_{\mathrm{i,j-1,k}} \\ +e\Phi_{\mathrm{i,j,k+1}} + f\Phi_{\mathrm{i,j,k-1}} + g\Phi_{\mathrm{i,j,k}} - h \end{aligned}$$

one gets $\Phi^*_{\mathrm{i,j,k}} = \Phi^{\mathrm{old}}_{\mathrm{i,j,k}} - r_{\mathrm{ijk}}g^{-1}_{\mathrm{ijk}}$ and hence

$$\Phi^{\mathrm{new}}_{\mathrm{i,j,k}} = \Phi^{\mathrm{old}}_{\mathrm{i,j,k}} - \frac{\mathrm{r_{ijk}}}{\mathrm{g_{ijk}}}\omega \tag{3.11}$$

In this formulation one can use the accumulated residual vector for a termination criterion of the iteration, since it is a measure for the total error of one iteration over the complete grid.

The best value of the relaxation factor ω is given through

$$\omega = \frac{2}{1+\sqrt{1-\rho^2_\mathrm{j}}} \tag{3.12}$$

where ρ_j is the spectral radius of the Jacobi matrix given through the diagonal elements of the iteration matrix M. While this ω is a good asymptotic value it is not necessarily a good initial choice, because the norm of error often grows by a factor of 20 before convergence sets in. Convergence can be improved, if one uses the Chebyshev acceleration. In this method one takes into account that the values of the iterated cells depend only on their direct neighbors. In the two-dimensional analogy of a chess board the black cells depend only one the white ones and vice versa. Hence one first makes one half iteration step over all black cells leaving the white ones on the old values and the second half iteration then runs over the white cells taking the changes of the black ones already in account. This procedure is known as odd-even ordering. ω is changed after each half sweep according to

$$\begin{aligned} \omega_0 &= 1 \\ \omega_{n+1/2} &= \frac{1}{1-\rho^2_\mathrm{j}\omega_n/4} \qquad n = 1/2, 1, ...\infty \end{aligned}$$

Using this iterative formula for ω, the norm of the error always decreases with each iteration. Note that this does not mean that the accumulated residuum also decreases. ω_n converges to the ideal ω for $n \to \infty$.

a. The choice of ρ_j

The implementation of SOR as outlined above is comparably simple and can be done without large effort. Unfortunately the calculation of ρ_j and hence the determination of ω for arbitrary grids is very difficult. In some cases ρ_j is known (see Press et al., 1986), but this is not the case for logarithmically spaced grids. The weak point of SOR is exactly the choice of the best ω. To get good convergence ω has to lie in a narrow window around the correct value. Therefore I tested the convergence of SOR for each grid setup using different values for ρ_j.

The higher the grid resolution is, the more the number of iterations depends on the correct value of ρ_j. I have done test calculations for a 21^3 and for a 101^3 grid. Choosing ρ_j by 0.5% to high results in 1.4 times more iterations for the 21^3 grid. For 101^3 already a mistake of 0.04% leads to the same additional expense in iteration number (Fig. 3.4). In addition, the single iterations take longer. This illustrates the need of investigating properly the behavior of the potential solver for each new grid setup. Since SOR is mainly used to calculate the potential on logarithmically space grids, I also want to note that test calculations revealed a dependence of the number of necessary iterations from the smallest grid size and not only from the number of grid cells. The finding of the best ρ_j can be time consuming but is absolutely necessary to ensure good performance during the simulation run.

Since the code of the SOR routine is comparably simple and clear, I use SOR as the potential solver for the parallel ver-

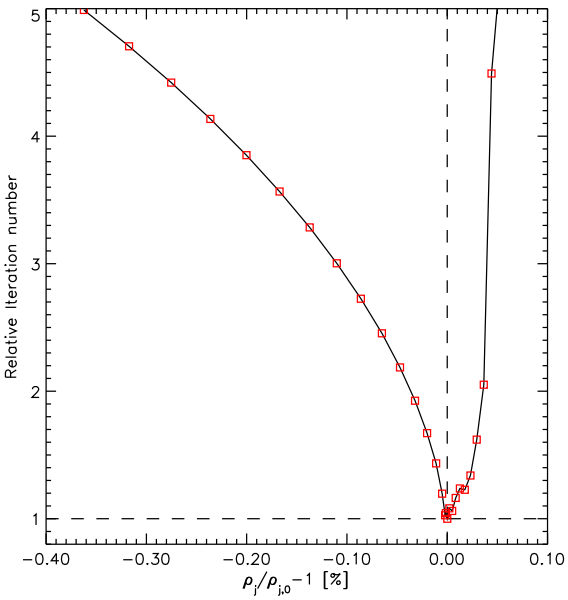

Figure 3.4. Numbers of iterations dependent on deviation of ρ_j from the best spectral radius $\rho_{j,0}$ for a 101^3 grid. Note that the deviation is given in percent, which means that ρ_j has to be chosen with an accuracy of at least 10^{-4}. The sharp rise in iteration number for ρ_j chosen to high reflects the common advice found in literature to chose ω (Eq. 3.12) rather too high than too low.

sion of the code (see Sect. B.3.), because on the PC cluster no free parallel potential solver is available at the moment.

3.3.2. Fast Fourier Transformation

In this paragraph I give a short overview of the Fast Fourier Transformation (FFT). The interested reader is referred to the books of Binney & Tremaine (1987), Press et al. (1986) and Hockney & Eastwood (1988) for further details.

To calculate the potential of a mass distribution, one can build a sum of the following form

$$\Phi_{\mathrm{i_0,j_0,k_0}} = \sum_{\mathrm{i=0}}^{N-1} \sum_{\mathrm{j=0}}^{N-1} \sum_{\mathrm{k=0}}^{N-1} \Phi_{\mathrm{i,j,k}}^{\mathrm{i_0,j_0,k_0}} M_{\mathrm{i,j,k}}^{*} \qquad (3.13)$$

where $\Phi_{\mathrm{i,j,k}}^{\mathrm{i_0,j_0,k_0}}$ is the potential at the center of cell i_0, j_0, k_0 generated by unit mass at the center of cell i, j, k. $M_{\mathrm{i,j,k}}^{*}$ is the mass in the grid cell i, j, k. In the method of the fast Fourier transformation one uses the fact that the above summation, which is very expensive to calculate, can be replaced by the multiplication of the Fourier transforms of the quantities involved (see Binney & Tremaine, 1987, for a detailed explanation).

But this is not the end of the story. A discrete Fourier transformation is an $O(N^2)$ process. The performance can be heavily increased by using the Danielson-Lanczos Lemma (Danielson & Lanczos, 1942) which states that a discrete Fourier transition of length N can be rewritten as the sum of two discrete Fourier transitions

$$F_{\mathrm{k}} = F_{\mathrm{k}}^{\mathrm{e}} + w^k F_{\mathrm{k}}^{\mathrm{o}}$$

where $w = e^{2\pi i/N}$ and F_k^e and F_k^o are the FT consisting of the even and odd numbered points of the original FT respectively. This procedure now can be used recursively. If N is an integer power of 2, this procedure can be repeated all the way down to transforms of length one, which is just the identity operation.

$$F_{\mathrm{k}}^{\mathrm{eooeo\ldots eooeooeee}} = f_{\mathrm{n}}$$

where n is given through the binary value of the reverse pattern of the e's and o's inserting $e = 0$ and $o = 1$, which is a direct consequence of the Danielson-Lanczos Lemma. This procedure is a $N \log_2(N)$ process, which for large N is dramatically faster than the standard Fourier transformation (Press et al., 1986).

Although this procedure works with decompositions other than 2, it is highly recommended to use only grid sizes which are integer power of 2. In Fig. 3.5 I calculated the performance of the FFT code, linked to my model, dependent on the grid size N. The total numbers of grid cells is given through N^3. In this routine special implementations for the integer numbers $2, 3, 4$ and 5 exist. In my models I use grid sizes of 129^3 and 257^3, indicated by the dotted lines. In both cases changing the grid size by one can lead to 10 times high computation time. For example, the potential on a grid size of 257^3 is determined in the same time as on a 138^3 grid.

3.3.3. SOR versus FFT

I implemented two numerical schemes to solve the gravitational potential. The SOR routine is short and directly implemented in the numerical model. The adaption of SOR to other architectures (see Sect. B.2.) is possible at comparably low cost. One of the mayor advantage of SOR over FFT is the ability to solve the potential on logarithmic scaled grids (compare Sect. 3.1) with free scaling factors, while FFT is restricted to equidistant grids.

The implementation of a high performing FFT is expensive and I therefore use a free FFT library which is linked to my numerical model. The advantage of FFT is the fast execution in simulation with strongly changing gravitational potential, since FFT calculates the potential in every iteration independent on the previous results. On the other hand in situations where the gravitational potential does not vary much, the use of SOR is recommended, since it uses the result of the previous timestep as a starting point for the iteration. Obviously, in a nearly constant potential this is already a very good guess and the number of iterations required are low.

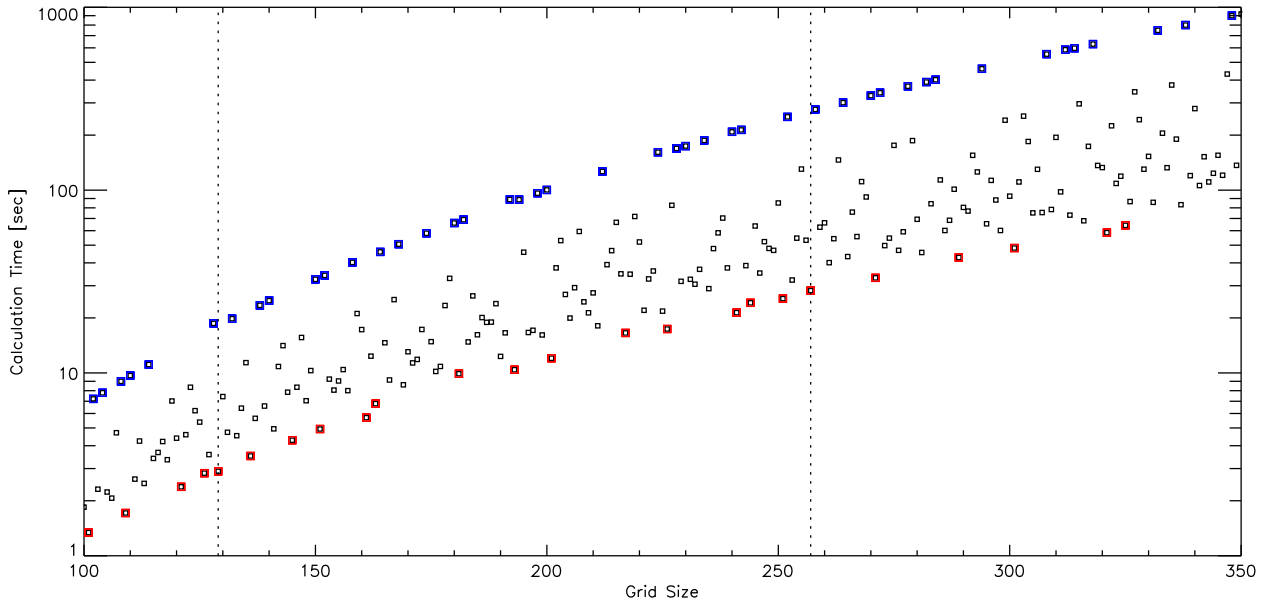

Figure 3.5. Performance of the FFT routine in calculating the potential dependent on the number of grid points per dimension. Performance is best, if the grid size minus one is a multiple of 2,3,4 or 5 (red dots). If it is a prime number (blue dots), the performance is unacceptably bad. The dotted lines represent the grid sizes chosen to calculate the gravitational potential in the disk evolution simulations.

3.3.4. Boundary Condition for the Gravitational Potential

Independent on the method used to calculate the gravitational potential, one has to specify the gravitational potential or its derivative at the boundary of the simulation volume.

In models, where the galaxy is simulated out to several tens of kpc or even out to the virial radius of the dark halo, I specified the gravitational potential on the boundary as a combination of the analytically known potential of the dark halo and the potential of the baryonic mass approximated by a point mass. Since I focus in the models presented here only on the disk and the simulation extend is of the same order as the disk size, the assumption of a point mass is no longer applicable directly. In the present model, the gravitational potential is calculated on a grid, which extends further out than the simulation volume. Then again the combination of the analytic halo potential and the point mass approximation can be used to determine the potential at the boundary of the larger grid.

3.4. Test Calculations

At this point, all ingredients needed for the hydrodynamical simulations have been discussed. The only exception is the dynamical time step control, which will be discussed in Sect. 3.7 in the context of the whole numerical model.

In this section I want to present some standard hydrodynamical tests, which can be used to examine the correct implementation of the hydrodynamical description. Additionally, the implementation of the potential solver is tested. Testing the implementations of hydrodynamical codes is a very important step in code development.

3.4.1. Shock-Tube

The shock tube problem, first used by Sod (1978), has become one of the most important tests in hydrodynamics. It involves setting up two discontinuous states, a hot dense gas at the left and a cold rarefied gas at the right. At time $t = 0$ the two regimes start to interact. A shock front propagates into the cold gas and a rare faction fan penetrates into the hot dense gas. The solution is known analytically and therefore this test can be used to check, whether the code reproduces the correct shock jump conditions.

The initial conditions are shown as dotted lines in Fig. 3.6. The hot dense gas at the left has a pressure $p_1 = 1.0$ and a density $\rho_1 = 1.0$, whereas the pressure of the cold gas is set to $p_2 = 0.1$ and the density to $\rho_2 = 0.125$. The discontinuity is located at $r = 0$ and the velocity is zero everywhere. The analytic solution after time $t = 0.245$ is given in solid lines. The numerical results of the sod shock-tube problem as calculated by the code using upwind transport (left column), van Leer transport (middle column) and van Leer transport with artificial viscosity (right column) are

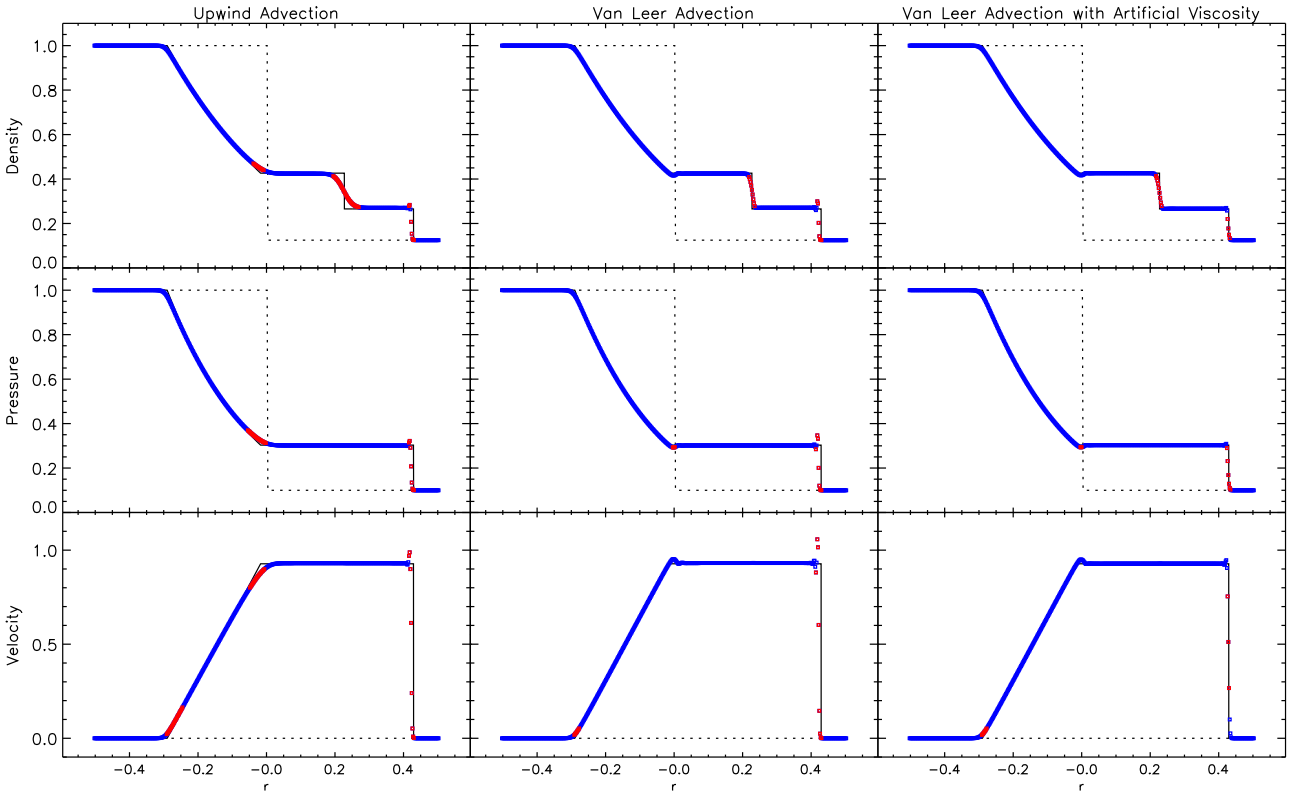

Figure 3.6. Density, pressure, and velocity for different advection schemes and artifi cial viscosity as indicated. The blue and red dots show the numerical solution. The red dots show the points, where the deviation from the analytic solution (black line) is larger than 2%. The dotted lines show the initial conditions.

given in blue and red points. The blue points approach the analytical solution better than 2% whereas the red points indicate deviations which are larger than 2%. The red points are located at the discontinuities. The diffusive nature of the upwind transport scheme is clearly visible at the edges. The analytic solution is better described by a van Leer transport scheme. Overshooting at the shock front is reduced through the artificial viscosity, which damps the amplifications emerging at the discontinuities. Small overshooting is still noticeable in the case with artificial viscosity, but Winkler & Norman (1986) showed that such overshoots are in fact the correct solution to the viscous finite difference equations as $\Delta x \rightarrow 0$.

3.4.2. Blast Waves

In further testing, the interaction of two strong blast waves in one dimension is considered. A gamma-law gas ($\gamma = 1.4$) is at rest between to reflecting walls in the domain $r \in [-0.5, 0.5]$. The density is 1 everywhere whereas the pressure is 1000 for $r < -0.4$, 100 for $r > 0.4$ and 0.01 in between. The pressure discontinuities will lead to strong shocks, which will interact with each other resulting in a complicated pattern of shocks. There exists no analytic solution but several high resolution reference calculations, to which the results can be compared (Stone, 1992; Woodward & Colella, 1984). The density distribution after a time $t = 0.038$ is given in Fig. 3.7. It is identical to the one presented in the literature.

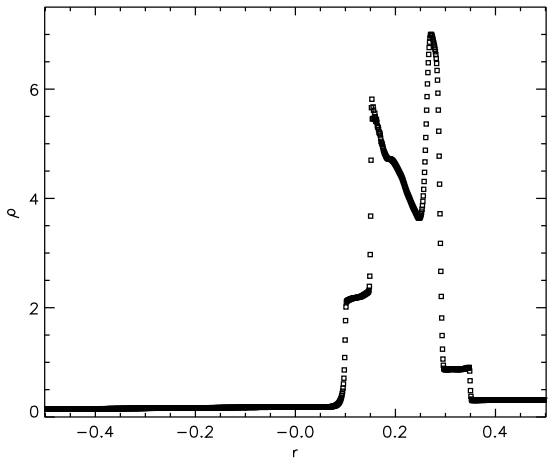

Figure 3.7. Blast waves: density distribution after $t = 0.038$. The result matches the one given in Stone (1992) for the case of van Leer advection.

The shock tube and the blast waves test have been done in every advection direction. This assures a correct implementation of the source and transport steps discussed above.

3.4.3. Free Collapse

The last two tests were done to investigate the behavior of the code at shock fronts and to check, whether the source and transport steps are implemented correctly. The present test provides the possibility to test the three-dimensional behavior of the model as well as the correct implementation of the gravitational potential. In the free collapse a homogeneous gas sphere with a density ρ_0 collapses under self gravity, without pressure forces. Also for this problem there exists an analytic solution. The equation of motion for the free collapse is

$$\frac{d^2r}{dt^2} = -\frac{GM}{r^2}$$

The parametrized solution to the equation is (Mestel, 1965)

$$r = R\cos^2\Theta$$
$$t = \sqrt{\frac{3}{8\pi G\rho_0}}(\Theta + \frac{1}{2}\sin(2\Theta))$$

where $\Theta \in [0, \pi/2]$. When Θ reaches the value $\pi/2$ the system is collapsed to one point. The time the system needs for the collapse, the so-called free fall time $t_{\rm ff}$ is hence given through insertion of $\Theta = \pi/2$ into the above equation

$$t_{\rm ff} = \sqrt{\frac{3\pi}{32G\rho_0}}$$

The analytic relation between collapse velocity and radius can be obtained by rewriting the equation of motion for this problem to $\frac{1}{2}\frac{du^2}{dr} = -\frac{GM}{r^2}$ and integrating of the radius R.

$$\frac{1}{2}(u^2 - u_0^2) = GM(\frac{1}{r} - \frac{1}{R})$$

Since the cloud is initially at rest ($u_0 = 0$) one derives the relation

$$\log(\frac{u}{r}) = \log(\frac{\pi}{2}\frac{R}{rt_{\rm ff}}\sqrt{\frac{R}{r} - 1})$$

The initial conditions are given through a sphere with a constant density $\rho_0 = 0.01\ {\rm M}_\odot{\rm pc}^{-3}$ and a radius $R = 17$ kpc. The freefall time of this system then is 80.9 Myr. The density profile is plotted at different times in the top panel of Fig. 3.8. The density gets higher but stays constant over the extension of the shrinking sphere. The theoretical slope of the envelope is -3 (red line), simply because the volume has a dependency on r^3 and thus the density grows with r^{-3}

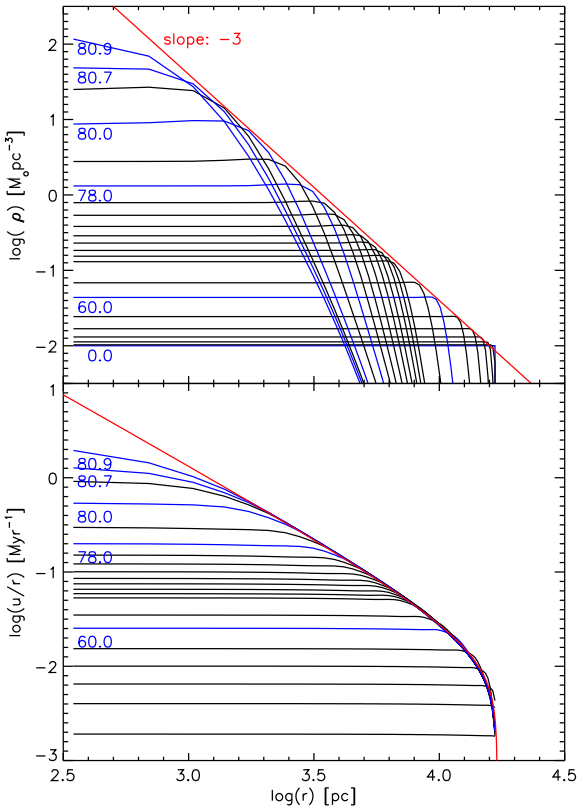

Figure 3.8. Density profile of the cold collapse at different timesteps (upper panel) and $\log(u/r)$ versus $\log(r)$ (lower panel).

because the mass is constant. The reason for the small differences lies in the fact that grid codes always show some level of diffusion. However, the difference in the present calculation is rather small.

There exist several other hydrodynamical tests, to which the code can be compared. Discussing all of those would be beyond the scope of this section. The potential solver can be tested directly by inserting the derived potential into the Poisson equation and comparing the gained density distribution to the original one.

3.5. Particle Mesh Method for the Stars

The dynamics of the stars is described using a particle-mesh method (Hockney & Eastwood, 1988). In the particle-mesh (PM) method, the spatial coordinates are discretized by setting up a rectangular grid over the three dimensional space. Field quantities like the gravitational potential are represented by the values at the grid points. The potential or the force acting on a particle is obtained by interpolating the values at the mesh points to the particles position. The opposite process is used to assign the mass of the particles to the grid for the determination of the potential. In this model the grid is identical to the one introduced to describe the

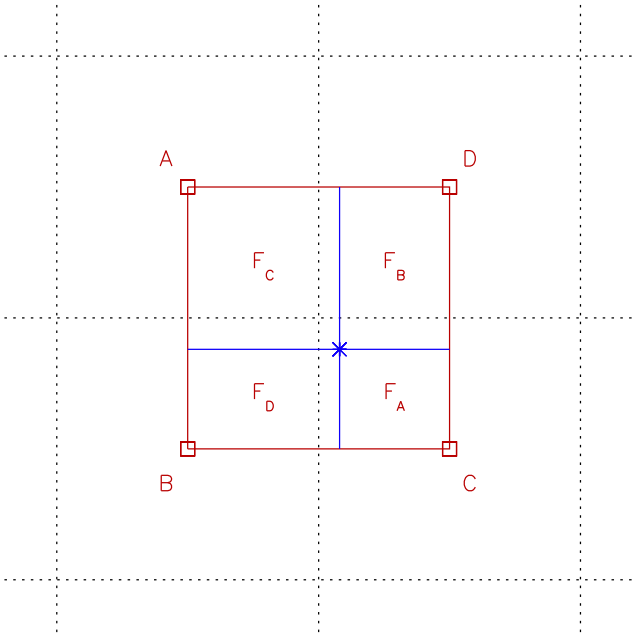

Figure 3.9. Schematic view of the cloud in cell method. The cell centers (squares) are connected through a rectangle in which the stellar particle (star) resides. The $F_{\rm k}$ stand for the areas spanned by the red and blue lines.

dynamics of the gas phases (see Sect. 3.1). The following points give a short outline over the procedure.

- *Mapping all the stellar masses to the grid*

  The simplest way of assigning the stellar masses to the grid is the method of the nearest grid point, in which the mass of a stellar particle is added to the nearest cell in 3D space. Since this is only a zeroth order interpolation, I use for the mapping the more accurate cloud in cell (CIC) method. In Fig. 3.9 the principle of the CIC method is shown for 2 dimensions. The mass $m_{\rm i}^*$ of the stellar particle i is distributed to the adjacent grid cells according to

  $$m_k = m_{\rm i}^* F_k/(F_A + F_B + F_C + F_D) \quad k \in [A, .., D]$$

  Each grid cell obtains therefore the fraction of the mass of stellar particle i that corresponds to the fraction of the opposing area to the area spanned by the grid points.

- *Calculation of the gravitational potential* Φ

  The gravitational potential is calculated for the mapped mass density. In the present model, the mass density of the two gas phases and the dark matter distribution are added to the stellar mass density to calculate the common potential.

- *Solving the equation of motion*

  After the calculation of the gravitational potential on the grid, its value at the location of the stellar particle i is determined using again the CIC method.

  $$\Phi_* = \frac{\Phi_A F_A + \Phi_B F_B + \Phi_C F_C + \Phi_D F_D}{F_A + F_B + F_C + F_D}$$

  The nearer the star is at a certain grid point, the larger the opposite area F_k is and hence the greater the importance of the potential at that grid point. The generalization to three dimensions is straight forward. Since variations on a scale smaller than the grid spacing are smeared out, PM should only be used for collision less systems, where 2-body relaxation is not important. Both requirements are fulfilled by the stellar phase in a normal galaxy.

- *Integrating the path of the stellar particles*

  The integration of the stellar particles is done by updating the stellar positions according to a standard leapfrog procedure.

3.6. Interactions

The interaction processes described in Chap. 2 have to be implemented in the numerical model. This is done by solving the set of ordinary differential equations explicitly in time for every grid cell. The determination of the timestep for the integration is discussed in Sect. 3.7.

The interactions between the stellar particles and the gas phases need a special treatment, since the grid-particles interactions cannot be calculated for each cell independently. The following two points describe how star formation and feedback from stellar particles is implemented.

- *Formation of stellar particles*

  As already mentioned the computational power available today does not allow for calculating every star as a particle and the stars are described by single stellar populations. To delineate star formation in the context of the model, the star forming mass according to Eq. 2.14 is accumulated over the grid in each cell during a time interval $\Delta t_{\rm sf}$, typically of the order of a few Myr. After that time interval the total over the grid accumulated mass is distributed onto a number $n_{\rm gen}$ new formed stellar particles. The positions of these particles are then taken randomly, where the accumulated star forming mass in a grid cell is taken as weight. Once a cell is chosen to make a new stellar particle, the particle gets the bulk velocity of the cloudy medium in the cell as well as its chemical composition. Additionally the particle gets a randomly oriented velocity to account for the velocity dispersion of the clouds.

- *Feedback from the stars*

  The mass and energy feedback of the stars is calculated as described in Sect. 2.3, using again the CIC method (see Fig. 3.9) to map the returned mass and energy onto the grid. This assures that mass and energy are given back in a smooth way as a particle moves over the mesh. Using the nearest grid point method would lead to a discontinuous energy feedback for individual grid cells, which is not only unphysical but also numerically critical, since abrupt changes can induce numerical oscillations. The CIC mapping procedure is time consuming and therefore the calculation of the feedback is done together with the mapping of the stars onto the grid (see Sect. 3.5). This step is called feedback precalculation, because the feedback to the gas phases is only accomplished in the interaction routine (see Fig. 3.17).

Since the feedback is mapped onto the same grid, where the gas phases are calculated, the interactions can now be solved for every grid cell independently.

3.7. Time Step Control

The correct choice of a time step is very important for the chemodynamical evolution code. Too low time steps can lead to unpredictable numerical diffusion and very expensive calculation times. On the other hand, one has to assure that each cell can only interact with its direct neighbors. Since information travels with the speed $u+c_s$, where u is the bulk motion and $c_s = \sqrt{\gamma P/\rho}$ the adiabatic sound speed, one gets the condition for the time step of the gaseous component in one dimension

$$\Delta t^{\mathrm{1D}}_{\mathrm{gas}} \leq \min\left[\frac{\Delta x_{\mathrm{i}}}{u_{\mathrm{i}} + c_{s,\mathrm{i}}}\right] \tag{3.14}$$

which is known as the Courant-Friedrichs-Lewy (CFL) condition. Δx_{i} is the extension of the grid cell i. The minimum is taken over all grid cells i. The generalization to three dimensions is straight forward

$$\Delta t_{\mathrm{gas}} \leq \min\left[\frac{\min(\Delta x_{\mathrm{i}}, \Delta y_{\mathrm{i}}, \Delta z_{\mathrm{i}})}{|\vec{u}_{\mathrm{i}}| + c_{s,\mathrm{i}}}\right]$$

If the artificial viscosity is used, one has also to take into account the timestep of this process, which is given through (Stone, 1992)

$$\Delta t_{\mathrm{visc}} \leq \min\left[\frac{\Delta x_{\mathrm{i}}}{4C_q\Delta u_{\mathrm{x,i}}}, \frac{\Delta y_{\mathrm{i}}}{4C_q\Delta u_{\mathrm{y,i}}}, \frac{\Delta z_{\mathrm{i}}}{4C_q\Delta u_{\mathrm{z,i}}}\right]$$

here C_q is the constant which is a measure for the strength of the artificial viscosity. Δx and $\Delta u_{\mathrm{x,i}}$ are the cell size and the velocity change of cell i.

For the other dynamical component, the stars, a similar argument as for the gas phase is used. The particles must not move over more than one grid cell per timestep. Hence the CFL condition for the stars reads

$$\Delta t_{\mathrm{stars}} \leq \frac{\min(\Delta x, \Delta y, \Delta z)}{\max(|\vec{v}_{\mathrm{stars}}|)}$$

The above timesteps are calculated for both gas phases and for every grid cell as well as for all the stars. To assure that the CFL condition (Eq. 3.14) is given for all cells and stars, one chooses the lowest of all the timesteps. Additionally, this timestep is multiplied by the Courant factor c_{cour}, which typically takes values between 0.1 and 0.5. Therefore the timestep is

$$\Delta t_{\mathrm{new}} = c_{\mathrm{cour}}\min(\Delta t_{\mathrm{gas}}, \Delta t_{\mathrm{visc}}, \Delta t_{\mathrm{stars}}) \tag{3.15}$$

Fast rising timesteps can cause unphysical oscillations of the system. In the model, the timestep can only rise a factor of 1.3 from one iteration to the next. To account also for a maximal timestep Δt_{max}, given for example through interval of the formation of stellar particles, the timestep for the next iteration is

$$\Delta t = \min(\Delta t_{\mathrm{new}}, 1.3 \cdot \Delta t_{\mathrm{old}}, \Delta t_{\mathrm{max}})$$

Since in this model not only the dynamical behavior of the components is calculated but also interactions between the ISM phases and the stars, one must also take into account the timescales of all the processes acting between the different phases. The important quantity similar to the CLF-condition is the timescale of a single interaction process $\tau_{\mathrm{i}} := X_{\mathrm{i}}/\dot{X}_{\mathrm{i}}$. If the timestep of the iteration is larger than the shortest timescale of a process, this can lead to unphysical results. As an example, if the timestep is larger than the cooling timescale of the gas, this would lead to negative energies, which obviously has to be prevented.

Principally, the timescales of the processes could simply be added to Eq. 3.15. But since the timestep of the interactions can be much smaller than the dynamical one, hydrodynamics would be described on a timestep which is much shorter than its appropriate one. Therefore the computational effort rises strongly and due to the numerical viscosity introduced by every iteration step, calculating hydrodynamics on a much too short timestep can result in numerical inaccuracies. For these reasons the interactions are calculated on a different timestep.

For all the interaction processes described in Chap. 2 the timescale is derived. The timestep with which the interactions are calculated is the timescale of the fastest process multiplied by a Courant factor of 0.1.

$$\Delta t_{\mathrm{int}} = 0.1 \cdot \min(\tau_{\mathrm{i}}) \qquad \mathrm{i} \in [\text{all processes}]$$

This timestep is calculated for every grid cell independently. If the timestep is larger than the one derived for the

hydrodynamics, then the timestep is set equal to the one from hydrodynamics. If it is the other way round, then the cell is iterated until the sum over the timesteps is equal to the one from hydrodynamics

$$\Delta t_{\rm hydro} = \sum_{\rm i=1}^{N} \Delta t_{\rm int,i}$$

where $t_{\rm int,N}$ is chosen to fit the above condition (see Fig. 3.10).

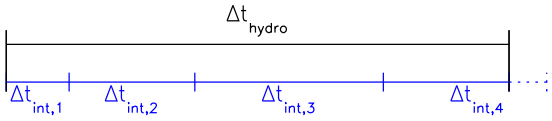

Figure 3.10. Schematic view of the choice of the interaction timestep. This procedure is applied at every grid cell independently.

3.8. Boundary Conditions

In modeling galactic evolution, it is impossible as well as unnecessary to include the whole universe in the simulation. Hence one needs to find a description for the boundary between the simulated volume and the outer world. The use of an adequate boundary condition is very important, since the effect of an improper boundary condition can influence the physical processes in the simulation volume. Obviously, this must be avoided.

One typically needs two grid cells at the boundary of the simulation volume to describe the boundary conditions. These cells are called the ghost cells. I first introduce some of the commonly used boundary conditions, where the difference lies in the way the ghost cells are set.

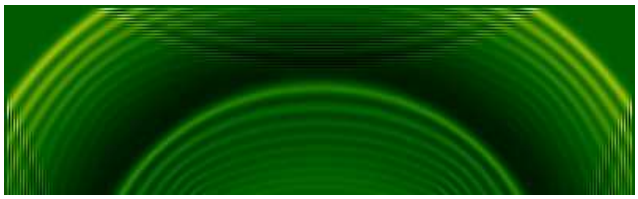

Figure 3.11. A density wave emerging from an explosion is reflected at the constant boundary and influences the simulation volume. This nicely illustrates the need for proper boundary conditions. Often the effect of the boundary is not this obvious, and a careful choice is needed.

- *Constant boundary condition*

  Using constant boundary conditions, the values of all quantities in the ghost cells are set to a reasonable constant value, independent of the evolution of the model. These conditions can be applied, if the physical processes happen at the center of the simulation and cause little influence on the boundary. Additionally the surrounding environment of the simulation volume should not change with time. Both conditions are not met by the disk evolution models, and hence constant boundary conditions are not used. As an example of the effect the constant boundary condition can have on the evolution of a shock front, I calculated a shock front emerging from a pressure gradient running into a constant boundary (Fig. 3.11). The waves are reflected at the boundaries and hence influence the simulation volume, which is exactly what should be avoided.

- *Cyclic or periodic boundary condition*

  Cyclic or periodic boundary conditions are applied to simulate an infinite expansion of the system under consideration. This can be used in simulating a flow through a tube of infinite length, as is the case in some hydrodynamical tests. The boundaries in the flow direction can be set periodically. Another possible application is to simulate a small part of an extended region at high resolution, as e.g. in inhomogeneous chemical evolution model (Argast et al., 2000). The ghost cells get the same values as the last simulated cells at the opposite end of the simulation volume (see Fig. 3.12).

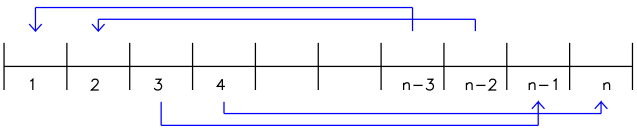

Figure 3.12. Schematic view of cyclic boundary conditions with 2 ghost zones.

- *Mirror boundary condition*

  Another way of defining boundary conditions are the mirror boundary conditions where a reflection at the boundary is simulated. This is achieved by setting the scalar quantities in the ghost cells equal to the last calculated cells (Fig. 3.13) and by inverting the vectorial quantities. I used the mirror boundaries in test simulations of a flow through a tube, where the walls are described through the mirror condition.

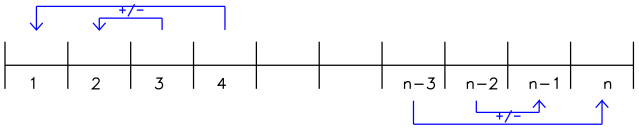

Figure 3.13. Schematic view of mirror boundary conditions with 2 ghost zones.

- *Open boundary condition*

  If the system is not closed and can freely lose or gain matter, energy and momentum over the boundaries one uses free or open boundary conditions. The values of the ghost cells are set equal to the last cell of the simulation volume (Fig. 3.14). Applied to galaxy evolution, open boundaries are well suited for simulations covering a large volume. Then, the density in the outer regions is low and hence also the mass flux over the boundaries. Generally, it is very difficult to control the mass flux over open boundary conditions. Because in disk simulations the boundaries are not far outside, I do not use the open boundary conditions due to the large numeric effort to control open boundary conditions in this case.

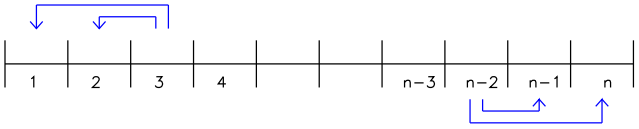

Figure 3.14. Schematic view of open boundary conditions with 2 ghost zones.

- *Multi-dimensional spherical boundary*

  In principle, boundary conditions can be fitted to every individual problem. The condition presented here enables the description of a spherically symmetric boundary in three dimensions, where the flow over the boundary is damped through the special setup shown in Fig. 3.15. The boundary is represented by the red line. Regions 1 and 2 contain the cells lying innermost of the boundaries, whereas region the region 3 and 4 are the ghost cells. The values of the ghost cells are set by averaging the values of the cells in region 2 and 3. This assures that the boundary adopts to the changes of the simulation and it additionally prevents the ghost cells from changing to much, which suppresses numerical oscillations. This boundary condition is particularly useful when simulating collapsing gas clouds.

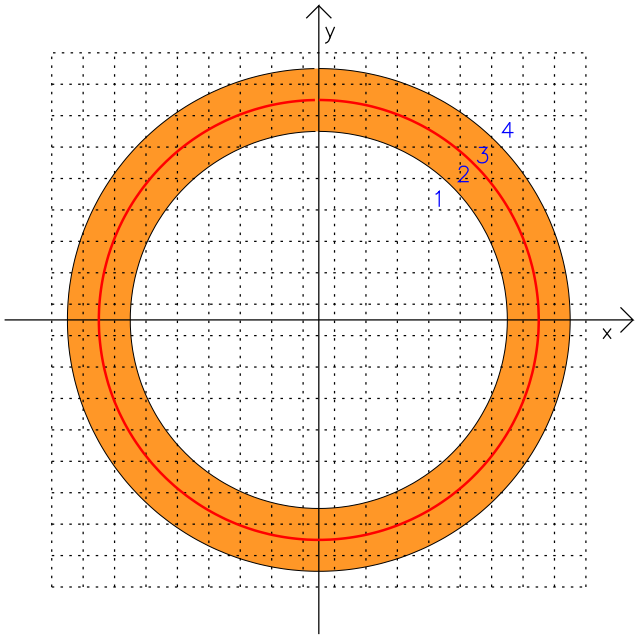

Figure 3.15. Special boundaries to simulate spherical symmetry.

3.8.1. Boundary Condition Used in the Disk Evolution Models

As already mentioned the use of boundary conditions near the galactic disk is not straight forward. The description of the galactic disk is done in a cylindrically shaped simulation volume. In this volume, the full interaction network as well as the hydrodynamical equations are solved. The region outside this volume is represented by a reservoir, into which out streaming matter can flow and from which in can return back into the simulation volume. The reservoir is represented by a mean mass, angular momentum, energy and metallicity. Outflow and infall can happen locally and depend on the local velocity over the boundary. After each advection step the quantities in the reservoir are averaged and set to the ghost cells, assuming a volume reservoir comparable to the simulation volume.

3.9. Initial Conditions

In every simulation a set of initial conditions has to be found, which is reasonable and to which the system is not too sensitive. Applied to galaxy formation, the initial conditions can be taken from cosmology (e.g. Steinmetz & Müller, 1995; Navarro & Steinmetz, 1997; Sommer-Larsen et al., 1999; Williams & Nelson, 2001; Samland & Gerhard, 2003), where mass infall rates and angular momentum distribution can be taken from numerical large scale simulation.

In the investigations about the evolution of a galactic disk, the initial conditions are given through a dark halo

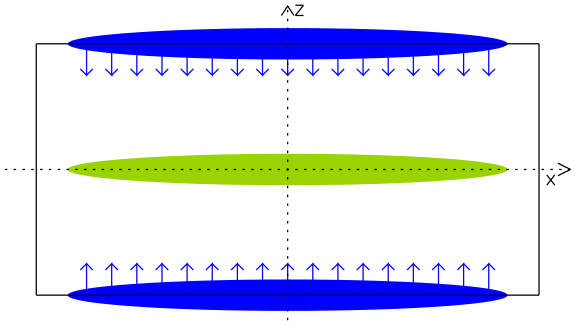

Figure 3.16. Initial conditions of the disk evolution models.

(NFW-profile), in which the baryonic matter enters homogeneously distributed along the z-axis (Fig. 3.16). The infall rate is 120 $M_{\odot}yr^{-1}$ an the infall lasts for 1 Gyr. According to Sommer-Larsen et al. (2002), this delayed infall of baryonic matter into the already relaxed dark halo can solve the angular momentum problem arising from ΛCDM structure formation simulations. The motivation for using a static halo was already given in Sect. 2.4. To build up the disk, the infalling material gets the circular velocity at the infall point. The initial conditions of the models under consideration are described also in the respective chapters (Chap. 4 and 5).

3.10. Flowchart of the Numerical Model

After having discussed all parts of the numerical model, I want to outline the order in which the single steps are executed in the model. In Fig. 3.17 the fbwchart of the numerical model is shown.

The initial conditions as described in Sect. 3.9 are set. followed by the boundary conditions, to ensure that the ghost cells get their correct start values.

The iteration now starts. In the first two steps, the mass and the feedback of the stars is mapped on the grid. These steps get computationally more expensive the longer the simulation lasts, since due to ongoing star formation the number of stars is growing with time. In the next step, the potential is calculated, directly followed by the calculation of the forces in the hydrodynamical as well as PM description.

Afterwards, the hydrodynamical source step for momentum conservation is calculated followed by the interactions and the hydrodynamical source step for energy conservation. Again, the boundaries are set. The next step ist the hydrodynamical advection step. The advection step uses much calculation time and is together with the potential solver and interaction routine the most expensive part of the simulation. After advection the setting of the boundaries is needed.

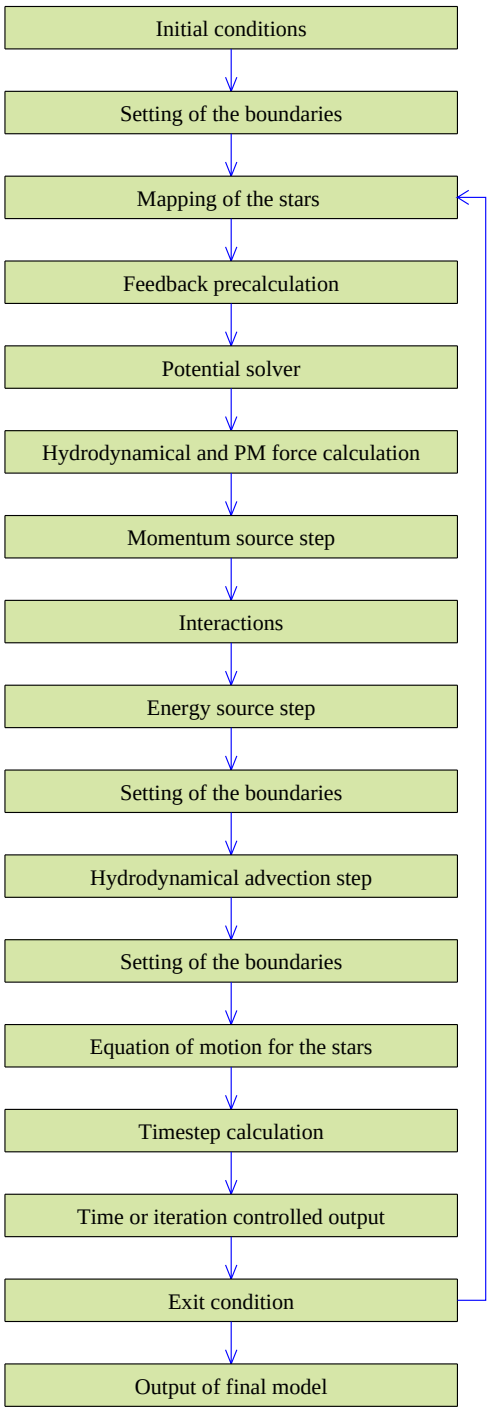

Figure 3.17. Flowchart of the numerical model.

Afterwards, the equation of motion for the stars is solved. The next step is the determination of the timestep for the next iteration. Depending on time or iteration index, either a time controlled output or an iteration dependent security output is made, from which the simulation can be restarted, if it is necessary (see Sect. B.1.).

The exit condition determines, if the simulation is stopped. This can be caused through achieving the time limit or it-

eration limit set in the beginning. Output of all quantities is done before exiting.

3.11. Code Optimization

Because typical simulations need up to 3 month of calculation time on a modern PC, it is very important to have a optimized code. I present in the appendix (App. B) some of the experience I gained during optimizing the model for execution on scalar, vector and parallel computers.

3.12. The New Parallel Chemodynamical Evolution Code

The "Parallel Chemodynamical Evolution (PaCE)" Code is an ongoing project. The goal is to have the whole chemodynamical model available in parallel executable form and hence galaxy models with significantly better resolutions can be calculated. At the moment the hydrodynamical module of PaCE is implemented.

As a first application I have calculated the impact of subsequent supernova explosions on a thin gas ($\rho_{\rm ISM} = 0.005\ {\rm M}_\odot{\rm pc}^{-3}$) simulated at 400 x 400 x 200 grid cells. The spatial resolution is 5 pc. Fig. 3.18 shows a cut through the xy-plane of the simulation volume at a time $10\ {\rm Myr}$ (top) and $45\ {\rm Myr}$, after the explosion of 100 and 450 supernovae respectively. A typical supernova energy of $10^{51}\ {\rm erg}$ was used, where 20% were assumed to accelerate the ISM.

In the upper panel, the enlarged region shows the evolution of a supernova remnant, originated from a supernova explosion in the shell of a previous remnant. One can nicely see how the supernova remnant gets an elongated form and that the material moves fast into the low density regions of the previous remnant. In the lower panel, the ISM is already well mixed and the form of the single supernova remnants depend strongly on their surroundings. However note that for an accurate description of the ISM the implementation of a cooling function and the more realistic onset of the supernovae remnant will be required.

These results are only given to demonstrate the resolution possible with the hydrodynamical module of PaCE. Since the single supernova remnants can be resolved enough to describe their dynamical evolution, I intent to apply the hydrodynamical module of PaCE to the inhomogeneous chemical evolution model, used by Argast et al. (2000) to investigate the scatter of the stellar metallicities at low [Fe/H]. This is particular interesting since new observations indicate that the scatter is smaller (Arnone et al., 2003) than was thought a few years ago and as Argast et al. (2000) noted, the scatter in their model would be reduced by the introduction of a dynamical description. Hence first results at least from a part of PaCE will follow soon (project with D. Argast and M. Samland).

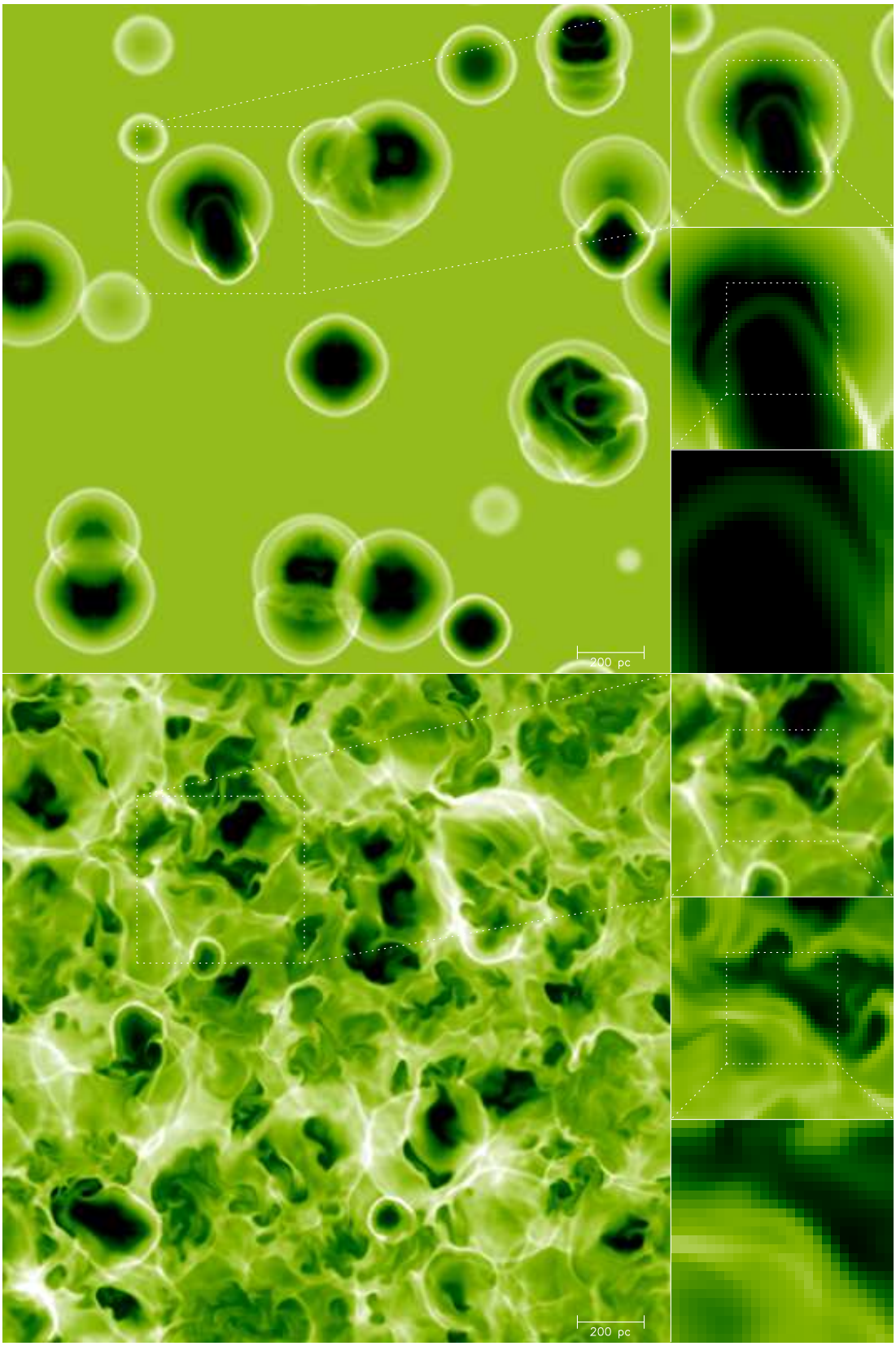

Figure 3.18. Density structure of the ISM after 100 (top) and 450 (bottom) supernovae explosions. The first supernovae remnants produce spherical bubbles, whereas the structure of the remnants in the late evolution strongly depends on their environment.

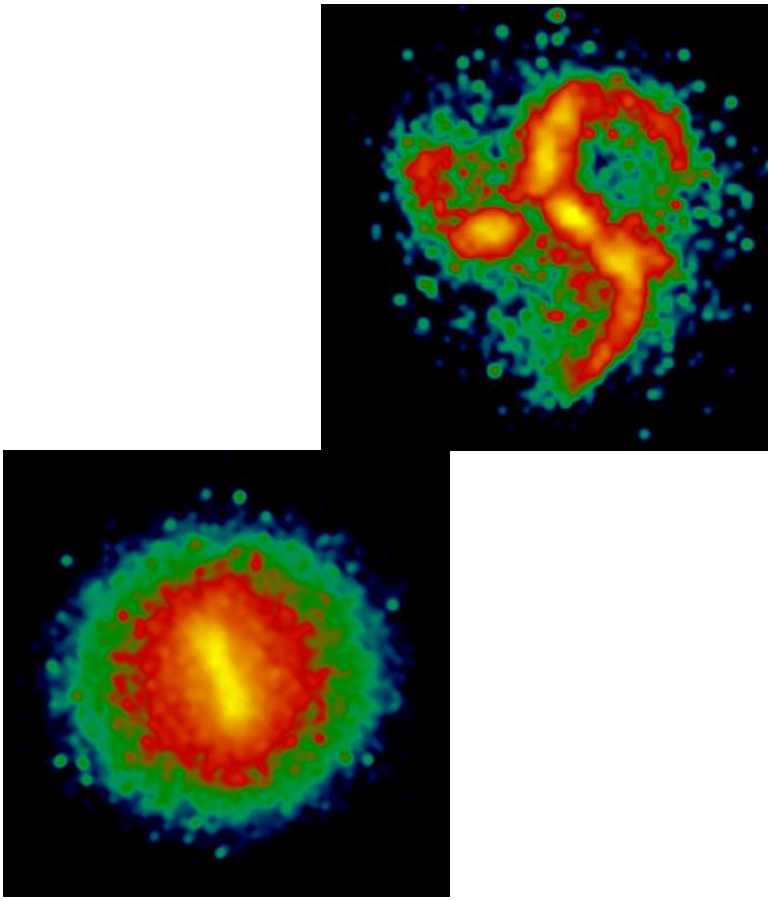

4

Gas Physics, Disk Fragmentation, and Bulge Formation in Young Galaxies

Abstract

We investigate the evolution of star-forming gas-rich disks, using a 3D chemodynamical model including a dark halo, stars, and a two-phase interstellar medium with feedback processes from the stars. We show that galaxy evolution proceeds along very different routes depending on whether it is the gas disk or the stellar disk which first becomes unstable, as measured by the respective Q-parameters. This in turn depends on the uncertain efficiency of energy dissipation of the cold cloud component from which stars form.

When the cold gas cools efficiently and drives the instability, the galactic disk fragments and forms a number of massive clumps of stars and gas. The clumps spiral to the center of the galaxy in a few dynamical times and merge there to form a central bulge component in a strong starburst. When the kinetic energy of the cold clouds is dissipated at a lower rate, stars form from the gas in a more quiescent mode, and an instability only sets in at later times, when the surface density of the stellar disk has grown sufficiently high. The system then forms a stellar bar, which channels gas into the center, evolves, and forms a bulge whose stars are the result of a more extended star formation history.

We investigate the stability of the gas-stellar disks in both regimes, as well as the star formation rates and element enrichment. We study the morphology of the evolving disks, calculating spatially resolved colours from the distribution of stars in age and metallicity, including dust absorption. We then discuss morphological observations such as clumpy structures and chain galaxies at high redshift as possible signatures of fragmenting, gas-rich disks. Finally, we investigate abundance ratio distributions as a means to distinguish the different scenarios for bulge formation.

4.1. Introduction

The formation of galaxies is one of the important questions in current astrophysical research. With HST and earthbound 10m class telescopes it is now possible to study the evolution of galaxies with redshift by direct observation. Although no complete picture is available at the moment, some facts are well established. Surveys undertaken around $z \simeq 1$ have shown that luminous elliptical and spiral galaxies were largely formed by then, and have only moderately evolved to the present time (Brinchmann et al., 1998; Lilly et al., 1998; Abraham et al., 1999; Abraham, 1999; Abraham & Merrifield, 2000; Dickinson, 2000). Beyond $z = 1.4$, there are far fewer high-luminosity galaxies off all types compared to low redshifts (Dickinson 2000, see also Driver et al. 1998). Thus the bulge-to-disk Hubble sequence of galaxies appears to have formed at redshifts slightly beyond $z \sim 1$ (Abraham & Merrifield, 2000; Kajisawa & Yamada, 2001), although part of the stellar populations of these galaxies might have formed earlier.

At $z \simeq 0.5$ spiral galaxies and barred galaxies are observed, and it seems that by then the full Hubble sequence is in place, quite similar to the galaxy distribution today. However, the frequency of barred galaxies drops sharply beyond $z \simeq 0.5$ (e.g., Abraham et al., 1999). van den Bergh et al. (2002) showed that this is not an selection effect. They shifted a local galaxy sample to higher redshifts and concluded that most of the barred galaxies would still be visible. Thus, the absence of bars at higher redshifts seems to be real.

Already at $z \sim 1$ around 30% of galaxies are morphologically peculiar. At higher redshifts many clumpy structures and compact objects are observed. Most of these cannot be attached to the traditional Hubble scheme, but show irregular morphologies (e.g., Abraham et al., 1996; van den Bergh et al., 2000). The anomalous morphologies observed in these high redshift objects cannot be explained through band-shifting effects alone, because the irregularities persist also in NICMOS observations (Dickinson, 2000), probing the visual restframe wavelength of these objects.

Observations of high redshift galaxies currently provide information only about the global properties of these objects. Detailed data like stellar metallicity distributions, stellar kinematics, or gas distributions are only available for local galaxies. To understand galaxy formation in a consistent picture, models must be developed that can be compared with observations over the whole observed redshift range. These models should be able to explain the properties of distant galaxies as well as the detailed data on local galaxies.

With high resolution cosmological simulations, large progress has been made in understanding cosmic structure formation (e.g., Navarro et al., 1996; Moore et al., 1998; Jenkins et al., 2001; Klypin et al., 2001). However, on galactic scales these simulations still lack the necessary resolution to describe the processes relevant for baryon dissipation and star formation. Therefore two approaches for describing galaxy formation and evolution have been developed. Semi-analytical modeling, based on simple assumptions to describe the baryonic physics and star formation in the dark halos that form in the cosmological simulations, has been used to analyze the global properties of galaxy samples (e.g., Kauffmann et al., 1993; Guiderdoni et al., 1998; Cole et al., 2000).

On the other hand, dynamical models, using a subset of the cosmological information as initial conditions on smaller scales, have been used to investigate the detailed structure of forming galaxies (e.g., Steinmetz & M¨uller, 1995; Navarro & Steinmetz, 1997; Sommer-Larsen et al., 1999; Williams & Nelson, 2001; Samland & Gerhard, 2003). These small-scale dynamical models still need to describe star formation with a simple parameterization, but they contain a much more detailed description of the dynamics, feedback, and, in some cases, element enrichment. Thus with these models it is possible to predict observable properties through the galaxy assembly process, and to compare directly with observations of high redshift galaxies (e.g., Contardo et al., 1998; Westera et al., 2002; Abadi et al., 2003). Because these models can be calculated over a Hubble time, one can also directly compare detailed present-day characteristics (e.g., metallicities and kinematics of stellar populations) with observations of local galaxies. Finally, with such models predictions can be made for dynamical and stellar population properties of high-redshift galaxies, which can be verified by future high resolution observations with the next generation telescopes.

The mass accumulation into dark matter halos is well understood in the context of the cosmological simulations and can be used as an input to model galactic evolution (e.g., Van den Bosch, 2002; Wechsler et al., 2002). Additionally, the angular momentum distributions of the forming dark halos have been calculated recently (Bullock et al., 2001; Chen & Jing, 2002). It is widely accepted, both in the semi-analytical approach and the small-scale dynamical models,

that galactic evolution depends sensitively on the mass and angular momentum distribution of the system.

Much less is known about the processes that govern the evolution of the baryons within a dark halo, and how these influence the properties of the forming galaxies. Stars in galaxies nearby are observed to form in molecular clouds much denser than the ambient medium in which these clouds are embedded. Most of the kinetic energy of this cloud fluid is in the motions of single clouds relative to the bulk flow. This kinetic energy can be dissipated by inelastic collisions (Larson, 1969) and augmented by supernova feedback (McKee & Ostriker, 1977). Under some conditions the macroscopic cloud system can be treated as an isothermal fluid (Cowie et al., 1980). Its energy dissipation rate is not well-determined, however. One expects that it depends on the geometrical structure of the clouds, on whether a major part of the dense medium is arranged in filaments, and on their self-gravitating structure and magnetic fields (Kim et al., 2001; Balsara et al., 2001). Thus the dynamics of the macroscopic cloud medium may be more or less dissipative, depending on the physical conditions, and may well vary between galaxies.

In the present paper we investigate the formation and dynamical evolution of galactic disks, varying the cloud dissipation rate. We use the interaction network and two-phase chemodynamical model of Samland & Gerhard (2003, SG03) to describe the assembly of a disk of stars, hot gas, and star-forming cold gas. We find that the dynamical stability of the disk depends sensitively on the cloud dissipation efficiency, here described by the parameter $c_{\rm coll}$. For large $c_{\rm coll}$, dynamical instabilities in the gas dominate the evolution, leading to fragmentation of the disk into a small number of star-forming clumps which subsequently merge to form a centrally concentrated bulge. For small $c_{\rm coll}$, on the other hand, the system forms stars until the stellar disk becomes unstable, leading to a stellar bar at late times. The different stability properties in both cases can be quantified in terms of the effective Toomre Q parameter for the stellar, gaseous, and combined system (e.g., Toomre, 1964; Jog & Solomon, 1984; Wang & Silk, 1994; Elmegreen, 1995).

The evolution of a system with high dissipation calculated at higher resolution is described in Immeli et al. (2003a), where it was shown that morphological and photometrical properties of several high redshift objects, like the chain galaxies (Cowie et al., 1995), can be explained by a fragmented disk model.

Several authors have suggested that galactic bulges can form by the secular evolution of a galactic disk, driven by interstellar gas or stars (e.g., Combes & Sanders, 1981; Pfenniger & Norman, 1990; Noguchi, 1999). Recent observations lend some support to these secular evolution scenarios. Bulges in late-type spirals show similar properties to their surrounding disks, in that their light profiles are better fit by an exponential rather than an $R^{1/4}$ law (Courteau et al., 1996; Seigar et al., 2002), and in their colours (Peletier & Balcells, 1996).

As shown here, the evolution of star-forming galactic disks may take different routes, depending on whether it is the gas or the stars that drives a disk instability. This in turn depends on the uncertain efficiency of energy dissipation in the cold cloud component. These different routes also lead to different formation scenarios for galactic bulges. Thus we suggest here that the morphological properties of galaxies may depend not only on cosmological variables like different mass or angular momentum distributions, or infall history, but also on internal physical processes during galaxy evolution.

In Sect. 4.2 we describe our model for star-forming disks. In Sect. 4.3 we describe the morphological evolution of these disks, depending on the dissipation efficiency of the cold gas. Sect. 4.4 discusses the stability and star formation rates in the models, and Sect. 4.5 describes the properties of the bulges that form in the two main evolutionary scenarios. Finally, Sect. 4.7 summarizes our findings.

4.2. The Model

We use a two-phase model for the interstellar medium, consisting of a hot, low-density phase and a cold cloud medium from which stars are formed. The chemical elements and most of the energy released from SNeII and later SNeIa are returned to the hot phase. However, the cloud velocity dispersion of the cold phase is heated by SNeII as well (McKee & Ostriker, 1977). We describe this system with a three-dimensional chemodynamical evolution code, which combines a hydrodynamical grid code for the two phases of the interstellar medium (ISM) with a particle mesh code for the stars. See SG03 for more details.

The interactions between the different ISM phases and the stars are described in detail in SG03. A difference exists in the characterization of the star formation rate (SFR), where we use here a simple Schmidt law (Schmidt, 1959),

$$\dot{\rho}_{\rm sf} = c_{\rm sf} \cdot \rho_{\rm cm}^{\alpha} \tag{4.1}$$

with $\alpha = 1.5$ and $c_{\rm sf}$ chosen to be consistent with the star formation rule derived by Kennicutt (1998). We here adopt a volume density star formation threshold $\rho_{\rm th}$, converted from the surface density threshold of $1 - 10\ {\rm M}_{\odot}{\rm pc}^{-2}$ obtained from observations by Kennicutt (1998), assuming a disk scale height of the order of the spatial resolution of our model. Thus $\rho_{\rm th} \simeq 1\ {\rm M}_{\odot}{\rm pc}^{-2}/500\ {\rm pc} = 0.002\ {\rm M}_{\odot}{\rm pc}^{-3}$. This is a lower value compared to other thresholds used in the literature (e.g. Noguchi, 1999). It ensures that gas does not clump simply because it is below a high star formation threshold and cools when there is no heating from star formation.

SG03 did an extensive investigation of the network of processes connecting the different ISM phases in this model. We use their values for most of the efficiency parameters that occur in this network, as determined through either theory or observation. As shown by SG03, this network is strongly self-regulating, so that the system is not sensitive to the precise values used for these efficiencies. They conclude that the cloud dissipation efficiency $c_{\rm coll}$ is the most uncertain parameter in the model. We now describe the relevance of this parameter in somewhat more detail.

The dynamics of the cold cloud medium (CM) is described in a statistical way through the hydrodynamic moment equations. Energy dissipation and gain are implemented through sink and source terms to the moment equations. The internal energy describes the kinetic energy of the single clouds relative to the bulk motion. The CM cools through reducing this kinetic energy, which in this model is assumed to happen through inelastic collisions between single clouds. Larson (1969) derived the dissipation rate in a CM consisting of spherically symmetric clouds with constant mass. Using the mass-radius relation for clouds given by Elmegreen (1989) the internal energy change can be written as

$$\frac{\partial \epsilon}{\partial t} = -c_{\rm coll} P_4^{-1/2} \rho^2 \sigma^3 \qquad (4.2)$$

where ρ is the density of the CM, σ its velocity dispersion, and $P_4 = (P_{\rm icm}/k)/10^4$ with $P_{\rm icm}$ denoting the pressure of the intercloud medium . All constants have been merged to $c_{\rm coll}$. $c_{\rm coll}$ also contains the deviation of the effective cross section for cloud-cloud collisions from the geometrical value due to magnetic fields, self gravity, and gravitational focusing. It also depends on whether the cold cloud medium is arranged mostly in clumpy structures or mostly in filaments, which is not well-understood. Thus the precise macroscopic description of cloud dissipation on a galactic scale is uncertain, and hence the value of $c_{\rm coll}$ in Eq. 4.2. It is therefore possible that the dissipation efficiency changes from one galaxy to another, and that this changes galactic evolution. It is equally possible that interstellar cloud physics is nearly universal, and that the main driver for galactic evolution is the baryonic infall rate per unit area, or disk growth time, as Noguchi (1999) has argued. In both cases, the local heating-collisional cooling equilibrium of the cloud medium is changed, and hence the star formation history.

To investigate the influence of cloud dissipation on disk evolution, we performed a sequence of simulations with different dissipation efficiencies $c_{\rm coll}$. The values given in Table 4.1 are normalized to the efficiency $c_{\rm coll}^D$ used in SG03. The range of $c_{\rm coll}$ values corresponds to the maximum variations given in Table 1 of SG03.

The dynamical set-up of the models describes the rapid formation of a massive galactic disk in a pre-existing, static dark matter halo with NFW-profile (Navarro et al., 1997).

model index	$c_{\rm coll}$ [$c_{\rm coll}^D$]	model index	$c_{\rm coll}$ [$c_{\rm coll}^D$]
A	20	E	1/5
B	10	F	1/10
C	5	G	1/20
D	1		

Table 4.1. Dissipation efficiencies used in the model sequence, normalized to model D, where $c_{\rm coll}^D = 0.025$ (SG03).

According to Sommer-Larsen et al. (2002) the delayed infall of the baryonic matter into the relaxed halo can solve the angular momentum problem arising from ΛCDM structure formation simulations. The primordial gas enters the simulation volume vertically at $|z| = 15.5$ kpc, and the infall is uniformly distributed over a radius of 17 kpc, with a rotation velocity equal to the circular velocity at the infall point. The infall rate is $120\,{\rm M}_\odot{\rm yr}^{-1}$ during one Gyr, resulting in a total mass of $1.2 \cdot 10^{11}\,{\rm M}_\odot$. The simulation volume has a diameter of 38 kpc and a vertical height of 31 kpc with a spatial resolution around 500 pc. The evolution of a higher-resolution simulation of model A is discussed in Immeli et al. (2003a). The higher resolution does not lead to different results, which indicates that the outcome of our simulations is not sensitive to the resolution used.

The chemodynamical model naturally provides ages and metallicities of all stars formed over time, as well as ISM densities and metallicities. This enables us to calculate HST- and UBVRIJHKLM-colours of the model, including dust absorption. This is done using the method described in Westera et al. (2002), but we adopt here a three times lower absorption coefficient. We will use the observable colours to discuss the morphological evolution.

4.3. Morphological Evolution

4.3.1. Settling of the Disk

The infall of the baryonic matter leads to the build-up of a gaseous disk. The settling of the disk is shown in Fig. 4.1, which shows a cut through the xz-plane of the density distribution for the cold gas component in models B, D and F at different times. The energy feedback from the first stars heats up the disk. In consequence the settling of the disk takes longer than a free-fall timescale, depending strongly on the cloud velocity dispersion and hence on the cloud dissipation efficiency $c_{\rm coll}$. Since the angular momentum does not play a role in the settling along the rotation axis, the z-component of the velocity dispersion alone prevents the clouds from completely falling to the disk plane.

After 500 Myr the cold gas phase shows a filamentary distribution in all three models. This is caused by the local energy feedback of the first supernovae of type II (SNeII) to

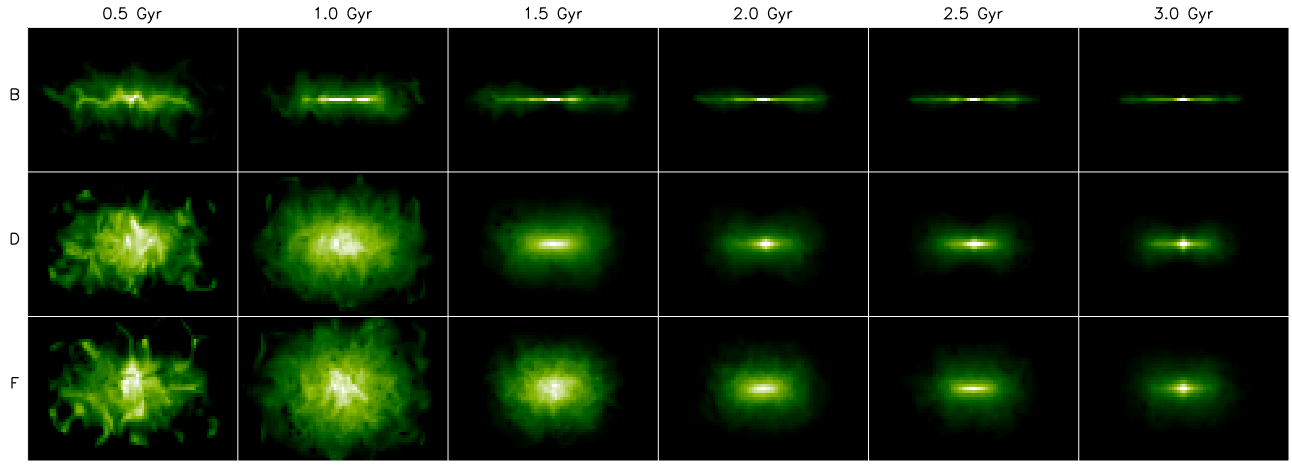

Figure 4.1. Cut through xz-plane of the cold gas density distribution for models B, D, F. Evolutionary time and model index are indicated.

the gas. This leads to local variations in the velocity dispersion of the cloud medium, which act like the analogues of pressure gradients in the hot gas phase. Thus the cold gas is compressed. In addition, in regions with enhanced energy input, the equilibrium between hot and cold gas phases is shifted to decrease the density of the cold medium.

The model with high dissipation (B, first row) settles to a thin disk which is almost completely supported by rotation. The timescale for the settling is relatively short because the energy input from SNeII can be dissipated efficiently. The less efficient energy dissipation of model D causes the disk to settle more slowly. The disk in this model also remains thicker during the whole evolution, because the equilibrium between the continuous energy input from SNeII and energy dissipation by cloud collisions is shifted to higher internal energies and thus higher cloud velocity dispersions. This is even more true in model F, where the even less efficient energy dissipation results in a yet thicker disk.

4.3.2. Face-On Evolution

Fig. 4.2 shows an overview of the face-on morphological evolution of all our models, presented in terms of the V-band restframe surface brightness calculated from the distribution of stars as described in Section 2. Model indices are indicated at the left for each row, and time is indicated at the top for each column. All images are normalized to the same surface brightness magnitude interval, which enables us to directly compare luminosities of the models. The absolute V-magnitude M_V of the galaxy is also given in each panel. Obviously, the morphological evolution depends strongly on the dissipation efficiency.

At 0.5 Gyr the formation of the disk is under way and none of the models shows an asymmetry in surface brightness yet. Generally, the colder models are brighter in absolute V-magnitude than their warmer counterparts. At 0.75 Gyr the coldest model (A) shows several knots of high density with enhanced star formation. In model B a ring like structure is visible. 200 Myr later the disks of these two models have fragmented, showing several nearby knots. At 1.05 Gyr some clumps in models A and B have already merged and fragmentation is also visible in model C. Whereas at 1.2 Gyr models D to G still show a symmetric surface brightness distribution, the clumps in models A to C have already fallen to the center and merged to form a bright bulge. This persists for the remainder of the simulation, together with a clear spiral pattern in the disk. Model D develops a bar like structure with spiral arms at around 2 Gyr. A very pronounced bar is visible in models E to G at around 2.8 Gyr. As can be seen in the last column of Fig. 4.2, these bars become shorter. Bar evolution is discussed further in Sect. 4.6.

The morphological evolution of models A, B, and C is similar in the sense that they all develop a fragmented disk and end up with a compact central concentration. Their exists a dependence on $c_{\rm coll}$, in such a way that the more efficiently the gas dissipates energy, the more pronounced is the clumping, because the lower velocity dispersion in the more dissipative models counterbalances the gravitational instabilities less well. In all the cold simulations a ring develops. This ring structure probably results from the form of the rotation curve in these models; see Cha & Whitworth (2003); Gingold & Monaghan (1983). It is important to note that the mass enhancement in the ring amounts to less than 10% of the total mass in the cloudy medium.

The galaxy models A-C in their fragmented phase resemble, when viewed edge-on, the chain galaxies first reported by Cowie et al. (1995, CHS95). These are high redshift galaxies observed with HST in the Hawaii Survey Fields, with large major-to-minor axis ratios, knotty structures and very blue colors. CHS95 suggest that chain galaxies in the redshift range $0.5 - 3$ have a mass comparable to that of

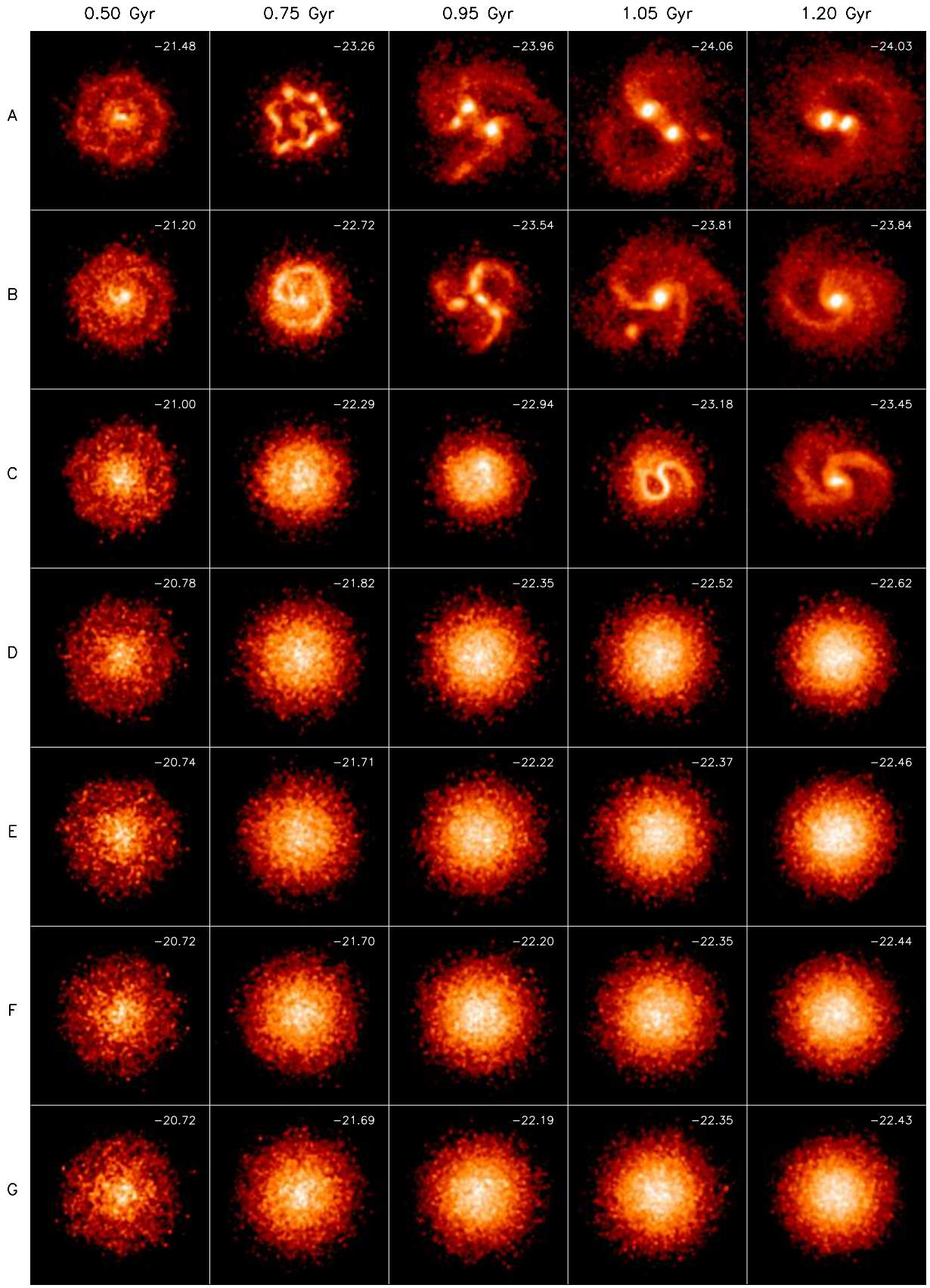

Figure 4.2. Morphological evolution of the seven models in terms of V-band restframe surface brightness. The panels show the whole simulation area of 38 kpc squared. The model indices are given at the left and time is indicated at the top. Between panels, time does not progress in constant intervals; this is to emphasize the interesting evolutionary phases of the models. M_V is given in each panel.

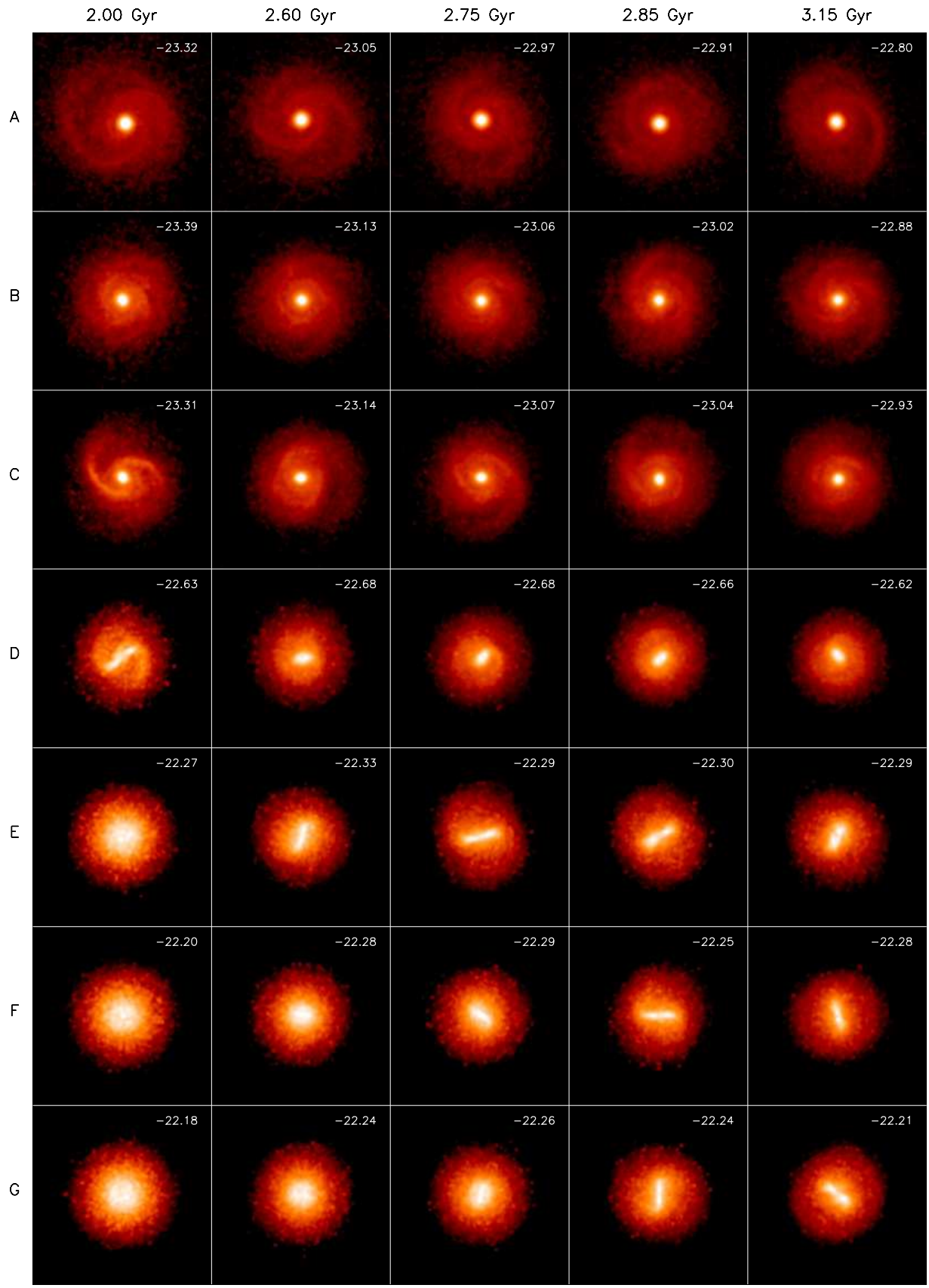

Figure 4.2. - *continued.*

a present-day galaxy and that they represent a new population of galaxies. Our model favors the interpretation of O'Neil et al. (2000) that the chain galaxies are clumpy disk-like structures seen edge-on. Model A, recalculated with higher resolution, is compared to observations in detail in Immeli et al. (2003a). The main results are that the extraordinary morphology as well as very blue colors observed by CHS95 are reproduced well. An investigation of the properties of the individual clumps in this model leads to typical stellar clump masses of a few 10^9 $\mathrm{M}_\odot$. Metallicity differences between individual clumps are not larger than 0.25 dex and the influence of individual clumps on the rotation curve can by as high as 100 km/s.

A similarity in the evolution can also be seen in models E to G. In these models the disk remains symmetric for a much longer time. At around 2.7 Gyr these models then become bar unstable, and a very prominent bar develops in about one dynamical time. Contrary to the fragmented disk models, the absolute luminosity of the models showing a bar instability does not vary much over the simulated time interval. The evolution of model D lies somewhere in between these two cases, showing a bar with spiral arms at around 2 Gyr.

Comparing models A and B shows that no qualitative differences in the evolution are visible. The same is true for models F and G, which indicates that the chosen values of c_{coll} (Table 4.1) covers the whole relevant range.

4.4. Global Properties

4.4.1. Stability of the Disk

As shown in the previous section, our models can be divided in two groups according to their dynamical evolution: Models A to C show an early fragmentation, whereas in models E to G a bar instability occurs at later times. Model D appears to be a transition case. In the remainder of this paper, we confine the discussion to models B, D, F, as representative models for the different evolutionary paths. First, we relate these more quantitatively to the stability of the multicomponent disk. The Toomre parameter Q (Safranov, 1960; Toomre, 1964) is an important quantity in investigations of disk stability. In a single component gaseous disk Q is given through

$$Q_{\mathrm{gas}} = \frac{\kappa \sigma_{\mathrm{gas}}}{\pi G \Sigma_{\mathrm{gas}}} \tag{4.3}$$

where Σ_{gas} is the surface density, κ the epyciclic frequency, G the gravitational constant, and σ_{gas} is the radial velocity dispersion of the gas. $Q = 1$ is a well-defined stability limit for such disks: disks with low velocity dispersions and high surface densities such that $Q < 1$ are subject to radial instabilities.

In a disk consisting of gas and stars the evaluation of Q is more difficult. As described above, the interstellar material in our model consists of two gas phases. Because the hot intercloud medium (ICM) only makes up for about 1% of the total gas mass and because it is pressure dominated and therefore stable in a Toomre sense, we can neglect the ICM contribution to the Toomre parameter. Henceforth, we consider a composite Q_{eff} for the stellar and the cold gas phases.

There have been several attempts to describe the stability of a two-component systems in the context of the Toomre parameter. Jog & Solomon (1984) derived a dispersion relation for a two-component system of stars and gas and evaluated it numerically. Romeo (1992) derived finite thickness corrections for disk systems. A simple approximation was inferred by Wang & Silk (1994)

$$Q_{\mathrm{eff}} \simeq \frac{\kappa}{\pi G}\left(\frac{\Sigma_{\mathrm{gas}}}{\sigma_{\mathrm{gas}}} + \frac{\Sigma_{\mathrm{stars}}}{\sigma_{\mathrm{stars}}}\right)^{-1} \simeq \left(\frac{1}{Q_{\mathrm{gas}}} + \frac{1}{Q_{\mathrm{star}}}\right)^{-1} \tag{4.4}$$

where Σ_{stars} is the stellar surface density and σ_{stars} is the radial velocity dispersion of the stars. Elmegreen (1995) gives a more accurate way of calculating the effective Q_{eff} parameter for a two component disk. He reformulates the dispersion relation of Jog & Solomon (1984) in such a way that the derived Q_{eff} is completely analogous to the one-phase Q. We use this more accurate method as well as the approach of Wang & Silk (1994) to evaluate Q_{eff} for the two-phase medium. Since the results are the same, we will not further distinguish between the two methods.

Fig. 4.3 shows maps of Q_{gas}, Q_{star}, and two-component Q_{eff} for models B and F. The white regions in the maps denote those parts of the disk where the number of stellar particles in a grid cell in the plane is less than five and no secure stellar velocity dispersion and hence no reliable Q_{star} could be determined. These maps show clearly that the Q values can vary substantially between different parts of the disk, both radially and azimuthally.

At around 0.4 Gyr, not many cells reach the stability boundary just discussed: all Q's have values above unity. Already at 0.6 Gyr the situation changes in model B. The gaseous component develops regions of instability, and Q_{eff} reveals an unstable disk over a large radial range. For comparison, the disk of model F is still stable at 1 Gyr in both components as well as in the composite Q_{eff}. In model B the violent evolution following the instability causes a sharp increase in the mean Q_{eff}. The instability converts energy from ordered motions to random motions, as well as driving up the SFR and SN heating, which indirectly increases the cloud velocity dispersion and hence the Toomre parameter.

At 1.8 Gyr the stellar disk of model F has a central Toomre parameter around 1.5. The gaseous phase has a Toomre parameter of at least 2 and therefore is stable not only to radial

but also to bar instabilities (Polyachenko, 1997). Nevertheless, the composite $Q_{\rm eff}$ already approaches values around 1 in the center. Thereafter, $Q_{\rm eff}$ drops further in the center, causing a bar instability at around 2.6 Gyr. The bar is visible in the instability map, but the signature becomes weaker as the bar evolves.

Globally, both models are stable after their respective instability, indicating that an equilibrium state has been reached and no further large morphological changes will occur (compare Sect. 4.6. However, model B remains marginally unstable in its outer parts, which drives the spiral pattern visible at late times (Fig.4.2). Consistent with the fact that this model has a thinner disk with higher rotational support than model F, the outer regions of the disk in model B also have a lower $Q_{\rm eff}$ than in model F.

In summary, the most striking difference between the two models is that the instability in model F occurs in the stellar disk in the central regions, at comparably late times, whereas in model B the instability develops in the cold gas phase over the whole of the disk, starting early-on. Thus the different morphological evolution discussed in the previous section can be attributed to the instability emerging in different phases.

To investigate the time evolution of the Toomre parameter, we averaged it over a central circle with radius 2 kpc. The progression of this average Q is shown in Fig. 4.4. Again we see that different components trigger the instability in the different models. In all models, the instability starts when $Q_{\rm eff} \simeq 0.8$. This value should not be taken as an absolute limit for stability, however, since it depends on the radius over which the Toomre parameter is averaged. Nevertheless, this shows that $Q_{\rm eff}$ is a good tracer of the instability. Also clearly visible is the increase of Q after the onset of instability.

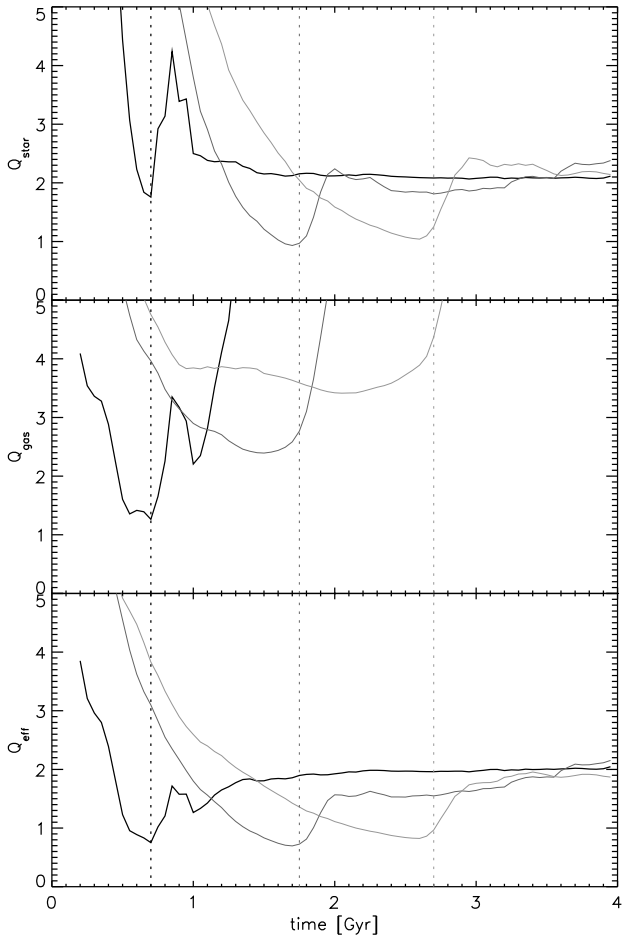

Figure 4.4. Time evolution of the Toomre parameter for the stellar component (top), the cold gas component (middle), and the composite Toomre parameter (bottom), for models B (black), D (dark grey) and F (light grey). The locations where the instability emerges are indicated by dashed lines.

4.4.2. Star Formation Rate

The different dynamical evolution along the sequence of models has a strong impact on the global star formation history. Fig. 4.5 shows the SFR as a function of time, for models B, D, and F. One immediately recognizes large differences in the absolute values as well as in the shape of the SFR. In the beginning, the SFR is low because the gas must first fall to the Galactic plane and reach the limiting volume density for star formation, $\rho_{\rm th}$. This takes around 200 Myr. After this the SFR increases as more material falls in. The energy feedback from the first stars heats the gas and the equilibrium found depends on the energy dissipation rate of the cold gas phase. The less efficiently energy can by dissipated, the higher the cold cloud velocity dispersion, and hence the more extended in the z-direction the cold gas disk is (Fig. 4.1). If, on the other hand, the dissipation efficiency is high, the velocity dispersion drops and the material settles in a high density disk. Since all models have identical mass infall and total mass, the density in the disk plane is lower in the thicker disks. Because the SFR follows a Schmidt law (Eq. 4.1), the overall SFR will be higher in the models with strong gas dissipation. This effect can be seen already at around 500 Myr, when the SFR rates of the models differ by a factor of two.

The subsequent shape of the SFR is dictated by the further evolution. In models A to C the cold gas phase of the disk becomes unstable, with the stars following the potential perturbations induced by the gas. The clumping of the gas leads to a strong enhancement of the SFR (Fig. 4.5, top panel). The clumps then fall to the center and, due to the efficient angular momentum redistribution during this phase, a large fraction of the gas is located in the center after the clumps have merged. In this stage, the SFR reaches a pronounced maximum, which can be as high as $200\ {\rm M}_\odot{\rm yr}^{-1}$.

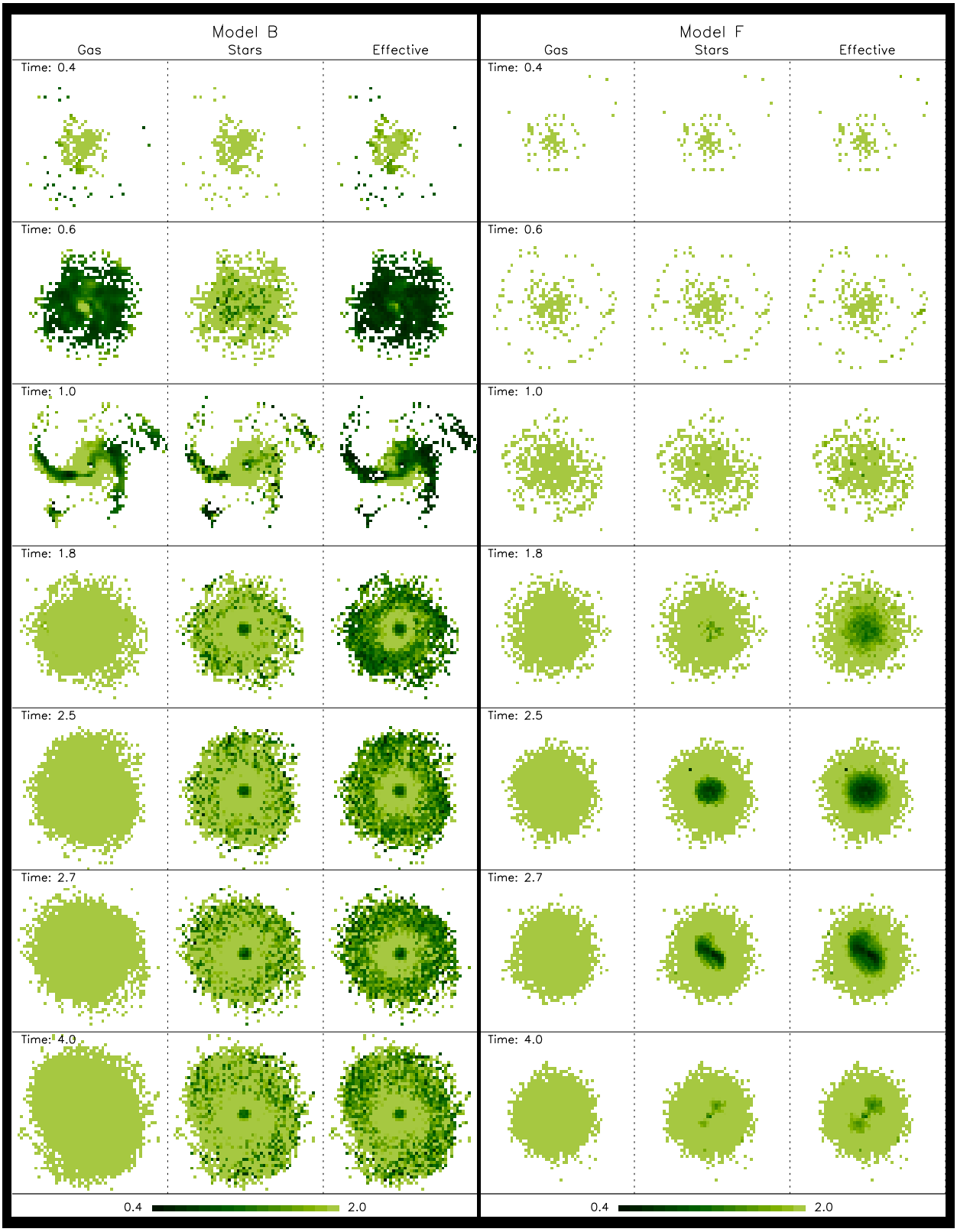

Figure 4.3. Toomre instability map for model B (left panels) and model F (right panels). The Q Parameter is given for the cold gas component and for the stars, and the effective Q is shown for the two-component system. Grey (light green), dark (dark green) and white colour in this map denotes regions of stability, instability, and undefi ned stellar and effective Q. Time is indicated in Gyr. The panels have a side length of 25 kpc.

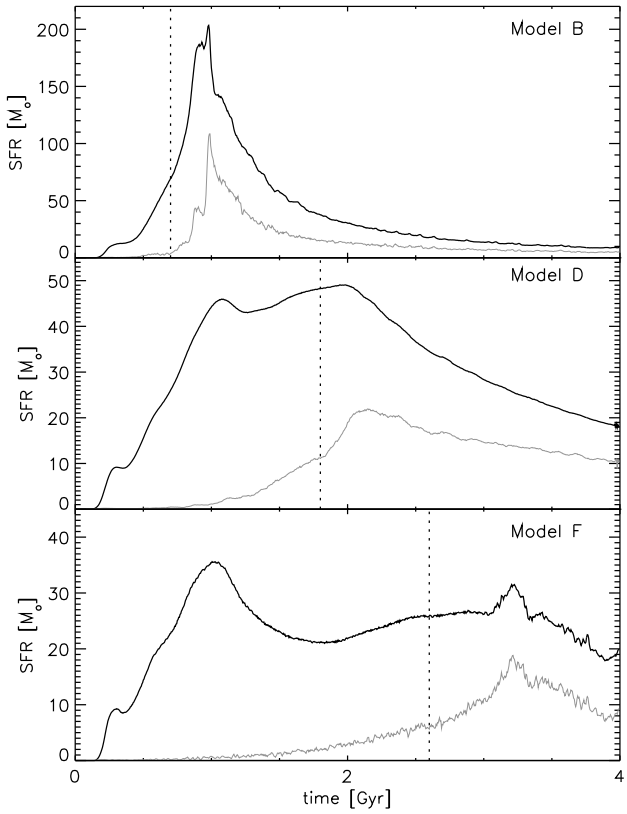

Figure 4.5. Global SFR (black line) and SFR in the innermost 2 kpc (grey line) in models B, D, and F. In all three models the instability, indicated by the respective dotted line, causes an increase in the central SFR.

The warmer models form stars at a much lower rate, after the initial rise driven by the infall. Because the gas phase remains stable, the cold cloud disk from which the stars form has no large density enhancements. Star formation then increases again when the instability of the stellar disk sets in. The bar causes an inflow of gas to the center, causing an increase in the central SFR which also reflects in the global SFR (Fig. 4.5, bottom panel). Indeed, Aguerri (1999) found a strong correlation between the global SFR and the barred structure of galaxies.

As a consequence of their diverse SFR, the integrated mass of stars formed in these models also varies strongly (Fig. 4.6): whereas after 2 Gyr model B has already converted 75% of its baryonic mass into stars, the corresponding value for model D is around 40% and that for model F is around 25%.

This illustrates how different the SFR in these models are despite their identical mass infall rates. The cooling efficiency, acting as a process on small scales, thus influences the strength and the shape of the SFR, consistent with results from Van den Bosch (2002). It is therefore difficult to constrain the mass accretion rate of a galaxy from the star formation history alone, without further assumptions. This shows the need for self-consistent modeling of galaxies.

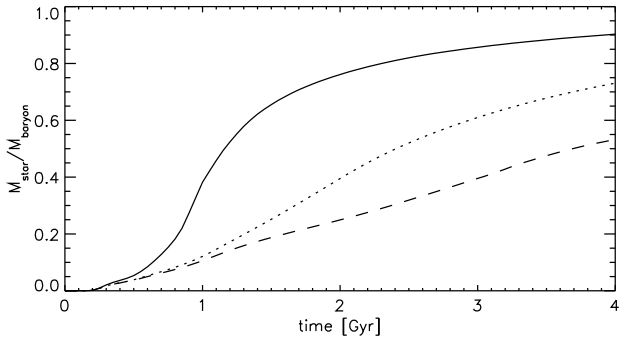

Figure 4.6. Stellar mass fraction of models B (solid line), D (dotted line) and F (dashed line).

4.4.3. Metallicity Distribution

Fig. 4.7 shows the metallicity distribution of the stars in models B and F after time 4 Gyr. Here we divide the stars in the model into halo, disk, and bulge components. The halo is defined as all stars with a distance to the disk plane of at least 3 kpc. The disk component is defined as all stars with z-distance from the plane $|r_z| < 0.5$ kpc and a minimal distance of 2 kpc from the center. All stars within 2 kpc from the center are taken to be the bulge component.

There exist clear differences in the metallicity distributions of both models, due to their different evolutionary histories. However, in both models the metallicity increases from the halo to the disk to the bulge. The halo has the lowest metallicities because the metal-enriched clouds falls through the halo towards the disk plane. When the clouds settle in the disk, the chemical enrichment can take place over a longer time-scale. The subsequent angular momentum redistribution from the instability causes the gas to flow inwards. The inflowing gas cannot escape from the galactic center, and when it is converted to bulge stars, it has the highest metallicities.

Since the settling of the baryons to the plane depends on the dissipation rate (Sect. 4.3.1), the enrichment time-scale for stars that end up in the halo is longer for model F than for model B, and so one expects a more advanced chemical enrichment of the halo in model F. Indeed, the halo metallicity distribution of the cold model B shows a peak at $[\mathrm{Fe/H}] \simeq -2$, whereas the peak in the distribution for model F lies approximately one dex higher at $[\mathrm{Fe/H}] \simeq -1$. The shape of the observed metallicity distribution of the halo of M31 (Durrell et al., 2001) is very similar to that of model F. This points to a relatively slow star formation

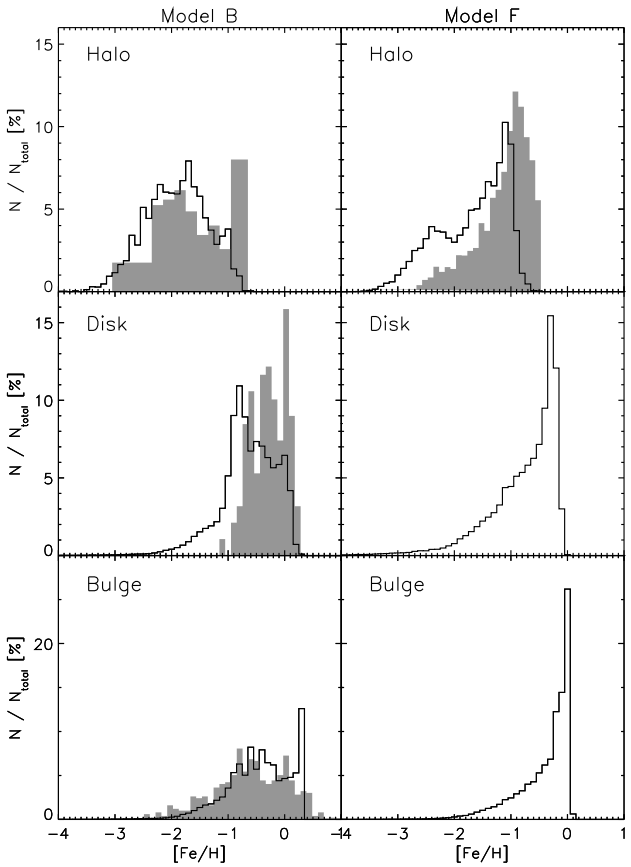

Figure 4.7. Distribution of stars in [Fe/H] for models B (left) and F (right), for Halo, Disk and Bulge stars as defined in the text (open histograms). Observational data are plotted as the shaded histograms (references in the text).

process for the M31 halo stars. By contrast, the metallicity distribution of the Milky Way halo (Chiba & Beers, 2000) resembles more the distribution created in the cold model B, and points to a faster settling of the gas to the disk in the early collapse of the Milky Way (see also SG03).

In the distribution of disk stars, the differences between both models are also clearly visible. In model B, the peak at relatively low metallicities mirrors the peak in the SFR at early times, before SNeIa play a significant role in the enrichment. This model is compared to data from Edvardsson et al. (1993). Note, however, that the observed sample contains stars that have formed much later than at 4 Gyr where the model calculation ends. The slower star formation process of model F leads to a steady increase of stars with high metallicities; in this model the gas is enriched by SNeIa before a large fraction of the stars is formed.

A similar argument applies to the bulge. Here the high early SFR of model B produces many metal poor bulge stars with $[\mathrm{Fe/H}] \simeq -0.7$. In model F, by contrast, the evolution is slower, leading to a steady increase in the stellar metallicity without a peak at low metallicities. Tiede & Terndrup (1999) reported a metallicity distribution for the Galactic bulge with a similar shape as produced in model B. On the other hand, results from Ramirez et al. (2000) and Zoccali et al. (2003) point to a more metal rich distribution. The formation of the Galactic bulge is discussed further in the next section.

Although clearly the cloud energy dissipation is not the only physical process that influences the metallicity distributions in galaxies, it does have an important impact on the dynamical, star formation, and chemical evolution of galaxies.

4.5. Bulge Formation

In our series of models we observe two qualitatively different paths to bulge formation. In those models where the gas disk fragments and develops massive clumps, the bulge is formed through the merging of these clumps at relatively early times (see also Noguchi, 1999). In the class of models where a bar forms through an instability of the stellar disk, the bulge is formed from this bar, at comparably late times. This is similar to the scenario proposed by Combes & Sanders (1981), Pfenniger & Norman (1990) and Raha et al. (1991).

These two routes do not cover the whole range of bulge formation processes: further ways in which a bulge may be formed are through mergers (Aguerri et al., 2001; Scannapieco & Tissera, 2003) or in the center of an early galactic collapse (Eggen et al., 1962). It is possible that all these routes may play a role in the formation of some bulges. Real bulges may even form through a combination of these processes, as indeed happens in the self-consistent models of SG03. In particular, some nuclear bulges would appear to be good candidates for the rapid SFR processes.

The least well-studied of these bulge formation processes is that from merging clumps in a fragmenting disk (Noguchi, 1999). Immeli et al. (2003a) compare a high-resolution simulation of model A with observations and conclude that this process may in fact be at work in the chain galaxies found by CHS95. Further observations of similar objects will thus be highly interesting.

Fig. 4.8 shows edge-on projections of the inner regions of models B, D, and F in terms of K-band surface brightness. The bulges also stand out in the K-band radial surface brightness profiles, plotted in Fig. 4.9. In the following subsections, we give some more specific predictions from our models.

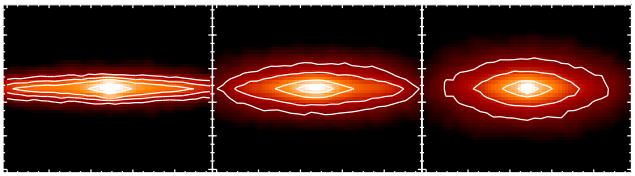

Figure 4.8. Edge-on view of the inner 11 kpc of models B, D, and F (from left to right), in K-band at time 3.8 Gyr.

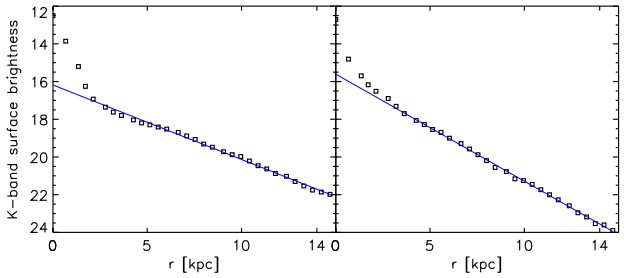

Figure 4.9. Radial surface brightness profi le in K-band for models B (left) and F (right). The violent evolution in model B leads to a more massive bulge than the mass transport to the center induced by the bar in model F.

4.5.1. Clump Merging

As we have seen, in the cold models (A to C) the disk fragments in an early evolutionary state and quickly develops several clumps of stars and gas. The clumps then spiral to the center, where they merge, causing a massive bulge to form. Because this process leads to very high gas densities, the SFR in the clumps and, especially, in the subsequently forming bulge is very high. This results in a rapid oxygen enrichment of the bulge stars, as can be seen from Fig. 4.10, where [O/Fe] is plotted against [Fe/H] (top panel for model B).

In this plot, [O/Fe] at low metallicities corresponds to the IMF averaged abundance ratio of supernovae of type II (SNeII) (Samland, 1998), which enrich the ISM on a timescale of order 10 Myr. The supernovae of type Ia (SNeIa), assumed in our model to arise from white dwarf binary systems on a timescale of around 1 Gyr, influence the chemical evolution of the ISM only at later times. The large amount of iron produced by the SNeIa lowers [O/Fe]. The metallicity at which this happens depends on how far the enrichment has progressed before this time, and so the location of the transition in Fig. 4.10 gives information about the star formation time-scale. In the case of the fragmenting model B, the short starburst produces a clearly defined path through the [O/Fe]-[Fe/H] diagrams, with a bend lying around $[\mathrm{Fe/H}] \simeq -0.4$. Thus SNeII have enriched the ISM already to this high metallicity before the feedback from SNeIa plays an important role.

After the starburst, 70% of the infalling baryonic matter in model B has been converted to stars. The fast SF history

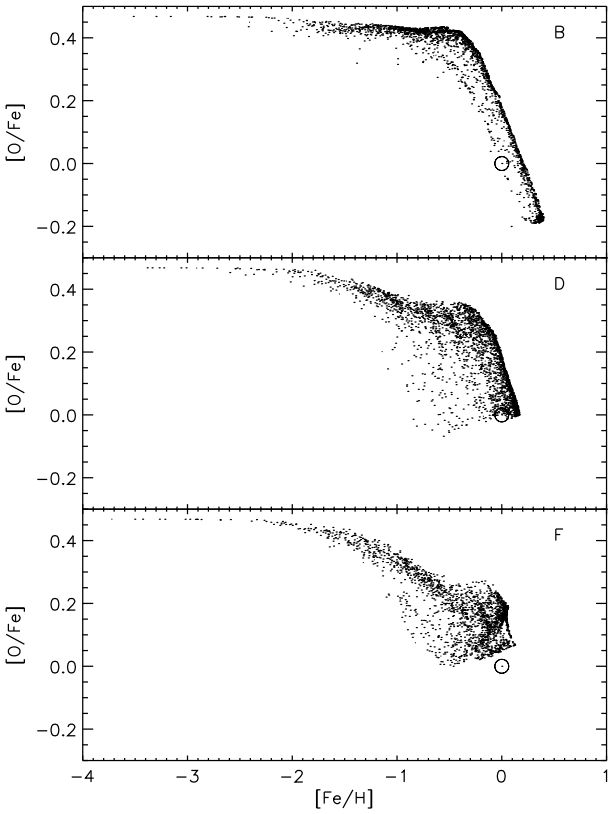

Figure 4.10. [O/Fe] against [Fe/H] for bulge stars in the three models B, D, F. The different transitions from SNeII to SNeIa dominated abundances are clearly visible.

is thus reflected in a large overabundance of α-elements. This is shown for the element Mg in Fig. 4.11. The distribution of [Mg/Fe] for all bulge stars at time 4 Gyr shown in Fig. 4.11 has a strong peak at [Mg/Fe] $= 0.4$. There is also a smaller peak at $[\mathrm{Mg/Fe}] \simeq -0.2$; this value corresponds to the maximum $[\mathrm{Mg/Fe}]$ reached in a closed box simulation, and is generated by an extended low level star formation at late times when the iron enrichment from SNeIa dominates.

The distribution in Fig. 4.11 for model B looks not unlike that for the Galactic bulge stars measured by McWilliam & Rich (1994) and shown as the dotted histogram in Fig. 4.11. Note, however, that the observed distribution will depend on the entire SF history following the simulated early phase. Thus, at the moment it is too early to say whether the old Galactic bulge could have formed out of an early fragmenting disk, but it is clearly a possibility that is worth further investigation.

The evolution of the velocity dispersion of the bulge stars is shown in Fig. 4.12, where both the (cylindrical) radial velocity dispersion σ_R and the vertical component σ_z are given. The figure shows two main effects: The first, visible in in both components, is a more or less linear rise of the velocity dispersion due to the growing mass concentration in the center of the disk.

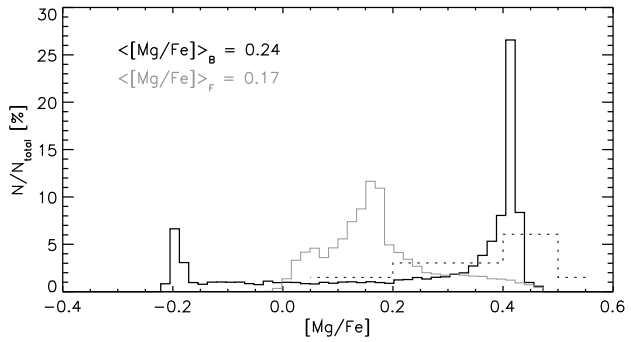

Figure 4.11. [Mg/Fe] distribution for bulge stars ($r < 2$ kpc) formed until the end of the simulation (at time 4 Gyr), in models B (black line) and F (grey line). The dotted histogram shows [Mg/Fe] for 11 stars measured by McWilliam & Rich (1994).

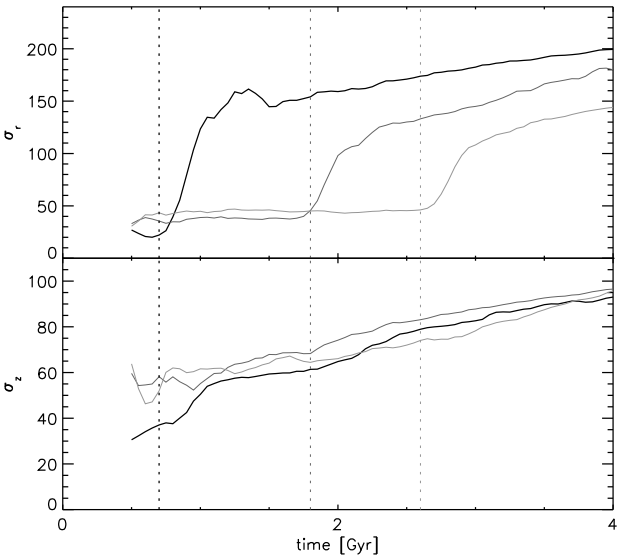

Figure 4.12. Stellar velocity dispersion of the bulge stars ($r < 2$ kpc) for models B (black), D (dark grey), and F (light grey). The effect of the instability on the velocity dispersion is clearly visible in the radial component σ_R.

The second effect originates in the instability and affects only the radial component. In model B, the violent evolution of the galactic disk with the final coalescence to a nuclear bulge leads to a strong rise in the radial velocity dispersion: when the instability sets in, σ_R rises sharply from around 30 $\frac{\mathrm{km}}{\mathrm{s}}$ to 150 $\frac{\mathrm{km}}{\mathrm{s}}$. The corresponding rise in models D and F occurs later; see Section 4.6. The z-component of the velocity dispersion increases less through the instability.

At early times, the vertical dispersion in this model exceeds σ_R. We believe this is a combination of the infall model used and a massive disk building up in the galactic plane. At the end of the simulation, the radial velocity dispersion is around 200 $\frac{\mathrm{km}}{\mathrm{s}}$ whereas the z-component lies around 90 $\frac{\mathrm{km}}{\mathrm{s}}$.

4.6. Bar Evolution

Fig. 4.13 shows the evolution of model F during the bar instability, through its face-on K-band surface brightness map. Model F is representative for the models with lower cloud energy dissipation, E to G. The bar forms between 2.6 Gyr and 2.8 Gyr, i.e., within a time interval of the order of the dynamical time, as is also observed in N-body simulations (Combes & Sanders, 1981). The bar instability causes a sudden increase in the radial component of the velocity dispersion (Fig. 4.12), whereas the z-component stays rather unaffected.

Right after its formation the bar becomes very pronounced, and then weakens again. To do a quantitative investigation, we made a Fourier decomposition of the mass distribution to derive the length of the bar. Fig. 4.14, bottom panel, shows that the bar becomes shorter with time. The bar length evolves from around 4.5 kpc to around 3.2 kpc within 1 Gyr. The shortening of the bar is accompanied by an increasing pattern speed (Fig. 4.14, top panel). The bar developed in the model is a fast bar with its end near the corotation radius. The rising pattern speed can be explained by the growing mass concentration in the center, since all relevant frequencies at a given radius r depend on $\sqrt{M_{\mathrm{central}}}$. This evolution is similar in all three models that form a bar.

Because at the time when the bar forms (Fig. 4.6), the gas content of models E to G is still high, up to 60%, the formation of the bar leads to a significant inflow of gas to the center. There the gas can form new stars (compare Sect. 4.4.2). The mass accumulation in the center then weakens the bar, as previously observed in numerical simulations (e.g Friedli & Benz, 1993; Norman et al., 1996). There is also observational evidence for the weakening of bars through central concentrations: Das et al. (2003) recently found an anti-correlation between central mass concentration and deprojected bar ellipticity in a sample of 13 barred nearby galaxies.

As we have already mentioned in the introduction, observations indicate an absence of bars at intermediate and high redshifts (Abraham et al., 1999). In the models presented here, the formation of an extended stellar disk with surface density high enough that it can become bar-unstable, takes a comparably long time. In addition, in these systems with large gas fraction, the bar formed is rapidly weakened due to strong gas transport to the center. Both effects could occur in high redshift disks, as the early disks might have larger cloud random motions because of the stronger infall, and would have higher gas contents. The two effects thus might explain the absence of bars at higher redshifts.

The metallicity distribution of the stars in the central bar/bulge (Fig. 4.10) reflects the slower enrichment process in the hotter models. The bend in [O/Fe] is shifted to lower [Fe/H], because of the smaller SFR in these models. The bump visible in this plot for models D and F at [Fe/H]

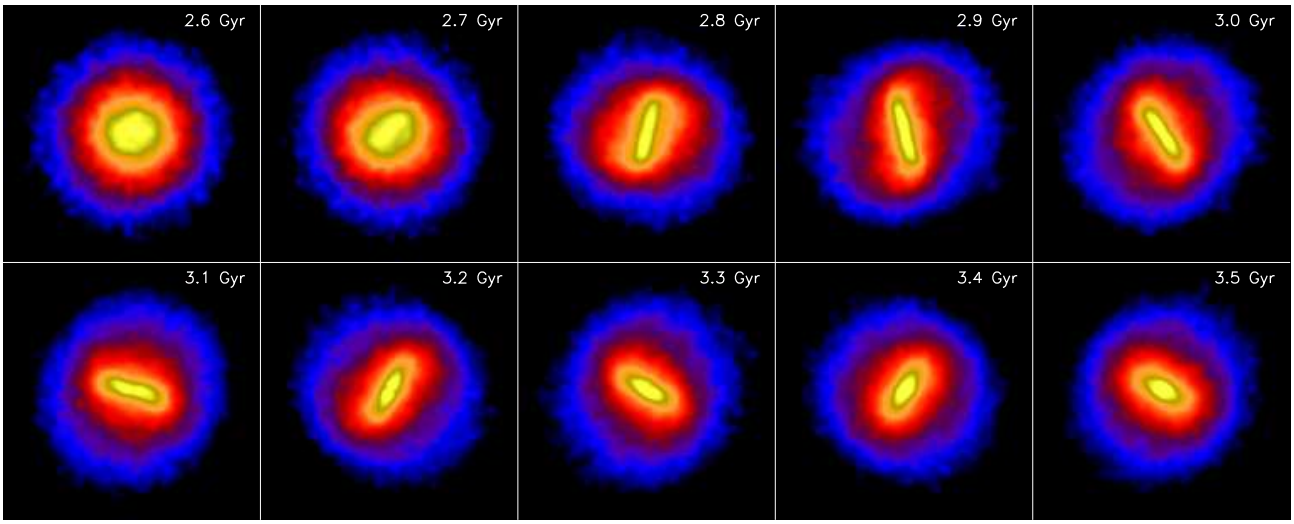

Figure 4.13. K-band restframe surface brightness map as mass tracer for the inner 12 kpc of model F.

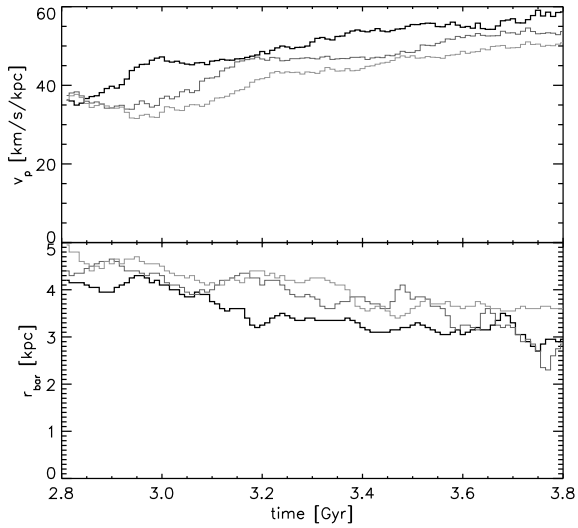

Figure 4.14. Evolution of the pattern speed (top) and bar length (bottom) for models E (black), F (dark grey) and G (light grey).

around -0.4 is mainly due to the increase of the central SFR caused by the instability. The SNeII formed in the central regions dominate the feedback again and enhance the abundance of α-elements. This effect together with the averaging over the central 2 kpc is also the source of the scatter in the plots for models D and F.

We note that, because we use an IMF-averaged yield for SNeII, we do not find a broad range of [O/Fe] values at low metallicities, as would be expected at early times when bulge stars are enriched by individual SNeII with different progenitor masses (Argast et al., 2000). The scatter seen for models D and F in Fig. 4.10 comes from the form of the SFR.

Contrary to the cold model B, the [Mg/Fe] abundance ratio distribution of the stars in model F (Fig. 4.11) has only a single peak around $[\mathrm{Mg/Fe}] \simeq -0.2$.The different maximum metallicities reflect the fact that the SF histories in the models are different (compare Fig. 4.6).

4.7. Conclusion

We have investigated a sequence of models for star-forming, gas-rich disks. The most important result from these models is that galaxy evolution proceeds very differently depending on whether it is the gas disk or the stellar disk which first becomes unstable, as measured by the respective Q-parameters. In our two-phase, star-forming interstellar medium description this depends on how efficiently the cold cloud medium can dissipate the kinetic energy it gains from dynamical and feedback heating. An additional important variable is the infall history (Noguchi, 1999), which influences the gas density and hence the local self-regulation equilibrium (Samland & Gerhard, 2003, SG03) and the disk stability.

When the cold gas cools efficiently and drives the instability, the galactic disk fragments and forms a number of massive clumps. The stellar disk fragments with the gas because of the strong gravity of the clumps, which begin to form stars at a high rate because of their large density. The clumps then spiral to the center of the galaxy in a few dynamical times and merge there to form a central bulge component in a strong starburst. This scenario is similar to that discussed by Noguchi (1999). We show that, in this mode of disk evolution, the bulge forms rapidly and early; the unstable region of the disk is completely disrupted, and the disk must be rebuilt by subsequent infall. Because of the starburst origin, many of the bulge stars formed in this way have large [α/Fe] abundance ratios.

On the other hand, if the kinetic energy of the cold clouds is dissipated at a lower rate, stars form from the gas in a more quiescent mode, while keeping the kinetic temperature high enough and the gas density low enough to prevent the gas from becoming dynamically unstable. In this case, an instability only sets in at later times, when the surface density of the stellar disk has grown sufficiently high. The system then forms a stellar bar, which channels gas into the center, evolves, and forms a bulge whose stars are the result of a more extended star formation history, i.e., have lower [α/Fe]. This scenario resembles the evolution described by Combes & Sanders (1981), Pfenniger & Norman (1990) and Raha et al. (1991). The comparably long formation time for bars and bulges in this mode and the weakening of the bar through inward gas flow in the still gas-rich disks might explain the absence of bars at high redshift (Abraham et al., 1999).

An example of a nearby galaxy in which the fragmentation process may be taking place, is the gas-rich, blue starburst galaxy NGC 7673 (Homeier & Gallagher, 1999). At higher redshifts, a number of morphologically unusual galaxies may be in similar evolutionary states, such as the so-called chain galaxies (Cowie et al., 1995) and other knotty galaxies seen in the HDF (van den Bergh et al., 1996); see Immeli et al. (2003a) for further discussion. On the other hand, the abundance ratios in the centers of nearby bulges show only a moderate α overabundance ([α/Fe]$\simeq$ 0.2; Proctor & Sansom (2002)), arguing that these stars were formed from gas enriched by more extended star formation histories. The few [Mg/Fe] abundance ratio measurements available for the Galactic bulge (McWilliam & Rich, 1994), on the other hand, point towards more enhanced [α/Fe]. Consistent with this, Puzia et al. (2002) find a similar enhancement in three Galactic bulge fields as in bulge globular clusters from integrated light measurements.

Clearly, mixed star formation histories would also be possible, in which a part of the bulge formed in an early starburst, preceding a slower build-up of bulge stars from secular evolution of the disk. In the multi-phase galaxy evolution model of SG03, which follows the formation of a large disk galaxy in a growing ΛCDM dark matter halo, the final bulge is indeed a superposition of these two components with, in that model, the larger part of the mass in the secular component. Our models suggest that the time-scale for secular disk evolution is comparable to or longer than that for Fe enrichment from SNeIa, while the central starburst occurs before SNeIa become important. Thus further spatially resolved measurements of [α/Fe] in bulges, and measurements of [α/Fe] vs Fe and radius for Galactic bulge stars will be key for disentangling bulge formation history.

It is well-known that the properties and evolution of a galactic disk depend on global parameters like mass, angular momentum, and infall rate. We have shown here that the evolution may also depend strongly on the physics of the baryonic component, in particular, the uncertain energy dissipation rate of the cold cloud medium from which most stars are formed. This also implies that one cannot simply derive the accretion rate onto a galaxy by determining its star formation history. Although all the models in our sequence have an identical gas infall, we observe very different SF histories from one model to the other. In all models, however, the instability causes gas transport to the center, and a subsequent increase of the central SFR leading to the build-up of a central bulge component.

We thank the referee, M. Noguchi, for his prompt report, the Schweizerischer Nationalfonds for financial support of this work under grant 20-64856.01, and the Centro Svizzero di Calcolo Scientifico (CSCS) for the opportunity of using their computing facilities.

5

Sub-Galactic Clumps at High Redshift: A Fragmentation Origin?

Abstract

We investigate the stability and star formation modes of a galactic disk forming by infall into a dark matter halo. We use a 3D chemodynamical simulation describing the dynamics of stars and a two-phase interstellar medium, as well as feedback processes from the stars. We find that, for high efficiency of energy dissipation in the cold cloud medium, the initially gaseous disk fragments and develops several clumps of gas and stars. We follow the evolution of the individual clumps and calculate masses, metallicities and velocities for them. A few dynamical times after fragmentation of the disk, the clumps merge and build up a massive bulge. Calculating HST- and UBVRIJHKLM-colors of the model, including absorption by interstellar dust, we determine the morphologies and colors of this model in HST images. Several peculiar morphological structures seen in the HDF can be well explained by a fragmented galactic disk model, including chain galaxies and objects consisting of several nearby knots.

5.1. Introduction

In the redshift range $0.5 < z < 3$, galaxies evidence a large diversity of morphological types (e.g. Abraham & van den Bergh, 2001; Steidel et al., 1996; van den Bergh et al., 1996, vdB96). Although some of the unusual morphological structures can be explained by the morphological K-correction, NICMOS observations (Dickinson, 2000) show that many galaxies indeed have a rest frame optical morphology that cannot be attached to the traditional Hubble scheme. Examples are the so-called chain galaxies that show elongated knotty structures (Cowie et al., 1995, CHS95). Here we investigate a model of a gaseous disk, which becomes unstable and develops several clumps of gas and stars. Comparing with observations in the HDF, we show that several of the unusual morphological types in the HDF are consistent with a fragmented disk model seen from different viewing angles.

5.2. The Model

We use a two-phase model for the interstellar medium, consisting of a hot, low-density phase and a cold cloud medium from which stars are formed. We describe this system with a three-dimensional chemodynamical evolution code, which combines a hydrodynamical grid code for the two phases of the interstellar medium (ISM) with a particle mesh code for the stars. The interactions between the different ISM phases are described in Samland & Gerhard (2003, SG03). For the star formation rate (SFR) we use a Schmidt Law (Schmidt, 1959), $\dot{\rho}_{\rm sf} = c_{\rm sf} \cdot \rho_{\rm cm}^{\alpha}$ with $\alpha = 1.5$ and $c_{\rm sf}$ consistent with the star formation (SF) rule derived by Kennicutt (1998).

The energy released from supernovae mostly goes into heating the hot phase, but also heats the cold phase. Most of the kinetic energy of the cloud fluid is in the motions of single clouds relative to the bulk flow. This kinetic energy can be dissipated by inelastic collisions (Larson, 1969) and augmented by supernova feedback (McKee & Ostriker, 1977). Its energy dissipation rate, here described by the parameter η_c, is not well-determined, and may well vary between galaxies. One expects that it depends on the geometrical structure of the clouds, on whether a major part of the dense medium is arranged in filaments, and on their self-gravitating structure and magnetic fields (Kim et al., 2001; Balsara et al., 2001). The influence of η_c on the dynamical evolution of gas-rich disks is investigated in more detail in Immeli et al. (2003a); here we compare one of their fragmenting disk models ($\eta_c = 0.5$) with observations of high-redshift galaxies.

The setup of our model describes an early and rapid formation of a massive galactic disk in a static dark halo. According to Sommer-Larsen et al. (2002) the delayed infall of the baryonic matter into the relaxed halo can solve the angular momentum problem arising in ΛCDM structure formation simulations. The primordial gas enters the simulation volume at $|z| = 7$ kpc vertically and uniformly distributed over a radius of 17 kpc, with a rotation velocity equal to the circular velocity at the infall point, and infall velocity $20\ \frac{\rm km}{\rm s}$. The infall rate is $120\ {\rm M}_{\odot}{\rm yr}^{-1}$ during one Gyr, resulting in a total baryonic mass of $1.2 \cdot 10^{11}\ {\rm M}_{\odot}$. The simulation volume has a diameter of 37.2 kpc and a vertical height of 14 kpc with a spatial resolution of 300 pc in the horizontal and 120 pc in the vertical direction. We have also done the simulation at lower resolution, with similar results, indicating that the outcome is not sensitive to the resolution used (Immeli et al., 2003a).

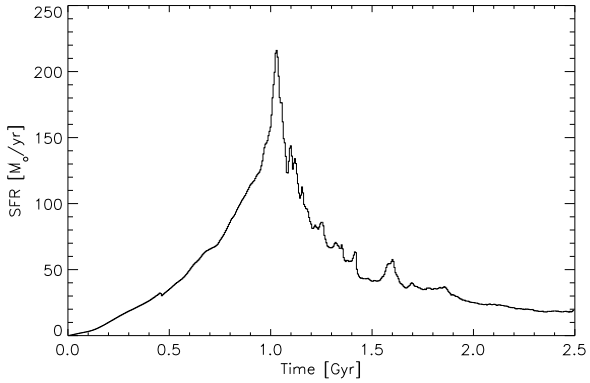

Figure 5.1. SFR of the model.

The chemodynamical model provides ages and metallicities of the stars formed, as well as ISM densities and metallicities. This enables us to calculate colors of the model at different redshifts, including absorption, using the method of Westera et al. (2002) except that we adopt here a three times lower absorption coefficient.

5.3. Results and Comparison to Observations

5.3.1. Global Evolution

The infall of the baryons leads to the build-up of a star-forming gaseous disk. Fig. 5.1 shows the SFR in the model. The energy input from the supernovae type II dominates that from the infall during most of the evolution and prevents formation of the disk on the free fall timescale.

At around 700 Myr the gas disk becomes unstable on large scales and begins to fragment. The lower-mass stellar system follows the gravitational potential perturbations induced by the gas. A face-on view of the model evolution from 500-1500 Myr is shown in Fig. 5.2 in terms of observed HST F606W surface brightness. The model was shifted to the redshift range indicated in the frames. The

high symmetry in the first two images reflects the symmetric infall of the gas. The pressure from the SF in the disk and the pressure from the infalling material causes the development of the ring-like structure at the border of the stellar disk, visible in the second image. This ring structure represents less than 10% of the total mass of the cloudy medium in the disk at this time. Yet the enhanced SF in this structure, due to feedback-induced large density fluctuations, causes a very prominent UV emission shifted to F606W at the redshift considered.

To quantify the fragmentation we use the asymmetry parameter A (Abraham et al., 1996) in rest frame U-band. The evolution of A is very similar to that of the SFR, which illustrates that the SF is driven by fragmentation. The maximum SFR reached in this simulation is around 220 $\mathrm{M}_{\odot}\mathrm{yr}^{-1}$, corresponding to a starburst (StB) galaxy. Indeed, Lowenthal et al. (1997) report similarities in stellar emission and interstellar absorption lines between $z \sim 3$ galaxies and local StB galaxies. The color selection criteria for Lyman Break Galaxies (LBG) also strongly favor StB galaxies (Steidel et al., 1996). Age determinations of stellar populations and enhanced abundances of α-elements in LBGs (Carollo & Lilly, 2001) indicate that the very high SFRs in these high-redshift objects persist only for a few hundred Myrs.

The clumps that form in the disk during the fragmentation phase spiral to the center, building a massive bulge. The time scale for this process is around 300 Myr. The high mass of the bulge is explained by the efficient angular momentum transfer during the fragmentation phase. Without newly infalling material there will be no major changes in the global structures of the galaxy after 2.5 Gyr. Formation of a bar is prevented due to the high-mass bulge. Numerical investigations of Noguchi (1999) showed a qualitatively similar evolution of a gaseous disk, with the main difference being that in his model the high SF threshold allow SF only after fragmentation of the disk. We discuss the stability properties of multi-phase star-gas disks, and the implications for bar and bulge formation, in more detail in a companion paper (Immeli et al., 2003a).

5.3.2. Comparison with Observations

In Fig. 3 the model morphology at different times during the fragmentation phase is compared to the morphologies of some objects in the HDF. Clearly, several HDF morphologies can be well explained by the fragmented disk model.

Enhanced spiral arms as seen in the model at about 1.35 Gyr, induced by the merging of the last two clumps, are also observed in the HDF (first row). In the second row the model at 1.3 Gyr is compared to a clumpy structure. Seen edge-on (third row) the model resembles a chain galaxy.

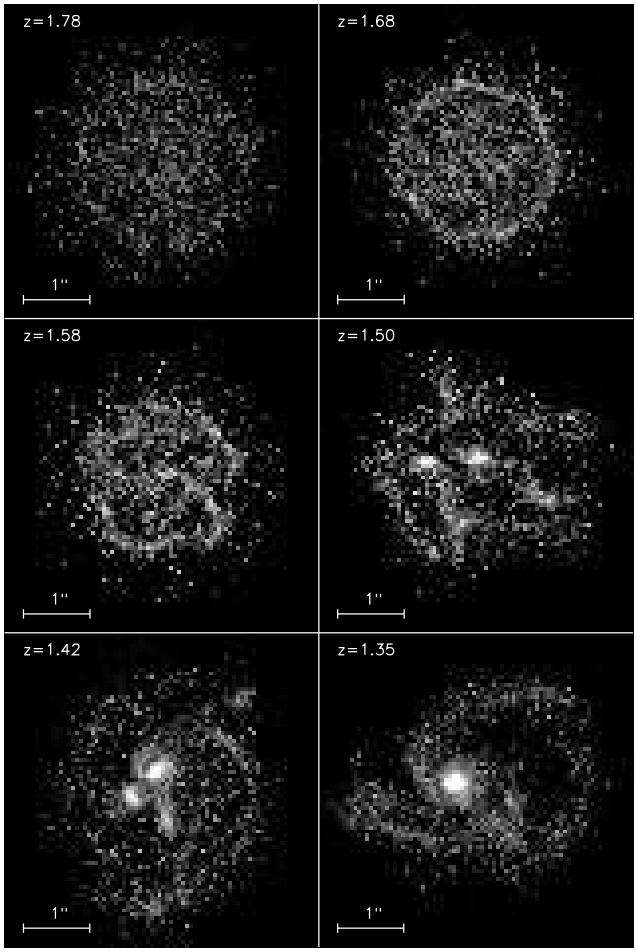

Figure 5.2. Fragmentation phase in observed F606W surface brightness, starting at 0.5 Gyr at top left in 200 Myr intervals. Redshifts normalized to the $z = 1.5$ panel are indicated in each map. The frames are 40 kpc a side. HST resolution and a detection limit of 28.21 mag (Williams et al., 1996) were used. Angular diameters were calculated using a ΛCDM cosmology with $\Omega_M = 0.3$, $\Omega_\Lambda = 0.7$, $h = 0.7$.

CHS95 reported observations of chain galaxies (chains), a new population of high redshift galaxies observed with HST in the Hawaii Survey Fields, with high major-to-minor axis ratios and very blue colors. vdB96 also found chain galaxies in the HDF. CHS95 suggested that chains lie in the redshift range $0.5 - 3$ and have a mass comparable to that of a present-day galaxy. They speculate that these objects may be linear arrangements in space where SF, once turned on, triggers SF along the line of maximum density. In some models the chains form in colliding supershells blown out of massive StB galaxies (Taniguchi & Shioya, 2001). Dalcanton & Shectman (1996) argued that LSB galaxies are local counterparts to chains at high or intermediate redshift. Finally, O'Neil et al. (2000) suggested from a comparison with less inclined objects that the chains do not belong to a new galaxy class but are knotty disk like structures seen edge on. Given the small number of chains compared to approximately 1000 known high redshift galaxies

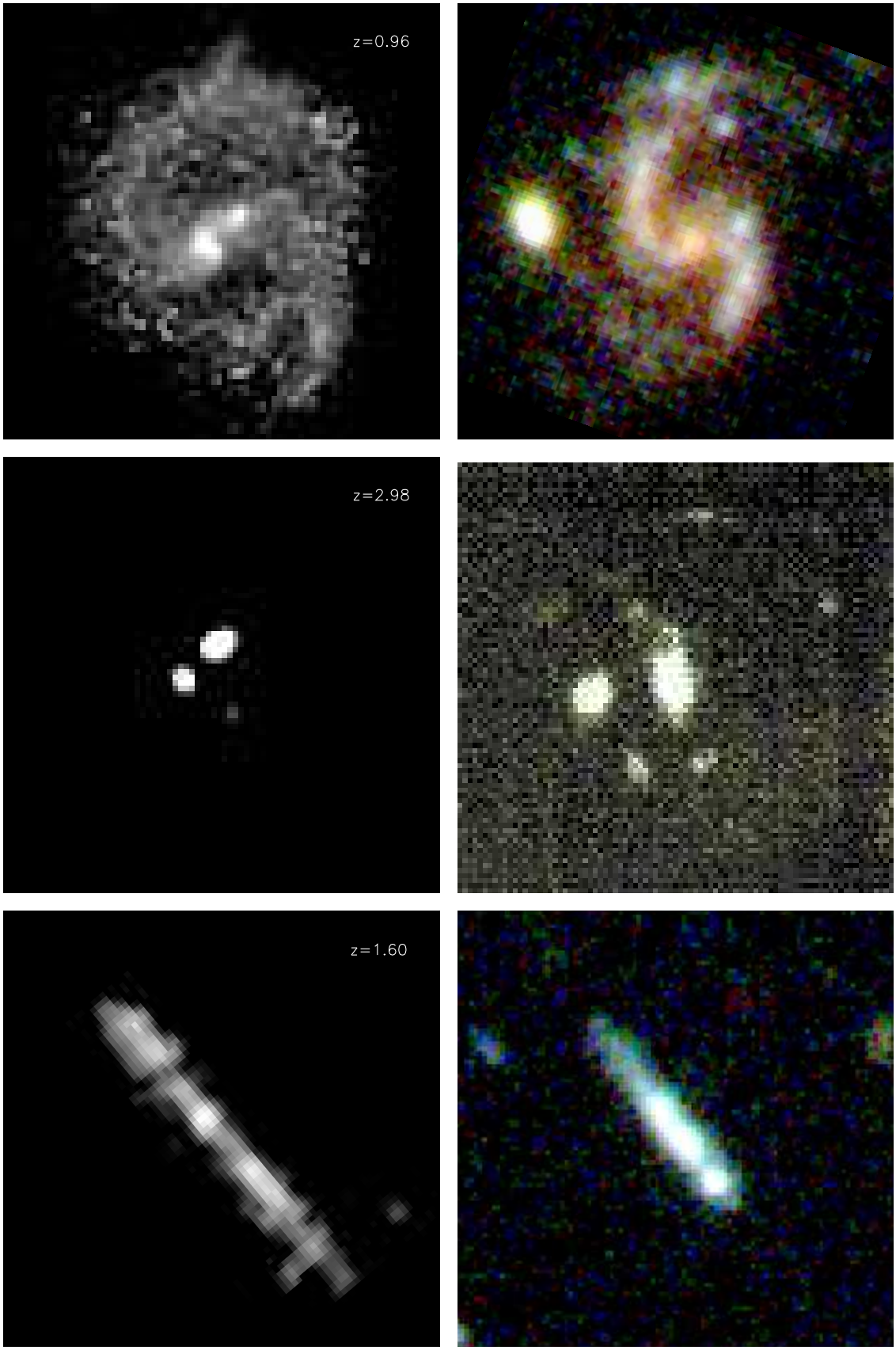

Figure 5.3. Comparison of observed HST F606W surface brightness of the model (left panels) with observations from vdB96 (right panels). The model was shifted to the indicated photometric redshifts of the observations (Fernandez-Soto et al., 1999).

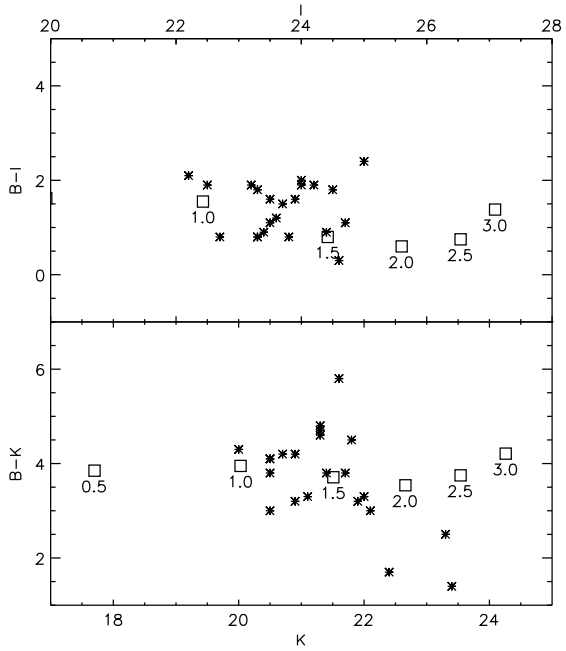

Figure 5.4. Colors of the model seen edge-on at 1.15 Gyr, shifted to the indicated redshifts (squares). Observational data for chains from CHS95 (stars).

(Giavalisco, 2002), it is likely that these objects are in a short evolutionary phase. Our model indicates that the interpretation of O'Neil et al. (2000) is correct. It shows chain structures when viewed edge-on and during a period of very high SFR. Because this period is short compared to a Hubble time, these objects will be relatively rare, and because of the high SFR, they are very blue. The model therefore naturally explains also the observation of CHS95 that a large fraction of chains is very blue. A comparison of the model colors with those of CHS95 is shown in Fig. 5.4. Best agreement is obtained if our model is shifted to redshifts between 0.8 and 1.8.

Do gas-rich disk systems at low redshift also tend to form fragments with enhanced SF? An example of a nearby galaxy in which the fragmentation process may be taking place, is the gas-rich, blue starburst galaxy NGC 7673 (Homeier & Gallagher, 1999). This object has a remarkably clumpy morphological appearance, seen in both the R-band and Hα, even though the Hα velocity field is that of a regular, rotating disk.

5.4. Merger or Fragmentation?

Kinematical data will be important to clarify the nature of chain galaxies. While in our fragmented disk model the massive clumps should still show the underlying disk rotation, in a merger scenario no similar alignment of the clump velocities is expected. Fig. 5.5 shows the predicted influence of the clumps on the disk rotation curve; deviations from the smooth rotation profile are up to 100 $\frac{\mathrm{km}}{\mathrm{s}}$. Thus while the basic rotation pattern remains visible during the fragmentation phase, it is severely disturbed by the innermost brightest knots.

Additionally, the metallicities of the clumps in a merger event are expected to vary significantly, depending on the mass and evolution history of the merging clumps. Contrarywise, one expects similar metallicities for the clumps in a fragmented disk. We investigate the metallicity of five clumps selected in the fragmented disk model as indicated in Fig. 5.6. We get abundance differences of up to 0.25 dex (Table 5.1), depending on the masses of the clumps ($\sim$ few $10^9\,\mathrm{M}_\odot$ for those in Fig. 5.6). No differences in oxygen-to-iron ratios can be measured, due to dominance and young age of the StB.

Many authors report observations of multiple knots (Driver et al., 1995; Steidel et al., 1996, vdB96). The fragmentation scenario naturally explains objects consisting of

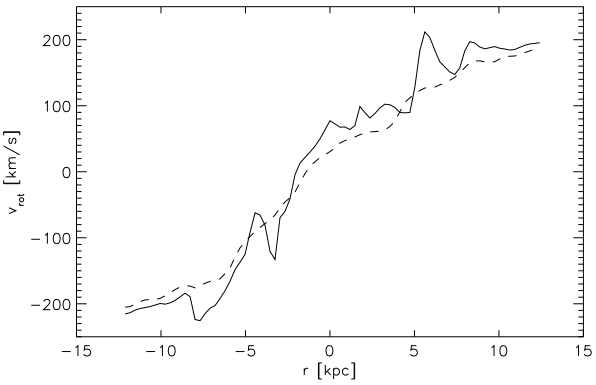

Figure 5.5. Mass-weighted rotation curve of the model after 1.15 Gyr, in the disk plane where the clumps dominate (solid line), and 0.5 kpc above the plane (dashed line).

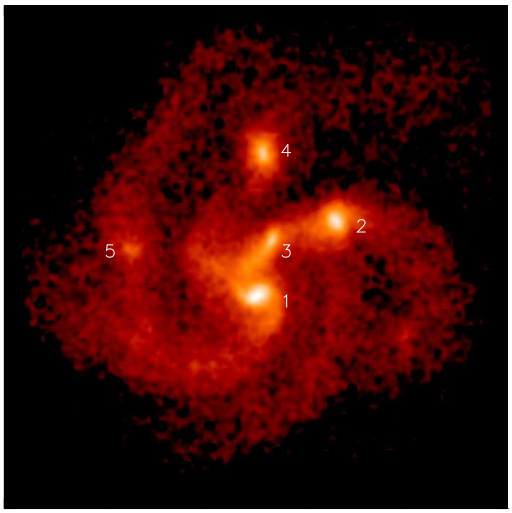

Figure 5.6. Smoothed stellar mass surface density of the model at 1.2 Gyr with numbering of the clumps.

Clump	Mass [$10^9 M_\odot$]	[O/H]	[Fe/H]	[O/Fe]
1	7.96	-0.32	-0.72	0.40
2	4.10	-0.38	-0.77	0.39
3	2.02	-0.44	-0.84	0.40
4	2.39	-0.42	-0.82	0.40
5	0.64	-0.59	-0.98	0.39

Table 5.1. Masses and metallicities of the stars in the clumps at 1.2 Gyr (see Fig. 5.6). Metallicity differences are up to 0.25 dex. [O/Fe] is constant because SNe Ia with a typical time delay of around 1 Gyr have not yet contributed signifi cantly to the chemical abundances.

several clumps, whereas in a merging scenario it is much less likely to see more than three nearby clumps merging at the same time. Also, the synchronized colors often observed in these clumpy objects (Abraham & van den Bergh, 2001) are naturally explained with the fragmented disk scenario. In the present model, the mean age of the stars seen edge-on in the clumps is constant within 70 Myr. At least some of the observed multi-clump systems may therefore represent fragmented disks.

5.5. Conclusions

A short formation timescale of a galactic disk due to a high dissipation rate for the cold gas phase leads to fragmentation and to the formation of a clumpy disk with an enhanced SFR in the clumps. After the fragmentation phase the clumps fall to the center building a massive bulge. Subsequent bar formation is prevented by the massive bulge.

Chain and multi-clump morphological structures, as well as synchronized colors observed in high redshift objects, can be well explained by a fragmented disk in a gas rich, single galaxy. Our model suggests that these galaxies are in their formation process and are observed during their relatively short fragmentation phase, with a high SFR, comparable to the model SFR of up to $220\ M_\odot\ \mathrm{yr}^{-1}$. Note that the high SFR is generated only by disk instability and there is no need for triggering through interaction or merger with other galaxies.

The effects of the single clumps on the mass-weighted rotation curve in our model can be as high as 100 $\frac{\mathrm{km}}{\mathrm{s}}$. Nonetheless the underlying rotation signature should be observable. Metallicity differences in the clumps of the fragmented disk are no larger than 0.25 dex, while their mean stellar ages are highly synchronized. Observations to test these predictions are highly desirable.

We thank the Schweizerischen Nationalfonds for financial support of this work and the Centro Svizzero di Calcolo Scientifico (CSCS) for giving us the opportunity to use their computing facilities.

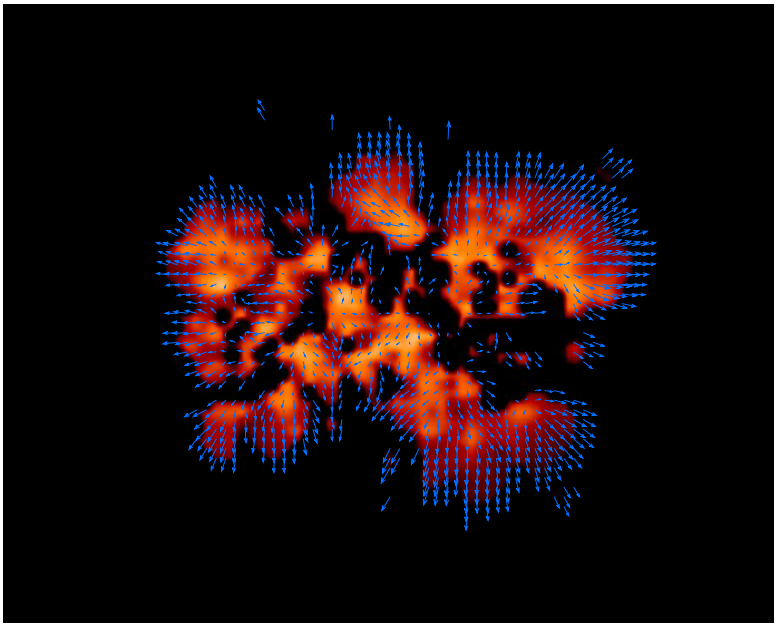

6

Supernova Induced Gas Flows

Abstract

The phenomenon of winds is important in many astrophysical situations. In the context of galaxy evolution, galactic winds transport mass and metals and hence connect different regions of the galaxy. I discuss how the wind properties in a thin and an extended ISM disk model depend on the SFR and the physics of the ISM, using the model sequence described in Chap. 4.

6.1. Introduction

Galaxies may loose mass by various processes. Ram pressure can strip the gas from galaxies moving through a cluster, jets emerging from AGNs can reach far out into the intergalactic medium, and in ULIRGs, which may be the result of major mergers, there is evidence for winds. However the probably most important mass loss mechanism of galaxies is the supernovae driven galactic superwind, which may occur in all type of star forming galaxies.

The energy input from supernova explosions leads to large scale gas flows within a galaxy. Several authors suggest that the high velocity clouds may be manifestations of a galactic fountain (e.g. Shapiro & Field, 1976; Wakker & van Woerden, 1997; Breitschwerdt, 2003). In this scenario, hot gas is ejected into the halo by multiple SN explosions. High above the disk, the ejected gas becomes thermally unstable, forms clouds and can fall back on the disk. The gas flows have strong impact on the metal and mass distribution within a galaxy. The redistribution of metals within the galaxy can be very important. As an example consider the metal enrichment of a galactic halo. If the winds emerging from the central star forming regions can transport significant amounts of metals into the halo and the disk, they can pre-enrich these components (Samland et al., 1997).

In galaxies with low mass or very high SFR the gas can be accelerated to escape velocity. Galactic superwinds, which throw mass and energy out of a galaxy, are of great interest for several reasons. For example, they transport large amount of gas and energy into the intergalactic medium. Since the gas presumably is enriched with heavy elements (Vader, 1986), these outflows are important for the IGM metallicities (e.g. Songaila & Cowie, 1996; Molendi et al., 1999).

In the following I show how large-scale gas flows and galactic winds depend on the spatial distribution and the rate of the SNe and on the physical processes in the galactic ISM.

6.2. The Model

To investigate the supernova-driven winds in morphologically different disk galaxies, I use the model sequence described in Immeli et al. (2003b, Paper I, see Chap. 4).

From the time evolution of the models B and D, I use for the present investigation a snapshot of model B after 1.5 Gyr (hereafter B1) and model D after 2 Gyr (D1). The snapshots were chosen at a time, when the two models show approximately the same star formation rate of around $50\ \mathrm{M_\odot yr^{-1}}$, and hence comparable energy input from SNII. Note however that these models have different star formation histories and hence also metallicities (Paper I). Model B shows a fragmented disk and a high SFR during its evolution. The effects of the clumps exhibiting high SFR on the wind structure will be discussed using a snapshot of model B at 1 Gyr (B0), when the SFR of the model is around $200\ \mathrm{M_\odot yr^{-1}}$.

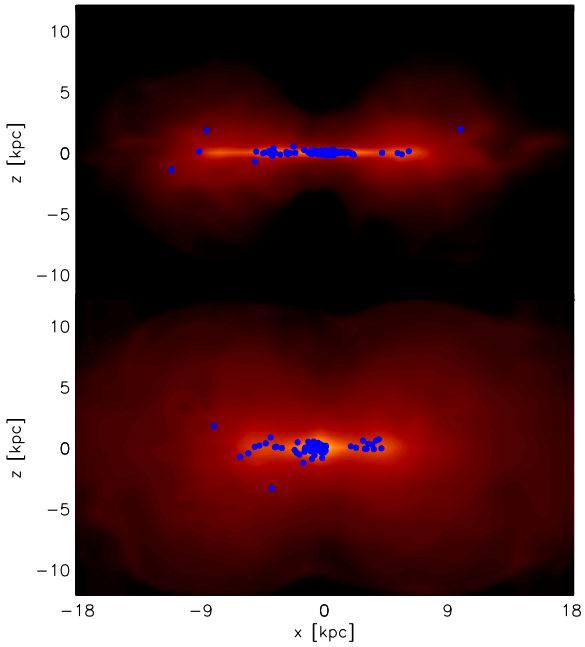

Figure 6.1. Cut through the cold gas distribution of model B1 (top) and model D1 (bottom). The blue dots represent stellar particles with ages younger than 30 Myr, to show the spatial distribution of SN-Explosions.

In Fig. 6.1 a cut through the density of the cold gas phase along the xz-plane is shown for model B1 and D1. Since the star formation rates of model B1 and D1 are approximately equal, the absolute amount of SN energy input is about the same in both models. Due to the differences in the dissipation efficiency in the models the gas distribution shows a diverse expansion along the z-axis (Paper I). Superimposed are the stellar particles with ages younger than 30 Myr and hence showing the places of the recent SNII explosions. One can clearly see that the SNII of the B1 model are more confined to the plane than those of model D1. Hence the energy input in the B1 model happens within or near the galactic disk whereas in the model D1 the SNII are distributed up to 2 kpc from the plane with some outliers even at 5 kpc.

I will discuss in the following sections, how the diverse energy input influences the wind pattern within a galaxy.

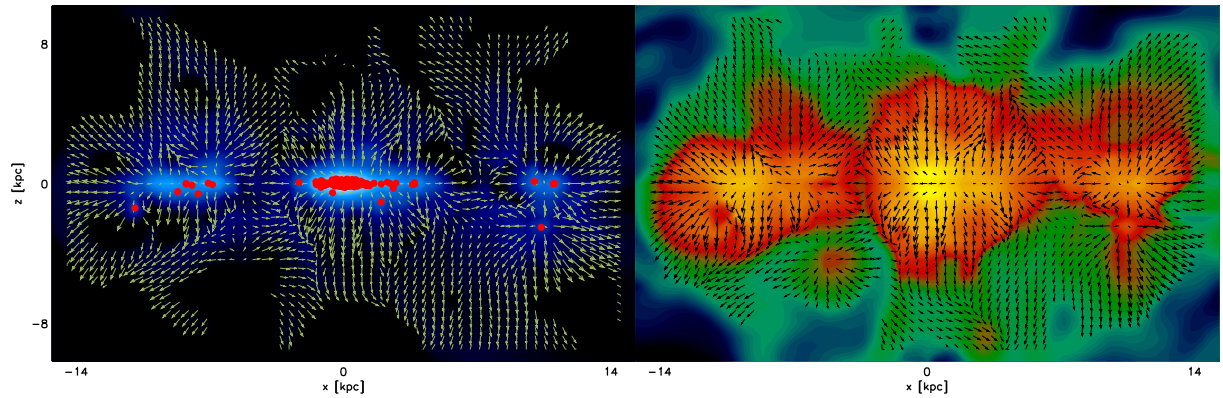

Figure 6.2. ICM-density (left) and ICM-metallicity (right) cut through the xz-plane of the clumpy disk of model B0. Each clump can drive its own wind because of the high SFR within the clumps.

6.3. Wind Structure

6.3.1. Peak Star Formation in a Clumpy Disk (B0)

During the evolution of model B, the gaseous disk fragments leading to several clumps of gas and stars (Paper I). At the fragmentation time, the model B (B0) shows a very high star formation rate of around 200 $\mathrm{M}_{\odot}\mathrm{yr}^{-1}$.

In the left panel of Fig. 6.2 a cut through the xz-plane of the ICM density of model B0 is shown. The location of the recent supernovae lying in this plane are indicated by red dots. The energy input is clearly concentrated in the clumps. Each clump drives its own wind. At least up to a height of 5 kpc above the plane the inhomogeneous structure of the disk is visible also in the wind pattern.

The right panel of Fig. 6.2 shows a cut through the xz-plane of the metallicity of the hot gas. The metallicity shows peak values in the clumps, which suggests the independent evolution of the clumps. Typical metallicity differences are discussed in (Immeli et al., 2003a, Letter I, see Chap. 5). The wind from the central clump is collimated through the energy input of the two outer clumps. This is best visible in the cut of the metallicity, since it represents a kind of time integrated wind structure.

The star formation rate determines the intensity of the outflow. The time sequence of the wind pattern is given for model B in Fig. 6.3, starting at 1 Gyr in steps of 250 Myr.

The out streaming hot gas in model B reaches peak velocities of around 350 $\frac{\mathrm{km}}{\mathrm{s}}$. This value reduces to around 200 $\frac{\mathrm{km}}{\mathrm{s}}$ in the late evolutionary phase, where the SFR is lower. This is consistent with high redshift observations of starburst driven winds, which are very common and show outflow velocities around 350 $\frac{\mathrm{km}}{\mathrm{s}}$ (Dawson et al., 2002). I will discuss mass loss in form of galactic superwinds for all models in Sect. 6.4.

6.3.2. Gas Flows in the Thin Disk (B1)

In Fig. 6.4 a cut through the density along the xz-plane of the hot and the cold gas phases of model B1 and D1 is shown. Superimposed are the gas velocities.

The peanut shape visible in the density of the cold gas (right panels) emerges from the shape of the gravitational potential. The roughly constant velocity dispersion within the disk causes a puffing up of the outer disk, since the gravitational potential in z-direction is deeper in the center than in the outer parts of the disk. This is especially prominent in model B1, where the instability of the gaseous disk led to a massive bulge. The clouds in model B1 can fall right to the center of the disk.

The left column in Fig. 6.4 shows the hot gas component of the two models. The concentrated energy input of model B1 leads to a collimation and high acceleration of the outflow. Since the pressure above the plane is lower than within the plane, the material is ejected perpendicular to the plane, analogously to investigations concerning the collimation of a galactic superwinds (Suchkov et al., 1994; Strickland et al., 2000a).

The B1 model cannot drive the hot gas to a galactic height of more than 4 kpc. This is because the gas is only heated by supernovae near the galactic plane. If the outflowing gas reaches the halo, heating rates are getting weaker and the gas begins to cool and forms clouds.

It has long been suggested that the observed high velocity clouds may be a manifestation of a galactic fountain (e.g. Shapiro & Field, 1976; Wakker & van Woerden, 1997; Breitschwerdt, 2003). In this scenario hot gas is thrown out of the plane through the energy input of successive supernovae explosions. The hot gas then forms clumps under the influence of a Rayleigh-Taylor instability and the clumps can fall back to the plane. In Fig. 6.5 the oxygen abundance [O/H] as a cut through the xz-plane is shown for B1 and D1. It is clearly visible that the hot outflowing gas

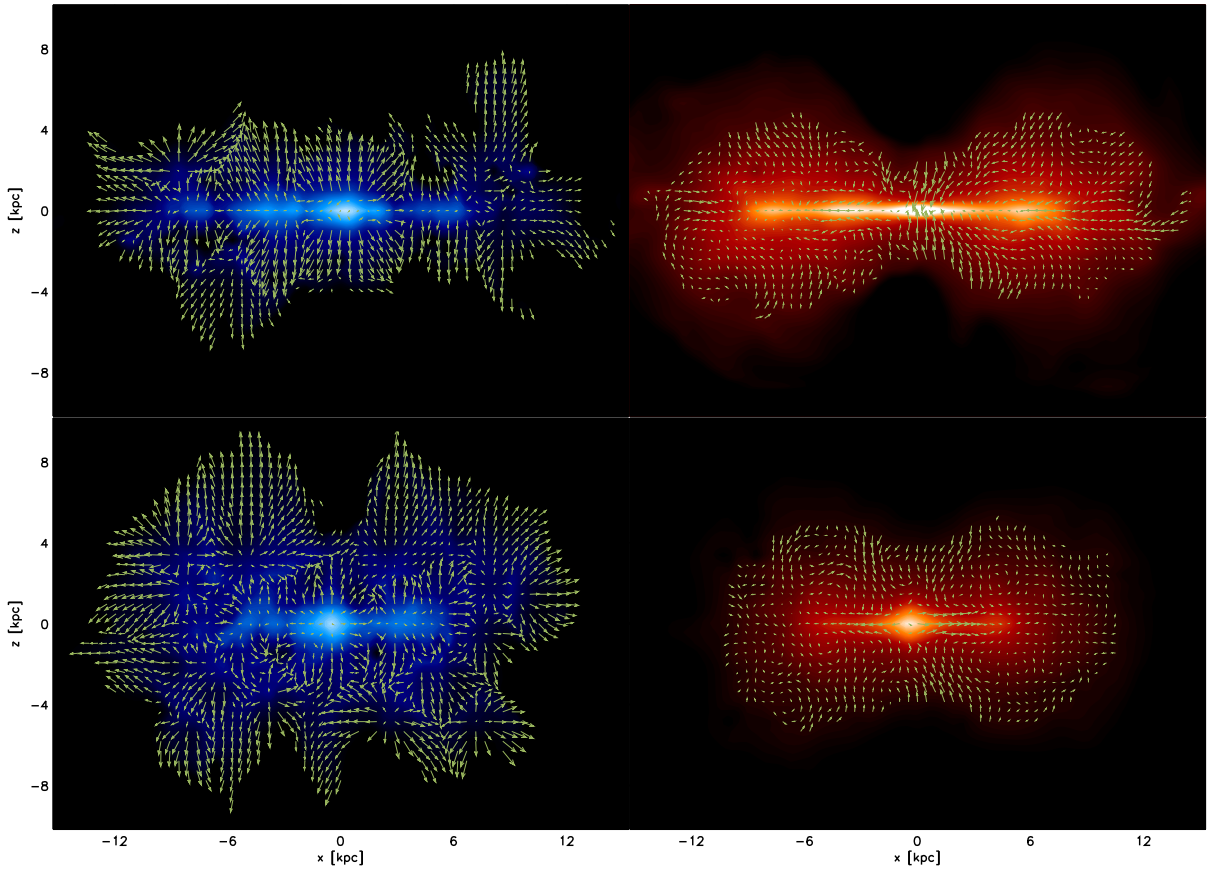

Figure 6.4. Wind structures of model B1 (top row) and D1 (bottom row) in the hot (left) and cold (right) gas phase. The velocities are indicated by arrows. The wind structure is only shown for the regions with high enough density to contribute a signifi cant mass flux.

is metal rich and that the metals are blown out to distances of several kpc above the plane.

Contrary to most galactic models, the present model uses a two-phase interstellar medium. Inflow of the clouds and outflow of the hot gas coexist in the models. Looking closer to the metallicity distribution of the clouds of the B1 model reveals an enrichment up to around 2 kpc above the plane. Since the clouds are falling onto the plane, and since the metal production through SNII is located in the plane, the metallicity has to emerge from condensation of outflowing hot gas. This may be a manifestation of a galactic fountain in this model. This view is supported by the fact that the hot gas does not leave the potential of the galaxy (see Sect. 6.4).

6.3.3. Gas Flows in the Extended Disk Model D1

Looking at the cloud velocities (Fig. 6.4, right column) one clearly recognizes that the low dissipation efficiency of model D1 leads to an earlier slow down of the clouds, which are falling to the plane. While in the cold model the clouds can fall readily to the plane, they fall in only to around 2 kpc in the D1 model, any the further infall takes place slower and the velocity field is distorted. The peanut shape of the cloudy medium is less prominent, because the central potential is not as deep as in model B1.

The expanded energy input in model D1 causes that the outfbwing gas is heated until around 4 kpc above the plane and only then cooling dominates. This causes that the material can flow further away from the disk than in model B1. However, in the extended disk model the gas is not accelerated to such high velocities. The distributed energy input leads to a less steep pressure gradient in the hot gas and hence a less efficient acceleration. Additionally SNII explosions above the plane are slowing down the outfbw arisen near the plane. Typical values reached are between $100\ \frac{\mathrm{km}}{\mathrm{s}}$ and $150\ \frac{\mathrm{km}}{\mathrm{s}}$, again depending on the star formation rate.

Model D shows a less extended metallicity distribution. One reason is that the metallicity of model D1 is lower than that of B1, since the models show a different star formation history (Chap. 4). Furthermore, the outstream velocities are slower which leads to a less efficient metal transport into the halo. In the hot gas of model D1 the red dots in outside the disk indicate, how supernovae explosions can locally enrich the hot gas.

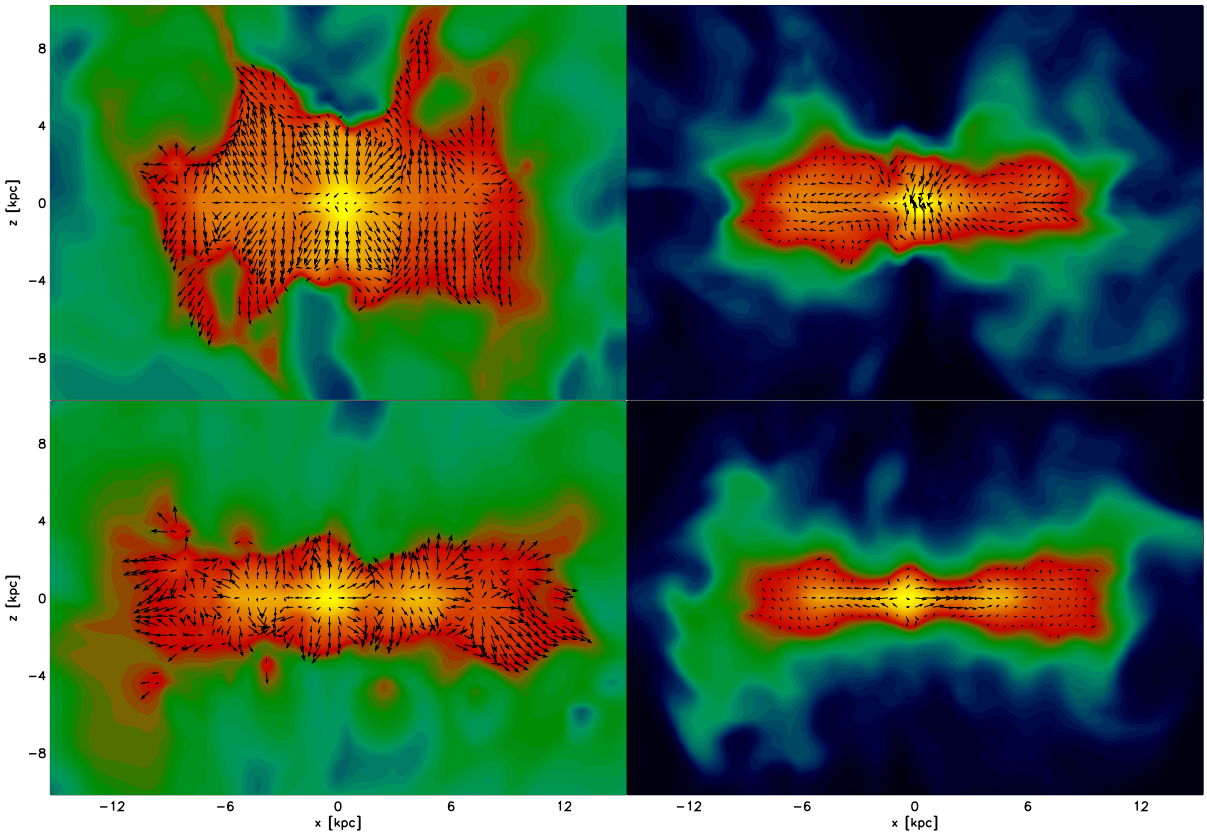

Figure 6.5. Oxygen abundance in the xz-plane of model B1 (top) and model D1 (bottom) in the hot (left) and cold (right) gas phase. High metallicities are indicated through yellow color, whereas low metallicities have blue colors.

6.4. Galactic Superwinds

Material can be ejected out of a galaxy in a so-called galactic superwind (Chevalier & Clegg, 1985; Suchkov et al., 1994, 1996; Mac Low & Ferrara, 1999; Strickland et al., 2000a; Silich & Tenorio-Tagle, 2001).

Since the present model sequence does not follow the gas up to the virial radius of the dark halo, where one can conclusively determine the lost gas mass fraction, I apply a local criterion to estimate the amount of ICM mass which could leave the galaxy. I determine the total energy of a mass element to decide whether its bound to the galaxy or not.

$$\Phi\rho_{\rm icm} + \epsilon_{\rm icm} + \frac{1}{2}\rho u^2_{\rm icm} > 0 \qquad (6.1)$$

According to this condition none of the cold gas clouds can escape the gravitational potential. This is different for the hot gas, where 8% for model B1 and 5% for model D1 have in principle enough energy to leave the galactic potential. For the high star formation rate in model B0 this fraction increases to 21%. However, this is an upper limit, since interaction processes, mostly cooling, will lower the pressure of the gas. For comparison, in M82 about 8% of the mass associated with the wind has high enough energies to escape the potential (Silich, 2003). But again, it is not clear, which fraction of the material can leave M82 or will fall back at later times.

The difference in the distribution of the matter which could in principle leave the galaxy (Fig. 6.6) is due to the fact that in the D1 model the mass elements are located farther away from the disk than in the B1 model, and near the star forming regions the hot gas in principle always has enough energy to leave the galaxy. The distribution of the material having enough energy to leave the galactic potential given in Fig. 6.6 is representative for arbitrary times of the model sequence. At all times the gas at 10 kpc height has not enough energy to leave the galaxy. This suggests that material has only enough energy as long as it is heated through supernova explosions. Once the material has left the region of energy input it rather quickly cools. The gas is accelerated only near the star forming regions. Modifying the escape criterion 6.1 in such a way that only the potential and the kinetic energy is considered leads to a reduction of the fraction of ICM that can leave the galaxy to 0.8% in model B1 and 0.1% in model D1. This material will be mixed with other material on its way out of the galaxy. Therefore, no outflow occurs in these systems.

This is consistent with the findings of other investigations (e.g. Mac Low & Ferrara, 1999) and with constraints from observations. It is important to note that mass loss from massive galaxies at high redshift is not excluded by the present model. In the early stages of galaxy evolution, when the gravitational potential of the halo is shallower, also massive galaxies may lose metals to the ISM. However, if the directly observed outflows in Lyman-break galaxies at $z \simeq 3$ (Pettini et al., 2000) can leave the gravitational potential of the massive galaxies, the energy input would severely disturb the IGM leading to large variations of baryons relative to the dark matter, which are not observed (Madau et al., 2001). This implies that if the enrichment of the IGM originates from outflows of massive galaxies, this has to happen at higher redshifts.

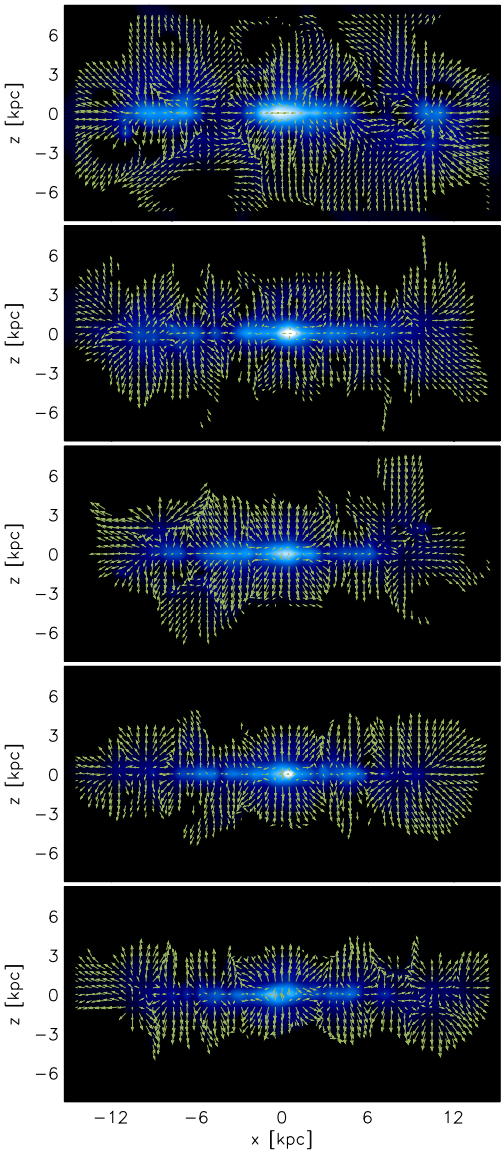

Figure 6.3. Time evolution of the wind pattern for model B, starting at 1 Gyr (top) in steps of 250 Myr.

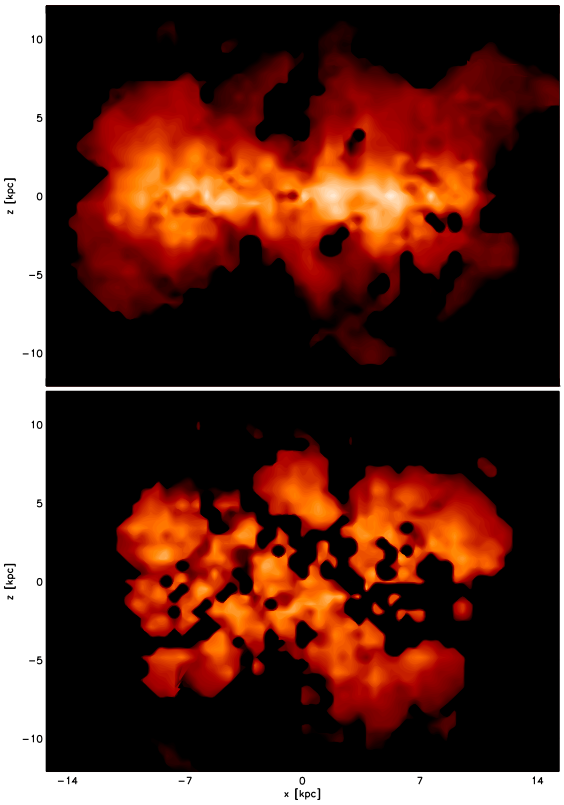

Figure 6.6. Distribution of the hot intercloud gas having high enough energy to leave the galactic potential.

The outflow of massive galaxies can be investigated by more realistic models concerning the simulation of the galaxy out to its virial radius to conclusively determine whether the material is lost. Another important point is the infall of baryonic matter and the build up of the dark halo (e.g. Samland & Gerhard, 2003).

6.5. Discussion of Wind Properties

Winds are very important for the evolution of galaxies since they connect different regions in the galaxy through energy and mass transport. I have started to investigate the wind emerging in the sequence of disk evolution models described in Paper I (Chap. 4), where I have taken model B as an example for a thin disk and model D as an example of an extended disk.

The high star formation rate in model B during the fragmented phase of the disk (B0) leads to a wind reaching up to 9 kpc above the plane. Each clump drives its own wind and the structure of the clumpy disk is visible in the wind structure up to 5 kpc. Even the high SFR of model B0 does not lead to a galactic superwind, mainly because the gravitational potential of the dark halo in the present model is too deep. This does not exclude early mass loss from massive

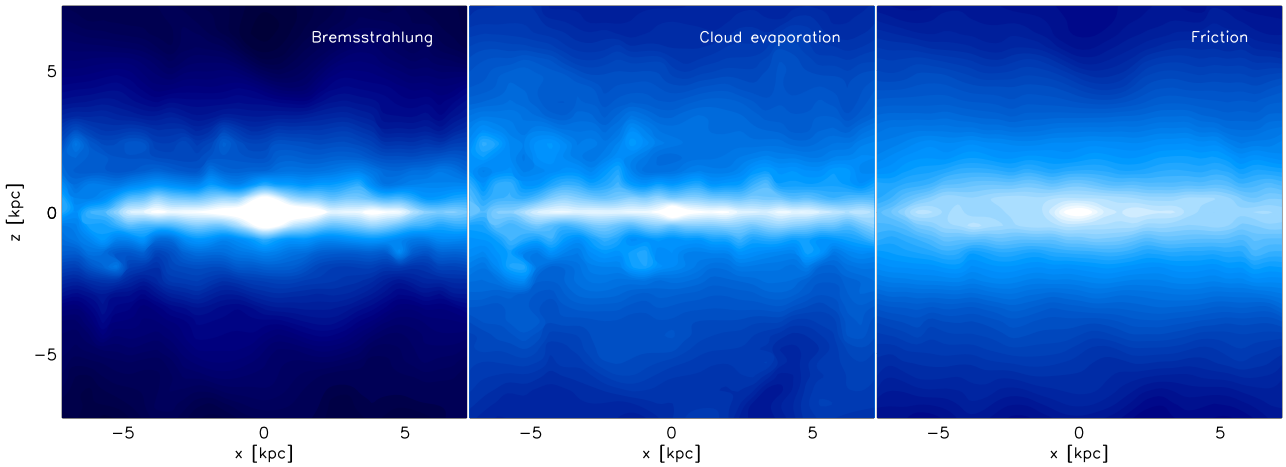

Figure 6.7. Qualitative X-ray emission of model B1. All fluxes are normalized. Clearly a different X-ray pattern is visible, depending on the origin of the X-ray emission. This enables investigations on X-ray properties of outflows.

galaxies in general. In models with growing dark halos, outflow can occur at early times (see Samland, 2003), when the SFR is high and the dark halo potential still shallow. Such an outflow at early times, when the ISM shows the typical α-enhancement of SNII ejecta compared to solar abundance, is consistent with observations of Songaila & Cowie (1996), who find evidence for enhancements of α-elements in Lyman forest clouds at high z.

The thin disk of model B1 drives a fast wind, with peak wind velocities around 350 $\frac{\mathrm{km}}{\mathrm{s}}$. The wind reaches height above the disk plane of around 4 kpc. With the declining star formation rate this value reduces to 2 kpc at the end of the simulation. The metallicity of the cloudy medium at 2 kpc is a manifestation of a galactic fountain in these models. The hot outflowing, metal enriched gas condenses and forms new clouds falling back into the disk.

In the extended disk model, the winds are accelerated to peak velocities of 150 $\frac{\mathrm{km}}{\mathrm{s}}$. The distributed energy input leads to a less efficient acceleration and instead of a fountain, a pressure supported bubble of hot gas is forming.

If galactic (super-)winds are powered by supernovae explosions one would expect the material associated with the wind to be metal enriched by supernova ejecta (Vader, 1986). However, the metallicity of the wind depends also on the metallicity and the amount of the ambient medium, which is carried along by the wind through the process of mass loading (Suchkov et al., 1996). Breitschwerdt (2003) argues that metallicity in winds is high, but generally little is known about the metallicity content in the outflowing wind of starburst galaxies.

The results of the simulation clearly indicate that the winds are metal enriched. As a direct consequence of the ejection of SNII material one expects the material being α-enhanced. The metallicities of model B0, [Fe/H]=-0.70 and [O/Fe]=0.35, reflect the α-enhanced outflow from the galaxy during the maximum SFR. Due to the influence of SNIa explosions, the metallicity of the outflow in model B1, [Fe/H]=-0.02 and [O/Fe]=0.15 does no longer show this prominent α-enhancement. Obviously, the abundance pattern at late times is influenced by SNIa and at around 3 Gyr the winds are enriched with a lot of iron.

The more quiescent star formation mode of model D1 leads to lower metallicity in the outflow and to moderate α-enhancement, [Fe/H]=-0.2 and [O/Fe]=0.2.

Note that the coupling between the hot and cold gas phase in the model through evaporation and condensation is very important. To obtain a significant wind in the hot gas phase, it is necessary that dynamical coupling of the gas phases is not strong. By this, infall in the cloudy gas phase and a wind in the hot gas phase are possible at the same time. The differences of the one and two phase interstellar media will be discussed in Samland, Immeli & Gerhard (in preparation).

6.6. X-ray Fluxes of Winds

In the framework of the present model detailed superwind investigations are possible. Using a simulation setup corresponding to starburst galaxies like M82 or NGC 253, the model will be able to produce X-ray fluxes, UBVK- and HST colors and absorption features which can be directly compared to observations. While the origin of the hard X-ray component is attributed to the starburst or AGN itself rather than the wind (Suchkov et al., 1994; Strickland et al., 2000a; Weaver et al., 2002), the origin of the soft X-ray emission is still under discussion. The model will be able to compare three different origins, proposed by Strickland et al. (2000a): Emission through bremsstrahlung, emission in the transition regions between

clouds and ICM (D'Ercole & Brighenti, 1999), in the context of the present model proportional to the evaporation rate, and interaction between the high velocity wind and the clouds of the ISM. As an example, Fig. 6.7 shows the different X-ray emissions calculated for model B1. As expected, the X-ray maps differ significantly for these three X-ray producing processes. A quantitative X-ray flux can be calculated using the emissivities of Strickland et al. (2000b) based on the emissivities from Raymond et al. (1976), and X-ray absorption can be included applying the cross sections σ_c of Morrison & McCammon (1983). This leads to prominent X-ray shadows in the disk plane, because there the cold gas density and thus the absorption is very high.

Due to the velocity differences between the outflowing ICM and clouds above the galactic center the drag forces between the two gas phases may be important. Samland (1994) investigated the influence of drag forces onto outflowing gas, finding velocity changes of only 70 $\frac{\mathrm{km}}{\mathrm{s}}$ in the outflow of a comparable galaxy with small variations for the outflow radius. Note that condensation and evaporation between the ICM and clouds lead to a momentum exchange similar to the effect of drag, which is significantly higher. Therefore drag forces can be neglected in galactic outflows (Samland, 1994). However, if the velocity differences in galactic superwinds are very high, it would be interesting to investigate the influence of drag forces in these systems, especially the changes in the X-ray fluxes.

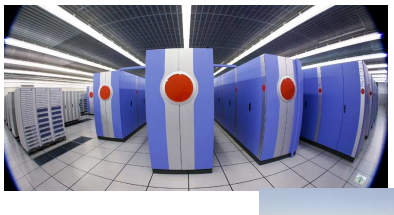

7

Summary and Outlook

“Reality is far from what I said”
D. Lynden-Bell at a conference in La Palma

This chapter summarizes the results of the thesis and gives an outlook to future projects.

7.1. Summary

Disk galaxies are very complex systems consisting of several components like the bulge, the disk and the halo. Additionally, substructures like extended HI disks, thin and thick stellar disks are observed. Contrary to elliptical galaxies, disk galaxies contain a significant mass fraction of gas. It is therefore an important question how gas physics influences the evolution of a galaxy, especially in its early state.

To address this question, I have presented a three-dimensional model for the chemodynamical evolution of galaxies, consisting of a hot and a cold gas phase and stars, embedded in a dark matter halo. The components interact with each other through several processes like star formation, evaporation and condensation, radiation cooling and dissipation, and mass and energy feedback from the stars. In this model, the dynamical, star formation and chemical evolution of the galaxy is followed. This enables comparison to a variety of observable properties, such as metallicity distribution or kinematics of the stars. Using the method of Westera et al. (2002) to calculate colors of the models at different redshifts including absorption, the models can also be directly compared to high redshift observations. The template of the numerical model was the three dimensional version of CoDEx (Samland et al., 1997). I have written the program in the F90 standard, which allowed for vectorization and partly parallelization of the code. Performance comparisons assure that the program runs very efficiently on different architectures.

Samland & Gerhard (2003) note that the poorly known cloud dissipation rate, the rate at which the cloudy medium can lose energy, is very important for galaxy evolution. It was pointed out in the description of the model that the cloud dissipation rate is not well-determined and may well vary between galaxies. To investigate its effect on disk evolution, I set up a sequence of models, where only the cloud dissipation efficiency was varied. I found that two evolutionary paths for the disk evolution exist in the context of the model, which are summarized below in more detail.

The evolutionary path of a galactic disk depends on whether it is the gas disk or the stellar disk which first becomes unstable. The stability analysis was done using the Toomre Q parameter of the cloudy and the stellar phase.

When the cold gas cools efficiently and drives the instability, the galactic disk fragments and forms a number of massive clumps. The stellar disk fragments with the gas because of the strong gravity of the clumps, which begin to form stars at a high rate because of their large density. The clumps then spiral to the center of the galaxy in a few dynamical times and merge there to form a central bulge component in a strong starburst. This scenario is similar to that discussed by Noguchi (1999). In this mode of disk evolution, the bulge forms rapidly and early; the unstable region of the disk is completely disrupted, and the disk must be rebuilt by subsequent infall. Because of the starburst origin, many of the bulge stars formed in this way have large [α/Fe] abundance ratios.

On the other hand, if the kinetic energy of the cold clouds is dissipated at a lower rate, stars form from the gas in a more quiescent mode, while keeping the kinetic temperature high enough and the gas density low enough to prevent the gas from becoming dynamically unstable. In this case, an instability only sets in at later times, when the surface density of the stellar disk has grown sufficiently high. The system then forms a stellar bar, which channels gas into the center, evolves, and forms a bulge whose stars are the result of a more extended star formation history, i.e., have lower [α/Fe]. This scenario resembles the evolution described by Combes & Sanders (1981), Pfenniger & Norman (1990) and Raha et al. (1991). The comparably long formation time for bars and bulges in this mode and the weakening of the bar through inward gas flow in the still gas-rich disks might explain the absence of bars at high redshift (Abraham et al., 1999). This is also consistent with the young age inferred for the Galactic bar (Cole & Weinberg, 2002).

An example of a nearby galaxy in which the fragmentation process may be taking place, is the gas-rich, blue starburst galaxy NGC 7673 (Homeier & Gallagher, 1999). At high redshift, chain and multi-clump morphological structures, as well as synchronized colors in clumpy objects, can be well explained by a fragmented disk model. The model suggests that these galaxies are in their formation process and are observed during their relatively short fragmentation phase, with a high SFR, comparable to the model SFR of up to 220 $\mathrm{M}_\odot\ \mathrm{yr}^{-1}$. Note that the high SFR is generated only by disk instability and there is no need for triggering through interaction or merger with other galaxies.

In the context of the model it is possible to examine the effect the clumps have on the observed rotation curve. In the clumpy phase, the effects of the single clumps on the mass-weighted rotation curve can be as high as 100 $\frac{\mathrm{km}}{\mathrm{s}}$. Nonetheless the underlying rotation signature should be observable. Additionally it is possible to investigate the metallicity difference between the single clumps. Although the clumps emerge from the same disk, their chemical evolution, depending mainly on their mass, can differ. However, the metallicity differences between the clumps are not larger than 0.25 dex.

The abundance ratios in the centers of nearby bulges show a moderate α overabundance ([α/Fe]$\simeq$ 0.2; Proctor & Sansom (2002)), arguing that these stars were formed from gas enriched by more extended star formation histories. The few [Mg/Fe] abundance ratio measurements available for the Galactic bulge (McWilliam & Rich, 1994), on the other hand, point towards more enhanced [α/Fe]. Consistent with this, Puzia et al. (2002) find a similar α-enhancement in three Galactic bulge fields as in bulge glob-

ular clusters, from integrated light measurements. Clearly, mixed star formation histories would also be possible, in which a part of the bulge formed in an early starburst, preceding a slower build-up of bulge stars from secular evolution of the disk. In the multi-phase galaxy evolution model of SG03, which follows the formation of a large disk galaxy in a growing ΛCDM dark matter halo, the final bulge is indeed a superposition of these two components with, in that model, the larger part of the mass in the secular component. The models suggest that the time-scale for secular disk evolution is comparable to or longer than that for Fe enrichment from SNIa, while the central starburst occurs before SNIa become important. Thus further spatially resolved measurements of [α/Fe] in bulges, and measurements of [α/Fe] vs Fe and radius for Galactic bulge stars will be key for disentangling bulge formation history.

The numerical simulations show that the energy input from supernovae leads to large scale gas flows within a galaxy, depending on the spatial distribution of the star forming regions. In the fragmented disk model each clump drives its own wind within a range of 5 kpc. Whereas in the thin disk model the collimated winds reach velocities of around 350 km/s, the outfbw velocities in the expanded disk models are around 150 km/s. The widely distributed star forming regions in the extended disk model cause less regular flow patterns. In both models, the hot gas cannot leave the potential of the galaxy. The distributed star formation in the extended disk model leads to a pressure supported bubble of hot gas, while the thin disk model exhibits a gas flow comparable to a galactic fountain. The winds occurring in the models show metallicities between 0.1 and 1 times solar abundance, depending on the mass loading and the star formation rate. Only at early times the winds show a significant α-enhancement.

It is well-known that the properties and evolution of a galactic disk depend on global parameters like mass, angular momentum, and infall rate. I have shown that the evolution may also depend strongly on the physics of the baryonic component, in particular, the uncertain energy dissipation rate of the cold cloud medium from which most stars are formed. This also implies that one cannot simply derive the accretion rate onto a galaxy by determining its star formation history. Although all the models in the sequence have an identical gas infall, very different SF histories are observed from one model to the other. In all models, however, the instability causes gas transport to the center, and a subsequent increase of the central SFR leading to the build-up of a central bulge component.

7.2. Outlook

I like to divide the outlook into two parts. In the first part I discuss possible improvements that can be made applying more detailed physical input and discuss shortly some technical aspects, mostly focused on the development of the Parallel Chemodynamical Evolution (PaCE) code. In a second part I give some examples of future scientific projects.

7.2.1. Physical and Technical Improvements

The improvements could consist of the following points:

- *Dark halo model*

  A growing halo according to the description of Wechsler et al. (2002) and Bullock et al. (2001) as applied by Samland & Gerhard (2003) can be implemented. The analytic halo could react on the gravitational potential of the baryonic matter through adiabatic contraction. A more sophisticated way is to implement a live dark halo. This requires a setup of an initially stable dark halo through particles or its consistent setup through input of cosmological simulations.

- *Substructure of the infall*

  Although some models calculated with clumpy infall with clump masses around 10^6 $M_\odot$ did not reveal significant changes to the disk evolution models, it will be interesting to see, how galaxy evolution changes under the influence of more massive infalling clumps. Also the infall of a dwarf galaxy, which not only consists of gas but also contains a significant fraction of stars is interesting to look at.

- *Interaction network*

  The interaction network described in the model may be complemented by further processes. The introduction of magnetic fields and thus an additional pressure could be important when describing outfbws and jets. However, the implementation of magneto-hydrodynamics would be time consuming and will increase the amount of memory significantly. Furthermore, UV background radiation or cosmic ray heating could be introduced. These heating mechanisms would influence mainly the gas in the halo, where SN heating is negligible.

- *Parallelization*

  The simulation is written in FORTRAN 90 and optimized to a high degree, on scalar and on vector environments. After the successful parallelization of the hydrodynamical part of the chemodynamical code, the next step is to implement a parallel version of the particle mesh code and the interactions. The main problem will be the interplay between the PM and the hydrodynamical code. The parallel version of the chemodynamical code will allow to calculate galaxy evolution models at

higher resolution and to larger radii than it was possible until now.

7.2.2. Future Scientific Projects

- *Disk evolution*

  The disk evolution models presented in this work can be further developed. Especially the role of a live dark halo and its interaction with the baryons mainly through angular momentum exchange, will be interesting to investigate. As was already mention in Chap. 4 the infall rate will influence the disk stability. Thus, models with varying infall rate could be calculated, to directly address this question. Additionally the infall and the build up of the dark halo should be implemented from the initial conditions of the cosmological simulations, as was already mentioned above.

- *Galactic superwinds*

  As was shown in Chap. 6, the structure of winds can be readily dealt with in the context of the chemodynamical model. Due to its importance for the enrichment of the intergalactic medium, it would be interesting to investigate a galactic wind from dwarf galaxies at an early epoch. An application of the model can also be the simulation of the observed superwinds in M82 and NGC 253. Several questions like the escape fraction of the material, the origin of the X-ray emission, the importance of mass loading and the mechanism of wind collimation could be investigated in such a model. The physics of the two-phase interstellar medium influences the winds (Samland, Immeli & Gerhard, in preparation), since the cooling/dissipation properties are different from a simple one phase interstellar medium used e.g. in the models of Mac Low & Ferrara (1999).

- *Dwarf galaxies*

  Using the mass accretion histories of the dark matter halos (Wechsler et al., 2002) allows for a self-consistent description. Such a model could also be used to explain properties of the dwarf galaxies, like the color-magnitude relation of dwarfs (Barazza & Binggeli, 2002) or the distribution of star formation regions in dwarf irregular galaxies (Parodi & Binggeli, 2003). Since in dwarf galaxies the detailed physics is very important, due to the weaker gravitational forces they are an excellent cite for understanding galaxy evolution.

- *Inhomogeneous chemical evolution*

  As already mentioned in Sect. B.3., an ongoing project is the investigation of the early halo enrichment using a similar model like Argast et al. (2000). The ability to resolve single supernova remnants allows for their dynamical description. As Argast et al. (2000) already mentioned the scatter in their model will get smaller, if a dynamical description is included. This is of particular interest, since recent observations reveal lower scatter in element abundances (Arnone et al., 2003). Because the scatter of the newer observations is very small, an efficient mixing is needed. One explanation might be that star formation in the early evolution of the halo takes mainly place in OB associations, since there the most efficient mixing of metals can be expected.

- *Galactic centers*

  With the high spatial resolution provided by PaCE it will become possible to simulate even the central bulge regions of galaxies, trying to explain recent observations of galaxy centers (Carollo et al., 2002). In the context of the disk evolution models, the influence of the formation path on the nuclear profiles can be determined.

To summarize, one can say that the applications for chemodynamical evolution models are very numerous. Especially their ability to predict observable quantities directly comparable to high redshift objects as well as to local observations make them a powerful tool.

A

Appendix: Dynamical Equations

A.1. Introduction

In this section I deduce the equations of motion for a gas consisting of particles with three spatial degrees of freedom. First, the derivation is done for a collision free system, using the moment approach, and in a second step the equations for a collision dominated system are derived, leading to the hydrodynamical equations for the ideal gas.

A.2. Vlasov and Boltzmann Equation

Because of the large number of particles in a gas the direct solution of the equations of motion for each particle is not possible. The dynamical description of the gas can only be done in a statistical way. Starting point of such a procedure is the definition of a time-dependent distribution function f, which is a function of the particle positions $\vec{x}$ and their momenta $\vec{p}$, in such a way that $f(\vec{x},\vec{p},t)d^3xd^3p$ gives the number of particles in the phase space volume element $d^3xd^3p = V_6$ at the time t. It follows directly from the definition that f must be integrable and positive everywhere. The evolution of the distribution function is described by the Boltzmann equation, which is derived here following Shu (1992).

Making the assumption that the mean free-flight timescale of a particle, given through the quotient of its mean free path and mean velocity, is much longer than the timescale, on which local interactions happen, the Hamilton function of a particle with mass m and phase space coordinates $(\vec{x},\vec{p})$ can be split into two terms:

$$H = H_{\rm sm} + H_{\rm col}$$

$H_{\rm sm}$ contains the effects of the slowly changing forces like gravity. Their properties can be described with conventional classical mechanics. In $H_{\rm col}$ terms like the collisions between atoms are collected, which can be only described by statistical means. The change of particles in the volume V_6 which comes from the smooth part of the Hamiltonian $H_{\rm sm}$ is caused by the flux through the surface of the volume V_6, which is given using the Hamilton equations

$$f\dot{x_i} = f\frac{\partial H_{\rm sm}}{\partial p_i} \qquad\qquad f\dot{p_i} = -f\frac{\partial H_{\rm sm}}{\partial x_i}$$

Another way for changing the number of particles in a phase space volume V_6 is through collisions with other particles. These collisions can be described as source term S and sink term O, as long as the mean free-flight time is much longer than the duration of the collisions. By using the divergence theorem to convert the surface integrals into volume integrals over V_6 one gets for the evolution of f

$$\int_{V_6} \frac{\partial f}{\partial t} + \frac{\partial}{\partial x_\mu}(f\frac{\partial H_{\rm sm}}{\partial p_\mu}) + \frac{\partial}{\partial p_\mu}(-f\frac{\partial H_{\rm sm}}{\partial x_\mu})d^3xd^3p = S - O \tag{A.1}$$

The term $S - O$ depends on the detailed physical processed involved in the scattering of particles. If like in a ideal gas the collisions only happen elastically, then the $S - O$ can be written as

$$S - O = \int_{V_6} (\frac{\partial f}{\partial t})_c d^3xd^3p \tag{A.2}$$

with the collisional term

$$(\frac{\partial f}{\partial t})_c = \int_{V_6} |\vec{v} - \vec{v_2}|\sigma(\Omega)[f(\vec{p_2'})f(\vec{p'}) - f(\vec{p_2})f(\vec{p})]d\Omega d^3p_2 \tag{A.3}$$

where $|\vec{v} - \vec{v_2}|$ is the relative velocity of the collision partners, which is a collisional invariant. $\sigma(\Omega)$ is the cross-section for elastic collisions, which is angle-dependent. The integration in equation A.3 spans all the solid angles and momenta of the collisional partner 2. A derivation of $(\frac{\partial f}{\partial t})_c$ is published in the book of Shu (1992). Since the integration volumes in equation A.1 can be chosen arbitrarily, the integrands in equation A.1 and A.2 have to be equal

$$\frac{\partial f}{\partial t} + \frac{\partial f}{\partial p_\mu}\frac{\partial H_{\rm sm}}{\partial x_\mu} - \frac{\partial f}{\partial x_\mu}\frac{\partial H_{\rm sm}}{\partial p_\mu} = (\frac{\partial f}{\partial t})_c$$

If it is assumed that the smooth changes are resulting from a gravitational potential Φ, $H_{\rm sm}$ can be replaced through $\frac{1}{2}\rho v_\mu^2 + m\Phi$ and one gets

$$\frac{\partial f}{\partial t} + v_\mu \frac{\partial f}{\partial x_\mu} - \frac{\partial \Phi}{\partial x_\mu}\frac{\partial f}{\partial v_\mu} = (\frac{\partial f}{\partial t})_c \tag{A.4}$$

where

$$(\frac{\partial f}{\partial t})_c = \int_{V_6} |\vec{v} - \vec{v_2}|\sigma(\Omega)[f(\vec{v_2'})f(\vec{v'}) - f(\vec{v_2})f(\vec{v})]d\Omega d^3 v_2 \tag{A.5}$$

Note that f is now the distribution function dependent on velocity rather than momentum, and m is the $\vec{x}, \vec{v}, t$-independent mass of a particle. Eq. A.4 is the well known Boltzmann equation. In the case of a collision free system, the collisional term is zero and we get the collisionless Boltzmann equation, which is also called Vlasov equation, given through

$$\frac{\partial f}{\partial t} + v_\mu \frac{\partial f}{\partial x_\mu} - \frac{\partial \Phi}{\partial x_\mu}\frac{\partial f}{\partial v_\mu} = 0 \tag{A.6}$$

A.3. Dynamical Equations of a Collision Free System

Since the Boltzmann equation is a 6^{th} order differential equation for the function f, depending on $6N$ variables, its direct solution is not practicable. But fortunately, to describe the evolution of a collision less system, one is not interested in the detailed velocity distribution of the particles at a position x at time t, but more in the density ρ, momentum density ρu and internal energy ϵ at this position. In other words, one is interested in quantities obtained by integrating over velocity space, the so-called moments. For a shorter notation, I use in the following the Einstein summation convention, which states that one has to take the sum over x, y, z for all double Greek indices within a mathematical term.

$$\frac{\partial v_\mu}{\partial x_\mu} = \sum_{\mu=x,y,z} \frac{\partial v_\mu}{\partial x_\mu}$$

There is no sum taken over the Latin indices like i and k. The mean $< . >$ of a quantity is defined through

$$<\chi>= \frac{1}{n}\int_V \chi f d^3 v \tag{A.7}$$

with $n := \int_V f d^3 v$. Below I use the notation

$$u :=<v> \qquad\qquad w := v - u$$

for the mean velocity or bulk velocity u and the peculiar velocity w.

To solve the Vlasov equation (Eq. A.6), it is multiplied with a power function $\chi(\vec{v})$ and integrated over the whole velocity space.

$$\int \left[\chi\frac{\partial f}{\partial t} + \chi v_\mu \frac{\partial f}{\partial x_\mu} - \chi\frac{\partial \Phi}{\partial x_\mu}\frac{\partial f}{\partial v_\mu}\right] d^3 v = 0$$

The single terms in the above equation are transformed to

$$\begin{aligned}
&\int \chi\frac{\partial f}{\partial t} d^3 v = \frac{\partial}{\partial t}\int \chi f d^3 v = \frac{\partial}{\partial t}(n <\chi>)\\
&\int \chi v_\mu \frac{\partial f}{\partial x_\mu} d^3 v = \frac{\partial}{\partial x_\mu}(\int \chi v_\mu f d^3 v) = \frac{\partial}{\partial x_\mu}(n <v_\mu \chi>)\\
&\int \chi\frac{\partial \Phi}{\partial x_\mu}\frac{\partial f}{\partial v_\mu} d^3 v = \frac{\partial \Phi}{\partial x_\mu}\int \chi\frac{\partial f}{\partial v_\mu} d^3 v = \frac{\partial \Phi}{\partial x_\mu}(\int \frac{\partial \chi f}{\partial v_\mu} d^3 v - \int \frac{\partial \chi}{\partial v_\mu} f d^3 v)\\
&\qquad = -\frac{\partial \Phi}{\partial x_\mu}\int \frac{\partial \chi}{\partial v_\mu} f d^3 v = -\frac{\partial \Phi}{\partial x_\mu} n <\frac{\partial \chi}{\partial v_\mu}>
\end{aligned}$$

where it was used that f vanishes faster for $\vec{v} \to \infty$ than any power of $\vec{v}$. This results in

$$\frac{\partial}{\partial t}(n <\chi>) + \frac{\partial}{\partial x_\mu}(n <v_\mu \chi>) + \frac{\partial \Phi}{\partial x_\mu} n <\frac{\partial \chi}{\partial v_\mu}>= 0 \tag{A.8}$$

A.3.1. Mass Conservation

The integral of $mf(\vec{x},\vec{v},t)$ over the velocity space is equal to the density ρ:

$$\rho = nm = \int_V mf(\vec{x},\vec{v},t)d^3v$$

To get the evolution of ρ one inserts $\chi = m$ into Eq. A.8.

$$\frac{\partial nm}{\partial t} + \frac{\partial}{\partial x_\mu}(nu_\mu m) + \frac{\partial \Phi}{\partial x_\mu} n <\frac{\partial m}{\partial v_\mu}>= 0$$

Since the mass m is not dependent on the velocity $\vec{v}$, this leads to the continuity equation or zeroth moment equation

$$\frac{\partial \rho}{\partial t} + \frac{\partial \rho u_\mu}{\partial x_\mu} = 0 \tag{A.9}$$

The continuity equation expresses the mass conservation. It also states that mass has to move continuously through the surface into or out of a volume element, it does not just vanish at one place and then shows up again at an other place.

A.3.2. Momentum Conservation

The first moment is the momentum density

$$\rho u_i = nm <v_i>= \int_V mv_i f(\vec{x},\vec{v},t)d^3v$$

Inserting $\chi = mv_i$ into equation A.8 and taking into account that $\frac{\partial v_i}{\partial v_\mu} = \delta_{i\mu}$ one gets

$$\frac{\partial}{\partial t}(\rho <v_i>) + \frac{\partial}{\partial x_\mu}(\rho <v_\mu v_i>) + \rho\frac{\partial \Phi}{\partial x_i} = 0 \tag{A.10}$$

The mean of the product of the velocity-components i and k can be expressed through the product of the mean velocities plus the mean of the relative velocities:

$$<v_iv_k>=<(u_i+w_i)(u_k+w_k)>= u_iu_k + u_k <w_i> + u_i <w_k> + <w_iw_k>= u_iu_k + <w_iw_k> \tag{A.11}$$

where the linearity of $<.>$ and $<w_k>= 0$ was used, which follows directly from the definition of the peculiar velocity. Next one defines

$$\sigma^2_{ik} :=<w_iw_k>=<v_iv_k> - u_iu_k \tag{A.12}$$

σ^2_{ik} is formally a component of a specific pressure tensor. The diagonal elements σ^2_{ii} describe the pressure acting along the coordinate axes, whereas the non-diagonal elements reflect the deflection of the pressure ellipsoid from the coordinate axes. From the definition of σ^2_{ik} one can directly recognize that it is a symmetrical tensor. Note that even if the system is collision-free, a formal pressure can be defined, as a cause of the diffusion in the system.

To get the 1. moment equation one inserts equation A.12 into equation A.10

$$\frac{\partial}{\partial t}(\rho u_i) + \frac{\partial}{\partial x_\mu}(\rho\sigma^2_{i\mu}) + \frac{\partial}{\partial x_\mu}(\rho u_iu_\mu) + \rho\frac{\partial \Phi}{\partial x_i} = 0 \qquad i = x,y,z \tag{A.13}$$

A.3.3. Energy Conservation

The differential equations for the second moments $\rho\sigma_{ik}$ for a collision free system are obtained by inserting $\chi = \frac{m}{2}v_iv_j$ into equation A.8.

$$\frac{\partial}{\partial t}(\rho <v_iv_j>) + \frac{\partial}{\partial x_\mu}(\rho <v_\mu(u_i+w_i)(u_j+w_j)>) + \frac{\partial \Phi}{\partial x_\mu}\rho <\frac{\partial v_iv_j}{\partial v_\mu}>= 0 \tag{A.14}$$

where the definitions of the mean and relative velocities was used. Using Eq. A.11, the first term is transformed to

$$\frac{\partial \rho <v_i v_j>}{\partial t} = \frac{\partial \rho u_i u_j}{\partial t} + \frac{\partial \rho <w_i w_j>}{\partial t}$$

and the second one

$$\begin{aligned}
&\frac{\partial}{\partial x_\mu}(\rho <v_\mu (u_i + w_i)(u_j + w_j)>) \\
&= \frac{\partial}{\partial x_\mu}(\rho <(u_\mu + w_\mu)(u_i + w_i)(u_j + w_j)>) \\
&= \frac{\partial}{\partial x_\mu}(\rho <u_\mu (u_i u_j + u_i w_j + u_j w_i + w_i w_j) + w_\mu (u_i u_j + u_i w_j + u_j w_i + w_i w_j)>) \\
&= \frac{\partial}{\partial x_\mu}(\rho (u_\mu u_i u_j + u_\mu <w_i w_j> + u_i <w_j w_\mu> + u_j <w_\mu w_i> + <w_\mu w_i w_j>)) \\
&= \frac{\partial \rho u_\mu u_i u_j}{\partial x_\mu} + \frac{\partial \rho u_\mu <w_i w_j>}{\partial x_\mu} + \frac{\partial \rho u_i <w_j w_\mu>}{\partial x_\mu} + \frac{\partial \rho u_j <w_\mu w_i>}{\partial x_\mu} + \frac{\partial \rho <w_\mu w_i w_j>}{\partial x_\mu} \\
&= \frac{\partial \rho u_\mu u_i u_j}{\partial x_\mu} + \frac{\partial \rho u_\mu \sigma_{ij}^2}{\partial x_\mu} + u_i \frac{\partial \rho \sigma_{j\mu}^2}{\partial x_\mu} + \rho \sigma_{j\mu}^2 \frac{\partial u_i}{\partial x_\mu} + u_j \frac{\partial \rho \sigma_{i\mu}^2}{\partial x_\mu} + \rho \sigma_{i\mu}^2 \frac{\partial u_j}{\partial x_\mu} + \frac{\partial \rho <w_i w_j w_\mu>}{\partial x_\mu}
\end{aligned}$$

and finally the third one

$$\frac{\partial \Phi}{\partial x_\mu} \rho <\frac{\partial v_i v_j}{\partial v_\mu}> = \frac{\partial \Phi}{\partial x_\mu} \rho (<v_j> \delta_{i\mu} + <v_i> \delta_{j\mu}) = \frac{\partial \Phi}{\partial x_i} \rho <v_j> + \frac{\partial \Phi}{\partial x_j} \rho <v_i> = \rho \frac{\partial \Phi}{\partial x_i} u_j + \rho \frac{\partial \Phi}{\partial x_j} u_i$$

Thus Eq. A.14 is equivalent to

$$\begin{aligned}
&\frac{\partial \rho \sigma_{ij}^2}{\partial t} + \frac{\partial \rho u_\mu \sigma_{ij}^2}{\partial x_\mu} + \rho \sigma_{j\mu}^2 \frac{\partial u_i}{\partial x_\mu} + \rho \sigma_{i\mu}^2 \frac{\partial u_j}{\partial x_\mu} + \frac{\partial \rho <w_i w_j w_\mu>}{\partial x_\mu} + \frac{\partial \rho u_i u_j}{\partial t} \\
&\qquad + \frac{\partial \rho u_\mu u_i u_j}{\partial x_\mu} + u_i \frac{\partial \rho \sigma_{j\mu}^2}{\partial x_\mu} + u_j \frac{\partial \rho \sigma_{i\mu}^2}{\partial x_\mu} + \rho \frac{\partial \Phi}{\partial x_i} u_j + \rho \frac{\partial \Phi}{\partial x_j} u_i = 0
\end{aligned} \tag{A.15}$$

Using the zeroth (Eq. A.9) and the first moment equation (Eq. A.13) one shows that

$$\begin{aligned}
&\frac{\partial \rho u_i u_j}{\partial t} + \frac{\partial \rho u_\mu u_i u_j}{\partial x_\mu} + u_j \frac{\partial \rho \sigma_{i\mu}^2}{\partial x_\mu} + u_i \frac{\partial \rho \sigma_{j\mu}^2}{\partial x_\mu} + \rho \frac{\partial \Phi}{\partial x_i} u_j + \rho \frac{\partial \Phi}{\partial x_j} u_i \\
&= \frac{\partial \rho u_i u_j}{\partial t} + \frac{\partial \rho u_\mu u_i u_j}{\partial x_\mu} + u_j \frac{\partial \rho \sigma_{i\mu}^2}{\partial x_\mu} + u_i \frac{\partial \rho \sigma_{j\mu}^2}{\partial x_\mu} - u_j \frac{\partial \rho u_i}{\partial t} - u_j \frac{\partial \rho \sigma_{i\mu}^2}{\partial x_\mu} - u_j \frac{\partial \rho u_i u_\mu}{\partial x_\mu} - u_i \frac{\partial \rho u_j}{\partial t} - u_i \frac{\partial \rho \sigma_{j\mu}^2}{\partial x_\mu} - u_i \frac{\partial \rho u_j u_\mu}{\partial x_\mu} \\
&= u_i \frac{\partial \rho u_j}{\partial t} + \rho u_j \frac{\partial u_i}{\partial t} + u_i \frac{\partial \rho u_\mu u_j}{\partial x_\mu} + \rho u_\mu u_j \frac{\partial u_i}{\partial x_\mu} - u_j \frac{\partial \rho u_i}{\partial t} - u_j \frac{\partial \rho u_i u_\mu}{\partial x_\mu} - u_i \frac{\partial \rho u_j}{\partial t} - u_i \frac{\partial \rho u_j u_\mu}{\partial x_\mu} \\
&= u_j \frac{\partial \rho u_i}{\partial t} - u_j u_i \frac{\partial \rho}{\partial t} + u_j \frac{\partial \rho u_\mu u_i}{\partial x_\mu} - u_j u_i \frac{\partial \rho u_\mu}{\partial x_\mu} - u_j \frac{\partial \rho u_i}{\partial t} - u_j \frac{\partial \rho u_i u_\mu}{\partial x_\mu} \\
&= - u_j u_i \frac{\partial \rho}{\partial t} - u_j u_i \frac{\partial \rho u_\mu}{\partial x_\mu} = -u_j u_i (\frac{\partial \rho}{\partial t} + \frac{\partial \rho u_\mu}{\partial x_\mu}) = 0
\end{aligned}$$

Equation A.15 therefore results in the 2. moment equation.

$$\frac{\partial \rho \sigma_{ij}^2}{\partial t} + \frac{\partial \rho u_\mu \sigma_{ij}^2}{\partial x_\mu} + \rho \sigma_{i\mu}^2 \frac{\partial u_j}{\partial x_\mu} + \rho \sigma_{j\mu}^2 \frac{\partial u_i}{\partial x_\mu} + \frac{\partial \rho <w_i w_j w_\mu>}{\partial x_\mu} = 0 \qquad i, j = x, y, z \tag{A.16}$$

In the description through the moment equations the n^{th} moment equation depends on the $n + 1^{th}$ moment. Hence, in principle the system of equations is infinite. However, the series can be aborted, if one moment is zero or negligible compared to the lower moments. The third moments, defined through

$$Q_{\mathrm{ijk}} := <w_\mathrm{i} w_\mathrm{j} w_\mathrm{k}>$$

conform to a heat flow tensor. In the zero heat flux approximation, the assumption is made that the spatial heat transport is negligible, which closes the system of momentum equations. This closure relation limits the system of differential

equations to a finite set. Application of the zero heat flux approximation is equivalent to the assumption that the cloud velocities are distributed according to a Schwarzschild distribution.

The moment equations derived above contain anisotropic velocity dispersions. The importance of the anisotropy is discussed widely in the literature concerning the dynamics of stellar systems. Also the clouds are not collision dominated in the sense of the hot gas, and therefore the collisions may not produce a isotropic pressure distribution, the ongoing creation and disruption of clouds in a galaxy tends to make the pressure isotropic.

Hence, the velocity dispersion of the clouds in this model is assumed to be *isotropic.*

$$\begin{aligned} \sigma_{ij} &= 0 \qquad & i \neq j \\ \sigma_{ii} &= \sigma_{jj} \qquad & i,j \in [x,y,z] \end{aligned}$$

Using these two approximations leads to the set of conservation equations used to describe the cloudy medium in this model.

- Mass conservation

$$\frac{\partial \rho}{\partial t} + \frac{\partial}{\partial x_\mu}(\rho u_\mu) = 0 \tag{A.17}$$

- Momentum conservation

$$\frac{\partial \rho u_i}{\partial t} + \frac{\partial \rho \sigma_{ii}^2}{\partial x_i} + \frac{\partial \rho u_i u_\mu}{\partial x_\mu} + \rho \frac{\partial \Phi}{\partial x_i} = 0 \qquad i = x,y,z \tag{A.18}$$

- Energy conservation

$$\frac{\partial \rho \sigma_{\mu\mu}^2}{\partial t} + \frac{\partial \rho u_\mu \sigma_{\nu\nu}^2}{\partial x_\mu} + 2\rho \sigma_{\mu\nu}^2 \frac{\partial u_\mu}{\partial x_\nu} = 0 \tag{A.19}$$

A.4. Dynamical Equations of a Collision Dominated System

In this section, I discuss the derivation of the hydrodynamical equations. In hydrodynamics one often uses the Lagrange derivative, which is defined as

$$\frac{D}{Dt} := \frac{\partial}{\partial t} + \vec{u} \cdot \vec{\nabla} \tag{A.20}$$

It describes the change which an observer sees, who is moving with the fluid. Its also called substantial derivative.

To derive the equations for a collision dominated system, I use the results obtained above. Analogously, the Boltzmann equation A.4 is multiplied with a function $\chi(\vec{v})$ and integrated over the whole velocity space.

$$\int \left[\chi \frac{\partial f}{\partial t} + \chi v_\mu \frac{\partial f}{\partial x_\mu} - \chi \frac{\partial \Phi}{\partial x_\mu} \frac{\partial f}{\partial v_\mu} \right] d^3v = \int \chi (\frac{\partial f}{\partial t})_c d^3v \tag{A.21}$$

Consider now the right side of this equation (see Eq. A.5). With the exception of $\chi(\vec{v})$, the integration variables $\vec{v}$ and $\vec{v_2}$ enter symmetrically, the following substitution can be made

$$\chi(\vec{v}) \rightarrow \frac{1}{2}[\chi(\vec{v}) + \chi(\vec{v}_2)]$$

Integration over the coated velocities instead of the uncoated ones yields the same result with the exception of the sign (Eq. A.5), because the relative velocity is a collisional constant. The change of the sign comes from the term $[f(\vec{v}_2')f(\vec{v}') - f(\vec{v}_2)f(\vec{v})]$. Another substitution is possible

$$\chi(\vec{v}) \rightarrow \frac{1}{4}[\chi(\vec{v}) + \chi(\vec{v}_2) - \chi(\vec{v}') - \chi(\vec{v}_2')]$$

where the change of the sign was accounted for in the last two terms. One sees that if $\chi(\vec{v})$ is a collisional invariant, the right side of A.21 equals zero. There exists five such χ in the non-relativistic regime of short-range forces.

$$\chi = m \qquad \chi = m v_i, \quad i = x,y,z \qquad \chi = \frac{m}{2}|\vec{v}|^2 \tag{A.22}$$

A.4.1. Mass Conservation

One gets the hydrodynamical equation for the mass by just doing some algebra. Equation A.9 gets

$$\frac{\partial \rho}{\partial t} + u_k \frac{\partial \rho}{\partial x_\mu} + \rho \frac{\partial u_k}{\partial x_\mu} = 0$$

which using the substantial derivate transforms to

$$\frac{D\rho}{Dt} + \rho \vec{\nabla} \vec{u} = 0 \tag{A.23}$$

This is the hydrodynamical equation for mass conservation.

A.4.2. Momentum Conservation

With σ_{ik}^2 it is possible to describe anisotropic pressures using the momentum equations. To derive the hydrodynamical equations for an ideal gas, where the pressure is assumed to be isotropic, one separates the trace of σ_{ik}

$$P := \frac{1}{3} \rho \sigma_{\mu\mu}^2 \tag{A.24}$$

referred to as gas pressure P from the rest, called the "viscous stress tensor" π_{ik}

$$\pi_{ik} := \rho(\frac{1}{3}\sigma_{\mu\mu}^2 \delta_{ik} - \sigma_{ik}^2)$$

Eq. A.13 can be written as

$$\frac{\partial \rho u_i}{\partial t} + \frac{\partial}{\partial x_\mu}(\rho u_i u_\mu + P\delta_{i\mu} - \pi_{i\mu}) = -\rho \frac{\partial \Phi}{\partial x_i} \qquad i = x, y, z$$

which is equivalent to

$$\frac{\partial \rho}{\partial t} u_i + \rho \frac{\partial u_i}{\partial t} + u_i \frac{\partial \rho u_\mu}{\partial x_\mu} + \rho u_\mu \frac{\partial u_i}{\partial x_\mu} + \frac{\partial}{\partial x_\mu}(P\delta_{i\mu} - \pi_{i\mu}) = -\rho \frac{\partial \Phi}{\partial x_i} \qquad i = x, y, z$$

Using equation A.9, the 1. and 3. term in the equation above vanish and one gets

$$\rho \frac{\partial u_i}{\partial t} + \rho u_\mu \frac{\partial u_i}{\partial x_\mu} + \frac{\partial}{\partial x_\mu}(P\delta_{i\mu} - \pi_{i\mu}) = -\rho \frac{\partial \Phi}{\partial x_i} \qquad i = x, y, z$$

Note that the flux of the ith component of the momentum density ρu_i in i-direction consists of the sum of a mean portion $\rho u_i u_\mu$ and a relative part, which is build from a isotropic component $P\delta_{i\mu}$ and an anisotropic (traceless) component $-\pi_{i\mu}$. Using the Einstein summation convention one can write in vector notation

$$\rho \frac{D\vec{u}}{Dt} = -\rho \vec{\nabla} \Phi - \vec{\nabla} P + \vec{\nabla} \pi \tag{A.25}$$

This is the hydrodynamical equation for momentum conservation.

A.4.3. Energy Conservation

The fifth collisional invariant is given through $\chi = \frac{1}{2} m |\vec{v}^2|$. The equation for this χ can be obtained, by using the equations for the 2. moment of the collision free system, by just adding the three 2. moment equations for diagonal elements (Eq. A.16). This leads to

$$\frac{\partial \rho \sigma_{\mu\mu}^2}{\partial t} + \frac{\partial \rho u_\nu \sigma_{\mu\mu}^2}{\partial x_\nu} + 2\rho \sigma_{\mu\nu}^2 \frac{\partial u_\mu}{\partial x_\nu} + \frac{\partial \rho < w_\nu w_\mu w_\mu >}{\partial x_\nu} = 0 \tag{A.26}$$

To obtain the hydrodynamical equations one defines the specific internal energy ϵ, which corresponds to the kinetic energy of the particles relative to bulk motion as

$$\epsilon := \frac{1}{2}\rho <w_\mu w_\mu>= \frac{1}{2}\rho\sigma^2 = \frac{3}{2}P$$

and the conductive heat flux F_i as

$$F_i := \frac{1}{2}\rho <w_i w_\mu w_\mu>$$

Note that through the definition of P and ϵ according to a ideal gas the equation of state of an ideal gas $P = (\gamma - 1)\epsilon$ with $\gamma = 5/3$ has been introduced. It is clear that through the definition of ϵ corresponding to the internal degrees of freedom the value of γ changes and therefore the hydrodynamical equations are valid with any γ.

Applying the definitions of the pressure and the viscous stress tensor leads to

$$\begin{aligned}\frac{\partial u_\mu}{\partial x_\nu}\pi_{\mu\nu} - \frac{\partial u_\nu}{\partial x_\nu}P =& \frac{\partial u_\mu}{\partial x_\nu}\rho <\frac{1}{3}w_\nu w_\nu \delta_{\mu\nu} - w_\mu w_\nu> - \frac{\partial u_\nu}{\partial x_\nu}\frac{1}{3}\rho <w_\nu w_\nu>= \\ & \frac{1}{3}\frac{\partial u_\mu}{\partial x_\nu}\rho <w_\nu w_\nu> \delta_{\mu\nu} - \frac{\partial u_\mu}{\partial x_\nu}\rho <w_\mu w_\nu> - \frac{\partial u_\nu}{\partial x_\nu}\frac{1}{3}\rho <w_\nu w_\nu>= -\rho\sigma^2_{\mu\nu}\frac{\partial u_\mu}{\partial x_\nu}\end{aligned}$$

and therefore equation A.26 is

$$\frac{\partial \epsilon}{\partial t} + \frac{\partial u_\mu \epsilon}{\partial x_\mu} = -P\frac{\partial u_\mu}{\partial x_\mu} - \frac{\partial F_k}{\partial x_k} + \pi_{\mu\nu}\frac{\partial u_\nu}{\partial x_\mu}$$

The last term is defined as the rate of the viscose dissipation

$$\Psi = \pi_{\mu\nu}\frac{\partial u_\nu}{\partial x_\mu}$$

On the left side there is again the continuity equation used

$$\begin{aligned}\frac{\partial \epsilon}{\partial t} + \frac{\partial u_\mu \epsilon}{\partial x_\mu} =& \rho\frac{\partial \epsilon/\rho}{\partial t} + \frac{\epsilon}{\rho}\frac{\partial \rho}{\partial t} + u_\mu\rho\frac{\partial \epsilon/\rho}{\partial x_\mu} + \epsilon\frac{\partial u_\mu}{\partial x_\mu} - \frac{\epsilon u_\mu}{\rho}\frac{\partial \rho}{\partial x_\mu}) \\ =& \rho\frac{\partial \epsilon/\rho}{\partial t} + u_\mu\rho\frac{\partial \epsilon/\rho}{\partial x_\mu} - \frac{\epsilon}{\rho}[\frac{\partial \rho}{\partial t} + \frac{\partial u_\mu \rho}{\partial x_\mu}] = \rho\frac{\partial \epsilon/\rho}{\partial t} + u_\mu\rho\frac{\partial \epsilon/\rho}{\partial x_\mu}\end{aligned}$$

with $\rho\frac{\partial \epsilon/\rho}{\partial x_\mu} = \frac{\partial \epsilon}{\partial x_\mu} - \frac{\epsilon}{\rho}\frac{\partial \rho}{\partial x_\mu}$ and one gets the hydrodynamical equation for energy conservation

$$\rho\frac{D}{Dt}(\frac{\epsilon}{\rho}) = -P\vec{\nabla}\vec{u} - \vec{\nabla}\vec{F}_{\rm cond} + \Psi \tag{A.27}$$

This is the equation for energy conservation in the form of the first sentence of thermodynamics. $-P\vec{\nabla}\vec{v}$ is the volume work, the two terms on the right describe the adding of heat through heat conduction and viscous conversion of ordered energy in differential fluid motions to disordered energy in random particle motions.

The hydrodynamical equations are five linear independent equations with 13 variables: ρ, u_i (3), P, π_{ik} (5 for a symmetric traceless tensor) und F_i (3). Hence, to solve these equations, we need closure relations. If the macroscopic length scale of the system is much larger the the mean free path for collisions of the atoms, the relations

$$F_i \simeq 0 \qquad \text{and} \qquad \pi_{\rm ik} \simeq 0$$

can be obtained by using the *Chapman-Enskog* procedure (Shu, 1992) to zeroth order. This leads to the Eulerian equations used to describe the dynamics of the ICM:

- continuity equation

$$\frac{D\rho}{Dt} + \rho\vec{\nabla}\vec{u} = 0 \tag{A.28}$$

- equations of motion

$$\rho \frac{D\vec{u}}{Dt} = -\rho \vec{\nabla} \Phi - \vec{\nabla} P \tag{A.29}$$

- internal energy equation

$$\rho \frac{D}{Dt}(\frac{\epsilon}{\rho}) = -P \vec{\nabla} \vec{u} \tag{A.30}$$

Applying the next order approximation of the Chapman-Enskog procedure, F_i and π_{ik} are not zero and one gets the Navier Stokes equations.

A.5. Formal Analogy and Description of the CM and the ICM

By applying the definitions for the pressure P and the internal energy density ϵ to the conservation equations of the clouds, one recognizes that they result in the hydrodynamical equations, as was shown in the above derivation. Therefore, a system described by the moment equations including isotropic pressure and zero heat flux approximation is formally equivalent to the hydrodynamical equations with the equation of state $P = (\gamma - 1)\epsilon$ with $F_i = 0$, $\pi_{ik} = 0$ and $\gamma = 5/3$.

The hot interstellar gas is described by the hydrodynamical equations. The particles of the gas are the single atoms, ions and electrons. The cold cloudy medium is described in a different way. The particles of the cloud gas are the clouds themselves. Because of the upper analogy, both gas phases can be described by the same equations, although they represent different physical systems.

B

Appendix: High Performance Computing

B.1. Code Optimization

In this appendix I discuss some of the experience I have gained when optimizing the code and porting it to vector and parallel environments. Due to the many different optimizations I have applied, it is not possible to give a complete optimization overview and I concentrate on some important points. I want to emphasize that this appendix is not meant for the expert programmer but should illustrate the importance of careful optimization and should be seen as a starting point for the novice programmer.

Simulating chemodynamical evolution of galaxies in three dimensions requires a large computation time effort. A typical simulation runs up to three months on a modern PC. Thus, it is very important to assure that the code is optimized to a high degree. This makes profiling of the code an indispensable task, which has to be done for every architecture individually. A code developed on a scalar machine has to be adopted to run efficiently under vector environment (Sect. B.2.). The expense is even higher when porting the code to parallel environments (Sect. B.3.).

In the following I mention some important points, I had to take care of to ensure good code performance. Some of these are well known and can be found in any book dealing with high performance computing, but others are more specific to the code used here. I have written the simulation in standard FORTRAN 90. The template was the three dimensional advancement of CoDEx, the 2D chemical evolution program (Samland et al., 1997), still written in FORTRAN 77. All examples use the F90 syntax. The compiler used is the Portland Group F90 compiler.

- *Nested loops*

  The numerical model is calculated on a three dimensional grid. The gas quantities, the gravitational potential, etc. are therefore three dimensional arrays. Since these arrays are aligned one-dimensionally in the memory of the computer one has to be careful in nesting loops over different dimensions. Loop nesting has to be done in such a way that the index of the innermost loop is the index which runs over the first index of the array, analog for the second one. This assures that the executing program can "walk" straight through the memory without any time-consuming jumps.

```
DO iy=1,n
 DO ix=1,n
  A(ix,iy) = expression
 END DO
END DO
```

  To show the effect of neglecting correct loop nesting I have compared correct versus false loop nesting. The outcome is shown in Fig. B.1 and clearly demonstrates the importance of this performance rule, because time loss can be up to a factor of 10. Since most of the computing time in the simulation is spent in nested loops, the careful check of each loop is indispensable and has to be done after each program modification or extension.

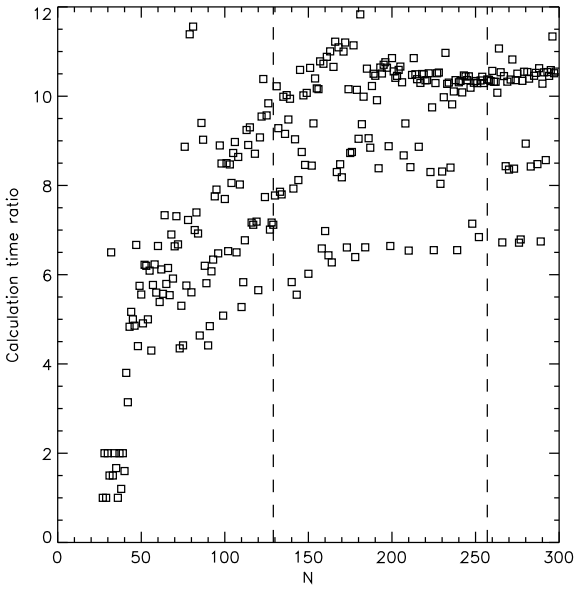

Figure B.1. Calculation time overhead of a falsely nested loop compared to the same correctly nested loop dependent on three dimensional grid size.

- *Array indexing within loops*

  In certain situations it is appropriate to give the indices to an array in form of a vector

```
DO ix=1,n
  A(index(ix)) = expression
ENDDO
```

  Since the compiler does not know the entries of `index` at compilation time, it can not apply certain optimization, which can heavily slow down the execution of the loop. Hence, in some parts of the code I had to turn down the elegance in programming to get a better performance.

- *Division through constants*

  Divisions are much more expensive than multiplications. In several parts of the code, divisions occur in the three dimensional loops. For a 100^3 grid every superfluous division has to be avoided, since it is done one million times per loop execution. If the division in a loop is done through a constant `const`, I defined an inverse constant `iconst = 1.0/const` and replaced the division through a multiplication. An analogous procedure is applied if the dividend is a variable that does

not change within the loop. Then the inverse of the variable is calculated right before the loop and again the division are replaced by multiplication. Although this fact is well known one has to check every loop on avoidable divisions time and again. I applied a similar procedure for multiplications of constants, which could be done before a loop, as e.g. in the calculation of the gas temperature from energy density and mass density.

- *Compiler directives*

  Several compiler directives are important. As an example, I will discuss the inline directive. Each subroutine call needs a certain amount of fbating point operations (FLOP). In the case of very small subroutines the fraction of the FLOPs used for the subroutine call in comparison to those used by the subroutine itself can get substantial. Therefore calls of short subroutines within large loops should be prevented. One possibility is to directly write the subroutine into the loop. Another, more elegant way is to give the compiler the directive to inline the subroutine at compilation time. I did the inlining for a subroutine which calculated the cooling function, and was invoked from the large loop calculating the interactions, and hence was called for every grid cell at least once. In connection with inlining the general rule applies: `DO` loops in subroutines not subroutines in `DO` loops.
  Another example would be loop unrolling, because also loop control statements need computation time and under certain circumstances short loops can be written in straight line code. However, I experienced that the compiler unroll directive does a better job than manual unrolling. Especially newer compilers apply optimizations to loops which they cannot apply to unrolled loops.
  Additionally I want to mention an important compiler flag of the compiler I used on the scalar machines (Portland Group). The use of the prefetch flag led to a 30% increase in performance of the program. This shows how important the testing of compiler directives and flags can be.

- *Code security vs. performance*

  F90 offers some of the "modern" programming features, like pointers, derived types, objects, etc. These structures can be used to enhance the code security very much. During development of the code I experienced that not all compilers optimize these features acceptably. For example the ABSOFT F90 compiler needs longer for the 3D vector addition, permitted in F90, than for the same addition written in correctly nested loops. Additionally, the pointers used in the scalar version of the code did inhibit vectorization (see Sect. B.2.).
  Due to the large memory effort, at some parts in the code the same arrays are used for different quantities (in the correct order, of course), which surely does not enhance code readability but is necessary to reduce the memory effort to get the simulation running on normal PCs. Generally, a fast executing code cannot be achieved with highest readability or code security. To get good performance, compromises to code security have to be made. This of course enlarges the effort needed to understand and edit the code. But the additional time needed to make changes in the code is easily compensated through the faster execution.

- *Potential solver*

  Fig. 3.5 and Fig. 3.12 already indicate that the application of a potential solver needs a careful implementation of the routines. As the test calculations I did for the FFT clearly show, choosing a "wrong" grid-size leads to performance loss of up to a factor of ten. These facts have to be remembered when using the FFT. The story is a bit more complex for SOR. There, for every new grid setup a best ω has to be found, mostly through testing. This procedure is time consuming but since the convergence depends strongly on the correct choice of ω, it is inevitable.

- *Algorithms*

  Much computation time can be saved by choosing an efficient algorithm. As an example I want to mention the determination of the location of a star on a logarithmically spaced grid. While in principle one could check one cell after the other whether the star is in this cell, it is much faster to apply a bisection method, where the grid range in which the star stays, is iteratively divided in half until the cell is found. As an example the search for a star using the direct check needs typically $n/2$ comparisons, whereas the bisection method only needs $\log_2(n)$ comparisons. This is only one example, where computation time can be saved by applying an efficient algorithm.

B.1.1. Data Output

A point more specific to the present simulation is the way of data output. Since the simulation typically allocates 1 Gigabyte of RAM, it is not practicable to save all data at every timestep. The output will therefore be restricted to certain quantities at given time step intervals. While developing the simulation I encountered three main points which are important concerning the output.

First, formatted output to ASCII files uses a lot of computation time and also disk space, since the ASCII output files are significantly larger than binary output. Additionally, the graphical visualization software, which I used to evaluate the model needs up to a factor of 10 more time to import

ASCII data instead of unformatted data. It is therefore absolutely necessary to direct all large data output into unformatted files. The additional effort in ensuring the portability of the data from one platform to the other (e.g. little endian format, big endian format) has to be accepted.

The second point deals with the large amount of data produced by the model. Not every timestep in the simulation can be saved and evaluated later. In the present case, the output is done after a time interval of 50 Myr. The disk evolution simulations discussed in Chap. 4, Chap. 5, and Chap. 6, are calculated for a time interval of 4 Gyr. Therefore typically 80 output files of around 200 MB result of a simulation run. Additionally to these $\sim$ 16 GB the stellar positions are saved every 10 Myr to enable the production movies of the evolution of the model. Hence a high resolution model (129^3 grid cells) typically needs 25 GB of disk space. When simulating the evolution over a Hubble time, the amount of data approaches 100 GB. This short estimation shows the importance of elaborated data management in analyzing the models. The above estimations are made for single precision output, which is accurate enough for further analysis.

As a third point I want to mention the location, where the output is done in the code. Any output interrupts the compiler optimization, which is especially grave for the performance on vector machines (Sect. B.2.). Hence output should take place at one point in the simulation, as can also be seen in the flowchart of the model (Fig. 3.17).

Another aspect about data output has to be mentioned. Due to the long calculation times of typically one to three months, the simulation must be able to restart after a machine shutdown. This is achieved by writing a restart file after a certain amount of iterations, corresponding to typically two hours of calculation time. In this file, all necessary data for the simulation restart is saved in double precision. To assure a trouble-free restart even if the simulation crashes during the writing of the restart file, I decided to implement an iterative restart file output, which writes the necessary data iteratively to two different files. This is especially important in parallel programs, since a network crash during the writing process would result in a damaged restart file.

B.1.2. Profiling

After I considered the points mentioned above I started with the profiling of the code. Generally, profiling of a simulation is a necessary step in code development. The information generated by profilers enables the identification of the functions, where the program spends the majority of the execution time. This allows for tracking down time consuming parts of the code, which ev. have to be rewritten or adopted. I found the profiling tools especially useful when porting the simulation to a new architecture.

During the profiling of the code, I applied the following iteration until the performance was satisfying

- Identification of the most time consuming routines using performance analysis tools available on the respective platform.
- Determination of the time consuming code sections within these routines.
- Optimization or rewriting of these code segments.

Since profiling tools reveal informations about subroutine or function calls, they can also be used to identify redundant or wrong calls and hence to improve code security.

B.2. Vectorization

When the scalar code was completed and first calculations were done, I had the opportunity to use the NEC SX-5 of the Centro Svizzero de Calcolo Scientifico (CSCS). Like many high performance computing systems the NEC SX-5 has a vector architecture. Vector machines can perform operations coeval on linear arrays of numbers, the so-called vectors (see Fig. B.2). I do not want to go into any further

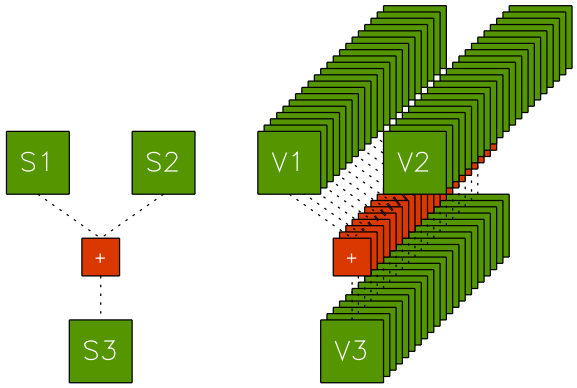

Figure B.2. Principle of vector architecture. The vector machine can perform operations coeval on linear arrays of numbers.

details of the different vector architectures but just mention some of the basic concepts, which have to be kept in mind when using vector machines.

As can be seen from the illustration in Fig. B.2, it is important that the vectorbanks are filled as much as possible. This is coterminous with the compiler being able to vectorize the code. Typically vectorization degrees of 90% are needed to benefit from the vector machine. Since the two dimensional code CoDEx already performed well on a CRAY Y-MP, which is also a vector machine, I decide to vectorize my numerical model.

I summarize the experience I gained when porting the code to the NEC SX-5. For a more complete reference of vectorization the reader is referred to the literature.

- In a nested loop, only the innermost loop is vectorizable. This was not a restriction for the present numerical model, since the innermost loop mostly runs over the x-dimension of the grid, which has a length of typically 129 grid cells. Problems may arise, when the innermost loop is very short and hence the vectorbanks can not be filled sufficiently. In such a case, the innermost loop would have to be unrolled, or the loop structure should be changed, if possible.
- Functions and subroutines should be inlined. As already mentioned above the subroutine for the cooling function was inlined in the loop, in which the interactions for all grid cells are calculated. Only this inlining allows for the vectorization of the large loop, which of course was important for the performance of the total simulation.
- Using pointers within a `DO` loop prevents vectorization. The compiler is not able to perform the dependency analysis needed to vectorize the loop. Since the scalar version of the code worked with pointers a minor effort had to be undertaken to rewrite the respective code sections.
- Any input or output within a `DO` loop prevents vectorization. A single `PRINT` statement can slow down the performance to unacceptable values. Hence I want to emphasize the implementation of a careful output structure again.
- While the above mentioned performance loss through dynamic array indexing on a scalar machine are under certain circumstances justifiable, the performance loss on a vector machine is unacceptable and this kind of array indexing has to be prevented (if possible, of course).
- Also recursion prevents vectorization. Since at one point in the model I could not circumvent recursion, I had to accept the performance forfeit. Since the routine is only called to place the new generated stars onto the grid about every 100^{th} iteration, this restriction is not grave.
- Branches inhibit vectorization in principle, but simple `IF-THEN-ELSE` statements, used e.g. in the advection routine, were vectorized without further effort.
- Other causes for prevention of vectorization are e.g. `CHARACTER` operations, jumps or branches into a `DO` loop, backward branches within a `DO` loop. Those constructs are not used in the model and hence these points did not influence the vectorization of the code.

A very important tool is the compiler listing, where the compiler gives detailed information about where the vectorization was successfully applied. Going through the listing reveals the passages of the code, which are not vectorized and possibly have to be circumscribed.

The present simulation achieved a vectorization degree of over 99% on the NEC SX-5 at CSCS, and therefore corresponding high performance values were reached. Direct quantitative comparison to other applications ensured that the numerical model is optimized to a high degree. The performance gain from the first try of executing the scalar code on the vector machine to the final vectorized version was a factor of 40, again showing the importance of careful optimization.

B.3. Parallelization

Vector machines are generally very expensive and consequently computation time contingents are normally not easy to get. A cheaper possibility of getting large calculation power is the setup of parallel environments, e.g. PC clusters. However, there is a drawback in the sense that adopting the code to parallel environments is very time consuming. To execute the simulation on a parallel machine, the compiler needs to have more information than a normal FORTRAN program can provide. For example, it should be possible to restrict parallelization to certain code segments and to assess the load and memory distribution onto the individual processors.

On the other hand, in a parallel environment numerical models can be calculated with high resolution and new projects can be faced (see Sect. 7.2.2). Whereas on a PC simulations with memory allocations of about 800 MB are possible, even an intermediate size PC cluster allows for 10-20 GB. This can be directly transferred to e.g. spatial resolution of the model.

To keep the effort as low as possible I decided to use High Performance FORTRAN (HPF) for the parallel version of the code. HPF offers the possibility of data parallel programming. The large part of the expensive and error-prone work of distributing the memory onto different processors is done by the compiler. Hence it is possible to achieve good parallel performance at reasonable expense. Since the code is written in F90 standard, the insertion of HPF commands is readily made. This can be totally different for FORTRAN 77 (F77) codes, where often large parts of the codes have to be rewritten, because e.g. common blocks can not be parallelized with HPF.

B.3.1. Parallelization with HPF

Although HPF provides a comparably low-cost way of creating parallel programs, the conversion of large programs still is far from straight forward. It is beyond the scope of this section to give a complete introduction to HPF. The interested reader is referred to the books of Gangsterer & Überhuber (2001) and Perrin & Darte

(1996). Additionally free introductions to HPF can be found at the Edinburgh Parallel Computing Center and one should also take a look at the HPF 2.0 language specification.

At the time of writing, I ported the hydrodynamical part of the numerical model to parallel architecture. First performance tests have been completed and look promising but clearly fine-tuning will be necessary to reach optimal performance. I summarize some of the experience a gained when adopting the hydrodynamics to the shared memory parallel environment of a PC cluster. Throughout the development of the parallel code, I used the HPF-compiler from the Portland Group. The PC cluster runs under the Scyld Beowulf Cluster Operating System.

- *Auto-parallelization*

  Auto-parallelization does a very bad job on large simulations like the present one. This option was completely useless, which is understandable looking at the partly complex code structure. The simulation could not even execute the setup routines, because a huge amount of unnecessary data transfer was done.

- *Memory alignment*

  Simulations of chemodynamical evolution need large amounts of memory. The full parallel code will use at least 10 GB of RAM. Hence it is very important that the memory is correctly distributed onto the single nodes and no unnecessary data transfer is done, because in the case of our PC cluster the network is the bottleneck. This all translates in the correct use of `DISTRIBUTE` and `ALIGN` directives of HPF. A wrong implementation of these directives slows down the execution of the program up to a factor of 100. This has the advantage that improper memory alignment is identified rather easily when executing the program. I further tried to minimize communication between the nodes through the specification of the `SHADOW` directive, used to define the overlap of the memory distribution. However, this did not influence the performance.

- *Data replication during loops*

  Loops in which every iteration can be calculated independently are well suited for parallelization. Since the compiler can often not decide on its own whether a loop is independent or not, the `INDEPENDENT` directive has to be given at the corresponding loops. Additionally, dummy variables introduced in the loop (e.g. to enhance code security or to save computation time) have to be "declared" as `NEW`. During the parallelization of the hydrodynamical code I could recognize wrong application of these directives very fast, because the performance loss in my numerical model was over a factor of 100. Only when all these directives are set correctly the parallel code performs acceptably on a distributed memory system.

- *Grid division*

  When first successful parallel tests of the hydrodynamical module were accomplished, I made an investigation on how the memory, or equivalently the grid, should be distributed on the single nodes. Using for example 8 processors, the division into eight equal sized cubes (Fig. B.3, left panel) on a first view seems to be the best choice, because the interfaces are the smallest and the communication expense the lowest. However, performance tests showed that the division along the z-axis (Fig. B.3, right panel) leads to a better result (Tab. B.1). I guess this is because the x and y-direction of the advection step can be done without any communication and therefore the computation time needed for this step nearly scales inversely with the number of processors used. On the other hand, the advection in z direction needs around a factor of 2.5 more computation time, due to the communication effort. At the time of writing I have no quantitative tests of other environments like the IBM SP 4 or other PC Clusters. I suspect that optimal grid division may depend on the machine used. These tests will soon be made, and hopefully give conclusive results about the importance of the network speed between the single nodes in respect to my numerical model.

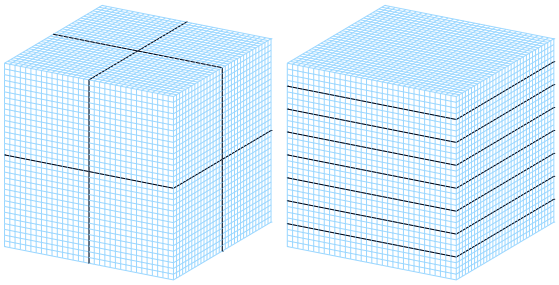

Figure B.3. Grid division for parallel computing. The best division depends on the numerical model used and one always should do some test calculations. In the case of the present numerical model, the best distribution is along the z-axis.

- *Choosing the nodes*

  The PC cluster of the astronomical institute has an inhomogeneous composition, since it grows from year to year. Some of the nodes are double processor machines. Not both processors of a single node should be used, since the network traffic to that node then doubles and performance goes down significantly. However, finding an appropriate compiler directive may solve this problem.

Abstract Processors	Distribution (b = block)	Calculation Time [msec]
(8)	(*,*,b)	272'580 (1.00)
(8)	(*,b,*)	291'120 (1.07)
(8)	(b,*,*)	575'544 (2.11)
(1,1,8)	(b,b,b)	374'322 (1.37)
(2,2,2)	(b,b,b)	369'786 (1.36)

Table B.1. Execution times of the advection routine in different abstract processor geometries. The dependence on the processor geometry is clearly visible. The advection was calculated for a 201^3 grid. In brackets the performance loss compared to the fastest geometry is given.

At the moment, the execution of the hydrodynamical routines lead to a performance gain of a factor of 3 calculated on 8 processors. This is comparably low but since the advection step is the routine where most communications has to be made the total numerical model should yield a performance gain of a factor 4 to 5. Clearly, fine tuning will be necessary in the code and on the PC cluster itself. Mature profiling tools are required for this task.

B.4. Analysis Library

Evaluating the numerical model presented in this chapter needs an elaborated data management which was already described in Sect. B.1.1. . The necessary data is written in equal time intervals to binary output files. To do the evaluation, I used the graphical visualization software PV-WAVE from Visual Numerics. I developed several routines to do the evaluation efficient and automatic as far as possible. The organization of my analysis library is as follows

- *Data import routines*

  These routines are able to import the data from the simulation output files. Due to the large amount of data, it is important to have import routines which can import only selected ranges from the binary data files of different models at different timesteps. This will be even more important when dealing with the output files of the parallel version of the program. These routines automatically recognize the file sizes and therefore determine parameters as grid resolution etc. on their own. This is very important for the automatization of the evaluation (see below).

- *Calculation routines*

  As was already mentioned, due to the large amount of data, only the really necessary data is stored. Any physical quantities which can be derived from others, will be calculated at evaluation time. This concerns for example quantities like surface densities, X-ray emissions, colors, temperatures, etc. Relatively short routines are directly written in the procedure language of WAVE, whereas larger routines are written in F90 and called from WAVE. This part of the library contains around 70 routines.

- *Visualization routines*

  These routines are responsible for the visualization of the results. Here, all routines which produce the plots used to discuss the models or to directly compare it to observations are included. The routines for movie creation also fall in this category. Due to the large diversity of graphical delineations there are by far more than 100 routines needed for an efficient evaluation.

- *Automatization of the evaluation*

  This point is very important when an overview over different models at different times is needed. These routines make completely automatic evaluations of the most important quantities of the model and produce graphical output (mostly jpeg-format). These files can be conveniently browsed with the use of php-scripts, accessible from each web browser, which has the authorization needed.

C

Appendix: Abbreviations and Symbols

C.1. Abbreviations

Abbreviation	Meaning
ALMA	Atacama Large Milimeter Array
CCD	Charge Coupled Device
CDM	Cold dark matter
CFL-condition	Courant-Friedrich-Lewi condition
CM	Cloudy medium
CMB	Cosmic microwave background
CIC	Cloud in cell
CoDEx	Chemo-dynamical evolution of galaxies
CSCS	Centro Svizzero de Calcolo Scientifico
F77	FORTRAN 77
F90	FORTRAN 90
FFT	Fast Fourier transformation
FT	Fourier transformation
GAIA	Global Astrometric Interferometer for Astrophysics
GISSEL	Galaxy Isochrone Spectral Synthesis Evolution Library
ICM	Intercloud medium
IGM	Intergalactic medium
ISM	Interstellar medium
JWST	James Webb Space Telescope
HDF	Hubble deep field
HMS	High mass stars
HPF	High performance FORTRAN
HST	Hubble Space Telescope
IMF	Initial mass function
IMS	Intermediate mass stars
LMS	Low mass stars
NFW-profile	Navarro-Frenk-White profile
NGC	New General Catalogue
NICMOS	Near Infrared Camera Multi-Object Spectrometer
PaCE	Parallel Chemodynamical Evolution Code
PM	Particle mesh
PN	Planetary nebula
SB/StB	Star burst
SFR	Star formation rate
SNIa	Supernova of type Ia
SNII	Supernova of type II
SOR	Successive overrelaxation
SSP	Single stellar population
ULIRG	Ultra luminous infrared galaxy
VLT	Very Large Telescope
WD	White dwarf
WMAP	Wilkinson Microwave Anisotropy Probe

C.2. Symbols

Symbol	Meaning
Cosmology	
z	redshift
$T_{\rm CMB}$	temperature of the cosmic microwave background
$\Omega_{\rm b}$	omega baryon
$\Omega_{\rm m}$	omega matter
Ω_Λ	cosmological constant
H_0	Hubble constant today
$\rho_{\rm crit}$	critical density of the universe
Dark matter halo	
$\rho_{\rm dark}$	dark matter density
$r_{\rm s}$	scale radius of the dark matter halo
r_0	smoothing length of the dark matter halo
$r_{\rm vir}$	virial radius of the dark halo
$z_{\rm f}$	formation redshift of the dark matter halo
M_h	mass of the dark halo in the mass accretion history
Gas	
$\rho, \rho_{\rm cm}, \rho_{\rm icm}$	gas density of the respective gas component
$\epsilon, \epsilon_{\rm cm}, \epsilon_{\rm icm}$	inner energy density of the respective gas component
$\vec{u}$	bulk or mean velocity
$\vec{v}$	velocity of a single gas particle
$\vec{w}$	velocity of a single gas particle relative to the mean motion
$f(\vec{x}, \vec{p}, t)$	one particle distribution function
$\sigma_{\rm CM}, \sigma$	cloud velocity dispersion
$T_{\rm icm}, T$	temperature of the ICM
T_6	$T/10^6$
$P, P_{\rm ICM}$	gas pressure of the respective gas component
$\tilde{P}$	ICM pressure in units of K cm^{-3} ($\tilde{P} := (P_{\rm icm}/k)/10^4$)
γ	adiabatic index ($\gamma = 5/3$)
Clouds	
$\lambda_{\rm F}$	Field length
$M_{\rm F}$	Field mass
$\lambda_{\rm k}$	effective mean free path for electron energy exchange
M_λ	corresponding mass to $\lambda_{\rm k}$
$M_{\rm lower}$	lower mass cut of the cloud mass function
$\Lambda(Z, T)$	ICM cooling function
$N(m)$	cloud mass function
β	exponent of the cloud mass function
$M_{\rm cloud}$	mass of a single cloud
$R_{\rm cloud}$	radius of a single cloud
$\phi_{\rm c}$	parameter for the influence of magnetic field on clouds structure
Stars	
$n(m)$	initial mass function of the stars
x	slope of the IMF
$M_{\rm l}$	lower mass cut of the IMF ($0.8\ {\rm M}_\odot$)
$M_{\rm u}$	upper mass cut of the IMF ($50\ {\rm M}_\odot$)
$M_{\rm m}$	limiting mass between low and high mass stars ($10\ {\rm M}_\odot$)

$\dot{\rho}_{\rm sf}$	star formation rate (SFR)
$\Sigma_{\rm sf}$	star formation surface density
$\Sigma_{\rm gas}$	gas surface density
M_i	initial mass of a stellar particle
$M(t,Z)$	mass-lifetime relation of the stars
$M_{\rm ret}$	mass return
$<M_{\rm SNII}>$	mean mass of SNII
$m_{\rm rem}(m)$	remnant mass
$e_{\rm SNII}$	energy input per mass of the SNII
$e_{\rm SNIa}$	energy input per mass of the SNIa
$e_{\rm PN}$	energy input per mass of the PN
Modell parameters	
$c_{\rm coll}$	efficiency parameter for cloud collisions
$c_{\rm evap}$	efficiency parameter for evaporation
$c_{\rm cond}$	efficiency parameter for condensation
$c_{\rm rad}$	efficiency parameter for radiation cooling
$c_{\rm sf}$	efficiency parameter for star formation
Colors	
ξ	band index (e.g. UBVK)
A_ξ	Absorption in the band ξ
c_ξ	Absorption parameter for band ξ
Diverse	
G	gravitational constant
m_h	proton mass
μ	mean molecular weight
k_b	Boltzmann constant
κ	coefficient of thermal conduction
$Q_{\rm eff}$	effective Toomre parameter
$Q_{\rm gas}$	Toomre parameter of the gas phase
$Q_{\rm star}$	Toomre parameter of the stellar phase
C_q	constant of the artificial viscosity
Φ	gravitational potential
Z	metallicity
t	time

Bibliography

Abadi, M. G., Navarro, J. F., Steinmetz, M., Eke, V. R. 2003, ApJ, 591, 499 52

Abraham, R. G., Tanvir, N. R., Santiago, B. X., Ellis, R. S, Glazebrook, K., van den Bergh, S. 1996, MNRAS, 279, L47 11, 52, 69

Abraham, R. G., Merrifield, M. R., Ellis, R. S., Tanvir, N. R., Brinchmann, J. 1999, MNRAS, 308, 569 11, 52, 64, 66, 82

Abraham, R. G. 1999, ApSS, 269, 323 52

Abraham, R. G., Merrifield, M. R. 2000, AJ, 120, 2835 11, 52

Abraham, R. G., van den Bergh, S. 2001, Science, 293, 1273 11, 68, 72

Abraham, R. G., van den Bergh, S. 2002, in "Disks of Galaxies: Kinematics, Dynamics and Perturbations", Eds. E. Athanassoula & A. Bosma, ASP Conf. Series 9, 11

Aguerri, J. A. L. 1999, A&A, 351, 43 61

Aguerri, J. A. L., Balcells, M., Peletier, R. F. 2001, A&A, 367, 428 13, 62

Anders, E., Grevesse, N. 1989, Geochim. Cosmochim. Acta, 53, 197 26

Argast, D., Samland, M., Gerhard, O., Thielemann, F.-K. 2000, A&A, 356, 873 11, 46, 49, 65, 84

Arnone, E., Ryan, S. G., Argast, D., "Inhomogenieties in the First Stars of the Galaxy", Poster at the UK National Astronomy Meeting (NAM2003 7/4/3), Trinity College Dublin, Ireland 49, 84

Aufderheide, M. B., Baron, E., Thielemann, F.-K. 1991, ApJ, 370, 630 26

Balsara, D., Ward-Thompson, D., Crutcher, R. M. 2001, MNRAS, 327, 715 53, 68

Barazza, F. D., Binggeli, B. 2002, A&A, 394, L15 84

Begelman, M. C., McKee, C.F. 1990, ApJ, 319, 575 20

Bekki, K., Shioya, Y. 1998, ApJ, 497, 108 13

Berczik, P. 1999, A&A, 348, 371 13

Bertoldi, F., McKee, C. F. 1995, Amazing Light, Ed. R. Y., Chiao, New York: Springer 30

Binney, J., Tremaine, S., Galactic Dynamics, Princeton University Press, 1987 31, 40

Boesgaard, A. M., Steigman G. 1985, ARAA 23, 319 8

Borkowski, K. J., Balbus, S. A., Fristrom, C. C. 1990, ApJ, 355, 501 19

Breitschwerdt, D. 2003, RevMexAA, 15, 311 74, 75, 79

Brinchmann, J., Abraham, R., Schade, D., Tresse, L., Ellis, R. S., Lilly, S., Le Fevre, O., Glazebrook, K., Hammer, F., Colless, M., Crampton, D., Broadhurst, T. 1998, ApJ, 499, 112 10, 52

Brinchmann, J., Ellis, R. S. 2000, ApJ, 536, L77 11

Bruzual, A. G., Charlot, S. 1993, ApJ, 405, 538 31

Buat, V., Deharveng, J. M., Donas, J. 1989, A&A, 223, 42 22

Buchmann, L., Azuma, R. E., Barnes, C. A., D'Auria, J. M., Dombsky, M., Giesen, U., Jackson, K. P., King, J. D., Korteling, R. G., McNeely, P. 1993, PhRvL, 70, 726 26

Bullock, J. S., Dekel, A., Kolatt, T. S., Kravtsov, A. V., Klypin, A. A., Porciani, C., Primack, J. R. 2001, ApJ, 555, 240 52

Bullock, J. S., Kolatt, T. S., Sigad, Y., Somerville, R. S., Kravtsov, A. V., Klypin, A. A., Primack, J. R., Dekel, A. 2001, MNRAS, 311, 559 8, 29, 83

Burkert, A. , Hensler, G. 1988, A&A, 199, 131 13

Burkert, A. 1995, ApJ, 447, L25 29

Buser, R. 1978, A&A, 62, 411 31

Carigi, L., Colin, P., Peimbert, M. 1999, ApJ, 514, 787 23

Carollo, C. M., Stiavelli, M., Mack, J. 1998, AJ, 116, 68 13

Carollo, C. M., Lilly, S. J. 2001, ApJ, 548, L153 69

Carollo, C. M., Stiavelli, M., Seigar, M., de Zeeuw, P. T., Dejonghe, H. 2002, AJ, 123, 159 84

Cha, S.-H., Whitworth, A. P. 2003, MNRAS, 340, 91 55

Chen, D. N., Jing, Y. P. 2002, MNRAS, 336, 55 52

Cheng, E. S., Cottingham, D. A., Fixsen, D. J., Inman, C. A., Kowitt, M. S., Meyer, S. S., Page, L. A., Puchalla, J. L., Ruhl, J. E., Silverberg, R. F. 1996, ApJ, 456, 71L 8

Chevalier, R. A., Clegg, A W. 1985, Nature, 317, 44 77

Chiba, M., Beers, T. 2000, AJ, 119, 2843 26, 62

Cimatti, A., Daddi, E., Mignoli, M., Pozzetti, L., Renzini, A., Zamorani, G., Broadhurst, T., Fontana, A., Saracco, P., Poli, F., Cristiani, S., D'Odorico, S., Giallongo, E.,

Gilmozzi, R., Menci, N. 2002, A&A, 381, L68 11

Cole, S., Lacey, C. G., Baugh, C. M., Frenk, C. S. 2000, MNRAS, 319, 168 13, 52

Cole, A. A., Weinberg, M. D. 2002, ApJ, 574, L43 82

Colella, P., Woodward, P. R. 1984, J. Comput. Phys., 54, 174 36

Combes, F., Sanders, R. H. 1981, A&A 96, 164 53, 62, 64, 66, 82

Contardo, G., Steinmetz, M., Fritze-v. Alvensleben, U. 1998, ApJ, 507, 497 52

Courteau, S., de Jong, R. S., Broeils, A. H. 1996, ApJ, 457, 73L 14, 53

Cowie, L. L., McKee, C. F. 1977, ApJ 211, 135 20

Cowie, L. L. 1980, ApJ, 236, 868 53

Cowie, L. L., McKee, C. F., Ostriker, J. P. 1981, ApJ, 247, 908 20

Cowie, L. L., Hu, E. M., Songaila, A. 1995, AJ, 110, 1576 (CHS95) 11, 53, 55, 66, 68

Cox, D. P. 1983, ApJ, 265, L61 30

D'Ercole, A., Brighenti, F. 1999, MNRAS, 309, 941 80

Dalcanton, J. J., Shectman, S. A. 1996, ApJ, 465, L9 69

Danielson, G. C., Lanczos, C. 1942, in "Some Improvements in Practical Fourier Analysis and Their Application to X-ray Scattering from Liquids", J. Franklin Inst., 233, 365 40

Das, M., Teuben, P. J., Vogel, S. N., Regan, M. W., Sheth, K., Harris, A. I., Jefferys W. H. 2003, ApJ, 582, 190 64

Davis, M., Wilkinson, D. T. 1974, ApJ, 192, 251 9

Dawson, S., Spinrad, H., Stern, D., Dey, A., van Breugel, W., de Vries, W., Reuland, M. 2002, ApJ, 570, 92 75

de Bernardis, P., Ade, P. A. R., Bock, J. J., Bond, J. R., Borrill, J., Boscaleri, A., Coble, K., Crill, B. P., De Gasperis, G., Farese, P. C., Ferreira, P. G., Ganga, K., Giacometti, M., Hivon, E., Hristov, V. V., Iacoangeli, A., Jaffe, A. H., Lange, A. E., Martinis, L., Masi, S., Mason, P. V., Mauskopf, P. D., Melchiorri, A., Miglio, L., Montroy, T., Netterfield, C. B., Pascale, E., Piacentini, F., Pogosyan, D., Prunet, S., Rao, S., Romeo, G., Ruhl, J. E., Scaramuzzi, F., Sforna, D., Vittorio, N. 2000, Nature, 404, 955 8

de Blok, W. J. G., McGaugh, S. S., Bosma, A., Rubin, V. C. 2001, ApJ, 552, L23 9, 29

Dickinson, M. 2000, in "Building Galaxies: From the Primordial Universe to the Present", XIXth Moriond Astrophysics Meeting, ed. F. Hammer et al. (Paris: Ed. Frontieres), 257 10, 11, 52, 68

Draine, B. T., Giuliani, J. L. 1984, ApJ, 281, 690 20

Dressler, A. 1980, Apj, 236, 351 13

Driver, S. P., Windhorst, R. A., Griffiths, R. E. 1995, ApJ, 453, 48 71

Driver, S. P., Fernandez-Soto, A., Couch, W. J., Odewahn, S. C., Windhorst, R. A., Phillips, S., Lanzetta, K., Yahil, A. 1998, ApJ, 496, 93 52

Durell, P. R., Harris W. E., Pritchet, C. J. 2001, ApJ, 121, 2557 61

Edvardsson, B., Andersen, J., Gustafsson, B., Lambert, D. L., Nissen, P. E., Tomkin, J. 1993, A&AS, 102, 603 12, 26, 62

Eggen, O. J., Lynden-Bell, D., Sandage, A. R. 1962, ApJ, 136, 748 12, 13, 62

Eke, V., Efstathiou, G., Wright, L. 2000, MNRAS, 315, L18 8, 9

Elmegreen, B. G. 1989, ApJ, 338, 178 16, 54

Elmegreen, B. G. 1989, ApJ, 344, 306 21

Elmegreen, B. G. 1994, ApJ, 425, L73 22

Elmegreen, B. G. 1995, MNRAS, 275, 944 53, 58

Elmegreen, B. G. 2001, in "From Darkness to Light", Asp Conf. Series, Eds Th. Montmerle and Ph. André. (San Francisco), ISBN 1-58381-081-1, 255 23

Ferguson, H. C., Dickinson, M., Williams, R. 2000, ARAA, 38, 667 10, 11

Ferguson, A. M. N., Irwin, M. J., Ibata, R. A., Lewis, G. F., Tanvir, N. R. 2002, AJ, 124, 1452 12

Fernandez-Soto, A., Lanzetta, K. M., Yahil, A. 1999, ApJ, 513, 34 11, 70

Ferrara, A., Tolstoy, E. 2000, MNRAS, 313, 291 26

Field, G. B., Goldsmith, D. W., Habing, H. J. 1969, ApJ, 155, L149 16

Font, A. S., Navarro, J. F., Stadel, J., Quinn, T. 2001, ApJ, 563, L1 9

Francois, P., Matteucci, F. 1993, A&A, 280, 136 13

Freeman, K., Bland-Hawthorn, J. 2002, ARAA, 40, 487 12

Friedli, D., Benz, W. 1993, A&A, 268, 65 14, 64

Fukugita, M., Shimasaku, K., Ichikawa, T. 1995, PASP, 107, 945 32

Gamow, G. 1948, Nature, 162, 680 8

Gangsterer, W., Überhuber, C. 2001, "Hochleistungsrechnen mit HPF", Springer-Verlag, Heidelberg, ISBN 2-540-42366-4 99

Giavalisco, M. 2002, ARAA, 40, 579 9, 11, 71

Gilmore, G., Wyse, R. F. G. 1986, Nature, 322, 806 12

Gingold, R. A., Monaghan, J. J. 1983, MNRAS, 204, 715 38, 55

G¨otz, M., K¨oppen, J. 1992, A&A, 262, 455 13

Godunov, S. K., 1959, Mat Sb, 47, 271 38

Grebel, E. K. 2001, ApSSS, 277, 231 12

Guiderdoni, B., Hivon, E., Bouchet, F. R., Maffei, B. 1998, MNRAS, 295, 877 13, 52

Hanany, S., Ade, P., Balbi, A., Bock, J., Borrill, J., Boscaleri, A., de Bernardis, P., Ferreira, P. G., Hristov, V. V., Jaffe, A. H., Lange, A. E., Lee, A. T., Mauskopf, P. D., Netterfield, C. B., Oh, S., Pascale, E., Rabii, B., Richards, P. L., Smoot, G. F., Stompor, R., Winant, C. D., Wu, J. H. P. 2000, ApJ, 545, L5 8

Hensler, G., Burkert, A. 1990, ApSS, 171, 149 13

Hockney, R. W., Eastwood, J.W. 1988, Computer Simulations Using Particles, Insitute of Physics Publishing, Bristol and Philadelphia 38, 40, 43

Hogg, D. W., Cohen, J. G., Blandford, R., Gwyn, S. D. J., Hartwick, F. D. A., Mobasher, B., Mazzei, P., Sawicki, M., Lin, H., Yee, H. K. C., Connolly, A. J., Brunner, R. J., Csabai, I., Dickinson, M., Subbarao, M. U., Szalay, A. S., Ferna'ndez-Soto, A., Lanzetta, K. M., Yahil, A. 1998, AJ, 115, 1418 11

Hogg, D. W. 1999, astro-ph/9905116 14

Homeier, N. L., Gallagher, J. S. 1999, ApJ, 522, 199 66, 71, 82

Hoyle, F., Fowler, W. A. 1960, ApJ, 132, 565 27

Hu, W., Dodelson, S. 2002, ARAA, 40, 171 8

Huang, S., Carlberg, R. G. 1997, ApJ, 480, 503 12

Ibata, R. A., Gilmore, G., Irwin, M. J. 1995, MNRAS, 277, 781 12

Imbriani, G., Limongi, M., Gialanella, L., Terrasi, F., Straniero, O., Chieffi, A. 2001, ApJ, 558, 903 26

Immeli, A. 1999, Diploma Thesis, University of Basel 13, 29

Immeli, A., Samland, M., Gerhard, O. E., Westera, P. 2003, ApJL, submitted 53, 54, 58, 62, 66, 68, 69, 75

Immeli, A., Samland, M., Gerhard, O. E., 2003, A&A, accepted 74

Jenkins, A., Frenk, C. S., White, S. D. M., Colberg, J. M., Cole, S., Evrard, A. E., Couchman, H. M. P., Yoshida, N. 2001, MNRAS, 321, 372 8, 9, 13, 52

Jog, C. J., Solomon, P. M., 1984, ApJ, 276, 114 53, 58

Karttunen, H., Kroeger, P., Oja, H., Poutanen, M., Donner, K.J. 2000, *Fundamental Astronomy*, Springer-Verlag, Berlin, ISBN: 3540609369 25

Kauffmann, G., White, S. D. M., Guiderdoni, B. 1993, MNRAS, 264, 201 13, 52

Kauffmann, G. 1996, MNRAS, 281, 487 13

Kajisawa, M., Yamada, T. 2001, PASJ, 53, 883 11, 52

Kennicutt, R. C. 1983, ApJ, 272, 54 23

Kennicutt, R. C., 1989, ApJ, 344, 685 22

Kennicutt, R. C., Tamblyn, P., Congdon, C.E. 1994, ApJ, 435, 22 23

Kennicutt, R. C., 1998, ApJ, 498, 541 22, 53, 68

Kim, J., Balsara, D., Mac Low, M.-M. 2001, JKAS, 34, 333 53, 68

Kippenhahn, R., Weigert, A. 1990, *Stellar Structure and Evolution*, Springer-Verlag, Berlin, ISBN: 3-540-58013-1 25

Klypin, A., Kravtsov, A. V., Bullock, J. S., Primak, J. R. 2001, ApJ, 554, 903 8, 13, 52

Klypin, A., Zhao, H., Somerville, R. S. 2002, ApJ, 573, 597 29

Koo, D. C., Kron, R. T. 1980, PASP, 92, 537 9

K¨oppen, J., Theis, C., Hensler, G. 1995, A&A, 286, 99 30

Kroupa, P. 2002, Science, 295, 82 23

Kuijken, K., Fisher, D., Merrifield, M. R. 1996, MNRAS, 283, 543 13

Landolt, A. U. 1983, AJ, 88, L439 31

Larson, R. B. 1969, MNRAS, 145, 405 17, 19, 53, 54, 68

Larson, R. B. 1975, MNRAS, 173, L671 13

Larson, R. B. 1992, in Star Formation in Stellar Systems, ed. G. Tenorio-Tagle, M. Prieto, & F. Sanchez (Cambridge: Cambridge Univ. Press), 125 22

Larson, R. B. 1999, in "Star Formation 1999", ed. T. Nakamoto (Nobeyama: Nobeyama Radio Observatory), 336 23

Lee, Y.-W., Joo, J.-M., Sohn, Y.-J., Rey, S.-C., Lee, H.-C., Walker, A. R. 1999, Nature, 402, 55 12

LeVeque, R. J., Numerical Methods for Conservation Laws, Birkh¨auser, 1992 38

LeVeque, R. J., Saas-Fee Advanced Course 27, Springer, 1998 38

Li, F., Ikeuchi, S. 1989, PASJ, 41, 221 13

Lilly, S., Schade, D., Ellis, R., Le Fevre, O., Brinchmann, J., Tresse, L., Abraham, R., Hammer, F., Crampton, D., Colless, M., Glazebrook, K., Mallen-Ornelas, G., Broadhurst, T. 1998, ApJ, 500, 75 52

Lowenthal, J. D., Koo, D. C. Guzman, R., Gallego, J., Phillips, A. C., Faber, S. M., Vogt, N. P., Illingworth, G. D., Gronwall, C. 1997, ApJ, 481, L673 69

Mac Low, M.-M., Ferrara, A. 1999, ApJ, 513, 142 77, 78, 84

Madau, P., Ferrara, A., Rees, M. J. 2001, ApJ, 555, 92 78

Maeder, A. 2001, ApSSS, 277, 291 26

Maeder, A., Meynet, G. 1989, A&A, 210, 155 24

Marcum, P. M., O'Connell, R. W., Fanelli, M. N., Cornett, R. H., Waller, W. H., Bohlin, R. C., Neff, S. G., Roberts, M. S., Smith, A. M., Cheng, K.-P., Collins, N. R., Hennessy, G. S., Hill, J. K., Hill, R. S., Hintzen, P., Landsman, W. B., Ohl, R. G., Parise, R. A., Smith, E. P., Freedman, W. L., Kuchinski, L. E., Madore, B., Angione, R., Palma, C., Talbert, F., Stecher, T. P. 2001, ApJS, 132, 129 10

Mather, J. C., Cheng, E. S., Eplee, R. E., Jr., Isaacman, R. B., Meyer, S. S., Shafer, R. A., Weiss, R., Wright, E. L., Bennett, C. L., Boggess, N. W., Dwek, E., Gulkis, S., Hauser, M. G., Janssen, M., Kelsall, T., Lubin, P. M., Moseley, S. H., Jr., Murdock, T. L., Silverberg, R. F., Smoot, G. F., Wilkinson, D. T. 1990, ApJ, 354, L37 8

Matthews, L. D., Gallagher, J. S., van Driel, W. 1999, AJ, 118, 2751 13

McKee, C. F., Ostriker, J. P. 1977, ApJ, 218, 148 16, 17, 19, 25, 26, 53, 68

McKee, C. F. 1990, in "The Evolution of The Interstellar Medium", ASP Conf. Proc. (San Francisco), 3 17

McKee, C. F., Begelman, M. C. 1990, ApJ, 358, 392 20, 21, 30

McWilliam, A., Rich, R. M. 1994, ApJS, 91, 749 63, 64, 66, 82

Merrifield, M. R. 2002, in "Disks of Galaxies: Kinematics, Dynamics and Perturbations", Eds. E. Athanassoula & A. Bosma, ASP Conf. Series 11

Mestel, L. 1965, Q.J.R.A.S., 6, 161 43

Meynet, G., Maeder, A. 1997, A&A, 321, 465 24

Miller, G. E., Scalo, J. M. 1979, ApJS, 41, 513 23

Miller, A. D., Caldwell, R., Devlin, M. J., Dorwart, W. B., Herbig, T. Nolta, M. R., Page, L. A., Puchalla, J., Torbet, E., Tran, H. T. 1999, ApJ, 524, L1 8

Molendi, S., de Grandi, S., Fusco-Femiano, R., Colafrancesco, S., Fiore, F., Nesci, R., Tamburelli, F. 1999, ApJ, 525, L73 74

M¨onchmeyer, R. , M¨uller, E. 1989, A&A, 217, 351 34

Moore, B., Governato, F., Quinn, T., Stadel, J., Lake, G. 1998, ApJ, 499, L5 8, 13, 52

Moore, B., Quinn, T., Governato, F., Stadel, J., Lake, G. 1999, MNRAS, 310, 1147 29

Moore, B., Ghigna, S., Governato, F., Lake, G., Quinn, T., Stadel, J., Tozzi, P. 1999, ApJ, 524, L19 9

Morrison M., McCammon D. 1983, ApJ, 270, 119 80

Motte, F., André, P., Neri, R. 1998, A&A, 336, 150 17

Navarro, J. F., White, S. D. M. 1994, MNRAS, 267, 401 13

Navarro, J. F., Frenk, C. S., White, S. D. M. 1996, ApJ, 462, 563 8, 52

Navarro, J. F., Frenk, C. S., White, S. D. M. 1997, ApJ, 490, 493 8, 29, 54

Navarro, J. F., Steinmetz, M. 1997, ApJ, 478, 13 47, 52

Noguchi, M. 1999, ApJ, 514, 77 14, 53, 54, 62, 65, 69, 82

Nomoto, K., Thielemann, F.-K., Yokoi, K. 1984, ApJ, 286, 644 11, 27, 28, 29

Nomoto, K., Iwamoto, K., Nakasato, N., Thielemann, F.-K., Brachwitz, F., Young, T., Shigeyama, T., Tsujimoto,

T., Yoshii, Y. 1996, RESCEU No. 28/96, (Tokyo: Univ. Tokyo) 11, 27, 29

Norman, M. L., Wilson, J. R., Barton, R. T. 1980, ApJ, 239, 968 35

Norman, C. A., Sellwood, J. A., Hasan, H. 1996, ApJ, 462, 114 14, 64

O'Neil, K., Bothun, G. D., Impey, C. D., 2000 ApJS, 128, 99 58, 69, 71

Osterbrock, D. E. 1989, Astrophysics of Gaseous Nebulae and Active Galactic Nuclei, University Science Books, Mill Valley (California) 27

Pagel, B. E. J. 1997, "Nucleosynthesis and Chemical Evolution of Galaxies", Cambridge University Press, ISBN 0 521 55958 8 15

Parodi, B. R., Binggeli, B. 2003, A&A, 398, 501 84

Partridge, R. B. 1974, ApJ, 192, 241 9

Peletier, R. F., Balcells, M. 1996, AJ, 111, 2238 53

Penzias, A. A., Wilson, R. W. 1965, ApJ, 142, 419 8

Perlmutter, S., Aldering, G., Goldhaber, G., Knop, R. A., Nugent, P., Castro, P. G., Deustua, S., Fabbro, S., Goobar, A., Groom, D. E., Hook, I. M., Kim, A. G., Kim, M. Y., Lee, J. C., Nunes, N. J., Pain, R., Pennypacker, C. R., Quimby, R., Lidman, C., Ellis, R. S., Irwin, M., McMahon, R. G., Ruiz-Lapuente, P., Walton, N., Schaefer, B., Boyle, B. J., Filippenko, A. V., Matheson, T., Fruchter, A. S., Panagia, N., Newberg, H. J. M., Couch, W. J. 1999, ApJ 517, 565 8, 9

Perrin, G.-R., Darte, A. 1996, "The Data Parallel Programming Model", Springer-Verlag, Heidelberg, ISBN 3-540-61736-1 99

Pettini, M., Steidel, C. C., Adelberger, K. L., Dickinson, M., Giavalisco, M. 2000, ApJ, 528, 96 78

Pfenniger, D., Norman, C. 1990, ApJ, 363, 391 14, 53, 62, 66, 82

Polyachenko, V. L, Polyachenko, E. V., Strel'Nikov, A. V. 1997, AstL, 23, 483 59

Power, C., Navarro, J. F., Jenkins, A., et al. 2003, MNRAS, 338, 14 29

Press W. H. , Teukolsky S. A., Vetterling W. T., Flannery B. P. 1986, Numerical Recipes in Fortran 77: The Art of Scientific Computing, Cambridge University Press 39, 40

Proctor, R. N., Sansom, A. E. 2002, MNRAS, 333, 517 66, 82

Puzia, T. H., Saglia, R. P., Kissler-Patig, M., Maraston, C., Greggio, L., Renzini, A., Ortolani, S. 2002, A&A, 395, 45 66, 82

Raha, N., Sellwood, J. A., James, R. A., Kahn, F. D. 1991, Nature, 352, 411 62, 66, 82

Rana, N. C., Wilkinson, D. A. 1986, MNRAS, 218, 497 13

Ramirez, S. V., Stephens, A. W., Frogel, J. A., DePoy, D. L. 2000, AJ, 120, 833 62

Raymond, J. C., Cox, D. P., Smith, B. W. 1976, ApJ, 204, 290 80

Riess, A. G., Filippenko, A. V., Challis, P., Clocchiatti, A., Diercks, A., Garnavich, P. M., Gilliland, R. L., Hogan, C. J., Jha, S., Kirshner, R. P., Leibundgut, B., Phillips, M. M., Reiss, D., Schmidt, B. P., Schommer, R. A., Smith, R. C., Spyromilio, J., Stubbs, C., Suntzeff, N. B., Tonry, J. 1998, AJ 116, 1009 8, 9

Romeo, B. R. 1992, MNRAS, 256, 307 58

Safranov, V. S. 1960, Ann. d'Ap., 23, 979 58

Salpeter, E. E., 1955, ApJ, 121, 161 23

Salucci, P., Burkert, A. 2000, ApJ, 537, L9 9, 29

Samland, M. 1994, PhD thesis, Univ. of Kiel, Germany 20, 21, 34, 80

Samland, M., Hensler, G. 1996, RvMA, 9, 277 30

Samland, M., Hensler, G., Theis, Ch. 1997, ApJ, 476, 544 12, 13, 15, 21, 74, 82, 96

Samland, M. 1998, ApJ, 496, 155 26, 28, 63

Samland, M., Gerhard, O. 2003, A&A, 399, 961 (SG03) 13, 15, 19, 21, 30, 33, 37, 47, 52, 53, 65, 68, 78, 82, 83

Samland, M. 2003, PASA, in press 79

Sandage, A. 1986, A&A, 161, 89 12

Sandage, A., Fouts, G. 1987, AJ, 93, 74 12

Sanders, D. B., Scoville, N. Z., Solomon, P. M. 1985, ApJ, 289, 373 17

Sarzi, M., Bertola, F., Cappellari, M., Corsini, E. M., Funes, J. G., Pizzella, A., Vega Beltran, J. C. 2001, ApSS, 276, 467 13

Scalo, J. M. 1986, Fund. Cos. Phys. 11, 1 23

Scalo, J. M. 1998, The Stellar Initial Mass Function, ASP Conference Series, Vol. 142, 201 23

Scannapieco, C., Tissera, P. B. 2003, MNRAS, 338, 880 14, 62

Schmidt, M. 1959, ApJ, 129, 243 22, 53, 68

Schramm, D. N., Turner, M. S. 1998, Rev. Mod. Phys., 70, 303 8

Scoville, N. Z., Evans, A. S., Thompson, R., Rieke, M. Hines, D. C., Low, J., Dinshaw, N, Surace, J. A., Armus, L. 2000, AJ, 119, 991 12

Searle, L., Zinn, R. 1978, ApJ, 225, 357 12

Seigar, M., Carollo, C. M., Stiavelli, M., de Zeeuw, P. T., Dejonghe, H. 2002, AJ, 123, 184 53

Shapiro, P. R., Field, G. B. 1976, ApJ, 205, 762 74, 75

Sheth, R. ., Tormen, G. 1999, MNRAS, 308, 119 9

Shu, F. H., The Physics of Astrophysics, Part II, Gas Dynamics, 1992 86, 92

Silich, S. A. 2003, RevMexAA, 15, 308 77

Silich, S. A., Tenorio-Tagle, G. 2001, ApJ, 552, 91 77

Sod, G. A., J. Comput. Phys., 27, 1, 1978 41

Sofue, Y., Habe, A. 1992, PASJ, 44, 325 13

Songaila, A., Cowie, L. L. 1996, AJ, 112, 335 74, 79

Sommer-Larsen, J., Gelato, S., Vedel, H. 1999, ApJ, 519, 501 47, 52

Sommer-Larsen, J., G¨otz, M., & Portinari, L. 2002, astro-ph/0204366 9, 48, 54, 68

Spergel, D. N., Verde, L., Peiris, H. V., Komatsu, E., Nolta, M. R., Bennett, C. L., Halpern, M., Hinshaw, G., Jarosik, N., Kogut, A., Limon, M., Meyer, S. S., Page, L., Tucker, G. S., Weiland, J. L., Wollack, E., Wright, E. L. 2003, ApJS, 148, 175 8

Spitzer, L. 1956, ApJ, 124, 20 16

Steidel, C. C., Giavalisco, M., Dickinson, M., Adelberger, K. L. 1996, AJ, 112, 352 68, 69, 71

Steidel, C. C., Adelberger K. L., Giavalisco M., Dickinson M. E., Pettini M. 1999, ApJ, 519, 1 9

Steinmetz, M., M¨uller, E. 1994, A&A, 281, L97 13

Steinmetz, M., M¨uller, E. 1995, MNRAS, 276, 549 47, 52

Stone, J. M., Norman, M. L. 1992, ApJS, 80, 753 33, 36, 42, 45

Strang, G., 1968, SIAM J. Num.Anal., 5, 506 35, 36

Strickland, D. K., Heckman, T. M., Waever, K. A., Dahlem, M. 2000, AJ, 120, 2965 75, 77, 79

Strickland, D. K., Stevens, I. R. 2000, MNRAS, 314, 511 80

Suchkov, A. A., Berman, V. G., Heckman, T. M., Balsara, D. S. 1996, ApJ, 463, 528 77, 79

Suchkov, A. A., Balsara, D. S., Heckman, T. M., Leitherer, C. 1994, ApJ, 430, 511 75, 77, 79

Sutherland, R. S., Dopita, M. A. 1993, ApJS, 88, 253 18

Tammann, G. A., L¨offler, W., Schr¨oder, A. 1994, ApJS, 92, 487 27

Taniguchi, Y., Shioya, Y. 2001, ApJ, 547, 146 69

Testi, L., Sargent, A. I. 1998, ApJ, 508, L91 17

Theis, C., Burkert, A., Hensler, G. 1992, A&A, 265, 465 13

Tiede, G. P., Terndrup, D. M. 1999, AJ, 118, 895 62

Thielemann, F.-K., Nomoto, K., Hashimoto, M. 1996, ApJ, 460, 408 11, 26

Timmes, F. X., Woosley, S. E., Weaver, T. A. 1995, ApJS, 98, 617 26

Tinsley, B. M. 1974, ApJ, 192, 629 11, 12

Tinsley, B. M. 1980, Fund. Cosm. Phys., 5, 287 12, 26

Toomre, A. 1964, ApJ, 139, 1217 53, 58

Vader, J. P. 1986, ApJ, 305, 669 74, 79

van den Bergh, S., Abraham, R. G., Ellis, R. S., Tanvir, N. R., Santiago, B. X., Glazebrook, K. G. 1996, AJ, 112, 359 11, 66, 68

van den Bergh, S., Cohen, J. G., Hogg, D. W., Blandford, R. 2000, AJ, 120, 2190 11, 52

van den Bergh, S., Abraham, R. G., Whyte, L. F., Merrifield, M. R., Eskridge, P. B., Frogel J. A., Pogge, R. 2002, AJ, 123, 2913 11, 52

van den Bosch, F. C. 2002, MNRAS, 332, 456 52, 61

Van den Hoek, L. B., Groenewegen, M. A. T. 1997, A&AS, 123, 305 27

Van Leer, B. 1977, J.Comp.Phys., 23, 276 36

Von Neumann, J., Richtmyer, R. D. 1950, Journal of Aplied Physics, 21, 232 37

Wakker, B. P., Van Woerden, H. 1997, ARAA, 35, 217 74, 75

Wang, B., Silk, J. 1994, ApJ, 427, 759 53, 58

Weaver, K. A., Heckman, T. M., Strickland, D. K., Dahlem, M. 2002, ApJ, 576, 19 79

Wechsler, R. H., Bullock, J. S., Primack, J. R., Kravtsov, A. V., Dekel, A. 2002, ApJ, 568, 52 8, 29, 52, 83, 84

Weidemann, V., Koester, D. 1983, A&A, 121, 77 24

Weinberg, S. 1977, *The First Three Minutes*, London, Andre Deutsch 7

Westera, P., Samland, M., Gerhard, O., Buser, R. 2002, A&A, 389, 761 31, 52, 54, 68, 82

White, S. M., Rees, M. J. 1978, MNRAS, 183, 341 9

Williams, R. E., Blacker, B., Dickinson, M., Dixon, W. VD., Ferguson, H. C., Fruchter, A. S., Giavalisco, M., Gilliland, R. L., Heyer, I., Katsanis, R., Levay, Z., Lucas, R. A., McElroy, D. B., Petro, L., Postman, M., Adorf, H.-M., Hook, R. 1996, AJ, 112, 1335 31, 69

Williams, P. R., Nelson, A. H. 2001, A&A, 374, 839 47, 52

Winkler, K.-H., Norman M. L., Astrophysical Radiation Hydrodynamics, Dodrecht Reidel, 1986, ISBN 90-277-2335-4 33, 34, 37, 42

Woodward, P. R., Colella, P., J. Comput. Phys., 54, 115, 1984 42

Woosley, S. E., Weaver, T. A. 1995, ApJS, 101, 181 11, 24, 26

Woosley, S. E. 1988, ApJ, 330, 218 25

Wyse, R. F. G., Gilmore, G. 1992, AJ, 104, 144 13

Wyse, R. F. G., Gilmore, G., Franx M. 1997, ARAA, 35, 637 13

Wyse, R. F. G. 1999, in "The Formation of Galctic Bulges", Eds. Carollo, Ferguson and Wyse, Cambridge Contemporary Astrophysics 13

Zoccali, M., Renzini, A., Ortolani, S., Greggio, L., Saviane, I., Cassisi, S., Rejkuba, M., Barbuy, B., Rich, R. M., Bica, E. 2003, A&A, 399, 931 62

List of Figures

1.1 WMAP, Credit: NASA/WMAP Science Team . . . 8
1.2 Structure Formation, Credit: Ben Moore, Virgo collaboration . . . 9
1.3 Galaxy Evolution from Observations . . . 10
2.2 Gas phases . . . 16
2.1 Interaction network . . . 17
2.3 Cooling function contributions . . . 18
2.4 Cooling Function . . . 19
2.5 Gas Evaporation in M16, Credit: J. Hester & P. Scowen (ASU), HST, NASA . . . 19
2.6 Values of $c_{\rm evap}$ . . . 21
2.7 Star formation Region, Credit: H. Yang (UIUC), HST, NASA . . . 22
2.8 Star formation surface density against gas surface density . . . 22
2.9 Different IMFs . . . 23
2.10 Mass lifetime relation . . . 24
2.11 Mass return rate . . . 25
2.12 Crab nebula, Credit: FORS Team, 8.2-meter VLT, ESO . . . 25
2.13 Little Ghost nebula, Credit: Hubble Heritage Team, NASA . . . 26
2.14 Supernova 1994D, Credit: High-Z Supernova Search Team, HST, NASA . . . 27
2.15 Supernova rate . . . 28
2.16 Dark halo profile . . . 29
2.17 Growing dark halo . . . 30
2.18 Color determination . . . 31
3.1 Grid numbering . . . 34
3.2 Advection Schemes . . . 36
3.3 SOR grid nomenclature . . . 38
3.4 SOR performance . . . 40
3.5 FFT performance . . . 41
3.6 Sod test . . . 42
3.7 Blast Waves . . . 42
3.8 Cold collapse . . . 43
3.9 Cloud in cell method . . . 44
3.10 Interaction timestep . . . 46
3.11 Example an improper set boundary . . . 46
3.12 Cyclic boundary condition . . . 46
3.13 Mirror boundary condition . . . 47
3.14 Open boundary condition . . . 47
3.15 Special boundary condition . . . 47

3.16 Initial Conditions . . . 48
3.17 Flowchart . . . 48
3.18 PaCE example . . . 50
4.1 Cut through the cold gas density . . . 55
4.2 Morphological evolution of the seven models . . . 56
4.2 Morphological evolution of the seven models - continued . . . 57
4.4 Time evolution of the Toomre parameter . . . 59
4.3 Toomre instability map . . . 60
4.5 Star formation rates . . . 61
4.6 Stellar mass fraction . . . 61
4.7 Distribution of stars in [Fe/H] . . . 62
4.8 Edge-on view of the inner 11 kpc . . . 63
4.9 Radial surface brightness profile . . . 63
4.10 [O/Fe] against [Fe/H] for bulge stars . . . 63
4.11 [Mg/Fe] distribution for bulge stars . . . 64
4.12 Stellar velocity dispersion of the bulge stars . . . 64
4.13 Bar evolution . . . 65
4.14 Pattern speed and bar length . . . 65
5.1 SFR of the model. . . . 68
5.2 Fragmentation phase in observed F606W surface brightness . . . 69
5.3 Comparison to observations . . . 70
5.4 Colors of the chain galaxy . . . 71
5.5 Rotation curve . . . 71
5.6 Stellar mass surface density . . . 71
6.1 Energy input distribution . . . 74
6.2 Wind in a clumpy disk . . . 75
6.4 Wind structure . . . 76
6.5 Oxygen distribution . . . 77
6.3 Time evolution of the wind pattern . . . 78
6.6 Surface density of high energy ICM gas . . . 78
6.7 Different X-ray sources . . . 79
B.1 Nested Loop Performance . . . 96
B.2 Vector architecture . . . 98
B.3 Grid division . . . 100

List of Tables

1.1 Cosmological parameters used in the model. 14
4.1 Dissipation efficiencies used in the model sequence, normalized to model D, where $c_{\rm coll}^{D} = 0.025$ (SG03). 54
5.1 Masses and metallicities of the stars in the clumps 72
B.1 Parallel Performance 101

Acknowledgements

At the completion of this work it is a great pleasure to thank the people who have supported me during my PhD Thesis.

I thank Markus Samland for his large effort he undertook in teaching me to work with numerical simulations. I also want to thank him for showing me, how scientific projects have to be planned and properly carried out. His guidance and insight has helped shape this work into what it is, and I appreciated very much his careful proof reading of draft papers and the final thesis manuscript. It was a great privilege to have a competent, patient and always friendly thesis adviser like him.

I thank Ortwin Gerhard for giving me the opportunity to write a PhD thesis in astronomy, for the scientific discussions and his effort in working through the publications.

Another thank goes to my former office colleague, Dominik Argast, even if he let me spent the last year alone in room number 9. It was always great fun to discuss with him the newest developments of the astronomical community as well as the latest happenings at the institute.

I want to thank my wife Maria for her patience when always having to listen to the problems arisen during the PhD and for helping me with mathematical questions. I thank my parents for supporting me during my studies.

I also want to thank the Centro Svizzero di Calcolo Scientifico (CSCS) for giving me the opportunity to use their computer facilities and for their always friendly and courteous way in helping me with any problems concerning the use of their machines. I also want to thank Hans Schwengeler for his effort in maintaining the institute's computation facilities.

I also want to thank Bono, Bruce, Herbert and the others for their assistance in times when motivation was needed.

Finally, I want to thank the Schweizerischer Nationalfonds for the financial support of the thesis.

Declaration

Ich erkl¨are, dass ich die Dissertation “Chemodynamical Modeling of Young Disk Galaxies” nur mit der darin angegebenen Hilfe verfasst und bei keiner anderen Fakult¨at eingereicht habe.

Basel, den 5. Oktober 2003

Andreas Immeli